Functional Annotation of Ion Channel Pores by Molecular Simulations



Shanlin Rao

Department of Biochemistry and

Hertford College, Oxford

A thesis submitted in partial fulfilment of the requirements for the degree of Doctor of Philosophy at the University of Oxford

Michaelmas 2020

Acknowledgements

My supervisors, **Prof. Mark Sansom** and **Prof. Stephen Tucker**, are to this project as sunlight to an autotrophic plant. For their trusting me to water and care for it; for their guidance, advice, and endless patience as I explored each branch that could be; and for all that they have taught me, both regarding the science and as a scientist, I am grateful beyond words.

I have been very fortunate to work alongside an amazing teammate, **Dr Gianni Klesse**, whose meticulous efforts in creating and enhancing CHAP as a software paved the way for my own side of the hydrophobic gating project, and whose physicist perspective and insights remain a greatly appreciated influence.

Much debt of gratitude is also owed to **Prof. Phill Stansfeld**, who first led me into the world of molecular modelling and simulations, and who has always been generous with his extensive knowledge, insightful suggestions, and enthusiasm in the subject. Like both my doctoral mentors, he has continued to be an inspiration as a dedicated, curious scientist.

Additionally, I would like to thank **Prof. Phil Biggin** and **Prof. Jason Schnell**, whose incisive comments at an early stage of the project have helped to resolve its focus and strengthen its subsequent development, and **Prof. Sudha Chakrapani** and her group for their generosity in entrusting their channel structures to these computational analyses.

SBCB has provided a most wonderful environment that nurtured this research, and I have much to learn from everyone still. An immense thank you is due particularly to **Dr Tom Newport**, **Dr George Hedger**, **Dr Laura Sobola**, **Dr Jemma Trick**, **Dr Viwan Jarerattanachat**, **Dr Anna Duncan**, **Prof. Chen Song**, **Prof. Maria Musgaard**, **Dr George Gerogiokas**, **Dr Jan Domański**, **Dr Owen Vickery**, **Dr Robin Corey**, and **Dr Wanling Song**, who have been incredibly kind in sharing their time and expertise in coding or MD with me; and to **Dr Richard Bryan**, **Dr John Elder**, **Martin Ackland**, **Michael Horrell**, **Dr Irfan Alibay**, and **Dr Nick Michelarakis**, who have been great saviours at times of IT crises.

Finally, the project owes its twigs and leaves to an unsung member of the team as well, who was made to work 24/7 more often than not, was hospitalised twice and recovered, dignified. My respect and thanks to workstation **M37**, for their solidity and resilience.

(Whilst it seems customary for one to end with thanks of a more personal nature, I do not feel it is the place to express my gratitude to family and friends, to whose support and company I am indebted in ways entirely independent of a piece of academic writing that documents research conducted through my years as a graduate student. This thesis would have been dedicated to my parents, but I believe they deserve nicer.)

Abstract

Ion channels constitute crucial components of biological membranes and represent a major class of pharmacological targets. In response to specific stimuli, conformational changes in these proteins may lead to expansion or constriction of the channel pore in its gate region(s) to permit or preclude transmembrane ion transport. With an increasing number of molecular structures being resolved for families of ion channels in alternative conformations, this thesis concerns the assessment of relative hydrophobicity of the pore lining to complement measurements of pore dimensions for predicting whether ion conduction is likely to be possible in each captured conformational state. Molecular dynamics simulations were used to examine the effect of hydrophobic gating, whereby the passage of water and ions through an apolar region may be energetically disfavoured without steric occlusion of the pore.

A hydrophobic gate was identified in the bestrophin-1 channel, with simulations upon *in silico* mutagenesis of its distinct pore-lining motif revealing a clear dependence of pore hydration on the polarity of the substituting amino acid. The combined influence of local hydrophobicity and pore radius was quantified based on simulations and machine learning-assisted analysis of 190 ion channel structures. A simple scoring model thus derived is able to rapidly detect the presence of hydrophobic barriers to permeation among channel structures. Evaluated against levels of ionic flux supported by channel structures, simulated via computational electrophysiology, the model performed reasonably reliably as a first indicator of ion channel conductive state. On the basis of the investigation, a three-tiered pipeline has been suggested to facilitate efficient annotation and classification of ion channel structures. This offers a starting point for more detailed functional and mechanistic studies. Furthermore, the approach is anticipated to be capable of aiding the design and engineering of peptide-based nanopores that contain switchable hydrophobic gates.

Publications

Results described in this thesis have contributed to the following publications:

1. Rao, S., Klesse, G., Stansfeld, P. J., Tucker, S. J. and Sansom, M. S. P. A BEST example of channel structure annotation by molecular simulation. *Channels (Austin, Tex.)* **11**, 347–353 (2017)

2. Rao, S., Lynch, C. I., Klesse, G., Oakley, G. E., Stansfeld, P. J., Tucker, S. J. and Sansom, M. S. P. Water and hydrophobic gates in ion channels and nanopores. *Faraday Discussions* **209**, 231–247 (2018)

3. Basak, S., Gicheru, Y., Rao, S., Sansom, M. S. P. and Chakrapani, S. Cryo-EM reveals two distinct serotonin-bound conformations of full-length 5-HT_{3A} receptor. *Nature* **563**, 270–274 (2018)

4. Rao, S., Klesse, G., Stansfeld, P. J., Tucker, S. J. and Sansom, M. S. P. A heuristic derived from analysis of the ion channel structural proteome permits the rapid identification of hydrophobic gates. *Proceedings of the National Academy of Sciences of the United States of America* **116**, 13989–13995 (2019)

5. Klesse, G., Rao, S., Sansom, M. S. P. and Tucker, S. J. CHAP: A versatile tool for the structural and functional annotation of ion channel pores. *Journal of Molecular Biology* **431**, 3353–3365 (2019)

6. Kumar, A., Basak, S., Rao, S., Gicheru, Y., Mayer, M. L., Sansom, M. S. P. and Chakrapani, S. Mechanisms of activation and desensitization of full-length glycine receptor in lipid nanodiscs. *Nature Communications* **11**, 3752 (2020)

7. Flegler, V. J., Rasmussen, A., Rao, S., Wu, N., Zenobi, R., Sansom, M. S. P., Hedrich, R., Rasmussen, T. and Böttcher, B. The MscS-like channel YnaI has a gating mechanism based on flexible pore helices. *Proceedings of the National Academy of Sciences of the United States of America* **117**, 28754–28762 (2020)

Contents

List of Figures **xi**

List of Tables **xiii**

1 Introduction **1**

1.1 Ion Channel Proteins: Features and Functions 1
1.1.1 Channels and pores in biological membranes 1
1.1.2 Gating, selectivity, and structure of ion channels 4
1.1.2.1 Pentameric ligand-gated ion channels 6
1.1.3 Ion channels as pharmacological targets 7
1.2 From Molecular Structures to Mechanistic Models 7
1.3 Hydrophobic Gating in Channels and Nanopores 10
1.3.1 Insights from simulation studies on model pores 11
1.3.2 Influence of hydrophobicity among ion channels 12
1.3.3 Molecular dynamics to aid functional annotation 14
1.4 Objectives and Approaches of Present Investigation 15

2 Theory and Methods **17**

2.1 Molecular Dynamics Simulations 17
2.1.1 Principles of molecular dynamics 17
2.1.1.1 Molecular mechanics 18
2.1.1.2 Energy minimisation 23
2.1.1.3 Integration algorithms 23
2.1.2 Simulation settings and parameters 24
2.1.2.1 Temperature and pressure control 24
2.1.2.2 Periodic boundary conditions 26
2.1.2.3 Force fields 26
2.1.2.4 Water models 27
2.1.3 Potential of mean force calculation 29
2.2 Poisson-Boltzmann Electrostatics 30
2.3 Measurement of Pore Dimensions 31
2.3.1 HOLE programme and alternatives 31
2.3.2 The Channel Annotation Package 33

3 Effects of size and polarity: Insights from bestrophin-1 mutants 35
3.1 Methods . . . 37
3.1.1 Equilibrium molecular dynamics simulations . . . 37
3.1.2 Boltzmann inversion and free energy profiles . . . 38
3.1.3 Umbrella sampling and potential of mean force calculation . . . 40
3.2 Results and Discussion . . . 40
3.2.1 A hydrophobic gate in the wild-type structure . . . 40
3.2.2 Pore widening removes the free energy barrier . . . 43
3.2.3 Robustness of protocol for structure annotation . . . 43
3.2.4 Increasing gate polarity yields distinct profiles . . . 45
3.3 Conclusion . . . 48

4 A global survey across the ion channel structural proteome 49
4.1 Methods . . . 52
4.1.1 Preparation of ion channel structures . . . 52
4.1.2 Equilibrium simulations and analysis . . . 54
4.1.3 Support vector machine modelling . . . 55
4.2 Results and Discussion . . . 55
4.2.1 Quantification of pore-lining hydrophobicity . . . 55
4.2.2 Protocol for channel simulation and analysis . . . 57
4.2.3 Analysis of the main energetic barrier in each structure . . . 59
4.2.4 Analysis of all residues lining ion channel pores . . . 66
4.2.5 A heuristic for prediction of pore hydration state . . . 71
4.3 Conclusion . . . 77

5 From water to ions: Assessment of channel conduction state 79
5.1 Methods . . . 84
5.1.1 Structure-based analysis and equilibrium simulations . . . 84
5.1.2 Computational electrophysiology . . . 85
5.1.3 Continuum electrostatic calculations . . . 86
5.2 Results and Discussion . . . 86
5.2.1 Choice of simulation conditions and robustness of the approach . . . 86
5.2.2 A pipeline for functional annotation of new channel structures . . . 91
5.2.3 Pore hydration level as indicator of ion channel conduction state . . . 102
5.3 Conclusion . . . 113

6 Summary and Future Directions 115

References 119

List of Figures

1.1 Examples of biological channel and pores embedded in a membrane . . . 3
1.2 Gate and selectivity filter regions of ion channels from two families 5
1.3 Number of published ion channel structures in the Protein Data Bank . . . 8
1.4 Structures of the glycine receptor in alternative conformational states . . . 9
1.5 Hydrophobic gating effect in pores of sub-nanometre dimensions 10
1.6 Influence of hydrophobicity on levels of hydration within nanopores . . . 12

2.1 Potential energy terms describing bonded interactions in a force field . . . 20
2.2 Potential energy terms describing non-bonded atomic interactions 22
2.3 Geometry of three- and four-point rigid fixed-charge water models 28
2.4 Schematic representation of probe-based pathway-finding method 32

3.1 Structure and inner pore surface of the closed bestrophin-1 channel 36
3.2 Molecular dynamics simulation and analysis of hydrophobic gating 39
3.3 De-wetting of hydrophobic neck region within bestrophin-1 pore 41
3.4 Radius and water free energy profiles of wild-type and mutant pores . . . 42
3.5 Robustness of the simulation approach to annotating channel pores 44
3.6 Free energy of water around gate region of bestrophin-1 mutants 46
3.7 Pore radius, hydrophobicity, and water free energy in mutant gates 47

4.1 Experimentally measured relative hydrophobicity of amino acids 51
4.2 Resolution of ion channel structures in the Protein Data Bank 52
4.3 Montage of 190 ion channel structures included in the analysis 53
4.4 Methods for estimating hydrophobicity profiles of the channel lining . . . 56
4.5 Pore profiles derived from simulations of a TRPV4 structure 58
4.6 Energetic barriers to water permeation through channel pores 59
4.7 Prevalance of pore-lining amino acid side chains at energetic barriers . . . 60
4.8 Distribution of local pore water density values sampled 67
4.9 Pore water free energy landscape in the hydrophobicity-radius plane . . . 68
4.10 Mean water free energy among subsets of channel structure data 69
4.11 Support vector modelling of local pore water free energy 70
4.12 Schematic of heuristic prediction approach for channel hydration state . . 71
4.13 Channel annotation summary page for a TRPV4 structure 72
4.14 Receiver operating characteristic evaluation of heuristic model 74
4.15 Illustration of prediction approach using two recent structures 75

4.16 Extended simulations for three selected ion channel structures 76

5.1 Two alternative methods of computational electrophysiology 81
5.2 Schematic description of the uniform electric field method 82
5.3 Simulated currents with or without application of protein restraints 88
5.4 Impact of truncating channel structures on simulated conductances 90
5.5 Concentration- and voltage-dependence of simulated conductances 91
5.6 Pore hydration analyses for recent glycine receptor structures 94
5.7 Simulated ionic flux through recent glycine receptor structures 95
5.8 Pore hydration analyses for recent 5-HT_3 receptor structures 99
5.9 Simulated ionic flux through a recent 5-HT_3 receptor structure 100
5.10 A pipeline for functional annotation of new channel structures 102
5.11 Pore radius and hydrophobicity distribution at water free energy maxima 103
5.12 Correlation between simulated conductance and minimum water density 105
5.13 Born energy profiles through glycine and 5-HT_3 receptor structures 109
5.14 Maximum Born energies as an indicator of ion channel conduction state . 110
5.15 Maximum Born energies and minimum water densities in selected pores . 111

List of Tables

4.1 Ion channel structures selected for equilibrium simulation and analysis . . 60

5.1 Ion channel structures selected for computational electrophysiology 108

"It is a capital mistake to theorise in advance of the facts."

From *The Return of Sherlock Holmes* by Sir A. C. Doyle, 1905

1 Introduction

1.1 Ion Channel Proteins: Features and Functions 1
1.1.1 Channels and pores in biological membranes 1
1.1.2 Gating, selectivity, and structure of ion channels 4
1.1.2.1 Pentameric ligand-gated ion channels 6
1.1.3 Ion channels as pharmacological targets 7
1.2 From Molecular Structures to Mechanistic Models 7
1.3 Hydrophobic Gating in Channels and Nanopores 10
1.3.1 Insights from simulation studies on model pores 11
1.3.2 Influence of hydrophobicity among ion channels 12
1.3.3 Molecular dynamics to aid functional annotation 14
1.4 Objectives and Approaches of Present Investigation 15

1.1 Ion Channel Proteins: Features and Functions

1.1.1 Channels and pores in biological membranes

Encapsulation of genetic and metabolic systems within lipid membranes during the origin of life on Earth[1], around or before 3,800 million B.C.[2,3], necessitated the evolution of transmembrane transport mechanisms to regulate the import and export of solute species[4]. In early cellular life, the presence of membrane-embedded, peptide-based channel molecules[5] with selective permeability to K^+ or Cl^- ions, for example, has been suggested to be critical for the maintenance of osmotic balance and thus integrity of the cell amidst sea water[4]. Diverse families of specialised membrane transport proteins

have since evolved[6], with their architectures and functionalities shaped via duplication, fusion, fission, and local mutation of the encoding genes, as evident from bioinformatic[7,8] as well as structural and experimental analyses[9].

Channel proteins are classically distinguished from transporters in that the permeant species entering a channel may travel towards and subsequently exit from the opposite side of the membrane without requiring structural rearrangement of the protein, whereas substrate translocation through a transporter is characterised by concomitant protein conformational transitions[10]. Without the elevated energetic barrier of the latter process, the rates of solute flux across transmembrane channels typically exceed 10^6 s^{-1} and may approach diffusion-limited values in some channels[11,12]. Whilst discoveries of individual proteins with dual, intermediate, or interconvertible channel- and transporter-like features have blurred the mechanistic distinction between the two broadly defined types of membrane transport proteins[13–15], such terminology continues to provide a useful framework for their characterisation.

The term *channel* is often employed to refer specifically to ion channels[10], which function as water-filled, ion-conducting integral membrane proteins of the α-helical class, although it may encompass other proteins that form pores through their transmembrane α-helices or β-barrel(s) (Figure 1.1). Aquaporins, for example, are ubiquitous membrane proteins that exhibit a high permeability to water, with a subset of the family, known as the aquaglyceroporins, also facilitating transport of small uncharged solutes[16]. In the outer membranes of diderm bacteria and of certain organelles such as the mitochondria, the site of aerobic cellular respiration found in most eukaryotes[17], β-barrelled porins constitute a major protein component[18]. These outer membrane proteins mediate substrate-specific or size-exclusive transport of ions, nutrients, and other molecules including antibiotics[18]. Gap junction channels, formed by the connexin and innexin families of proteins in vertebrates and invertebrates, respectively[19], represent another notable group, spanning the membranes of two adjacent cells and allowing direct transit of molecules as large as second messengers through the cytoplasmic connection[20].

Ion channels, which are the subject of investigation in this thesis, are crucial for cellular physiology across all kingdoms of life[25]. Embedded in the plasma and (eukaryotic) organellar membranes, they contribute to processes including cell volume regulation,

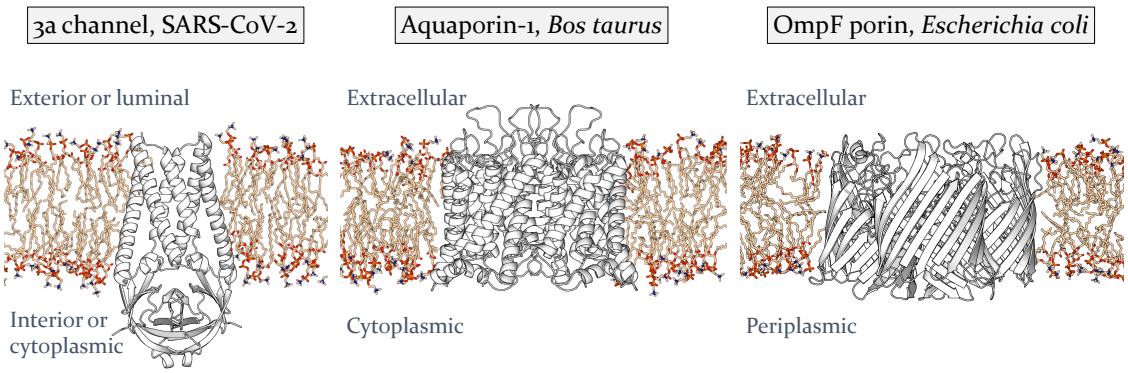


Figure 1.1 Examples of biological channels and pores (white ribbons, as visualised in PyMOL[21]), showing their approximate configuration with respect to a simple phosphatidylcholine lipid bilayer membane (orange). Structures of a viral ion channel, a mammalian aquaporin tetramer, and a bacterial outer membrane porin trimer, with Protein Data Bank IDs of 6XDC[22], 1J4N[23], and 2OMF[24], respectively, are oriented with their cytoplasmic or periplasmic side at the bottom. The depiction of a surrounding membrane does not reflect the lipid (and, in the case of OmpF, lipopolysaccharide) composition of the physiological environment of these proteins.

calcium-dependent intracellular signalling, establishment of the resting membrane potential, and electrical excitability of cells such as neurons and cardiac myocytes[25]. Ion channels are also found in the membranes of enveloped viruses and fulfil various functions in stages of the viral life cycle[26].

Unlike transporters, which may allow active transport of substrates against their concentration gradients by utilising an energy source such as another solute gradient or hydrolysis of ATP[10], ion channels exclusively facilitate passive diffusion across the membrane. In their open, conductive state, ion channels support ionic flux as thermodynamically driven by the transmembrane electrochemical potential difference of each permeant species,

$$\Delta\bar{\mu}_x = RT \ln \frac{[x]_i}{[x]_o} + z_x F \Delta\Phi \tag{1.1}$$

where $[x]_i$ and $[x]_o$ are the concentrations of species x inside and outside the membrane-bound compartment, z_x is the ionic charge of x, $\Delta\Phi$ is the electric potential on the inside relative to the outside of the membrane, R is the molar gas constant, T is the absolute temperature, and the Faraday constant F is the electric charge per mole of electrons[27]. The high rates of transport that may be achieved by electro-diffusion through ion channels are fundamental to their central role in the rapid transmission of electrical signals, for example during the initiation and propagation of action potentials in the nervous system[10].

1.1.2 Gating, selectivity, and structure of ion channels

Following early experimental studies on excitable membranes, including the pioneering electrophysiological analyses and mathematical modelling of ionic currents in the squid giant axon by Hodgkin and Huxley [28], the advent of molecular cloning technology in the 1970s[29] led to accelerated identification and characterisation of individual ion channels and channel families[30]. As alluded to above, most ion channels form a continuous transmembrane pathway only when in an open, active state. Channel proteins may undergo conformational rearrangements, in response to particular external or internal stimuli, to permit or preclude ionic flow. In addition to such activation and inactivation behaviour, known as *gating*, the ability to discriminate between ionic species constitutes another elemental property, the *selectivity*, of ion channels. Their open pores allow passage of a restricted class of small ions and may exhibit varying degrees of relative permeability between and among cations and anions[25].

Ion channels may be activated by a range of biochemical and physical stimuli, depending on physiological functions of the channel[31]. Three exemplar superfamilies of ligand-gated ion channels include the pentameric cysteine-loop and tetrameric ionotropic glutamate neurotransmitter receptors[32] and the trimeric purinergic P2X receptors[33], each responding to the binding of extracellular signalling molecules. Also gated via biomolecular interactions are members of inwardly rectifying potassium channels, including the ATP-sensitive and G protein-coupled subfamilies[34], and others such as the Orai channel, which is activated by the STIM1 protein upon depletion of calcium stores in the endoplasmic reticulum[35]. The activity of proton-gated channels reacts to changes in pH, for example in the case of acid-sensing ion channels[36] and of the archetypal bacterial potassium channel, KcsA[37]. Members of the voltage-gated ion channel superfamily, which include voltage-gated potassium, sodium, calcium, and proton channels as well as families of non-selective cation channels, constitute a most prominent group among channels that sense changes in the membrane potential[38]. Further examples of ion channels that respond to other physical stimuli include the channelrhodopsin photoreceptors of green algae[39], the bacterial mechanosensitive MscS and MscL channels[40] and eukaryotic Piezo channels[41], both groups gated by mechanical stress, and thermally activated ion channels, most of which belonging to the transient receptor potential (TRP) family[42].

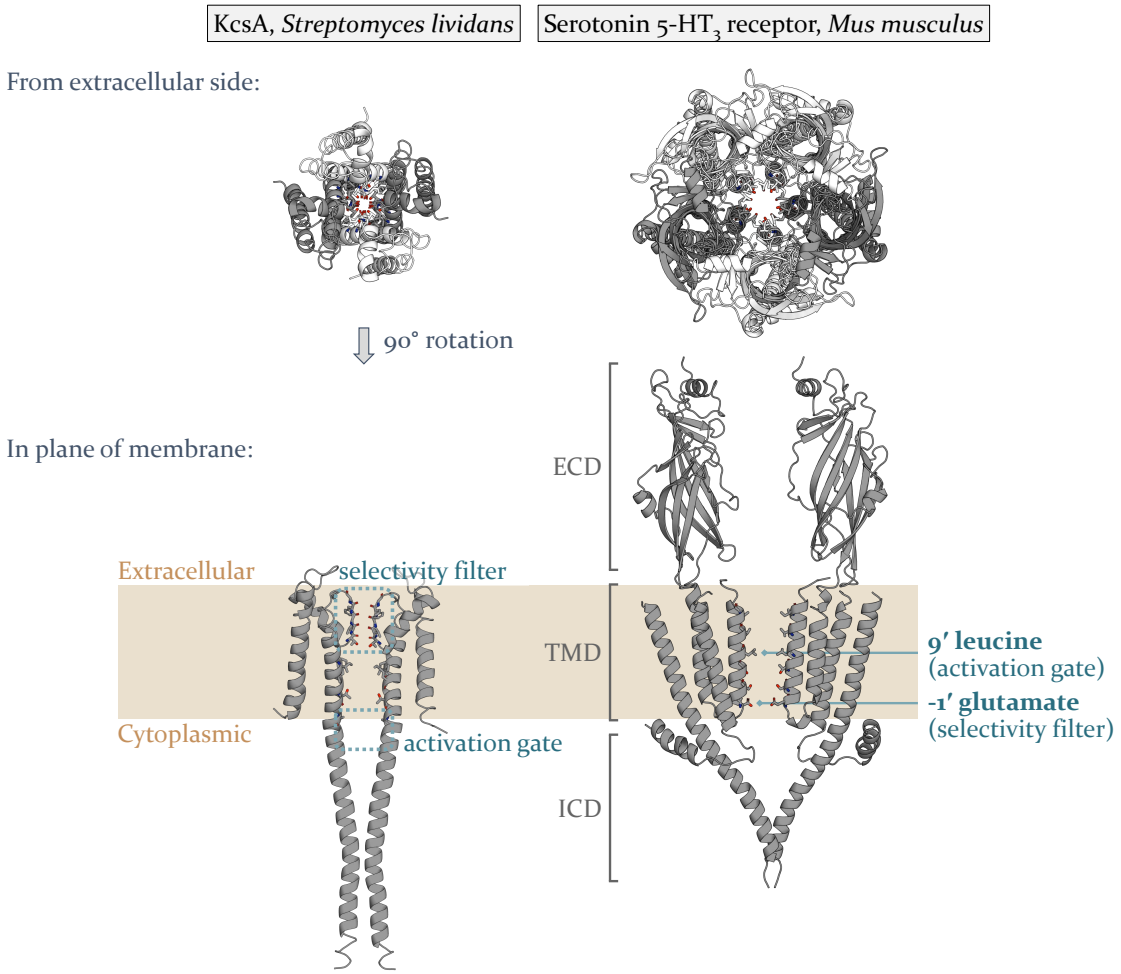


Figure 1.2 Molecular structures of KcsA, a tetrameric pore-loop potassium channel, and the serotonin 5-HT$_3$ receptor, a pentameric ligand-gated ion channel, with respective Protein Data Bank IDs of 3PJS[43] and 4PIR[44], showing the top view of each protein (white and grey ribbons, as visualised in PyMOL[21]) and a side view of the two non-adjacent subunits highlighted in grey. The approximate position of the membrane is represented by the beige shading, and the extracellular domain (ECD), transmembrane domain (TMD), and intracellular domain (ICD) portions of the 5-HT$_3$ receptor are indicated. Individual non-hydrogen atoms and bonds are shown for amino acid residues whose side chains are oriented towards the transmembrane pore, as well as for those with backbone carbonyl groups constituting the pore-loop selectivity filter sequence of KcsA.

Since the determination of the molecular structure of KcsA by X-ray crystallography in 1998[45], an expanding collection of ion channel structures at atomic or near-atomic resolution have been instrumental in revealing principal molecular bases of channel properties. Amino acid residues forming one or more channel gates, which interrupt ionic flow in the resting or inactivated state of the protein, and selectivity filters, which confer ion selectivity, are typically situated in distinct regions along channel pores (Figure 1.2).

The selectivity filter of some channels may additionally function in gating, as has been reported for KcsA and several other potassium channels containing the signature TVGYG sequence motif[46]. Conversely, the putative gate residues of a non-canonical potassium channel, TMEM175, have been implicated in K^+ ion selectivity[47]. The TMEM175 gate has also been suggested to conceal the main selectivity-determining site of the channel from access to the pore in its closed conformation[48].

1.1.2.1 Pentameric ligand-gated ion channels

Members of the pentameric ligand-gated ion channel (pLGIC) superfamily, including the cationic serotonin 5-HT_3 and nicotinic acetylcholine receptors and the anionic glycine and γ-aminobutyric acid $GABA_A$ receptors, mediate fast synaptic transmission in the nervous system of bilaterian animals, where these channels are alternatively named the cysteine-loop receptors after a characteristic disulphide-bridged loop in their N-terminal extracellular domain[49]. The pair of eponymous cysteine residues are absent from prokaryotic pLGICs[50], and a proline position has instead been identified to be conserved across the superfamily by more recent phylogenetic analysis[51].

A pLGIC is composed of a symmetric (homomeric) or pseudosymmetric (heteromeric) arrangement of its five identical or homologous protein subunits around the central channel pore, with the extracellular and transmembrane domains adopting a conserved molecular architecture (Figure 1.2). The extracellular domain is based on the β-sandwich fold and contains ligand-binding pockets at the interface between adjacent subunits. The subunits that contribute to the binding process and the number of binding sites thus formed vary between pLGICs[52]. The four transmembrane α-helices of the protein are consecutively designated M1 to M4 in the N- to C-terminal direction, of which the M2 helix of each subunit lines the channel pore. Residues of the M2 helix are conventionally numbered with a prime (′) notation, beginning from the N-terminal, cytoplasmic side.

Conserved hydrophobic amino acids at the 9′ position approximately at the midpoint of the M2 helices, most frequently a ring of leucine residues[49], have been shown by lines of experimental and structural studies to constitute part of the activation gate of pLGICs[52], whereas the identity of residue motifs at the cytoplasmic end of M2 correlates with cation or anion selectivity of the channel in metazoans[49]. In the 5-HT_3 receptor, the glutamate ring at the -1′ position functions as a main selectivity filter[53] (Figure 1.2).

1.1.3 Ion channels as pharmacological targets

Defects in ion channels and dysregulation of their functions, which may arise from genetic mutations or acquired causes, are associated with a broad range of diseases, referred to as channelopathies, including neurological, neuromuscular, cardiovascular, respiratory, metabolic, and renal disorders[54]. The aberrant expression or dysfunction of a number of ion channels and channel families has also been implicated in promoting the hallmarks of cancer in different types of tumours[55]. With over 400 genes identified to encode ion channel subunits in the human genome[56], ion channels represent the second largest class of proteins targeted for drug discovery, after G protein-coupled receptors, and are responsible for the therapeutic effect of approximately 18 % of the currently approved small-molecule drugs[57]. In addition, ion channels are targets of both local[58] and general[59] anaesthetics. However, the therapeutic potential in modulating ion channel function remains under-exploited, with available pharmacological agents acting on a small percentage of known channels[60].

Considerable efforts are being made towards the rational design of drugs that selectively target particular ion channels and their isoforms or conformational states, with reduced side effects and improved efficacy[61,62]. State-dependent sodium channel blockers, for example, interact predominantly with the open and inactivated states of the channel and are used clinically as anticonvulsants and anti-arrhythmic agents, whereas tetrodotoxin, the prototypical state-independent blocker of the pore, is highly toxic[61]. An increased molecular understanding of ion channel behaviour, under physiological as well as pathological conditions, and of mechanisms underlying its modulation by endogenous molecules or administered agents, continues to inform the drug discovery process[58].

1.2 From Molecular Structures to Mechanistic Models

Recent years have seen remarkable advances in membrane protein structural biology, particularly with technological breakthroughs in single-particle cryo-electron microscopy (cryo-EM)[65–67], among the most notable of which is the introduction of direct electron detectors[68] and novel image processing algorithms[69,70]. Since the start of the investigation described in this thesis, the number of available ion channel structures has more than

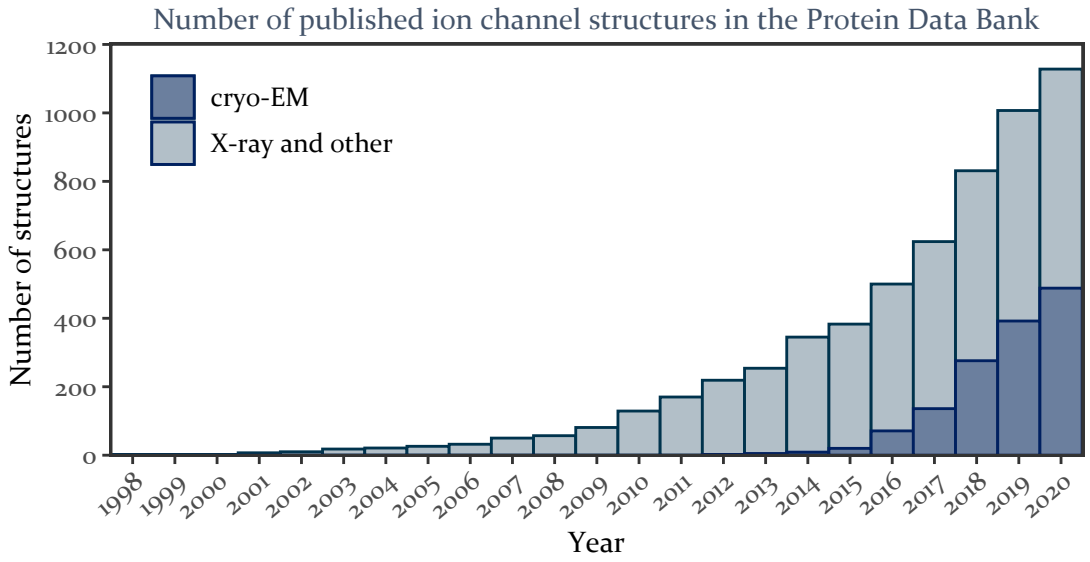


Figure 1.3 The cumulative number of ion channel structures deposited in the Protein Data Bank (`https://www.rcsb.org/`)[63], as of November 2020, and its annual growth since the publication of the first ion channel structure. The vast majority of these structures were resolved by either X-ray diffraction (including conventional X-ray crystallography and, more recently, with the use of X-ray free-electron lasers[64]) or cryo-electron microscopy (cryo-EM), with around 20 structures determined via solution or solid-state NMR spectroscopy.

doubled (Figure 1.3), and there are, to date, over 1,000 structures of over 150 unique ion channel proteins deposited in the Protein Data Bank (PDB)[63,71]. Approximately 40 % of these structures were determined by cryo-EM, including the majority of the TRP channel structures and of recent pLGIC structures, as well as structures of various other larger channels such as the ryanodine receptors[72] and mechanosensitive Piezo channels[73].

Not only may structural information serve to guide further functional characterisation of ion channels by electrophysiology and other experimental approaches, for example upon site-directed mutagenesis within and at the interface between elements of the protein structure[74,75], the abundance of molecular structures also provide starting models for the dynamic properties of these proteins to be probed by computational methods, leading to experimentally verifiable predictions that contribute towards the elucidation of channel gating, ion conduction, and modulatory mechanisms[76]. Applying molecular dynamics (MD) simulations with an enhanced sampling method[77], Lev *et al.* [78] have recently demonstrated the potential of the approach for identifying minimum free energy pathways of conformational transition associated with ion channel activation or inactivation, which

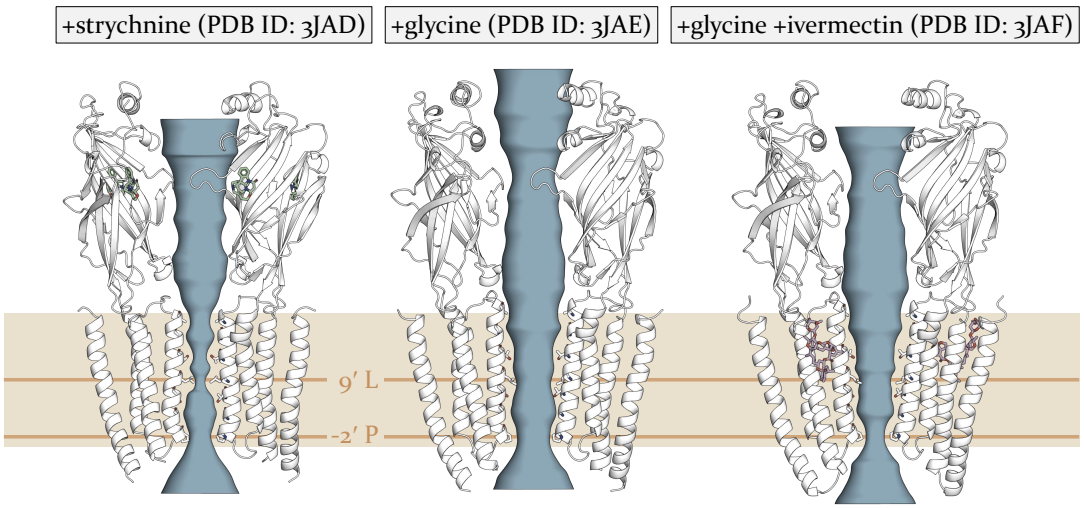


Figure 1.4 Structures of the zebrafish α_1 glycine receptor in alternative conformational states, respectively with Protein Data Bank (PDB) IDs of 3JAD, 3JAE, and 3JAF, as determined by cryo-electron microscopy[79]. Two non-adjacent subunits are displayed for each structure, in a ribbon representation as visualised in PyMOL[21], with individual non-hydrogen atoms and bonds shown for residues with side chains oriented towards the transmembrane pore and for the bound strychnine (green) and ivermectin (purple) molecules. The inner pore surface, as calculated using the Channel Annotation Package[80], is coloured blue. Approximate positions of the 9′ leucine and -2′ proline residues of the M2 helix relative to the membrane (represented by the beige shading) are indicated.

typically occurs on timescales of micro- to milliseconds or beyond[76]. Based on atomistic simulations of crystal structures of the *Gloeobacter* ligand-gated ion channel (GLIC) at different pH, a mechanistic model has been described for the allosteric communication from agonist-induced rearrangements in the extracellular domain to movements of M2 helices lining the transmembrane pore of this proton-activated bacterial pLGIC[78].

When examining molecular structures of channel proteins, dimensions of the channel pore often present an initial indicator of functional state, and comparisons among structures of the same protein or its homologues may allow identification of putative channel gates in pore regions that are observed to constrict or expand depending on the conditions under which the conformation has been captured. Structures of the zebrafish α_1 glycine receptor, for example, were first resolved by cryo-EM in three alternative conformations (Figure 1.4), respectively stabilised by the antagonist strychnine, the agonist glycine, and the presence of both glycine and ivermectin, an allosteric modulator[79]. The structures were proposed to represent an open, conductive state, a closed state, and a potentially desensitised or partially open state, with the pore conformations supporting the role

of the 9′ leucine and -2′ proline residues in gating the channel[81], although it is worthy of note that the physiological relevance of the aforementioned open configuration of the glycine receptor has since been questioned[82,83].

1.3 Hydrophobic Gating in Channels and Nanopores

Measurements of the physical dimensions of ion channel pores are routinely performed for newly determined structures using software such as the HOLE programme[84], yielding profiles of pore radius (or diameter) along the channel axis. Whilst minimum pore radius values may be directly compared with the size of each permeant species to infer whether ion conduction is likely to be possible in a given conformational state, emerging evidence has highlighted the importance of considering the physico-chemical properties of the pore lining for more reliable annotation and classification of ion channel structures[85]. Ion permeation may readily occur through polar regions only slightly larger than the radius of the permeant ion, whereas a hydrophobic pore segment of comparable dimensions may undergo spontaneous de-wetting to form a local nanoscale region devoid of water and ions (Figure 1.5), a phenomenon that has been referred to as 'hydrophobic gating'[86], 'bubble gating'[87], or a 'vapour lock'[88].

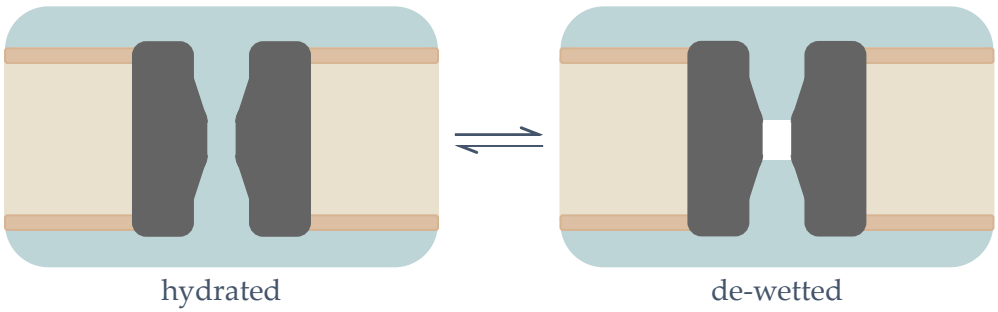


Figure 1.5 The hydrophobic gating effect in pores of sub-nanometre dimensions, whereby spontaneous de-wetting transitions in an apolar region may confer closure to conduction through a sterically unobstructed channel. A schematic representation is shown for a cross-section of the channel (dark grey) embedded in a membrane (beige).

The theoretical basis of hydrophobic de-wetting was first expressed in 1973 by Stillinger [89] via an adaptation of scaled-particle theory. With depletion of hydrogen-bonding in water near apolar surfaces, distinctive properties of water molecules confined within hydrophobic pores and cavities of nanometre dimensions[90], in particular, have been the subject of a number of computational and experimental studies for over two decades[91].

1.3.1 Insights from simulation studies on model pores

As a possible mechanism for gating channels and nanopores, early examinations of hydrophobic de-wetting were based on MD simulations of carbon nanotubes[92,93] and model nanopores[86,94–96]. Stochastic liquid-vapour transitions were observed, on a nanosecond timescale, within hydrophobic pores of around one nanometre in length and over a small range of pore radii above and below 0.5 nm[93,94,96], comparable to the inner dimensions of biological channels. Above a threshold radius of approximately 0.55 nm, the liquid-filled state was shown to become globally thermodynamically stable, whereas water density approached zero in narrower model pores below a radius of 0.45 nm[94].

In simulation systems solvated with an aqueous solution of NaCl, the equilibrium density of ions in model hydrophobic pores exhibited a similar dependence on pore radius to that of water, with a steeper transition between conducting and non-conducting states and a higher critical radius of approximately 0.65 nm[97]. With significant free energy penalties associated with desolvation of ions such as Na^+, K^+, and Cl^- (respectively with hydration free energies of -371, -298, and -373 kJ mol^{-1}), and even greater values for divalent ions like Ca^{2+} (-1493 kJ mol^{-1}) and Mg^{2+} (-1820 kJ mol^{-1})[98], vapour regions formed at a hydrophobic constriction present significant dielectric barriers to ion conduction[99].

By increasing the polarity of the pore surface, via introduction of partial charges to yield dipole moments each with a magnitude comparable to that of the peptide bond, the radius threshold for pore hydration was demonstrated to be lowered until, in the case of hydrophilic pores, a liquid-filled state was stable at radii comparable to the size of a water molecule[97] (Figure 1.6). The liquid-vapour equilibrium of confined water is also influenced by factors such as temperature, pressure, osmolyte concentration, and local flexibility of the pore wall[91,97].

Pore hydration may additionally be controlled through application of an external electric field, as was initially investigated by simulations of hydrophobic nanopores[100,101] and carbon nanotubes[102,103]. Consistent with predictions of the effect from computational analyses, voltage-dependent dehydration gating and ion transport have received support in experimental measurements on track-etched polyethylene terephthalate nanopores with a methyl-esterified inner surface[104].

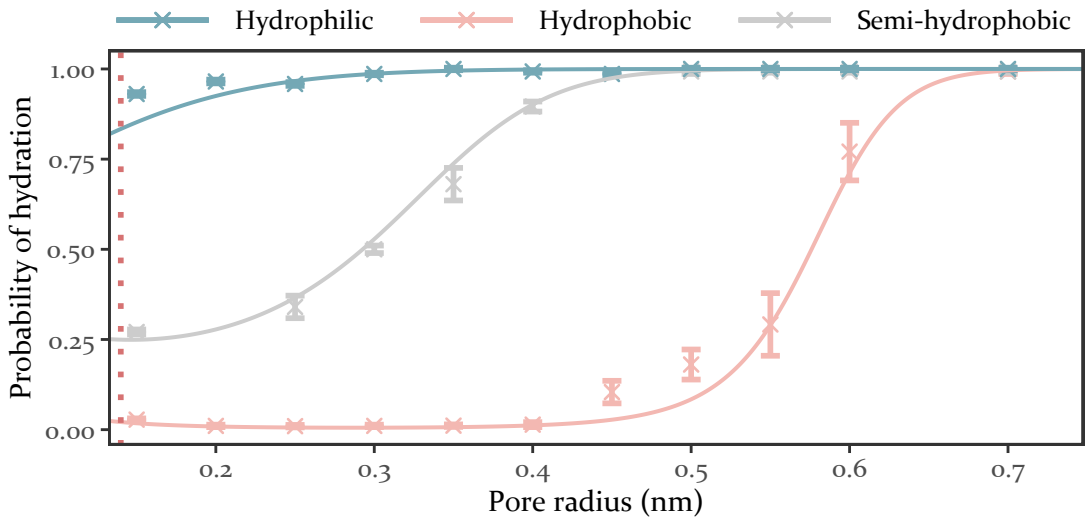


Figure 1.6 Influence of hydrophobicity on the probability of pore hydration, fitted to a sigmoidal expression, as computed by Beckstein and Sansom [97] based on molecular dynamics simulations of model nanopores. The approximate radius of a water molecule is represented by the red dotted line. Adapted from Aryal *et al.* [85].

1.3.2 Influence of hydrophobicity among ion channels*

Observations of de-wetting in hydrophobic regions of channel pores have increasingly been reported in structural studies of ion channels[85]. The first direct lines of evidence for hydrophobic gating in a biological ion channel were provided by studies on the small-conductance mechanosensitive channel, MscS, one member of a family of bacterial proteins that protect against hypo-osmotic shock[106]. During atomistic MD simulations of water in a crystal structure of the protein[107], liquid-vapour transitions were observed within the channel in a hydrophobic region where the minimum pore radius was approximately 0.25 nm[88,108]. The de-wetting region was surrounded by side chains of leucine residues and considered to form a closed hydrophobic gate in the structure, preventing ion conduction in such a conformation[88]. By contrast, a hydrophilic mutation at the constriction, substituting polar serine amino acids for one of the two leucine rings, yielded stable hydration through the channel under the same simulation conditions[88]. An open conformation was subsequently resolved for the protein, showing a widened channel pore with radius greater than 0.6 nm[109]. Further simulation studies examined

* An earlier version of this section has formed part of the following review:

Lynch, C. I., Rao, S. and Sansom, M. S. P. Water in nanopores and biological channels: A molecular simulation perspective. *Chemical Reviews* **120,** 10298–10335 (2020)

pore de-wetting and hydration in models of both MscS and the related large-conductance mechanosensitive channel, MscL, supporting the role of channel pore hydrophobicity and consequent wettability in the gating of both proteins[110].

Among members of the pLGIC superfamily, the conserved 9′ position of M2 helices was first demonstrated to constitute a hydrophobic gate by simulations of the M2 helix bundle of a nicotinic acetylcholine receptor structure[111], in which narrowing of the permeation pathway to around 0.3 nm in radius by two consecutive pore-lining rings formed by the 9′ leucine and 13′ valine residues was calculated to present an energetic barrier to water and ion passage[112]. Consistent with such simulation results, effects of mutagenesis of the hydrophobic rings on channel electrophysiology were reported by a number of experimental studies[113–116].

Later studies on GLIC and another bacterial homologue, the *Erwinia* ligand-gated ion channel, respectively having isoleucine and phenylalanine in the 9′ position, showed de-wetting of both proteins around this region in their simulated structures, conferring closure to the putative hydrophobic gate[117,118]. For GLIC, liquid-to-vapour transitions were reported during string-method MD simulations of the transmembrane domain from its putative open conformation to a non-conductive state[119], and the free energy cost of hydrating the hydrophobic gate was further estimated[120]. The hydration state of the pore in this region was suggested to be a principal determinant of the ion conduction state of the channel based on calculations from the latter study, whereby pore hydration was associated with an increase in free energy of approximately 46 kJ mol^{-1}, compared with the smaller energetic cost (about 5 kJ mol^{-1}) of transferring a Na^+ ion into a hydrated gate in the non-conductive relative to the open conformation of the channel[120].

In the superfamily of tetrameric pore-loop cation channels, de-wetting of a hydrophobic region located towards the cytoplasmic side has been implicated to play a role in gating among members of several potassium channel families[85], as supported by MD simulations of crystal structures of a voltage-gated potassium channel[121,122] and the TWIK-1 channel of the tandem-pore domain family[123], as well as simulations of homology models for the large-conductance calcium-activated potassium channel[124]. In the case of TWIK-1, significance of the hydrophobic barrier was further validated by electrophysiological measurements, where a hydrophilic substitution led to enhanced channel activity

in whole-cell current recordings[123]. Evidence is also emerging for the presence of hydrophobic residues at the gates of TRP channels, a family of non-selective cation channels whose members fulfil diverse functions in sensory physiology[125,126], with the temperature dependence of the hydration equilibrium within TRPV1 suggested to contribute to the biological function of the protein as a temperature sensor[127].

The presence of hydrophobic gates and their functional significance continue to be reported for other cation and anion channels as well. Simulated pore wetting events in the CorA magnesium channel, concurrent with small increases in pore diameter, have been suggested to mediate control of ion conduction by regulatory ions[128], and a combination of spectroscopy and electrophysiology have demonstrated coupling of ion conduction to hydration of transmembrane helices among the light-activated channelrhodopsin family[129,130].

1.3.3 Molecular dynamics to aid functional annotation

In the light of a developing understanding of the hydrophobic gating effect, and with the annual increase in the number of resolved ion channel structures beginning to exceed 100 that year (Figure 1.3), Trick *et al.* [131], in 2016, proposed that equilibrium MD simulations of water behaviour in the channel pore may be used as a tool for assessing the likely conductive state represented by ion channel conformations, at moderate computational expense. Following an automated protocol for embedding protein structures into lipid membranes[132], atomistic simulations of 100 ns in duration allowed estimation of free energy profiles for water along the channel axis, based on simulated water density within the pore[131].

The approach was illustrated on structures of the 5-HT_3 and glycine receptors, two metazoan pLGICs[44,79]. In the case of the 5-HT_3 structure[44], prediction of a dehydration barrier around its 9′ leucine position was supported by results from two alternative, more computationally intensive methods, namely computational electrophysiology simulations, in which a transmembrane potential difference of 800 mV was applied, and calculation of ion potential of mean force profiles[131]. The sensitivity of the equilibrium simulation-based analysis to the employed (non-polarisable) model of water was also examined, yielding consistent water free energy profiles for the glycine receptor structures[79,131].

1.4 Objectives and Approaches of Present Investigation

The MD-based investigation presented in this thesis sought to further explore the use of computational tools to facilitate efficient annotation and classification of ion channel structures by their predicted functional state. Focusing on the captured conformation of each channel pore, the examination primarily concerns the identification of non-conductive structures that are closed by hydrophobic gating.

Towards the start of the project, publication of the structure of a bestrophin channel mutant provided an opportunity for assessing the applicability of the equilibrium simulation method introduced above to channels with an architecture distinct from that of the pLGIC superfamily. As will be described in Chapter 3, additional mutants of the bestrophin protein were generated *in silico* to examine the effect of polar amino acid substitutions in the lining of a putative hydrophobic gate on the energetic barrier to water permeation through the region.

A more quantitative analysis is detailed in Chapter 4, seeking to model (i) the variation in hydrophobicity within biological channel pores and (ii) its influence on the critical radius for the transition between de-wetted and hydrated states. Based on simulations of a curated subset, approximately 20 %, of the PDB collection of ion channel structures at the time, the larger-scale survey was enabled by the concurrent development of the Channel Annotation Package by Klesse *et al.* [80], an implementation of the protocol from Trick *et al.* [131] as a software tool.

With a simple model thus derived for predicting the likelihood of dehydration gating from the local pore radii and estimated hydrophobicity through a static structure alone, the focus of Chapter 5 turns to the evaluation of results from the water-centric approach against simulations of ion conduction by computational electrophysiology. The utility and limitations of the model will be discussed, with a suggested pipeline of its application demonstrated on recent structures of the 5-HT_3 and glycine receptors.

"You know my method. It is founded upon the observation of trifles."

From *The Adventures of Sherlock Holmes* by Sir A. C. Doyle, 1892

2

Theory and Methods

2.1 Molecular Dynamics Simulations 17
2.1.1 Principles of molecular dynamics 17
2.1.1.1 Molecular mechanics 18
2.1.1.2 Energy minimisation 23
2.1.1.3 Integration algorithms 23
2.1.2 Simulation settings and parameters 24
2.1.2.1 Temperature and pressure control 24
2.1.2.2 Periodic boundary conditions 26
2.1.2.3 Force fields 26
2.1.2.4 Water models 27
2.1.3 Potential of mean force calculation 29
2.2 Poisson-Boltzmann Electrostatics 30
2.3 Measurement of Pore Dimensions 31
2.3.1 HOLE programme and alternatives 31
2.3.2 The Channel Annotation Package 33

2.1 Molecular Dynamics Simulations

2.1.1 Principles of molecular dynamics

Molecular dynamics (MD), an *in silico* method commonly applied for characterising time-dependent behaviour of molecular systems, simulates physical motion of interacting particles within a defined system by integrating the classical equations of Newtonian mechanics (Section 2.1.1.3). Whilst a precise representation of atoms and chemical bonds

would ideally require consideration of electronic configuration and orbital models, a level of atomic detail attained by quantum mechanical (QM) calculations, the associated increase in computational expense restricts the feasible application of such studies to small systems, or reactive regions of larger systems[133], and short timescales, typically of a few tens of picoseconds[134]. In classical MD simulations, molecular mechanics (MM) force fields are instead employed to approximate the QM energy surface[135], thereby allowing greater length scales as well as timescales of up to and beyond microseconds to be achieved for conformationally complex biomolecular systems like proteins, lipid bilayers, nucleic acids, and carbohydrates[136].

The fundamental Born-Oppenheimer approximation[137] underlying MM methodologies allows separation of nuclear and electronic motions, which differ in timescale as influenced by particle mass, thus enabling description of atomic interaction using potential energy as functions of nuclear coordinates, without explicit modelling of electrons. Relying on two additional assumptions, namely additivity and transferability, MM force fields describe the potential energy of a system as a sum of potential terms each with a distinct physical interpretation, as detailed in Section 2.1.1.1 below. Functions describing properties such as bond deformation, electrostatic interactions, and dispersion forces are developed from analyses on a small set of molecules and applied to a broader range of molecules with similar chemical groups[136]. Parameters associated with the potential energy functions are derived and optimised based on empirical data, obtained through various techniques, historically including small-molecule X-ray crystallography[138] and infrared[139] and NMR spectroscopy[140]. With advances in computational power, these are supplemented by *ab initio* QM calculations[141].

2.1.1.1 Molecular mechanics

An MM force field consists of mathematical equations that have been appropriately parameterised to model corresponding potential energy terms. For a system containing N atoms, with Cartesian coordinates of

$$\boldsymbol{r}^N = \left\{x^1, y^1, z^1, \ldots, x^N, y^N, z^N\right\} \tag{2.1}$$

assigned to their nuclei, the potential energy function $U(\boldsymbol{r}^N)$ is generally calculated from a summation of bonded and non-bonded components,

$$U(\boldsymbol{r}^N) = U_{\text{bonded}} + U_{\text{non-bonded}} \tag{2.2}$$

which in conjunction with $K(\boldsymbol{p}^N)$, the kinetic energy as a function of momenta, form the two summands of the Hamiltonian of the system, $H(\boldsymbol{r}^N, \boldsymbol{p}^N)$.

2.1.1.1.1 Bonded interactions

The potential energy terms of a molecular system that are associated with covalent contributions (Figure 2.1) may be expressed as

$$U_{\text{bonded}} = \frac{1}{2}\sum_{\text{bonds}} k_b\,(b - b_0)^2 + \frac{1}{2}\sum_{\text{angles}} k_\theta\,(\theta - \theta_0)^2 + \frac{1}{2}\sum_{\text{dihedrals}} k_\omega\left(1 + \cos(n\omega - \phi)\right) + \frac{1}{2}\sum_{\text{improper}} k_\psi\left(\psi - \psi_0\right)^2 \tag{2.3}$$

where the first three terms respectively describe bond stretching, angle bending, and torsional rotations, followed by an additional stereochemical term.

The bond stretching and bending terms are each modelled using a harmonic potential. The energy associated with the approximating harmonic oscillator varies with the square of the displacement of the bond length b or bond angle θ from its equilibrium position, denoted by the reference bond length b_0 or angle θ_0, according to Hooke's law. The force constant for bond stretching is represented by k_b, its magnitude correlating to the large amount of energy required to significantly stretch or compress a chemical bond. The harmonic potential provides a reasonable approximation to the potential energy of interest for small deviations from b_0[136]. For larger deviations, which are rarely observed in simulations of biological macromolecules, the Morse potential would form a more accurate representation[142]. Values of the force constant k_θ for the change in potential energy upon deformation of bond angles are typically lower than those for bond stretching, reflecting the lower energetic barrier to deviations in bond angle from the reference value. Higher-order terms may additionally be incorporated to increase the accuracy of the force field, for example when modelling highly strained molecules, but are generally not included in common force fields[136].

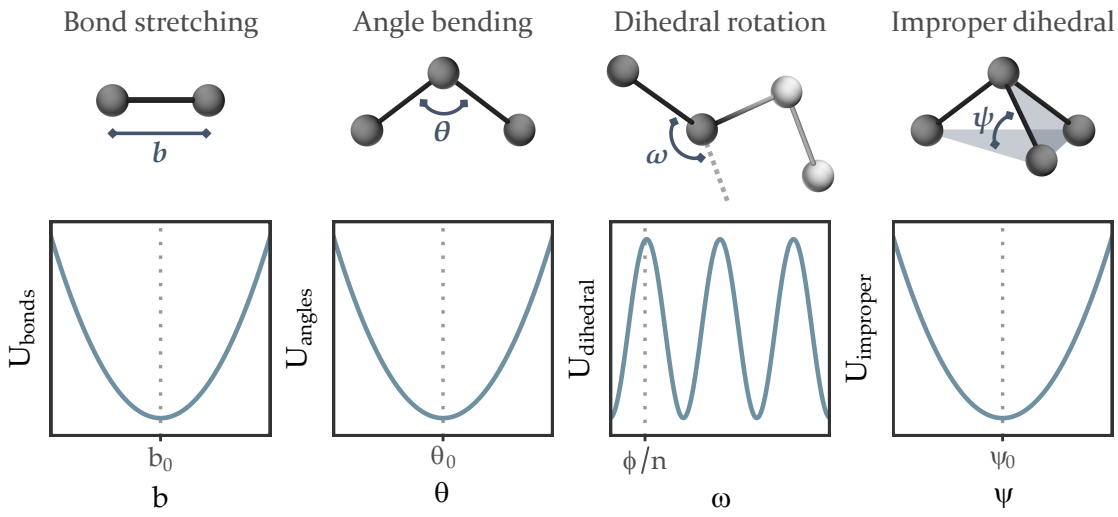


Figure 2.1 Four fundamental types of bonded interactions usually considered in molecular dynamics force fields. A schematic representation of the atoms involved and the functional form of the potential energy term are shown for each component.

The dihedral or tortional term represents the potential energy of the system as a function of the rotation about each dihedral angle, ω, and includes interactions between atoms that are separated by three bonds. The torsional force constant k_ω relates to the height of the barrier to rotation, the multiplicity n indicates the number of minima or maxima in the energy function, and the phase factor ϕ determines their positions. There is often more than one term for each dihedral in a molecule, yielding a truncated cosine series. The thermodynamic changes involved are significantly smaller than those consequent of bond stretching or angle bending[136].

A fourth term is usually introduced to the expression for U_{bonded} (Equation 2.3) to preserve the planarity of groups with flat geometry, as well as the chirality of certain groups. In the first instance, a penalty function is specified for out-of-plane bending, examples of which include the peptide bond in proteins and benzene and indole rings of aromatic amino acid side chains[136,143].

Although separation of the potential energy of a molecular system into summands with distinct physical interpretations is not justified on the basis of the quantum nature of intra- and intermolecular interactions, the approximation has proved useful for examining the determinants of molecular structure and dynamics[136]. The coupling of equilibrium bond lengths to bond angles and torsional energies in a system may further be accounted

for by introducing cross-terms into the force field, albeit rarely employed in large-scale simulations of biological macromolecules[136]. The Urey-Bradley potential, for example, describes the variation in energy upon angle bending as a function of the distance between atoms separated by the two bonds forming the angle[144]. As there is no unique solution for an optimal set of functions and parameters to translate QM effects into classical mechanical equations, the potential energy surface may be reproduced by summation of contributions that differ between alternative force fields.

2.1.1.1.2 Non-bonded interactions

Two types of non-bonded interactions (Figure 2.2) are considered between all pairs of atoms i and j that are separated by three or more intramolecular bonds or constitute different molecules, respectively giving rise to the van der Waals and electrostatic components of the potential energy of a molecular system, collectively expressed as a function of the internuclear distance r_{ij} and any partial charges q_i and q_j carried by the atoms,

$$U_{\text{non-bonded}} = \sum_{i=1}^{N-1} \sum_{j=i+1}^{N} \left\{ 4\epsilon_{ij} \left[\left(\frac{\sigma_{ij}}{r_{ij}} \right)^{12} - \left(\frac{\sigma_{ij}}{r_{ij}} \right)^{6} \right] + \frac{q_i q_j}{4\pi\epsilon_0 r_{ij}} \right\} \tag{2.4}$$

in which the van der Waals term U_{vdW} is often modelled through the Lennard-Jones potential[145],

$$U_{\text{vdW}} = \sum_{i=1}^{N-1} \sum_{j=i+1}^{N} 4\epsilon_{ij} \left[\left(\frac{\sigma_{ij}}{r_{ij}} \right)^{12} - \left(\frac{\sigma_{ij}}{r_{ij}} \right)^{6} \right] \tag{2.5}$$

where σ_{ij} indicates the distance at which the energy between the pair of atoms equals zero and ϵ_{ij} measures the interaction strength. Both parameters are dependent upon the participating atomic species. The function contains an attractive and a repulsive term, the former originating from the London dispersion forces generated between instantaneous dipoles, which arise from fluctuations in electronic charge distribution in all molecules. The repulsive term reflects the observation of atomic repulsion at very short ranges, typically below around 0.3 nm, an effect that is physically due to the Pauli exclusion principle[136]. The form of the repulsive potential with a power of 12 provides a computationally efficient approximation of the exponential function $\exp\left(-2kr_{ij}/a_0\right)$, where a_0 is the Bohr radius[136]. The Lennard-Jones potential rapidly approaches zero with increasing r_{ij} and is usually truncated below a specified cut-off radius, with smoothing of the interaction energy via application of shifting functions[136].

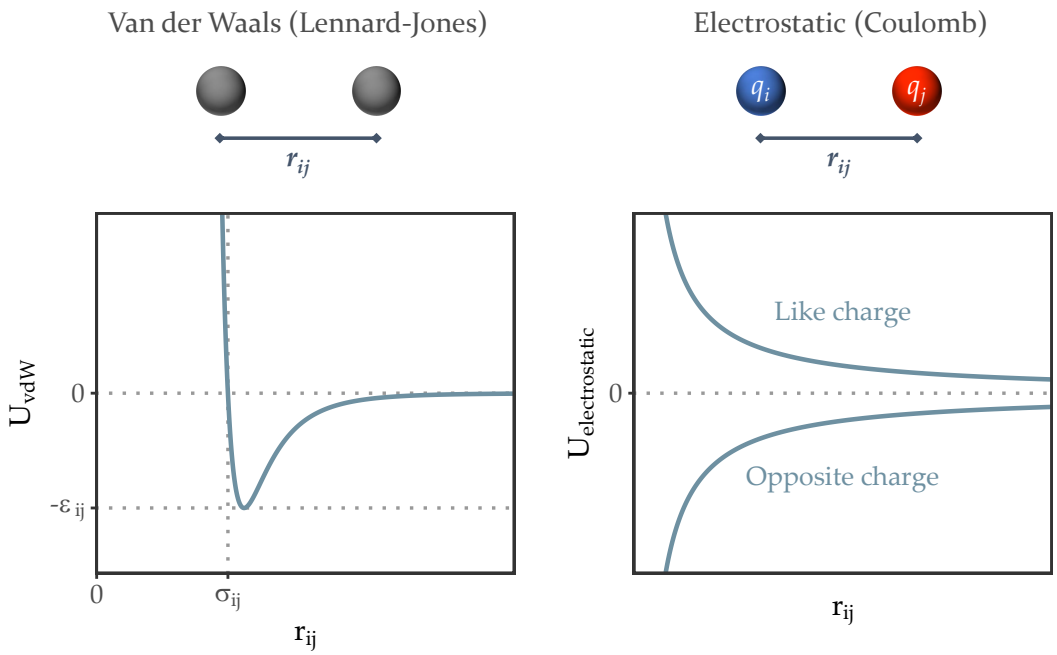


Figure 2.2 Potential energy terms describing pairwise van der Waals and electrostatic interactions, between atoms i and j, in molecular dynamics force fields. They are respectively modelled through the Lennard-Jones and Coulomb potential functions.

Consequent of variation in electronegativity between different atoms, electric charge in molecules is not evenly distributed. By placement of partial charges on atomic nuclei, the second term in the expression for $U_{\text{non-bonded}}$ (Equation 2.4), the electrostatic potential $U_{\text{electrostatic}}$, is calculated based on Coulomb's law,

$$U_{\text{electrostatic}} = \sum_{i=1}^{N-1} \sum_{j=i+1}^{N} \frac{q_i q_j}{4\pi\epsilon_0 r_{ij}} \tag{2.6}$$

where ϵ_0 denotes the vacuum permittivity. The decay of electrostatic interactions is inversely proportional to r_{ij}, much slower than that of the Lennard-Jones potential, and more consideration is required for treatment of this type of long-range interaction in MD simulations[146].

2.1.1.1.2.1 The particle mesh Ewald method

Lattice sum techniques for calculating long-range electrostatic interactions assume periodicity of the simulation cell, imposed by periodic boundary conditions (Section 2.1.2.2), and use a Fourier-based approach to solve the Poisson equation for the infinitely replicated system. The particle mesh Ewald (PME) method[147,148] is most commonly used. The basis of PME is an interpolation of the reciprocal-space Ewald sum[149], a method

originally devised to compute electrostatic energies of ionic crystals. All interactions in the constructed array of periodic cells are summed, with the calculation of electrostatic interactions separated into a short-range and a long-range series, respectively able to converge rapidly within the real and Fourier space. Their rates of convergence are dependent upon the width of the cancelling Gaussian distributions added to the nuclear point charges. A cut-off distance is applied for the real space term, with a limited number of modes for the Fourier. Implementation of the PME method reduces the computational time complexity of performing the electrostatic calculations from the order of N^2 to $N \log(N)$, where N is the number of atoms in the system[147].

2.1.1.2 Energy minimisation

Prior to initiation of an MD simulation, any large steric clashes or close contacts within and between structures are reduced to give a more stable starting conformation. Two main methods for such minimisation of potential energy are the steepest descent and conjugate gradient algorithms, both involving a gradual change in the Cartesian coordinates of particles towards a lowered energy of the molecular system. The steepest descent method seeks the minima by following an iterative line search strategy along the negative gradient direction of the energy function at each successive position, whereas the conjugate gradient method accounts for previous vectors in determining subsequent search directions, which eliminates repeated minimisation along the same directions[142].

2.1.1.3 Integration algorithms

Within a molecular system of interacting atoms, the net force $\boldsymbol{F}_i$ experienced by each atom i by virtue of its position $\boldsymbol{r}_i$ is the negative partial derivative of its potential energy function $U(\boldsymbol{r}_i)$,

$$\boldsymbol{F}_i = -\frac{\partial U(\boldsymbol{r}_i)}{\partial \boldsymbol{r}_i} \tag{2.7}$$

which according to Newton's second law of motion produces an instantaneous acceleration that is inversely proportional to the mass m_i of the atom, relating the time-dependent coordinates of an atom to the effecting force,

$$\frac{\partial^2 \boldsymbol{r}_i}{\partial t^2} = \frac{\boldsymbol{F}_i}{m_i} \tag{2.8}$$

thereby forming the basis of MD simulations of atomic trajectories in the system over time.

With the force on each atom dependent upon its position relative to all interaction partners, it is not possible to obtain analytical solutions to these differential equations, necessitating a finite difference method to solve them numerically. The integration is temporally divided into a large number of small steps, successively separated by a fixed time interval, δt. The overall force on an atom at time t is computed as a vector sum from its interactions with other atoms. Accelerations of the atoms are determined from the forces and combined with the positions and velocities at that instant to calculate the positions and velocities at time $(t + \delta t)$, with the assumption that the force remains constant during the short time step. Reassessment of forces on the atoms at their temporally advanced positions then yields coordinates and velocities at time $(t + 2\delta t)$, and so forth. Upon beginning an MD simulation, initial velocities are normally assigned at random according to the Maxwell-Boltzmann distribution, and the aforementioned process is iterated throughout the simulation[142].

The default integration algorithm that the GROMACS package[150,151] employs for such calculations, the leap-frog algorithm[152], is a modification of the Verlet algorithm based on two Taylor series expansions[153]. The latter algorithm uses particle positions and accelerations at time t, as well as positions from the previous step, $\boldsymbol{r}(t - \delta t)$, to derive the updated positions $\boldsymbol{r}(t + \delta t)$, whereas the leap-frog algorithm calculates velocities at half time intervals and uses positions at time t and velocities at time $(t - \frac{1}{2}\delta t)$ instead:

$$\boldsymbol{v}(t + \frac{1}{2}\delta t) = \boldsymbol{v}(t - \frac{1}{2}\delta t) + \delta t\, \boldsymbol{a}(t) \tag{2.9}$$

$$\boldsymbol{r}(t + \delta t) = \boldsymbol{r}(t) + \delta t \boldsymbol{v}(t + \frac{1}{2}\delta t) \tag{2.10}$$

2.1.2 Simulation settings and parameters

2.1.2.1 Temperature and pressure control

Direct integration of Newton's equations of motion produces the microcanonical or NVE ensemble, where the number of particles N, the volume V, and the total energy E of the system are conserved. For biomolecular simulations an alternative approach, the isothermal-isobaric or NPT ensemble, requires barostat and thermostat algorithms to respectively maintain the pressure P and temperature T at constant physiological

values. The velocity-rescaling thermostat[154] and Parrinello-Rahman barostat[155] are used in the present investigation.

2.1.2.1.1 Velocity-rescaling temperature coupling

The system temperature in MD is a statistical quantity expressed as a function of the position and momenta of all particles, and may be estimated from the kinetic energy for a system containing a sufficiently large number of particles,

$$K_{NVT} = \sum_{i=1}^{N} \frac{1}{2} m_i \boldsymbol{v}_i^2 = \frac{3}{2} N k_\mathrm{B} T \tag{2.11}$$

where k_B is the Boltzmann constant. The velocity-rescaling thermostat couples the system to an external heat bath that is fixed at the specified temperature T_0, and proportionally scales particle velocities to correct any deviation of the system temperature from T_0, with deviations decaying exponentially with a time constant τ_T,

$$\frac{\mathrm{d}T(t)}{\mathrm{d}t} = \frac{T_0 - T(t)}{\tau_T} \tag{2.12}$$

The velocity-rescaling thermostat is similar to the more commonly known Berendsen weak-coupling algorithm[156], sharing the advantage of conferring first-order decay of temperature deviations without oscillations, yet with the improvement that a stochastic term is added to ensure correct kinetic energy distribution by modifying it according to

$$\mathrm{d}K = (K_0 - K)\frac{\mathrm{d}t}{\tau_T} + 2\sqrt{\frac{KK_0}{N_f}}\frac{\mathrm{d}W}{\sqrt{\tau_T}} \tag{2.13}$$

where N_f is the number of degrees of freedom and $\mathrm{d}W$ a Wiener process[157].

2.1.2.1.2 Parrinello-Rahman pressure coupling

Constant pressure on a system may be maintained by changing its volume, which is inversely related to pressure by Boyle's law for an ideal gas. The system is coupled to a pressure bath, with a first-order kinetic relaxation of the pressure towards a given reference pressure P_0,

$$\frac{\mathrm{d}P(t)}{\mathrm{d}t} = \frac{P_0 - P(t)}{\tau_P} \tag{2.14}$$

where τ_P is the coupling constant. In systems containing a lipid bilayer membrane, full pressure coupling would diminish the surface area of membrane lipids, and semi-isotropic coupling is instead employed, whereby pressure changes along the x-y plane are allowed to vary independently of those in the z direction[146].

2.1.2.2 Periodic boundary conditions

Simulation of a finite system, as limited by computational expense, is subject to artefacts. Applying closed boundaries would generate surface effects where a proportion of particles reside in the proximity of a vacuum, potentially significantly influencing physical behaviour, whereas an open system would lead to undesirable density drifts[134]. Imposition of periodic boundary conditions on a simulation cell has the effect of infinitely duplicating the system in all (x, y, and z) directions to form a continuous lattice, such that particles in each three-dimensional periodic image move identically. When a particle leaves the central primary cell at a periodic boundary, one of its images from an adjacent cell will enter through the opposite face. It is thus sufficient to solely monitor the primary cell and the constant number of particles therein[134].

For protein-membrane simulations, periodic boundaries extend each small patch of bilayer assembly within a simulation cell to stacks of infinite extended sheets. There are several complications associated with application of such a setting for characterisation of membrane properties and behaviour, including (i) suppression of thermal fluctuations, a natural feature of soft condensed matter, by small simulation cells and (ii) the non-physiological spectrum of undulation modes consequent of lowered amplitudes at the edges of the simulation cell, with absence of wavelengths longer than the cell dimensions[146]. For the objectives of the present project, focusing on channel pores within membrane-embedded proteins, however, a most relevant aspect is the treatment of interactions. The minimum-image convention is used to approximate short-ranged forces, with only the nearest image of each particle considered for pairwise interactions[157], and the PME method is implemented to calculate long-range electrostatic interactions (Section 2.1.1.1.2.1).

2.1.2.3 Force fields

As described in Section 2.1.1.1, a force field consists of mathematical equations and their associated parameters, chosen to model the potential energy of a system of particles. The force field includes a list of particle types as well as parameters describing their bonds, angles, dihedrals, improper dihedrals, and non-bonded interactions. Four major atomistic force fields commonly used in MD simulations of biomolecules include the Assisted Model

Building with Energy Refinement (AMBER)[158,159], Chemistry at Harvard Macromolecular Mechanics (CHARMM)[160,161], Groningen Molecular Simulation (GROMOS)[162,163], and Optimised Potentials for Liquid Simulations (OPLS)[164] force fields. Each force field is able to reasonably accurately reproduce many protein characteristics, although the lack of electronic polarisability in their simplified modelling of electrostatic interactions between nuclear point charges (Equation 2.4) limits the accuracy of properties such as the relative orientation of aromatic residues and interactions with ions[165,166]. Recent versions of AMBER, CHARMM, and OPLS are all-atom force fields, with explicit modelling of every atom, including all hydrogen atoms, whereas united-atom force fields such as GROMOS combine each aliphatic carbon and its associated hydrogen atoms into a single interaction site.

Two most widely used force fields for simulating phospholipids are that constituting the all-atom CHARMM force field[167] mentioned above, and one which was developed with parameters based on united-atom versions of OPLS and AMBER[168]. Both representations have been demonstrated to yield agreement with available experimental information on the structure and dynamics of phospholipid bilayers, particularly for the experimentally extensively studied phosphatidylcholine lipids[169], which is the lipid type employed for the current investigation.

Whilst the additional computational cost of simulating aliphatic hydrogen atoms is comparatively small for proteins, simulation of lipids in an all-atom representation is much more computationally expensive relative to that of united-atom lipids, due to the significantly higher particle density and thus total number of interactions in the former case, as well as the greater number of atoms per lipid. Given these considerations, the OPLS all-atom protein model is used with a united-atom lipid model, as implemented in the GROMACS package[157]. The force field combination has been previously evaluated for performance and suggested to be a reasonable approach for membrane protein simulations[169].

2.1.2.4 Water models

Rigid, non-polarisable water models, which represent water as a set of point charges at fixed positions relative to the nucleus of the oxygen atom, are the simplest and most

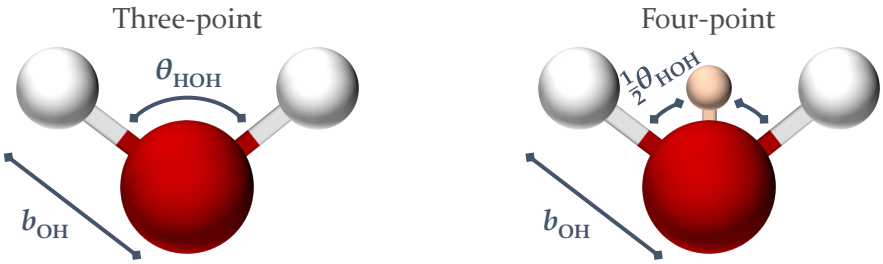


Figure 2.3 Geometry of three- and four-point rigid fixed-charge water models, respectively consisting of three and four interaction sites for Coulomb and/or van der Waals forces. The three interaction sites of three-point models typically correspond to the nuclei of the oxygen (red) and hydrogen (white) atoms of a water molecule, whereas four-point models comprise an additional, massless virtual site (orange) that is located on the H-O-H bisector and carries a negative charge.

widely used among the large number of models developed to reproduce properties of water in atomistic simulations[105,170,171]. The simple point charge (SPC)[172] and transferable intermolecular potential (TIP)[173] models constitute two notable families, respectively based on the geometry of molecules within ice and water vapour. Three-point models such as the commonly employed SPC/E[174] and TIP3P[175] each consist of three interaction sites arranged in a chevron shape, corresponding to the three atoms of a water molecule, whereas the four-point TIP4P model[175,176] includes a fourth interaction site near the oxygen atom, along the bisector of the H-O-H angle (Figure 2.3). The additional site was introduced to reproduce the large quadrupole moment of the water molecule and improve the modelled charge distribution[177]. In a more recently developed four-point model, the optimal point charge (OPC) model, the three classical point charges were displaced from the oxygen and hydrogen nuclei to further optimise description of electrostatic features of the molecule[178]. Five-, six-, and seven-point models have also been designed[179–182]. The TIP5P model, for example, has the single negative charge on the H-O-H bisector of TIP4P replaced with two negative charges located at the positions of the lone pair of electrons[179].

Two water models are employed for simulations presented in this thesis, namely TIP4P[175], which was used in the parameterisation of the OPLS force field[164], and TIP4P/2005, a TIP4P-based general purpose model that was fine-tuned with respect to a range of properties and thermodynamic states[183]. TIP4P/2005 has been reported as a comparatively accurate model in several benchmark studies evaluating the transferability and predictive quality of water models[184–186].

2.1.3 Potential of mean force calculation

The potential of mean force (PMF) $\mathcal{W}(\xi)$ describes the change in free energy of a system along a chosen reaction coordinate ξ and is related to the probability distribution $P(\xi)$ through the Boltzmann equation,

$$\mathcal{W}(\xi) = -k_{\mathrm{B}}T \ln P(\xi) + \mathcal{W}_0 \tag{2.15}$$

where $\mathcal{W}_0$ is an arbitrary constant, usually defined such that a suitable reference state is at zero free energy[187,188]. Whilst $P(\xi)$ may, in principle, be estimated directly from MD simulation trajectories, application of such an approach is limited by the level of sampling of the configurational space that could be attained within a computationally feasible time frame, particularly when in the presence of energetic barriers. More efficient computation of the PMF may be achieved through enhanced sampling methods[189] such as umbrella sampling[190,191].

In umbrella sampling, a biasing potential $w(\xi)$, typically harmonic in form, is introduced to favour sampling within prescribed regions along ξ. A number of simulations are performed, each referred to as a window i where

$$w_i(\xi) = \frac{1}{2} k_\xi \left(\xi - \xi_i\right)^2 \tag{2.16}$$

confines variations of the ξ-coordinate in the vicinity of ξ_i, with a force constant k_ξ, thereby ensuring sampling of the full domain of ξ in successive, overlapping intervals.

The probability distributions $P_i(\xi)$ obtained from these biased simulations may then be combined, with correction for the bias consequent of $w_i(\xi)$, to yield the overall $P(\xi)$. The widely applied weighted histogram analysis method[192], which has been implemented in GROMACS[193], is based on iteratively solving a set of coupled non-linear equations,

$$P(\xi) = \frac{\sum_i n_i P_i(\xi)}{\sum_j n_j \exp\left(-\frac{w_j(\xi) - F_j}{k_{\mathrm{B}}T}\right)} \tag{2.17}$$

$$\exp\left(-\frac{F_i}{k_{\mathrm{B}}T}\right) = \int \mathrm{d}\xi \, P(\xi) \exp\left(-\frac{w_i(\xi)}{k_{\mathrm{B}}T}\right) \tag{2.18}$$

where n_i is the number of independent data points used to construct $P_i(\xi)$ and F_i represents the free energy associated with introduction of the biasing potential into the system[188].

2.2 Poisson-Boltzmann Electrostatics

Continuum descriptions of electrostatic interactions in solution as based on the mean-field Poisson-Boltzmann theory[194,195] provide a simplified and less computationally intensive alternative to MD simulations, allowing estimates of the PMF (Section 2.1.3) to be obtained from calculations on a static representation of the system. Entropic contributions are not considered in these approximations.

Fundamentally, the electrostatic potential at position $\boldsymbol{r}$, $\phi(\boldsymbol{r})$, is related to the charge density $\rho(\boldsymbol{r})$ through the Poisson equation,

$$-\nabla \cdot \left(\epsilon_0 \epsilon(\boldsymbol{r}) \nabla \phi(\boldsymbol{r})\right) = \rho(\boldsymbol{r}) \tag{2.19}$$

where ϵ is the relative electric permittivity and ϵ_0 denotes the permittivity of vacuum. The overall charge density is calculated as a sum of two components, ρ_{fixed} and ρ_{mobile}, respectively representing contribution from (partial) charges that are assumed to occupy known positions, such as those associated with biomolecular atoms, and from mobile ions in the system[196]. Partial atomic charges of the biomolecule are modelled using Dirac delta functions, each centred at the position vector $\boldsymbol{r}_i$ of the atom and with a magnitude of q_i, giving rise to

$$\rho_{\text{fixed}}(\boldsymbol{r}) = \sum_i q_i \delta(\boldsymbol{r} - \boldsymbol{r}_i) \tag{2.20}$$

whereas the mean density of mobile charges may be expressed, assuming a Boltzmann distribution for each ionic species j, as

$$\rho_{\text{mobile}}(\boldsymbol{r}) = \sum_j q_j n_j \exp\left(-\frac{q_j \phi(\boldsymbol{r})}{k_{\text{B}} T}\right) \tag{2.21}$$

where q_j is the ionic charge of the species and n_j is its number density in the bulk solution. Substitution of ρ_{fixed} and ρ_{mobile} into Equation 2.19 yields the Poisson-Boltzmann equation, which in the case of a monovalent electrolyte like NaCl may be reduced to

$$-\nabla \cdot \left(\epsilon_0 \epsilon(\boldsymbol{r}) \nabla \phi(\boldsymbol{r})\right) + \bar{\kappa}^2(\boldsymbol{r}) \sinh\left(\phi(\boldsymbol{r})\right) = \rho_{\text{fixed}}(\boldsymbol{r}) \tag{2.22}$$

in which

$$\bar{\kappa}^2(\boldsymbol{r}) = \frac{e^2 I}{\epsilon_0 k_{\text{B}} T} \chi(\boldsymbol{r}) \tag{2.23}$$

incorporates an ion accessibility function $\chi(\boldsymbol{r})$, which takes on a value of one in regions accessible to ions and zero elsewhere, as well as the Debye-Hückel screening parameter[197], with e denoting the elementary charge and the bulk ionic strength I defined as

$$I = \frac{1}{2} \sum_j n_j \frac{q_j^2}{e^2} \tag{2.24}$$

The non-linear term $\sinh\left(\phi(\boldsymbol{r})\right)$ in Equation 2.22 may be approximated by $\phi(\boldsymbol{r})$ under low-potential conditions, producing the linearised Poisson-Boltzmann equation[198],

$$-\nabla \cdot \left(\epsilon_0 \epsilon(\boldsymbol{r}) \nabla \phi(\boldsymbol{r})\right) + \bar{\kappa}^2(\boldsymbol{r}) \phi(\boldsymbol{r}) = \rho_{\text{fixed}}(\boldsymbol{r}) \tag{2.25}$$

which, like the full Poisson-Boltzmann equation, is commonly solved numerically through a multigrid finite-difference method[199,200] and has been demonstrated to yield comparable results in applications to biomolecular systems[201].

2.3 Measurement of Pore Dimensions

2.3.1 HOLE programme and alternatives

Methods for detecting molecular cavities may be classified, according to their algorithmic framework, into those based on (i) Voronoi diagrams, (ii) grids, (iii) probes, (iv) molecular surfaces, and combinations thereof[202,203]. In the case of open cavities such as channels or tunnels, software tools including HOLE[84], MOLE[204,205], and CAVER[206,207] are among the most popular. Both the MOLE algorithm and the latest version of CAVER utilise Voronoi diagrams to initiate computation of cavities and pathways[205,208], whereas grid-based approaches such as the original CAVER software project macromolecular structures onto a three-dimensional grid, with the void grid voxels subsequently processed and connected[206]. The probe-based HOLE programme, used in the present investigation, is one of the earliest tools for identifying a possible molecular path and specialises in tracking channel pathways[84,209].

Unlike surface-based approaches, which define molecular interfaces like the solvent-accessible or solvent- or ligand-excluded surface, most methods of the first three categories mentioned above apply a hard-sphere model to approximate protein atoms[202]. In HOLE, atoms in the input coordinate file are represented as van der Waals spheres[84]. A spherical

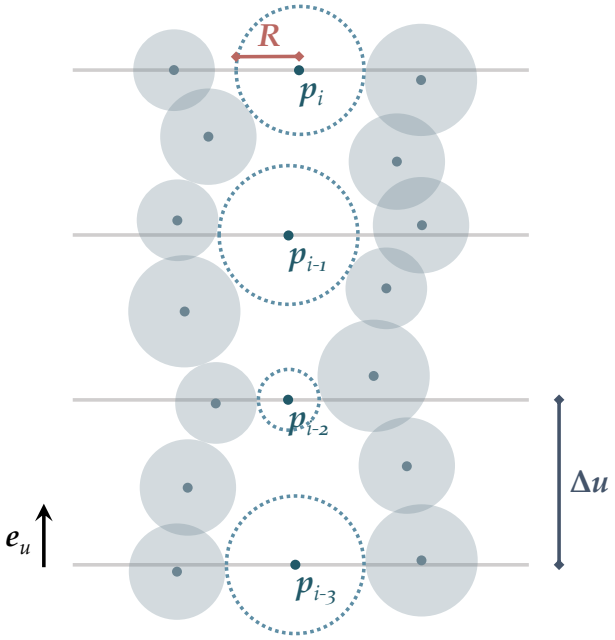


Figure 2.4 Schematic representation of the probe-based method for computing channel pathways as used in the HOLE programme[84] and Channel Annotation Package[80]. Protein atoms are approximated as van der Waals spheres (grey discs), and a spherical probe (dotted circles) is steered through the channel pore in steps of Δu along the direction of a unit vector $\boldsymbol{e}_u$, as specified by the user. The position of the probe, $\boldsymbol{p}_i$, on successive planes (represented as parallel lines) orthogonal to the channel direction vector is adjusted such that the probe radius R is maximised without overlapping the van der Waals sphere of any protein atom. The step size Δu is not shown to scale relative to the atomic radii. Adapted from Klesse *et al.* [80].

probe is steered through the channel pore, from an initial position $\boldsymbol{p}_0$, in steps of Δu along the direction of a unit vector $\boldsymbol{e}_u$ (Figure 2.4),

$$\tilde{\boldsymbol{p}}_i = \boldsymbol{p}_{i-1} + \Delta u \boldsymbol{e}_u \tag{2.26}$$

with each resulting position used to initialise a Monte Carlo simulated annealing procedure[210,211] that seeks to maximise the radius of the probe, $R(\boldsymbol{p})$, without overlapping the van der Waals sphere of any protein atom,

$$R(\boldsymbol{p}) = \min_{j \in [1,N]} \left\{ ||\boldsymbol{q}_j - \boldsymbol{p}|| - r_j \right\} \tag{2.27}$$

where r_j is the radius of atom j, centred on its coordinates $\boldsymbol{q}_j$, and N is the number of atoms present. The optimisation procedure is performed in the plane supported by $\tilde{\boldsymbol{p}}_i$ and spanned by the unit vectors $\boldsymbol{e}_v$ and $\boldsymbol{e}_w$, which are orthogonal both to $\boldsymbol{e}_u$ and mutually,

$$\boldsymbol{p}_i = \arg\max_{v,w} R(\tilde{\boldsymbol{p}}_i + v\boldsymbol{e}_v + w\boldsymbol{e}_w) \tag{2.28}$$

The process is repeated on successive planes along the direction of $\boldsymbol{e}_u$ (Figure 2.4) until the probe radius exceeds a threshold value, selected to indicate that the end of the channel has been reached. A second iteration is then performed in the -$\boldsymbol{e}_u$ direction, beginning from the same initial position, $\boldsymbol{p}_0$. Profiles of pore radii thus constructed from the resulting sequence of probe positions and associated maximum radius values along the channel axis, as determined by the HOLE programme[84], are routinely reported as new channel structures are resolved.

2.3.2 The Channel Annotation Package

The Channel Annotation Package (CHAP)[80], a software tool recently developed to facilitate efficient analyses of structures and simulations of channels and nanopores, employs a probe-based method similar to that of the HOLE algorithm[209] for defining physical dimensions of the pore (Figure 2.4). The downhill simplex optimisation algorithm[212] is implemented to improve the robustness of the pathway-finding procedure, and a probe step of 0.1 nm, the approximate van der Waals radius of a hydrogen atom, has been shown to be sufficiently small to yield converged pore radius estimates[80].

In CHAP, the set of calculated probe positions $\{\boldsymbol{p}_i\}$ are connected via B-spline interpolation into a continuous spatial curve $\boldsymbol{S}(s)$, allowing a continuous pore radius profile to be derived by interpolating the probe radii along the curve[80]. For radially symmetrical transmembrane pores, this is equivalent to the z-axis orthogonal to the plane of the membrane, whereas the advantage of describing the pathway through channel pores (and motions of particles therein, when analysing MD simulation trajectories) with respect to a one-dimensional reaction coordinate s is particularly notable in the case of non-linear pathways[213], which are unsuited to being projected onto a single Cartesian axis.

As part of its detection of channel pores, an additional functionality of CHAP relevant to the present investigation is the automated identification of amino acid residues lining the pore[80]. The side chain of residue i of the protein is considered to be pore-lining if the centre of geometry of the residue is located (i) within a cut-off distance d_0 from the pore surface and (ii) nearer than its α-carbon is to the centre line $\boldsymbol{S}(s)$ of the channel pathway,

$$\rho_i < R(s_i) + d_0 \tag{2.29}$$

$$\rho_i < \rho_i^{C\alpha} \tag{2.30}$$

where $R(s_i)$ is the pore radius at the s-coordinate of the centre of geometry of residue i and ρ_i and $\rho_i^{C\alpha}$ are, respectively, the distance from the residue centre-of-geometry and α-carbon position to the pathway centre line.

A d_0 value of 0.55 nm is generally used for ion channel structures examined in this thesis, with channel-specific adjustments of the parameter upon visual inspection of the identified residues to ensure inclusion of all side chains oriented towards the permeation pathway, with exclusion of those where access to the pore is obstructed by another residue. When the above analysis is performed on an MD simulation trajectory, a pore-lining amino acid side chain is defined as one that meets the conditions given by Inequalities 2.29 and 2.30 in over half of the analysed frames.

"Mr Holmes, they were the footprints of a gigantic hound!"

From *The Hound of the Baskervilles* by Sir A. C. Doyle, 1902

3

Effects of size and polarity: Insights from bestrophin-1 mutants

3.1 Methods **37**
3.1.1 Equilibrium molecular dynamics simulations 37
3.1.2 Boltzmann inversion and free energy profiles 38
3.1.3 Umbrella sampling and potential of mean force calculation . . . 40
3.2 Results and Discussion **40**
3.2.1 A hydrophobic gate in the wild-type structure 40
3.2.2 Pore widening removes the free energy barrier 43
3.2.3 Robustness of protocol for structure annotation 43
3.2.4 Increasing gate polarity yields distinct profiles 45
3.3 Conclusion **48**

Eukaryotic bestrophin proteins are calcium-activated chloride channels with a broad tissue distribution[214]. Bestrophin-1 (BEST1) is highly expressed in the retinal pigment epithelium, and dysfunction of the human channel has been associated with macular degenerative disorders[215,216]. Crystal structures of chicken BEST1[217] and its bacterial homologue from *Klebsiella pneumoniae*, KpBest[218], have revealed a symmetric assembly of five subunits surrounding a central pore (Figure 3.1). The extracellular end of the transmembrane channel forms a wide vestibule that leads into a narrow 'neck' region towards the cytoplasmic side, lined by three rings of conserved hydrophobic amino acids. In the BEST1 structure, these residues correspond to the isoleucine 76, phenylalanine 80, and phenylalanine 84 positions. The channel pore widens through the cytoplasmic

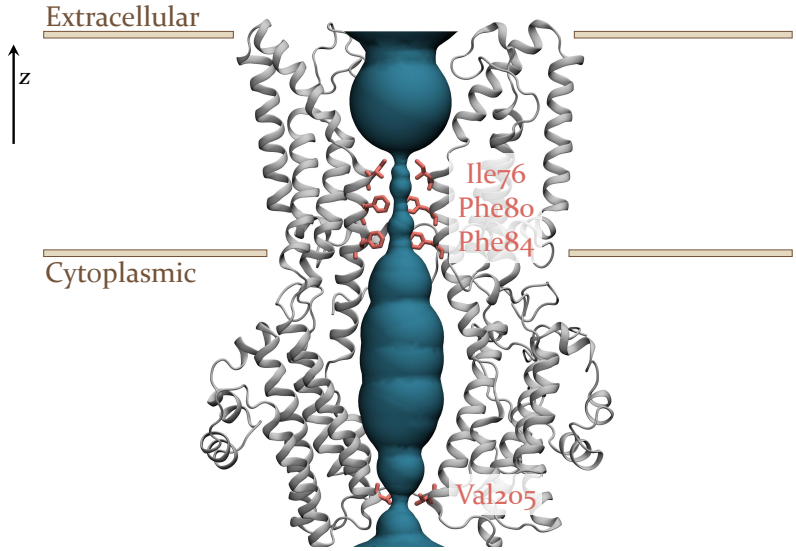


Figure 3.1 Structure of the bestrophin-1 channel (PDB ID: 4RDQ)[217]. The protein is oriented with its cytoplasmic side in the negative z direction orthogonal to the plane of the membrane, the approximate position of which is indicated by the beige lines. For clarity, only two non-adjacent subunits of the pentameric channel are displayed, in a ribbon representation. The inner pore surface, as calculated using the HOLE programme[84] and visualised in VMD[219], is shown in dark blue. Hydrophobic side chains lining the neck and aperture regions of the channel pore are coloured orange.

domain before reaching an additional constriction, the 'aperture', formed by the side chain of valine 205 from each subunit[217].

Recent studies have suggested that the neck region observed in these first bestrophin structures functions in the gating mechanism of the channel[220]. A triple-alanine mutant of BEST1, in which the three bulky hydrophobic positions were each substituted with a ring of alanine residues, was shown to exhibit substantially elevated transport activity by electrophysiological current recordings and ionic flux assays on the liposome-reconstituted channels[220]. The structure of the triple-alanine mutant has also been resolved, revealing increased pore radius at the proposed channel gate[220].

As discussed in Section 1.3.3, Trick *et al.* [131] have demonstrated the utility of molecular dynamics (MD) simulations of water behaviour in examining hydrophobic gating in channels pores for functional annotation of ion channel structures. In particular, the approach was applied to members of the pentameric ligand-gated ion channel (pLGIC) superfamily, the conserved hydrophobic gate among which have been a focus of much previous research (Section 1.3.2).

Using structures of BEST1, belonging to a family of channels unrelated to pLGICs, the present investigation set out to further assess the applicability of the equilibrium simulation approach. The recently resolved triple-alanine mutant structure is compared with that of the wild-type channel, and the ability of the analysis to provide a consistent indicator regarding the functional state of a channel pore is evaluated. In addition, by simulating changes in water behaviour upon several alternative, *in silico* mutations of the protein at equivalent pore-lining positions, the influence of the degree of pore hydrophobicity is explored.

Results described in the chapter include those presented in the following publications:

Rao, S., Klesse, G., Stansfeld, P. J., Tucker, S. J. and Sansom, M. S. P. A BEST example of channel structure annotation by molecular simulation. *Channels (Austin, Tex.)* **11,** 347–353 (2017)

Rao, S., Lynch, C. I., Klesse, G., Oakley, G. E., Stansfeld, P. J., Tucker, S. J. and Sansom, M. S. P. Water and hydrophobic gates in ion channels and nanopores. *Faraday Discussions* **209,** 231–247 (2018)

3.1 Methods

3.1.1 Equilibrium molecular dynamics simulations

MD simulations were performed, in GROMACS version 5.1[151], on the wild-type BEST1 and KpBest structures, with Protein Data Bank (PDB) IDs of 4RDQ[217] and 4WD8[218], respectively, the triple-alanine BEST1 mutant structure (PDB ID: 5T5N)[220], and additional mutant structures generated in PyMOL[21] based on the wild-type BEST1 conformation. Each structure was embedded into a phospholipid (POPC, 1-palmitoyl-2-oleoyl-*sn*-glycero-3-phosphocholine) bilayer membrane (Figure 3.2A), solvated on either side with aqueous NaCl at a concentration of 0.15 M.

A sequential multiscale procedure developed by Stansfeld and Sansom [223] was employed for the preparation and equilibration of membrane systems, whereby the protein structure was first converted into a coarse-grained model and simulated for 100 ns in the presence of coarse-grained lipids, water particles, and Na^+ and Cl^- ions using version 2.2 of the Martini force field[224,225]. During the simulation, lipid molecules would spontaneously

assemble into a bilayer around the protein. Upon visual inspection to confirm that none obstructed the channel pore, the resulting protein-membrane configuration was reconverted into its atomistic representation, using the original atomic coordinates of the experimentally resolved protein conformation. Six such simulation systems were independently assembled, in the case of the wild-type BEST1 structure, for subsequent initiation of replicate simulations. Three independent systems were prepared for each of its mutants and for KpBest.

The OPLS all-atom protein force field was used with united-atom lipids[164] and the TIP4P water model[175] for atomistic simulations in the isothermal-isobaric ensemble. Temperature and pressure were maintained at 37 °C and 1 bar, using the velocity-rescaling thermostat[154] with a coupling constant of 0.1 ps and a semi-isotropic Parrinello and Rahman barostat[155] with a coupling constant of 1 ps. Long-range electrostatic interactions were treated using the smooth particle mesh Ewald method[147,148] with a real-space Coulomb cut-off of 1 nm, a Fourier spacing of 0.12 nm, and charge interpolation through fourth-order B-splines. Lennard-Jones interactions were calculated with a cut-off of 1 nm, and a long-range dispersion correction was applied to the energy and pressure. Time integration was performed using a leap-frog integrator with a step size of 2 fs. The linear constraints solver algorithm LINCS[226,227] was used to constrain covalent bonds. Harmonic positional restraints, with a force constant of 1000 kJ mol^{-1} nm^{-2}, were placed on either all protein atoms or the protein backbone during simulations.

Replicate simulations each of 100 ns were initially performed for the wild-type and triple-alanine mutant structures of BEST1. Based on an assessment of the typical length of time required for equilibration, the duration of further simulations was reduced to 50 ns for all structures.

3.1.2 Boltzmann inversion and free energy profiles

Under equilibrium conditions, the time-dependent number density of water molecules at a given position z along the channel pore, $n(z)$, is related to the free energy, $G(z)$, through

$$n(z) = C \exp\left(-\frac{G(z)}{k_{\mathrm{B}}T}\right) \tag{3.1}$$

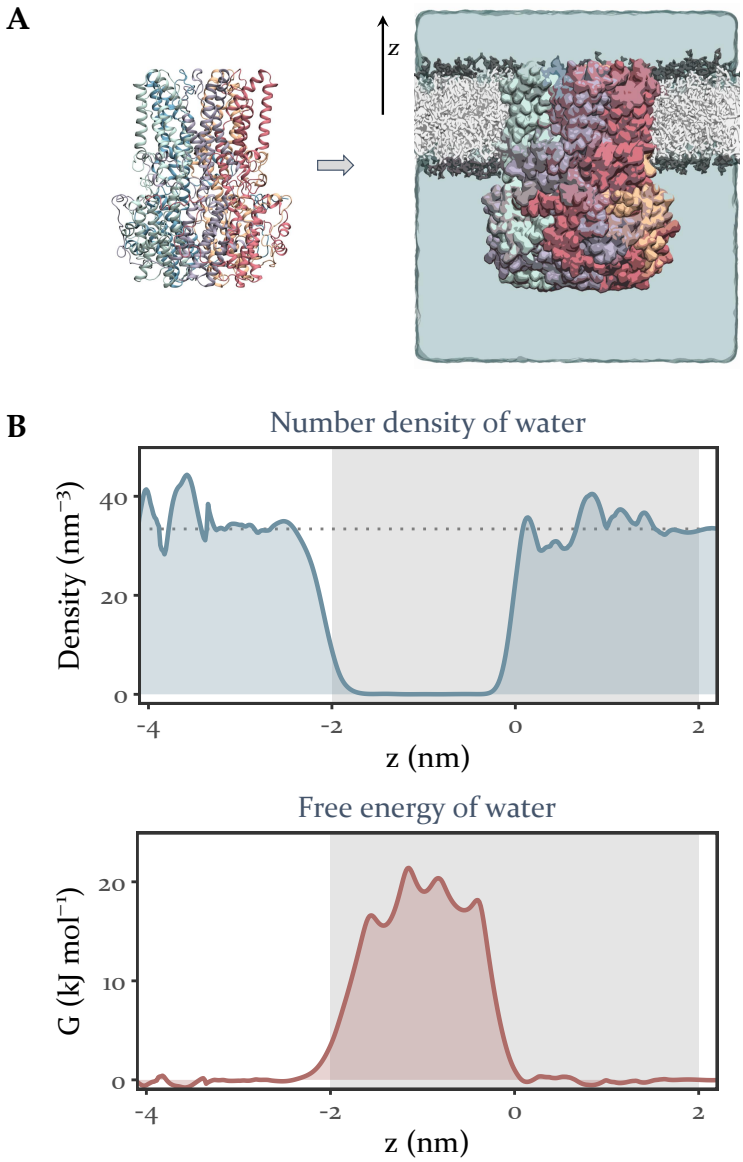


Figure 3.2 Molecular dynamics simulation and analysis of hydrophobic gating, with (**A**) the ion channel structure (in a ribbon or surface representation) embedded within a membrane and (**B**) a free energy profile calculated for water molecules in the channel pore from their mean number density along the channel axis z during the simulation, based on the Boltzmann distribution. The approximate bulk water density of 33.4 nm^{-3} is represented by the dotted line. The membrane position is indicated by the grey shading.

where z is the Cartesian coordinate normal to the plane of the membrane, k_B is the Boltzmann constant, T is the absolute temperature, and C is a normalisation constant related to the partition function of the system. Inversion of the above relationship yields

$$G(z) = -k_B T \left(\ln n(z) - \ln C\right) \tag{3.2}$$

in which the constant C may be determined by the convention of setting the free energy in the bulk water region on either side of the pore to zero (Figure 3.2B). The number density through the channel was defined as the number of water particles per unit volume, with the local cross-sectional area of the pore approximated as circular and calculated from pore radius values given by the HOLE programme[84]. Kernel density estimation was applied, whereby each discrete water molecule position was associated with a Gaussian probability distribution, using a smoothing bandwidth of 0.1 nm, and the overall density was obtained via summation of all Gaussians.

3.1.3 Umbrella sampling and potential of mean force calculation

Umbrella sampling simulations were initiated using an equilibrated atomistic system containing the membrane-embedded transmembrane domain of the wild-type BEST1 structure surrounded by an aqueous NaCl solution at a concentration of 0.15 M, as described above. In 36 consecutive sampling windows, a single Cl^- ion was placed at successive z positions along the central channel axis, spaced at 0.1 nm intervals. The sampling windows spanned the neck region and extended approximately 1 nm from its either side. A harmonic biasing potential was applied to the z-coordinate of the Cl^- ion with a force constant of 1000 kJ mol^{-1} nm^{-2}. Each window was simulated for 5 ns, during which positional restraints of 1000 kJ mol^{-1} nm^{-2} were placed on protein backbone atoms. Potential of mean force (PMF) profiles were computed using the weighted histogram analysis method[192], and statistical errors on the free energy profile were estimated using the Bayesian bootstrapping method[193]. Convergence was assessed by comparing free energy profiles computed from consecutive fractions of simulation time.

3.2 Results and Discussion

3.2.1 A hydrophobic gate in the wild-type structure

The pore radius of approximately 0.15 to 0.2 nm in the neck region of the wild-type BEST1 structure is comparable to that of a dehydrated Cl^- ion[228] (Figure 3.3A), and the region was previously hypothesised to be able to accommodate single-file ion passage[217]. However, more recent evidence supports a role of the three rings of hydrophobic residues in channel gating, and it was suggested that the structure, despite being determined

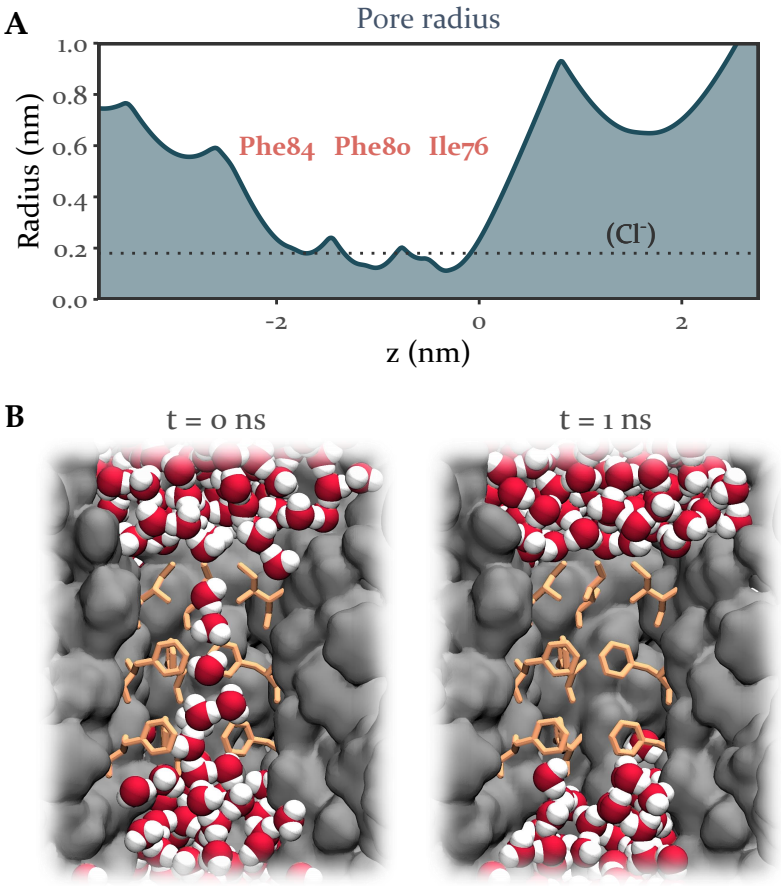


Figure 3.3 (**A**) Pore radius profile around the neck region of a wild-type bestrophin-1 structure (PDB ID: 4RDQ)[217], showing the positions of the three rings of hydrophobic residues, and (**B**) the behaviour of water within the region in the first nanosecond of a molecular dynamics simulation of the structure, during which positional restraints were applied to protein backbone atoms. De-wetting was observed on a similar timescale in simulations where all protein atoms were restrained. The pore radius was calculated using the HOLE programme[84] and plotted along the central channel axis, z, orthogonal to the plane of the membrane, oriented such that the cytoplasmic side of the channel corresponds to the negative z direction. The approximate radius of a dehydrated Cl^- ion[228] is indicated by the dotted line. Molecular graphics images were prepared in VMD[219], with water molecules shown as red and white spheres and the hydrophobic side chains in orange. The remainder of the protein is represented as a grey surface.

in the presence of Ca^{2+} ions, may instead correspond to a closed or inactivated state of the calcium-activated channel[220]. In MD simulations of the structure, the small number of water molecules that were initially present in the hydrophobic constriction were invariably expelled from the region on a sub-nanosecond timescale (Figure 3.3B). The hydrophobic neck of the structure, approximately 2 nm in length along the channel axis, remained predominantly devoid of water over the course of up to 100 ns simulations.

Water free energy profiles estimated from these simulations revealed a value of around 20 kJ mol^{-1} within the neck region (Figure 3.4), presenting a sizeable thermodynamic barrier to permeation compared with the mean thermal energy of approximately 2.6 kJ mol^{-1} at physiological temperature. The low density of water in this region contrasted with the pore water distribution on its either side, where the resulting free energy of water was equal to the bulk phase value of zero (Figure 3.4). The observed de-wetting behaviour is consistent with the isoleucine and phenylalanine rings forming a closed hydrophobic gate in the structure, in support of the assignment of a non-conductive conformation.

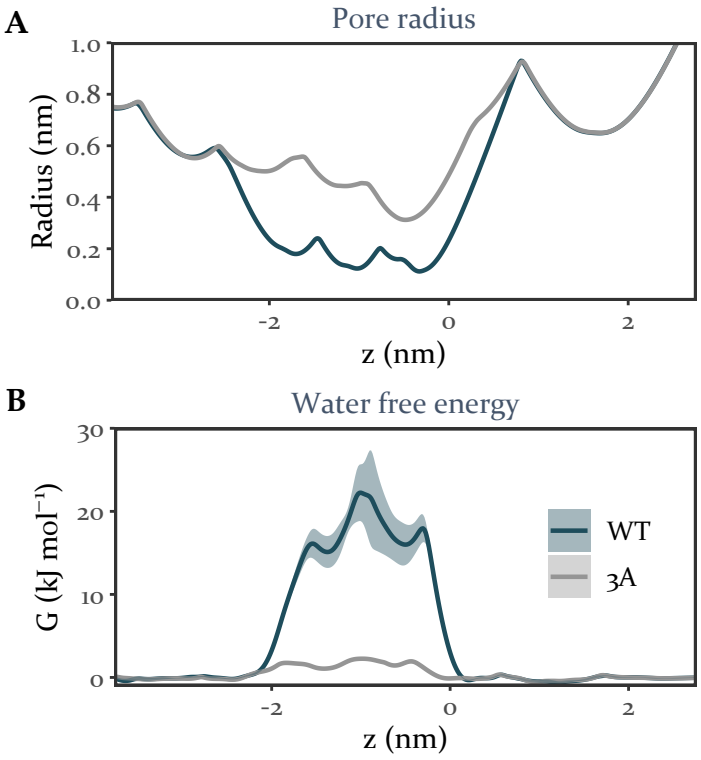


Figure 3.4 (**A**) Pore radius and (**B**) water free energy profiles around the hydrophobic constriction of a wild-type (WT) bestrophin-1 structure (PDB ID: 4RDQ)[217] and in the corresponding region of its triple-alanine (3A) mutant (PDB ID: 5T5N)[220]. Pore radii were calculated using the HOLE programme[84] and plotted along the central channel axis, z, orthogonal to the plane of the membrane, oriented such that the cytoplasmic side of the channel corresponds to the negative z direction. Replicate-averaged free energy profiles were derived from independent 50 ns simulations where positional restraints were applied to all protein atoms, showing the mean and standard deviation between six replicates for the WT structure and between three replicates for the 3A mutant.

3.2.2 Pore widening removes the free energy barrier

Substitution of the three rings of hydrophobic residues with alanine led to an increase in pore radius in the region to above 0.3 nm (Figure 3.4A). Upon equilibrium simulations, the mutant BEST1 structure remained hydrated through its channel pore, and the water free energy profile showed a maximum value within the range allowed by thermal fluctuations, in sharp contrast with the large energetic barrier calculated for the wild-type channel (Figure 3.4B).

On the basis of these simulations, the triple-alanine mutation is suggested to functionally open the channel by diminishing the effect of hydrophobic gating. The isoleucine-phenylalanine-phenylalanine motif of BEST1 appears to provide a more complex example of a hydrophobic gate than the conserved 9′ leucine ring of the pLGIC superfamily (Section 1.1.2.1) and further exemplifies the capability of the simulation method to inform the functional annotation of ion channel structures by identification of dehydration barriers.

The putative open conformation of the wild-type channel has since been structurally resolved[229], showing dramatic widening of the gate region, with the isoleucine and phenylalanine side chains rotated away from the pore. The minimum pore radius in the region is increased to approximately 0.5 nm, even greater than that of the triple-alanine mutant structure[220].

3.2.3 Robustness of protocol for structure annotation

The water free energy profiles presented above (Figure 3.4B) were each derived from simulations in which the ion channel conformation was strictly preserved by imposing positional restraints on all protein atoms. However, thermal fluctuations may be expected to permit dynamic changes in the conformation of amino acid side chains lining the pore, and earlier studies of hydrophobic gating have demonstrated that permeation of water and ions through a channel is influenced by the local flexibility in the pore wall[97]. To address this issue, the structures were also simulated with restraints applied only to the protein backbone, thereby allowing for a degree of local rotameric flexibility of pore-lining residues.

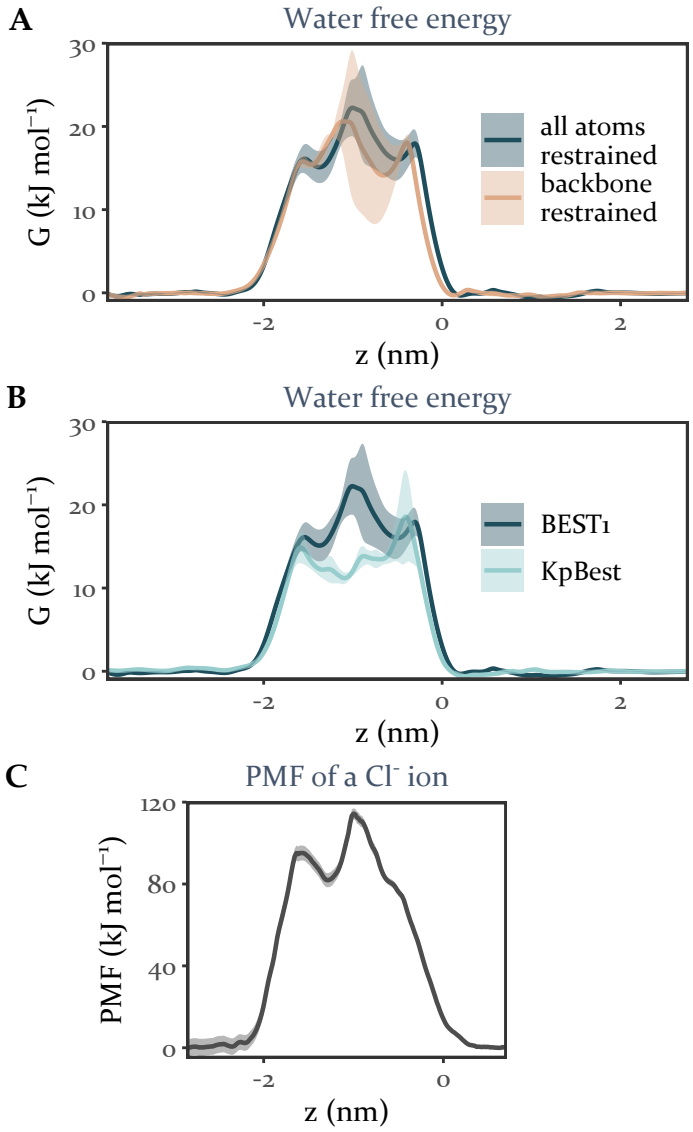


Figure 3.5 Comparisons of water free energy profiles in the closed hydrophobic gate region of bestrophin (**A**) between those derived from simulations of the bestrophin-1 (BEST1) structure (PDB ID: 4RDQ)[217] in which alternative positional restraints were applied, (**B**) between those determined for structures of BEST1 and its bacterial homologue, KpBest (PDB ID: 4WD8)[218], each simulated under all-atom restraints, and (**C**) with the potential of mean force (PMF) profile calculated for a Cl^- ion traversing the region within the BEST1 structure, computed from umbrella sampling simulations of its transmembrane domain. The protein is oriented such that its cytoplasmic side corresponds to the negative direction along the central channel axis, z, orthogonal to the plane of the membrane. Replicate-averaged free energy profiles were derived from independent 50 ns simulations, showing the mean and standard deviation between six replicates in the case of the BEST1 structure with all protein atoms restrained and between three replicates for both other sets of simulations. Statistical errors on the PMF profile were estimated via Bayesian bootstrapping[193].

Despite the increased degree of conformational mobility and resulting shifts in pore radii, with deviations of less than 0.1 nm relative to the original structure, the large free energy barrier to water permeation within the hydrophobic neck of the wild-type structure remained (Figure 3.5A). The mean water free energy profile determined for the triple-alanine mutant structure, as averaged between independent triplicates, was indistinguishable between the two sets of simulations.

The homologous KpBest channel, which shares the architecture and protein fold of BEST1, had been captured in a similar conformation[218] to the wild-type BEST1 structure[217]. Its hydrophobic neck region is constricted by the side chains of isoleucine and phenylalanine residues, as in BEST1, albeit with isoleucine instead of phenylalanine forming the central ring of the motif. Analysis of channel hydration in the corresponding region of the KpBest pore yielded a comparable energetic profile, as would be expected for a closed hydrophobic gate, with a slightly lower barrier height of around 15 kJ mol^{-1} (Figure 3.5B).

Underlying the use of simulations of water behaviour within ion channel pores to predict functionally closed channel conformations is the assumption that hydrophobic de-wetting would present a thermodynamic barrier that precludes ion passage[97,120]. To assess the energetic favourability of ion permeation through the neck region of the BEST1 chloride channel, umbrella sampling simulations[230] were performed for estimation of the PMF of a Cl^- ion as a function of its axial position along the pore of the membrane-embedded transmembrane domain of the wild-type structure. The PMF profile revealed a considerable energetic barrier, with a maximum value of above 100 kJ mol^{-1} (Figure 3.5C). The shape of the PMF corresponded reasonably closely to the water free energy profiles estimated from equilibrium simulations, particularly where the two rings of phenylalanine side chains yielded discernible peaks (Figure 3.5C).

3.2.4 Increasing gate polarity yields distinct profiles

The nature of the hydrophobic gate identified above was further explored through *in silico* mutagenesis. Six additional mutants of BEST1 were modelled based on the wild-type structure[217]. The isoleucine-phenylalanine-phenylalanine motif of pore-lining side chains were substituted, respectively, with three rings of isoleucine, leucine, valine, asparagine, threonine, or serine residues.

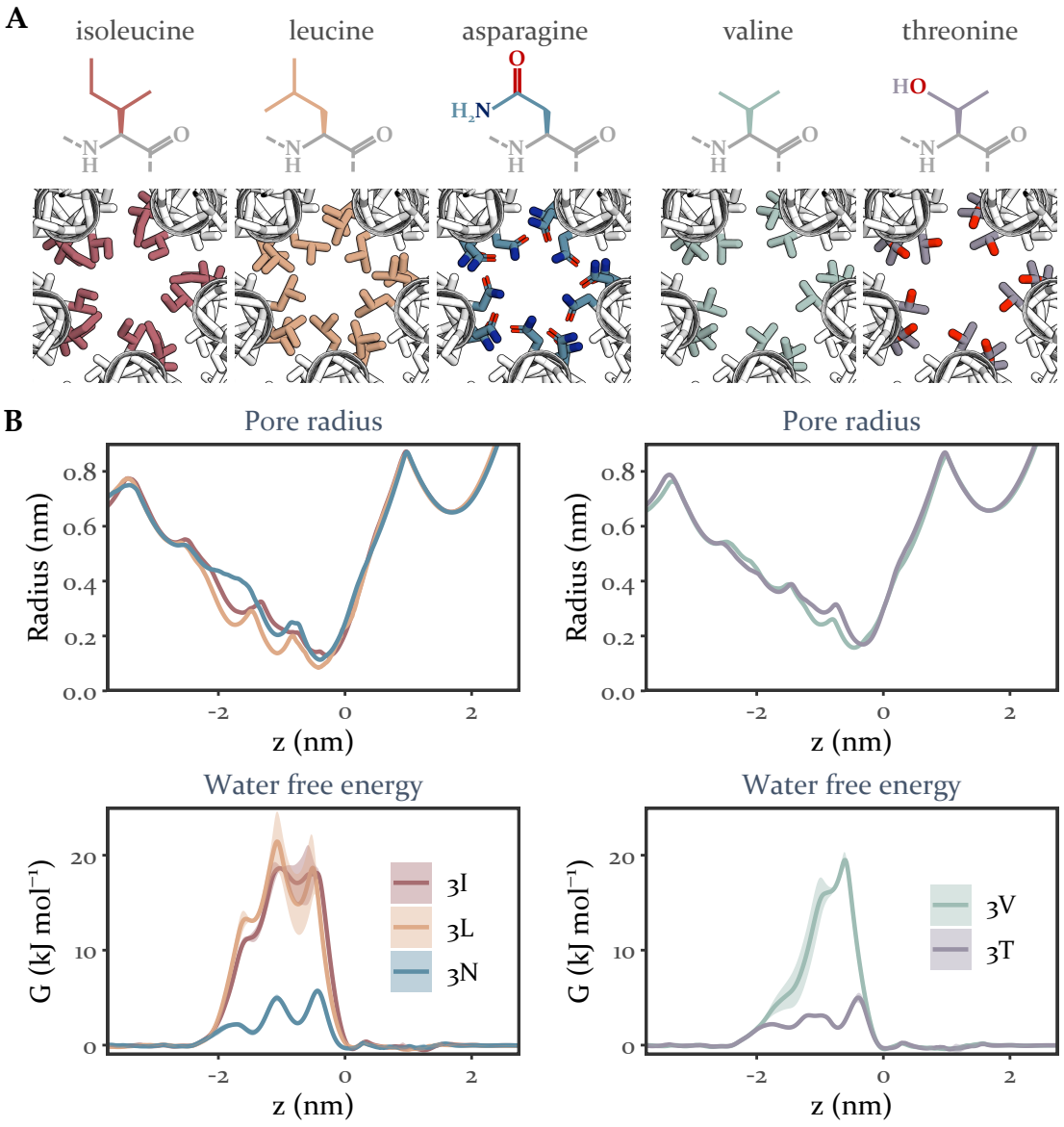


Figure 3.6 (**A**) Gate regions of five *in silico* mutants based on the putative closed conformation of bestrophin-1 (PDB ID: 4RDQ)[217], as viewed from the extracellular side of the pore, and (**B**) their water free energy profiles, each derived from three independent 50 ns simulations of the membrane-embedded channel, showing the mean and standard deviation between replicates. The triple-isoleucine (3I), triple-leucine (3L), triple-asparagine (3N), triple-valine (3V), and triple-threonine (3T) mutant structures were oriented such that their cytoplasmic side corresponds to the negative direction along the central channel axis, z, orthogonal to the plane of the membrane. Protein backbone atoms were restrained during simulations.

Pore radius profiles of the triple-isoleucine, triple-leucine, and triple-asparagine mutants were estimated to be very similar, each retaining the appearance of a relatively narrow neck with a minimum radius of below 0.15 nm (Figure 3.6B). Following the same equilibrium simulation protocol, the hydrophobic isoleucine and leucine side chains each gave rise to a water free energy barrier comparable in magnitude to that calculated for the wild-type structure. By contrast, introduction of polar carboxamide groups in the gate region led to a distinctly lowered free energy maxima of approximately 5 kJ mol^{-1} in the case of the triple-asparagine mutant (Figure 3.6C).

Another notable comparison could be made between mutant gates formed by smaller side chains of the two isosteric amino acids, valine and threonine (Figure 3.6). Whilst

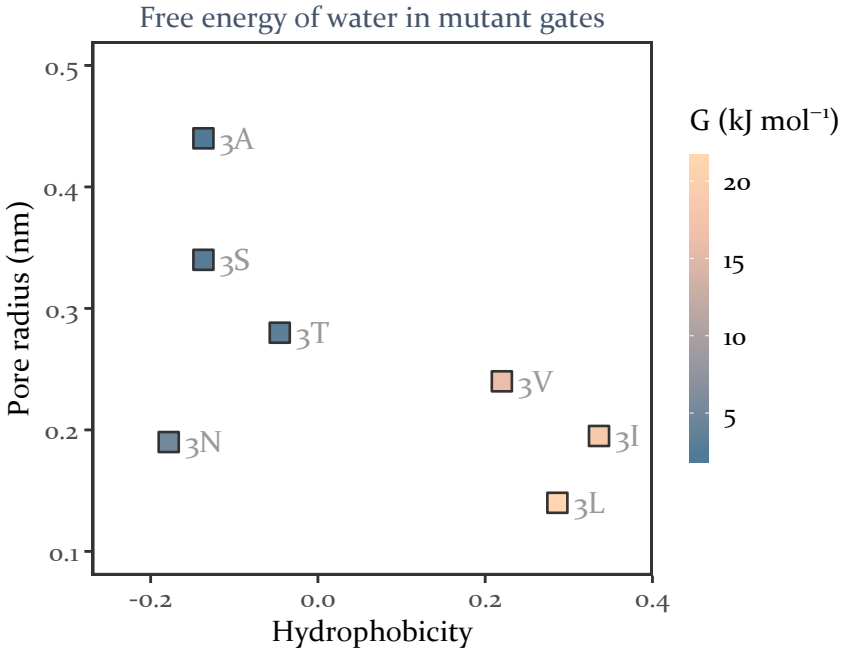


Figure 3.7 Pore radii at the axial centre of the gate region within seven *in silico* bestrophin-1 mutants, relative hydrophobicity of the substituting amino acids as assigned by the Wimley-White scale[231], and the maximum free energy of water in each mutant gate. The triple-isoleucine (3I), triple-leucine (3L), triple-asparagine (3N), triple-valine (3V), triple-threonine (3T), triple-serine (3S), and triple-alanine (3A) mutant structures were based on the putative closed conformation of bestrophin-1 (PDB ID: 4RDQ)[217]. The original numerical values of the amino acid hydrophobicity scale were linearly normalised such that the zero position was unshifted and the largest absolute value among amino acids was equal to one unit, with the biochemical convention of associating positive values with hydrophobic residues, yielding a range between -1 and 0.34, in relative units. Water free energy values were taken from replicate-averaged profiles derived from three independent 50 ns simulations of each membrane-embedded channel, during which positional restraints were applied to protein backbone atoms.

both sets of mutations yielded minimum pore radii of about 0.2 nm, the triple-valine gate, where the hydrophobicity was reduced by the presence of hydroxyl groups, exhibited markedly greater levels of pore hydration upon simulations. Its mean water free energy value of around 3 kJ mol^{-1} thus obtained was of the order of thermal fluctuations.

The effect of pore widening and of increasing the polarity in the channel lining on the simulated behaviour of water within the BEST1 gate may be visualised by constructing a water free energy plot on axes of local pore radii in the region against the degrees of hydrophobicity of the substituting amino acids (Figure 3.7). For comparability, an *in silico* triple-alanine mutant was also modelled and included among the analysed set of mutant structures. The pattern of their segregation into lower- and higher-energy areas further highlights the influence of hydrophobicity, particularly with the triple-asparagine gate more hydrated than the triple-valine gate despite the larger pore radius in the latter region.

3.3 Conclusion

This chapter has focused on analyses of structures of a single protein, BEST1, belonging to the bestrophin family of ion channels. An equilibrium MD simulation-based approach, previously demonstrated on members of the pLGIC superfamily[131], was applied to assess the likely functional state represented by a known conformation of the wild-type channel and a recently resolved mutant structure. A hydrophobic gate has thus been identified, its distinct motif of pore-lining amino acids providing a template for investigating the effect of pore size and polarity on water permeation through a given region of the channel.

The robustness of the protocol has been examined with respect to the use of conformational restraints in the simulation protocol, and the utility of the method for detecting hydrophobic barriers in channel pores has been further validated. These results may help to facilitate subsequent refinement and automation of the simulation-based tool and constitute a basis for larger-scale analyses of hydrophobic gating.

"He remarks that, while the individual man is an insoluble puzzle, in the aggregate he becomes a mathematical certainty."

From *The Sign of the Four* by Sir A. C. Doyle, 1890

4

A global survey across the ion channel structural proteome

4.1 Methods **52**
4.1.1 Preparation of ion channel structures 52
4.1.2 Equilibrium simulations and analysis 54
4.1.3 Support vector machine modelling 55
4.2 Results and Discussion **55**
4.2.1 Quantification of pore-lining hydrophobicity 55
4.2.2 Protocol for channel simulation and analysis 57
4.2.3 Analysis of the main energetic barrier in each structure 59
4.2.4 Analysis of all residues lining ion channel pores 66
4.2.5 A heuristic for prediction of pore hydration state 71
4.3 Conclusion **77**

Using model nanopores with a hydrophobic or polar pore lining, previous simulation studies (reviewed in Section 1.3.1) have systematically examined the influence of pore radius and hydrophobicity on the nanoscale liquid-vapour transitions that underlie channel hydration and de-wetting[86,94,97]. The vapour or de-wetted state was demonstrated to be stable below a critical pore radius of around 0.5 nm within a uniformly hydrophobic constriction, with the threshold radius decreasing upon introduction of partial charges in the pore wall[97]. Whilst ion channel structures containing hydrophobic regions with radii of up to approximately 0.3 nm have been reported to represent de-wetted, non-conductive conformations[112,124], identification of hydrophobic gates by analyses of structural features

alone is hampered by a lack of detailed understanding of the combined effect of the dimensions and physico-chemical properties of biological channel pores.

A number of hydrophobicity scales have been defined, based on various experimental and computational methods, for characterisation of individual amino acids[232]. An early hydropathy scale, for example, was constructed by Kyte and Doolittle [233] from an amalgamation of literature data on the distribution of residues in the interior versus exterior of globular proteins[234] as well as the water-vapour transfer free energies of amino acid side chain analogues[235–237]. In another study, Monera *et al.* [238] used the retention times of peptide analogues in reversed-phase high-performance liquid chromatography as a measure of hydrophobicity. The whole-residue scale introduced by Wimley and White [231], which has been referred to in Section 3.2.4 and will also be the main hydrophobicity scale employed for the present investigation, was derived from the transfer free energies of oligopeptides from water into a phospholipid membrane interface and into octanol[239].

Such relative numerical measurements (Figure 4.1) for each of the 20 standard amino acids have provided reference values for quantifying the degrees of hydrophobicity in channel pore regions, with contribution from combinations of pore-lining residues. Three additional hydrophobicity scales (Figure 4.1) that will be included for comparative analysis in this chapter include two with a more biological basis: Hessa *et al.* [240] quantified the efficiency of recognition of designed transmembrane segments by the endoplasmic reticulum translocon, Sec61, whereas Moon and Fleming [241] determined the thermodynamics of protein mutants folding into lipid bilayers, using the outer membrane phospholipase A as scaffold. More recently, a molecular dynamics (MD) approach was devised by Zhu *et al.* [242], simulating contact angles of a water nanodroplet on planar peptide networks composed of amino acid side chain repeats. For several hydrophilic residues that yielded a contact angle of 0°, artificial cosine values were obtained by extrapolation based on the excess chemical potential of a probe solute[243] at each network-water interface[242].

In the preceding chapter, a plot of simulated water free energies in corresponding regions within mutants of the bestrophin-1 channel (Figure 3.7) began to reveal a qualitative pattern consistent with a lowered threshold radius between the de-wetted and hydrated states as hydrophilic residues were substituted for the wild-type gate. However, the

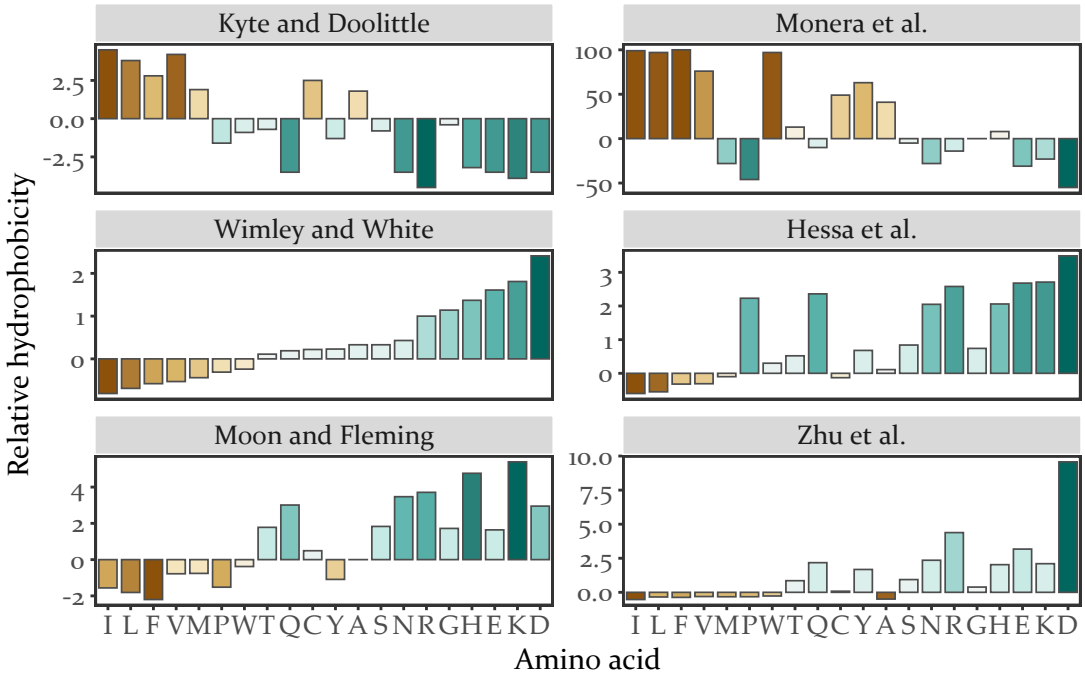


Figure 4.1 Relative hydrophobicity of the 20 standard amino acids as defined by six exemplifying experimental hydrophobicity scales, arranged in chronological order of their publication. The original numerical values reported, respectively, by Kyte and Doolittle [233], Monera *et al.* [238], Wimley and White [231], Hessa *et al.* [240], Moon and Fleming [241], and Zhu *et al.* [242] are displayed without normalisation. The amino acids are ranked, according to the Wimley and White [231] hydrophobicity scale, from highly hydrophobic (coloured brown) to highly hydrophilic (coloured teal). Depending on the method with which each set of measurements had been obtained, hydrophobic residues were assigned positive or negative values, and vice versa. For comparability, subsequent analyses in the chapter will follow the biochemical convention of associating positive hydrophobicity with hydrophobic residues and regions.

limitation of examining amino acid variants upon a single protein structure was also apparent. Due to the discrete nature and sparsity of the data points, and with the most highly hydrophobic amino acids being the bulkiest, regions on the pore hydrophobicity-radius landscape where phase transitions of water might occur could not be discerned. For further sampling of the range of accessible pore hydrophobicity-radius combinations represented by the ion channel structural proteome, the present investigation sought to exploit the expanding supply of structural data in the Protein Data Bank (PDB)[63,71].

At the time of the project, there were around 900 structures of over 100 unique ion channel proteins deposited in the PDB (Figure 1.3). Furthermore, the Channel Annotation Package (CHAP) was being developed by Klesse *et al.* [80] as an improved software tool for automatable analyses of channel pore dimensions and simulated water behaviour,

enabling a systematic examination of hydrophobic gating to be conducted. In this chapter, the influence of local pore radius and hydrophobicity on channel dehydration gating is quantified based on water behaviour in MD simulations of 190 ion channel structures. The results of the survey allow derivation of a simulation-free heuristic model for rapid identification of hydrophobic gates among channel conformations as new structures continue to be resolved. The method is also anticipated to facilitate the design of novel nanopores[244] containing dehydration barriers[245,246].

The same set of results have been described in the following publication:

Rao, S., Klesse, G., Stansfeld, P. J., Tucker, S. J. and Sansom, M. S. P. A heuristic derived from analysis of the ion channel structural proteome permits the rapid identification of hydrophobic gates. *Proceedings of the National Academy of Sciences of the United States of America* **116,** 13989–13995 (2019)

4.1 Methods

4.1.1 Preparation of ion channel structures

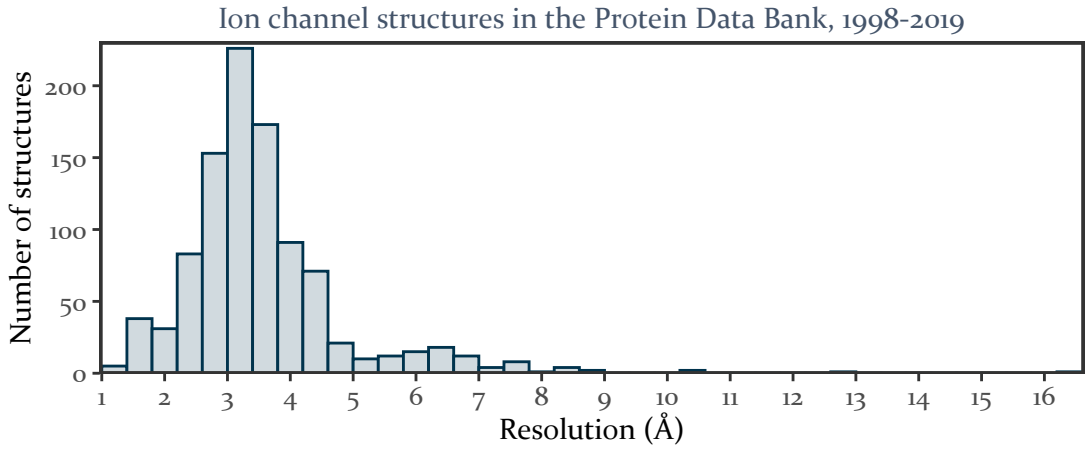


Figure 4.2 Distribution of resolution among over 900 ion channel structures determined by X-ray crystallography or cryo-electron microscopy in the Protein Data Bank, as of the end of the year 2019. 19 NMR structures have been excluded from the plot.

The collection of ion channel structures in the PDB were manually curated for the quality of the structural models, primarily based on their resolution (Figure 4.2), as well as the structural redundancy between them. Lower-resolution structures, resolved at 5 Å or greater, were excluded from subsequent simulation and analysis, as were those with an

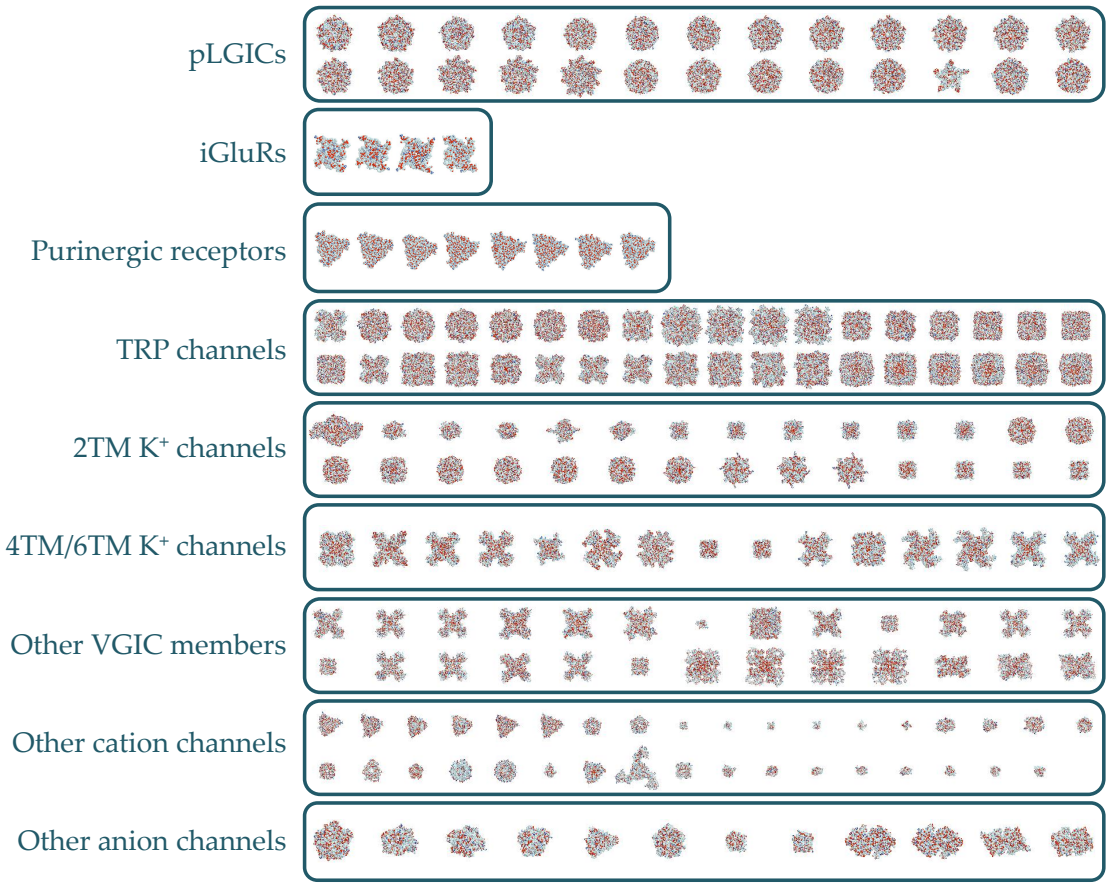


Figure 4.3 Montage of the 190 ion channel structures selected for simulation and analysis. The proteins are grouped into nine broad families: the pentameric ligand-gated ion channels (pLGICs), ionotropic glutamate receptors (iGluRs), purinergic receptors, transient receptor potential (TRP) channels, two-transmembrane domain (2TM) and four- or six-transmembrane domain (4TM or 6TM) potassium (K^+) channels, other members of the voltage-gated ion channel (VGIC) superfamily, other cation channels, and other anion channels. Each structure is viewed through its pore from the extracellular or luminal side. 12 structures of size greater than 3,000 amino acids, including all four iGluR structures, were truncated to include only the transmembrane or pore domain (Table 4.1).

incomplete backbone in their pore-lining segments. Where multiple structures of the same channel protein were available, their pore radius profiles were compared using the HOLE programme[84], their atomic coordinates were visually inspected in PyMOL[21], and root-mean-square deviations were measured between structures. Among those of a similar pore conformation according to such assessments, only the higher-resolution structure(s) of the wild-type protein were selected.

For the reduced data set of 190 structures thus produced (Figure 4.3), any auxiliary subunits, fused antigen-binding fragments or other proteins, ligands, ions, or water

molecules present in each PDB entry were removed from the coordinate file. 12 multi-domain channel structures of size greater than 3,000 amino acids were truncated to include only the transmembrane or pore domain (Table 4.1). Incomplete protein side chains were modelled using the WHAT IF server (`https://swift.cmbi.umcn.nl/whatif/`)[248].

4.1.2 Equilibrium simulations and analysis

Equilibrium MD simulations were performed in GROMACS version 5.1[151]. Channel structures were embedded into a phospholipid (POPC, 1-palmitoyl-2-oleoyl-*sn*-glycero-3-phosphocholine) bilayer membrane via the multiscale protocol developed by Stansfeld and Sansom [223], as described in Section 3.1.1. Three independent protein-membrane systems, solvated with aqueous NaCl at a concentration of 0.15 M, were prepared and equilibrated for each structure, and triplicate 30 ns simulations were performed. The OPLS all-atom protein force field was employed with united-atom lipids[164] and the TIP4P water model[175]. Temperature and pressure were maintained at 37 °C and 1 bar, using the velocity-rescaling thermostat[154] in combination with a semi-isotropic Parrinello and Rahman barostat[155], with coupling constants τ_T and τ_P of 0.1 ps and 1 ps, respectively. Long-range electrostatic interactions were treated using the smooth particle mesh Ewald method[147,148] with a real-space Coulomb cut-off of 1 nm, a Fourier spacing of 0.12 nm, and charge interpolation through fourth-order B-splines. Lennard-Jones interactions were calculated with a cut-off of 1 nm, and a long-range dispersion correction was applied to the energy and pressure. Time integration was performed using a leap-frog integrator with a step size of 2 fs. Covalent bonds were constrained through the linear constraints solver algorithm LINCS[226,227]. A harmonic restraint with a force constant of 1000 kJ mol^{-1} nm^{-2} was placed on the protein backbone atoms during simulations.

Identification of pore-lining side chains, measurement of water density along channel permeation pathways, and inverse Boltzmann calculations of water free energy profiles (Section 3.1.2) were performed by CHAP[80]. Trajectory frames from the final 20 ns of each simulation were sampled at 0.5 ns intervals. A kernel bandwidth of 0.14 nm, the approximate radius of a water molecule, was applied for pore water density estimation.

4.1.3 Support vector machine modelling

Support vector regression was conducted using the Caret package[249] in R version 3.4.4 (`https://www.r-project.org/`)[250]. The data set of 190 channel structures were randomly partitioned into training, validation, and testing sets, at a ratio of 64 %:16 %:20 %. Support vector machines were trained using repeated 10-fold cross-validation, with a linear, polynomial, or radial kernel. Resultant contour lines from the support vector regression were used to predict whether the testing set of 38 channel structures were each likely to contain an energetic barrier to water consequent of hydrophobic gating. The kernel function that produced the most accurate prediction performance was then selected.

4.2 Results and Discussion

4.2.1 Quantification of pore-lining hydrophobicity

For channel proteins consisting of symmetrically arranged subunits around a central pore axis, such as the bestrophin channel (Chapter 3) and homomeric subtypes of pentameric ligand-gated ion channels (Section 1.1.2.1), a profile of hydrophobicity along the channel pore could be defined by their sequence of consecutive rings of pore-lining amino acid side chains. The isoleucine-phenylalanine-phenylalanine or IFF gate in bestrophin-1, for example, is one combination among 4,200 possible triplet motifs that may theoretically arise from the 20 standard amino acids, accounting for palindromic symmetry. Approximately 7 % of these possible combinations were identified in the pore lining of the 99 unique ion channel proteins in the present data set, in regions where distinct tiers of residues could be discerned. 60 variants were observed in more than one channel, with 22 of the motifs occurring in at least three different proteins (Figure 4.4A). Using a weighted scoring method, the experimental hydrophobicity values of three or more amino acids forming a given pore-lining sequence motif could be used to estimate its overall hydrophobicity.

To generate a continuous hydrophobicity profile through the permeation pathway in each of the 190 selected structures, including those of heteromeric and monomeric channels, however, a more broadly applicable approach was used to represent contribution from all pore-lining side chains identified within a channel (Section 2.3.2), as has

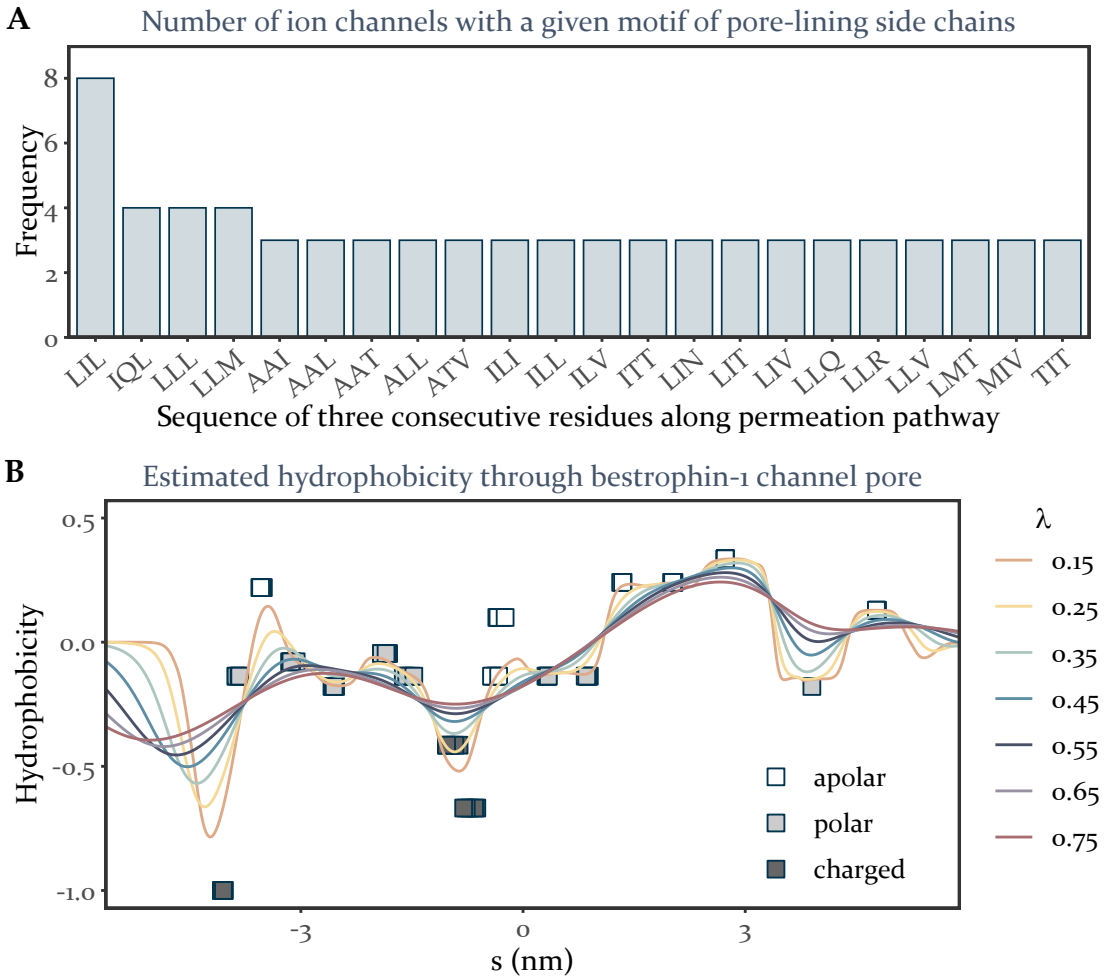


Figure 4.4 (**A**) Recurring pore-lining side chain motifs among the 190 channel structures analysed, displaying only triplet sequences identified in at least three different proteins, and (**B**) hydrophobicity profile along the permeation pathway (s) of a bestrophin-1 structure (PDB ID: 4RDQ)[217]. The Nadaraya-Watson estimator is used to calculate a kernel-weighted average from relative hydrophobicity values of individual pore-lining amino acids (white and grey squares), as assigned by the Wimley and White [231] scale. The effect of varying the smoothing bandwidth λ of the Gaussian kernel is illustrated.

been implemented in CHAP[80]. The relative hydrophobicity $H(s)$ along a channel pathway s was calculated from a distribution of discrete values, H_i, each associated with a pore-lining residue i at a centre-of-geometry position s_i, by taking a Nadaraya-Watson kernel-weighted average[251,252],

$$H(s) = \frac{\sum_i K_\lambda(s, s_i) H_i}{\sum_i K_\lambda(s, s_i)} \tag{4.1}$$

where each

$$K_\lambda(s, s_i) = \exp\left(-\frac{|s - s_i|^2}{2\lambda^2}\right) \tag{4.2}$$

is a Gaussian kernel with a smoothing bandwidth λ. A value of 0.45 nm, the rise per three residues of an α-helix, was selected for the hydrophobicity estimation (Figure 4.4B).

4.2.2 Protocol for channel simulation and analysis

Assessment of water behaviour in channel pores was based on three independent replicates of 30 ns atomistic MD simulations, as detailed in Section 4.1.2. Ion channel structures were embedded within a phospholipid bilayer, with NaCl added on either side of the membrane at a concentration of 0.15 M. With the aim of analysing the behaviour of water within channel conformational states represented by the set of available structures, positional restraints were applied to the protein backbone atoms to preserve the experimentally determined pore conformation whilst allowing for local side chain flexibility.

From CHAP[80] analyses of channel pore dimension, amino acid composition of the pore lining, and water density during simulations, time-averaged profiles were calculated for the local radius, hydrophobicity, and free energy of water as a function of position along each channel pathway (Figure 4.5A). Mean values were then taken between simulation replicates for characterisation of individual structures (Figure 4.5B). Based on more extended simulations of a subset of 25 channel structures, it was established that equilibrium simulations for a duration of 10 to 30 ns were able to provide robust estimates of the free energy landscape for water within an ion channel, even in the presence of a hydrophobic gate (Figure 4.5C). Tracking individual water molecules within such gate regions, hydrated before the initiation of each simulation, revealed de-wetting transitions within the first or first few nanoseconds, as was previously observed in hydrophobic gating of model nanopores[245,253] as well as for the closed structure of bestrophin-1 (Section 3.2.1).

Using the estimated levels of water free energy as a quantitative indicator of pore hydration and de-wetting behaviour in channel pores[131], the present protocol enables identification and comparison of hydrophobic barriers to permeation among the analysed ion channel structures. Furthermore, any given point along a channel pathway is thus associated with corresponding values for three variables of interest: the pore radius, hydrophobicity, and free energy of water in that region of the pore, enabling the dependence of water free energy on local radius and hydrophobicity to be investigated across the 190 channel structures of the data set (Table 4.1).

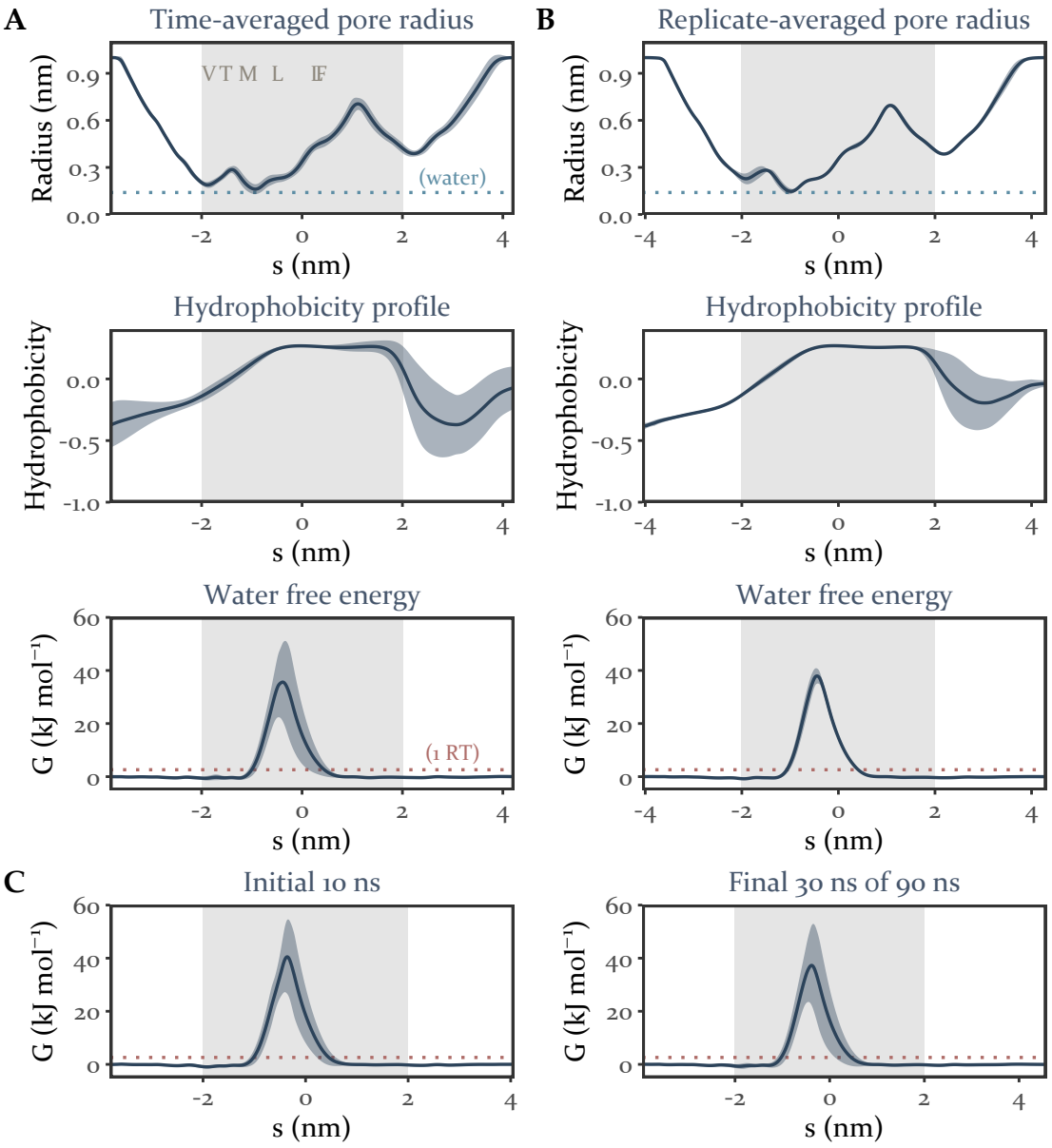


Figure 4.5 Channel pore annotation via equilibrium molecular dynamics simulations of water behaviour, illustrated for a recent structure of the TRPV4 ion channel (PDB ID: 6BBJ)[254]. (**A**) Time-averaged profiles of pore radius, hydrophobicity, and free energy of water as a function of position, s, along the channel axis, calculated from the final 20 ns of a 30 ns simulation where positional restraints were applied to protein backbone atoms, sampling at 0.5 ns intervals and showing the standard deviation over time. The grey shaded area represents the approximate position of the membrane, with the cytoplasmic side in the negative s direction. Mean s-axis coordinates of pore-lining residues with side chains that were oriented towards the pore in over half of the analysed trajectory frames are labelled. The blue and red dotted lines indicate, respectively, the approximate radius of a water molecule and an energy value of 1 RT (2.6 kJ mol^{-1}). (**B**) Pore profiles derived from three independent 30 ns simulations of the structure, showing the mean and standard deviation between replicates. (**C**) Water free energy profiles obtained from the initial 10 ns of the same simulation replicate as the first panel and, upon extension of the simulation to yield an overall duration of 90 ns, from the final 30 ns of the trajectory. The standard deviation over time is shown in each case, with a sampling interval of 0.5 ns.

4.2.3 Analysis of the main energetic barrier in each structure

Around 70 % of the 190 channel pores were annotated as containing one or more functionally closed gates, on the basis of their equilibrium simulation data (Table 4.1). Significant thermodynamic barriers, with maximum water free energy above 1 *RT* (or approximately 2.6 kJ mol^{-1}, the mean thermal energy at physiological temperature), frequently occurred in hydrophobic regions. The distribution of the magnitude of the main energetic barrier identified in each channel structure on the pore hydrophobicity-radius landscape (Figure 4.6) was in qualitative agreement with predictions from simplified models of hydrophobic gating[94,97] and with observations on mutant structures of the bestrophin-1 channel in the previous chapter (Figure 3.7).

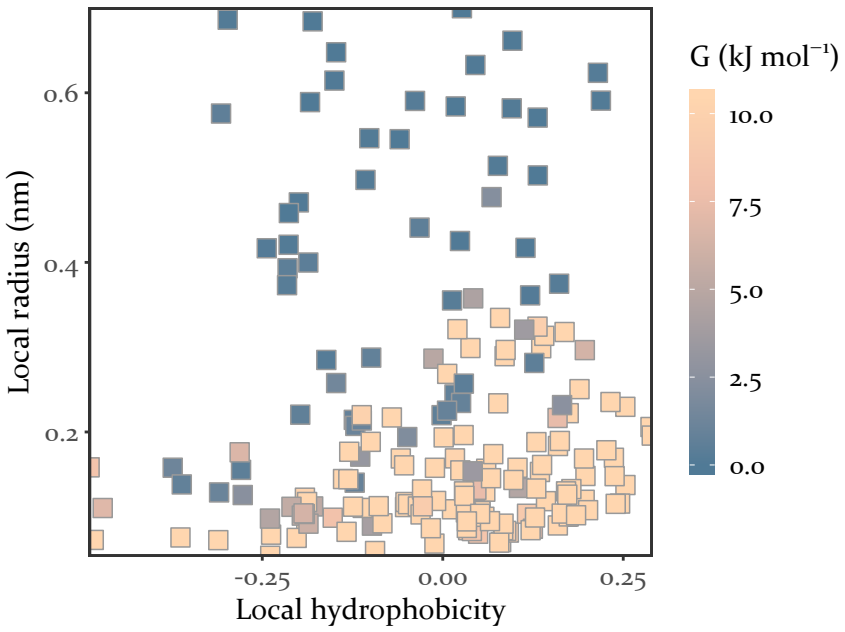


Figure 4.6 Analysis of the main energetic barrier to water in each of 190 ion channel pores. Channel structures are represented by individual points, indicating the pore radius and hydrophobicity at the mean maximum water free energy through their permeation pathway (averaged across three independent 30 ns simulations), as listed in Table 4.1. Points with energy values outside the colour scale range are shown in the same colour as the lower or upper bound. For potassium channel structures containing a narrow pore-loop selectivity filter, the section on their water free energy profile corresponding to the filter region was excluded when locating the maximum energy position to represent the structure. Relative hydrophobicity was estimated using the Wimley and White [231] scale, linearly normalised such that the zero position was unshifted and the largest absolute value among amino acids was equal to one unit, with more positive values indicating greater hydrophobicity, yielding a range between -1 and 0.34.

Relative to polar and charged amino acids, hydrophobic pore-lining residues showed distinctively high prevalence in regions exhibiting elevated water free energy. Aliphatic side chains of leucine, isoleucine, and valine residues were found to be most prevalent, followed by the aromatic phenylalanine and the small, aliphatic alanine (Figure 4.7).

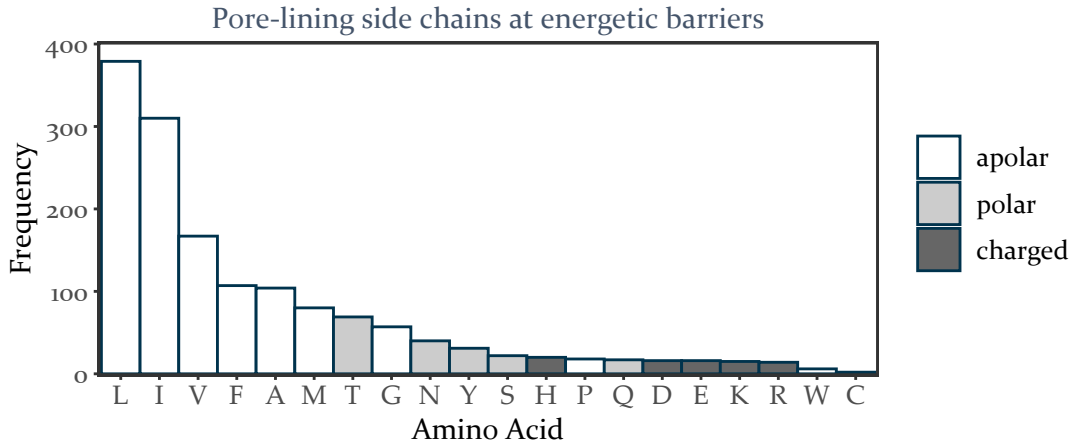


Figure 4.7 Frequency of occurrence of the 20 different pore-lining side chains at energetic barriers in the structures analysed, including all instances where the water free energy was greater than 1.5 *RT* (3.9 kJ mol^{-1}) at the mean position of the residue along the channel axis. Multiple amino acids may occur at each energetic barrier.

Table 4.1 Ion channel structures analysed. Any auxiliary subunits, fused antigen-binding fragments or other proteins, ligands, ions, or water molecules present in a Protein Data Bank (PDB) entry were removed prior to three independent 30 ns simulations of the membrane-embedded channel, with positional restraints applied to protein backbone atoms. Large structures that were truncated to include only the transmembrane or pore domain for analysis are indicated by an asterisk (*) next to their PDB ID. Where available, the likely functional state of a conformation as suggested upon its publication is noted. The mean height of the main energetic barrier to water (G_{water}) is recorded for each structure, with values coloured red (above 1 *RT*) or blue (less than or equal to 1 *RT*).

Protein	PDB ID	Method	Resolution (Å)	Proposed functional state	G_{water} (kJ mol^{-1})
Pentameric ligand-gated ion channels					
5-HT$_3$R, *M. musculus*	4PIR	X-ray	3.50	–[44]	41.6
5-HT$_3$R, *M. musculus*	6BE1	cryo-EM	4.31	closed[255]	44.3
ELIC, *E. chrysanthemi*	2VL0	X-ray	3.30	closed[256]	90.1
ELIC, *E. chrysanthemi*	3RQW	X-ray	2.91	closed[257]	78.8
GABA$_A$R, *H. sapiens*	4COF	X-ray	2.97	desensitised[258]	0.8
GABA$_A$R, *H. sapiens*	6A96	cryo-EM	3.51	open[259]	0.1
GABA$_A$R, *H. sapiens*	6D6T	cryo-EM	3.86	desensitised[260]	2.2

Continued on following page

Table 4.1 *Continued from previous page*

Protein	PDB ID	Method	Resolution (Å)	Proposed functional state	G_{water} (kJ mol^{-1})
$GABA_AR$, *H. sapiens*	6D6U	cryo-EM	3.92	desensitised[260]	28.3
GLIC, *G. violaceus*	2XQ7	X-ray	3.40	open[261]	0.5
GLIC, *G. violaceus*	3EHZ	X-ray	3.10	open[262]	0.2
GLIC, *G. violaceus*	4F8H	X-ray	2.99	–[263]	0.3
GLIC, *G. violaceus*	4HFI	X-ray	2.40	open[264]	0.5
GLIC, *G. violaceus*	4NPP	X-ray	3.35	open[265]	0.6
GLIC, *G. violaceus*	4QH5	X-ray	3.00	open[266]	0.2
GLIC, *G. violaceus*	5J0Z	X-ray	3.25	desensitised[267]	0.7
GLIC, *G. violaceus*	5L47	X-ray	3.30	closed[268]	48.3
GluCl, *C. elegans*	3RHW	X-ray	3.26	open[269]	0.8
GluCl, *C. elegans*	3RIF	X-ray	3.35	open[269]	0.9
GluCl, *C. elegans*	4TNV	X-ray	3.60	closed[270]	12.0
GlyR, *D. rerio*	3JAD	cryo-EM	3.90	closed[79]	4.6
GlyR, *D. rerio*	3JAE	cryo-EM	3.90	open[79]	0.0
GlyR, *D. rerio*	3JAF	cryo-EM	3.80	desensitised/ intermediate[79]	1.1
GlyR, *H. sapiens*	5CFB	X-ray	3.04	closed[271]	22.9
GlyR, *H. sapiens*	5VDH	X-ray	2.85	desensitised/ intermediate[272]	23.6
nAChR, *T. marmorata*	1OED	cryo-EM	4.00	closed[111]	9.6
nAChR, *T. marmorata*	2BG9	cryo-EM	4.00	closed[273]	3.6
nAChR, *H. sapiens*	5KXI	X-ray	3.94	desensitised[274]	0.0
Ionotropic glutamate receptors					
GluA, *R. norvegicus*	5WEK*	cryo-EM	4.60	closed[275]	4.0
GluA, *R. norvegicus*	5WEL*	cryo-EM	4.40	closed[275]	6.7
GluA, *R. norvegicus*	5WEO*	cryo-EM	4.20	open[275]	0.6
GluN, *X. laevis*	5UOW*	cryo-EM	4.50	open[276]	0.9
Purinergic receptors					
P2X3, *H. sapiens*	5SVJ	X-ray	2.98	closed[277]	25.6
P2X3, *H. sapiens*	5SVK	X-ray	2.77	open[277]	0.0
P2X3, *H. sapiens*	5SVL	X-ray	2.90	desensitised[277]	22.6
P2X4, *D. rerio*	3H9V	X-ray	3.10	closed[278]	38.6
P2X4, *D. rerio*	3I5D	X-ray	3.46	closed[278]	43.1
P2X4, *D. rerio*	4DW0	X-ray	2.90	closed[279]	36.2
P2X4, *D. rerio*	4DW1	X-ray	2.80	open[279]	0.2
P2X7, *G. gallus*	5XW6	X-ray	3.10	closed[280]	55.8

Continued on following page

Table 4.1 *Continued from previous page*

Protein	PDB ID	Method	Resolution (Å)	Proposed functional state	G_{water} (kJ mol^{-1})
Transient receptor potential channels					
NOMPC, *D. melanogaster*	5VKQ*	cryo-EM	3.55	closed[281]	11.0
PC2, *H. sapiens*	5K47	cryo-EM	4.22	closed[282]	10.1
PC2, *H. sapiens*	5MKE	cryo-EM	4.30	open[283]	1.2
PC2, *H. sapiens*	5MKF	cryo-EM	4.20	closed[283]	12.6
PC2, *H. sapiens*	5T4D	cryo-EM	3.00	closed[284]	32.0
PC2, *H. sapiens*	6D1W	cryo-EM	3.54	open[126]	14.8
PC2L1, *M. musculus*	5Z1W	cryo-EM	3.38	open[285]	28.8
TRPA1, *H. sapiens*	3J9P	cryo-EM	4.24	closed[286]	76.5
TRPM2, *N. vectensis*	6CO7	cryo-EM	3.07	closed[287]	44.4
TRPM4, *M. musculus*	6BCL	cryo-EM	3.54	closed[288]	9.3
TRPM4, *M. musculus*	6BCQ	cryo-EM	3.25	closed[288]	9.6
TRPM4, *H. sapiens*	6BQR	cryo-EM	3.20	closed[289]	8.3
TRPML1, *H. sapiens*	5WJ5	cryo-EM	3.72	closed[290]	27.3
TRPML1, *H. sapiens*	5WJ9	cryo-EM	3.49	open[290]	1.4
TRPML1, *M. musculus*	5WPV	cryo-EM	3.59	closed[291]	8.9
TRPML3, *C. jacchus*	5W3S	cryo-EM	2.94	closed[292]	6.9
TRPML3, *H. sapiens*	6AYE	cryo-EM	4.06	closed[293]	16.1
TRPML3, *H. sapiens*	6AYF	cryo-EM	3.62	open[293]	0.1
TRPML3, *H. sapiens*	6AYG	cryo-EM	4.65	closed[293]	10.1
TRPV1, *R. norvegicus*	3J5P	cryo-EM	3.27	closed[294]	8.9
TRPV1, *R. norvegicus*	3J5Q	cryo-EM	3.80	open[295]	4.9
TRPV1, *R. norvegicus*	3J5R	cryo-EM	4.20	closed[295]	5.2
TRPV1, *R. norvegicus*	5IRX	cryo-EM	2.95	open[296]	0.7
TRPV1, *R. norvegicus*	5IRZ	cryo-EM	3.28	closed[296]	8.4
TRPV1, *R. norvegicus*	5IS0	cryo-EM	3.43	closed[296]	8.6
TRPV2, *O. cuniculus*	5AN8	cryo-EM	3.80	desensitised[297]	66.8
TRPV2, *O. cuniculus*	6BWJ	X-ray	3.10	closed[298]	73.2
TRPV2, *R. norvegicus*	5HI9	cryo-EM	4.40	open[299]	38.3
TRPV4, *X. tropicalis*	6BBJ	cryo-EM	3.80	closed[254]	39.6
TRPV5, *O. cuniculus*	6B5V	cryo-EM	4.80	closed[300]	21.4
TRPV6, *R. norvegicus*	5IWK	X-ray	3.25	closed[301]	31.6
TRPV6, *R. norvegicus*	5IWP	X-ray	3.65	closed[301]	21.1
TRPV6, *R. norvegicus*	5WO6	X-ray	3.31	–[302]	20.0

Continued on following page

Table 4.1 *Continued from previous page*

Protein	PDB ID	Method	Resolution (Å)	Proposed functional state	G_{water} (kJ mol^{-1})
TRPV6, *H. sapiens*	6BO8	cryo-EM	3.60	open[303]	0.7
TRPV6, *H. sapiens*	6BOB	cryo-EM	3.90	closed[303]	36.6
Two-transmembrane domain potassium channels					
GsuK, *G. sulfurreducens*	4GX5	X-ray	3.70	closed[304]	12.3
K_{2P}1.1, *H. sapiens*	3UKM	X-ray	3.40	open[305]	0.2
K_{2P}2.1, *M. musculus*	5VKP	X-ray	2.80	–[306]	0.0
K_{2P}4.1, *H. sapiens*	4WFE	X-ray	2.50	open[307]	0.0
K_{2P}10.1, *H. sapiens*	4BW5	X-ray	3.20	open[308]	0.5
K_{2P}10.1, *H. sapiens*	4XDL	X-ray	3.50	open[308]	0.6
KcsA, *S. lividans*	1K4C	X-ray	2.00	–[309]	33.6
KcsA, *S. lividans*	2ITD	X-ray	2.70	–[310]	44.4
KcsA, *S. lividans*	3EFF	X-ray	3.80	closed[311]	48.6
KcsA, *S. lividans*	3FB5	X-ray	2.80	partially open[312]	0.0
KcsA, *S. lividans*	3PJS	X-ray	3.80	open[43]	0.0
KcsA, *S. lividans*	4UUJ	X-ray	2.40	closed[313]	24.5
K_{ir}2.2, *G. gallus*	3JYC	X-ray	3.11	closed[314]	19.8
K_{ir}2.2, *G. gallus*	3SPC	X-ray	2.45	closed[315]	28.0
K_{ir}2.2, *G. gallus*	3SPI	X-ray	3.31	closed[315]	37.2
K_{ir}3.2, *M. musculus*	3SYA	X-ray	2.98	closed[316]	3.1
K_{ir}3.2, *M. musculus*	3SYO	X-ray	3.54	closed[316]	1.0
K_{ir}6.2, *R. norvegicus*	6BAA	cryo-EM	3.63	closed[317]	29.0
K_{ir}6.2, *H. sapiens*	6C3O	cryo-EM	3.90	–[318]	37.1
K_{ir}Bac1.1, *B. pseudomallei*	2WLL	X-ray	3.65	closed[319]	13.5
K_{ir}Bac1.3/K_{ir}3.1, *M. musculus/B. xenovornas*	2QKS	X-ray	2.20	closed[320]	26.9
K_{ir}Bac3.1, *M. magnetotacticum*	2WLH	X-ray	3.28	closed[321]	45.0
K_{ir}Bac3.1, *M. magnetotacticum*	2WLI	X-ray	3.09	closed[321]	10.2
K_{ir}Bac3.1, *M. magnetotacticum*	2WLJ	X-ray	2.60	closed[321]	7.4
MthK, *M. thermautotrophicus*	1LNQ	X-ray	3.30	open[322]	0.0
NaK, *B. cereus*	2AHY	X-ray	2.40	closed[323]	20.0
NaK, *B. cereus*	3E86	X-ray	1.60	open[324]	0.5
NaK/Na_VSulP, *B. mycoides/S. pontiacus*	3VOU	X-ray	3.20	closed[325]	59.5

Continued on following page

Table 4.1 *Continued from previous page*

Protein	PDB ID	Method	Resolution (Å)	Proposed functional state	G_{water} (kJ mol^{-1})
Four- or six-transmembrane domain potassium channels					
KCNQ1, *X. laevis*	5VMS	cryo-EM	3.70	closed[326]	88.7
K_V1.2, *R. norvegicus*	2A79	X-ray	2.90	open[327]	0.0
K_V1.2, *R. norvegicus*	2R9R	X-ray	2.40	open[328]	0.0
K_V1.2, *R. norvegicus*	3LUT	X-ray	2.90	open[329]	0.0
K_V10.1, *R. norvegicus*	5K7L*	cryo-EM	3.78	closed[330]	17.5
K_V11.1, *H. sapiens*	5VA1*	cryo-EM	3.70	open[331]	0.0
K_VAp, *A. pernix*	1ORQ	X-ray	3.20	open[332]	0.0
K_VLm, *L. monocytogenes*	4H33	X-ray	3.10	closed[333]	13.6
K_VLm, *L. monocytogenes*	4H37	X-ray	3.35	closed[333]	10.9
MloK1, *M. loti*	3BEH	X-ray	3.10	closed[334]	22.3
MloK1, *M. loti*	6EO1	cryo-EM	4.50	open[335]	0.1
Slo1, *A. californica*	5TJ6	cryo-EM	3.50	open[336]	0.1
Slo1, *A. californica*	5TJI	cryo-EM	3.80	–[337]	0.1
Slo2.2, *G. gallus*	5U70	cryo-EM	3.76	open[338]	0.1
Slo2.2, *G. gallus*	5U76	cryo-EM	3.76	closed[338]	0.0
Other members of the voltage-gated ion channel superfamily					
Ca_V1.1, *O. cuniculus*	5GJV	cryo-EM	3.60	closed[339]	80.4
Ca_VAb, *A. butzleri*	4MVM	X-ray	3.20	–[340]	7.3
Ca_VAb, *A. butzleri*	5KLB	X-ray	2.70	–[341]	27.2
TAX5 (CNG), *C. elegans*	5H3O	cryo-EM	3.50	open[342]	1.1
LliK (CNG), *L. licerasiae*	5V4S	cryo-EM	4.20	closed[343]	33.1
HCN1, *H. sapiens*	5U6O	cryo-EM	3.50	closed[344]	27.8
H_V1, *M. musculus*	3WKV	X-ray	3.45	closed[345]	32.3
InsP3R1, *R. norvegicus*	3JAV*	cryo-EM	4.70	closed[346]	46.7
Na_V1.4, *E. electricus*	5XSY	cryo-EM	4.00	open[347]	28.1
Na_VAb, *A. butzleri*	4EKW	X-ray	3.21	closed[348]	18.8
Na_VAb, *A. butzleri*	4MW8	X-ray	3.26	–[340]	2.5
Na_VAb, *A. butzleri*	5EK0	X-ray	3.53	closed[349]	89.5
Na_VAb, *A. butzleri*	5VB2	X-ray	3.20	closed[350]	119.5
Na_VAb, *A. butzleri*	5VB8	X-ray	2.85	open[350]	6.3
Na_VAe1, *A. ehrlichii*	4LTO	X-ray	3.46	closed[351]	85.4
Na_VMm, *M. marinus*	4CBC	X-ray	2.66	open[352]	25.2
Na_VMm, *M. marinus*	4OXS	X-ray	2.80	open[352]	28.2

Continued on following page

Table 4.1 *Continued from previous page*

Protein	PDB ID	Method	Resolution (Å)	Proposed functional state	G_{water} (kJ mol^{-1})
Na_VPaS, *P. americana*	5X0M	cryo-EM	3.80	closed[353]	40.9
Na_VRh, *R. HIMB114*	4DXW	X-ray	3.05	closed[354]	57.8
RyR1, *O. cuniculus*	3J8H*	cryo-EM	3.80	closed[72]	11.4
RyR1, *O. cuniculus*	5TB0*	cryo-EM	4.40	closed[355]	8.0
RyR2, *S. scrofa*	5GO9*	cryo-EM	4.40	closed[356]	11.9
RyR2, *S. scrofa*	5GOA*	cryo-EM	4.20	open[356]	0.2
TPC1, *A. thaliana*	5DQQ	X-ray	2.87	closed[357]	38.9
TPC1, *M. musculus*	6C96	cryo-EM	3.40	closed[358]	55.6
TPC1, *M. musculus*	6C9A	cryo-EM	3.20	open[358]	2.1
Other cation channels					
ASIC1, *G. gallus*	2QTS	X-ray	1.90	desensitised (-like)[359]	22.9
ASIC1, *G. gallus*	3S3W	X-ray	2.60	desensitised (-like)[360]	20.9
ASIC1, *G. gallus*	4NTW	X-ray	2.07	open[361]	0.5
ASIC1, *G. gallus*	4NTY	X-ray	2.65	open[361]	0.5
ASIC1, *G. gallus*	4NYK	X-ray	3.00	desensitised[362]	17.5
ASIC1, *G. gallus*	5WKU	X-ray	2.95	closed[363]	38.0
ExbB/ExbD, *E. coli*	5SV0	X-ray	2.60	–[364]	0.2
ExbB/ExbD, *E. coli*	5SV1	X-ray	3.50	–[364]	0.1
M2, *Influenza A*	3BKD	X-ray	2.05	closed[365]	4.6
M2, *Influenza A*	4QKC	X-ray	1.10	–[366]	6.0
M2, *Influenza A*	5JOO	X-ray	1.41	–[64]	5.9
M2, *Influenza A*	5TTC	X-ray	1.40	–[64]	5.9
M2, *Influenza A*	5UM1	X-ray	1.45	–[64]	6.3
M2, *Influenza B*	2KIX	aq. NMR	–	closed[367]	5.4
MCU, *C. elegans*	5ID3	aq. NMR	–	closed[368]	87.3
MgtE, *T. thermophilus*	2ZY9	X-ray	2.94	closed[369]	69.3
MgtE, *T. thermophilus*	4U9N	X-ray	2.20	closed[370]	55.9
MscL, *M. tuberculosis*	2OAR	X-ray	3.50	closed[371]	45.6
MscL, *S. aureus*	3HZQ	X-ray	3.82	intermediate[372]	0.0
MscL, *M. acetivorans*	4Y7J	X-ray	4.10	expanded/ intermediate[373]	0.0
MscL, *M. acetivorans*	4Y7K	X-ray	3.50	closed[373]	80.9
MscS, *E. coli*	2OAU	X-ray	3.70	open[107]	14.5
MscS, *E. coli*	2VV5	X-ray	3.45	open[109]	0.0

Continued on following page

Table 4.1 *Continued from previous page*

Protein	PDB ID	Method	Resolution (Å)	Proposed functional state	G_{water} (kJ mol^{-1})
NNT, *T. thermophilus*	5UNI	X-ray	2.20	–[374]	71.1
Orai, *D. melanogaster*	4HKR	X-ray	3.35	closed[375]	8.3
Piezo1, *M. musculus*	6BPZ	cryo-EM	3.80	closed[73]	36.7
TMEM175, *C. minutus*	5VRE	X-ray	3.30	–[376]	45.0
TRIC, *C. elegans*	5EGI	X-ray	3.30	–[377]	6.9
TRIC, *C. elegans*	5EIK	X-ray	2.30	–[377]	12.1
TRIC, *S. acidocaldarius*	5WUC	X-ray	1.60	closed[378]	71.0
TRIC, *S. acidocaldarius*	5WUE	X-ray	2.40	open[378]	0.3
TRIC, *C. psychrerythraea*	5WUF	X-ray	2.40	–[378]	2.4
YetJ, *B. subtilis*	4PGR	X-ray	1.95	closed[379]	28.6
YetJ, *B. subtilis*	4PGS	X-ray	2.50	open[379]	4.3
YetJ, *B. subtilis*	4PGU	X-ray	3.40	closed[379]	57.6
Other anion channels					
BEST1, *G. gallus*	4RDQ	X-ray	2.85	open[217]	76.3
KpBest, *K. pneumoniae*	4WD8	X-ray	2.30	closed[218]	71.4
CFTR, *H. sapiens*	5UAK	cryo-EM	3.87	closed[380]	15.1
CFTR, *D. rerio*	5UAR	cryo-EM	3.73	closed[381]	58.5
CFTR, *D. rerio*	5W81	cryo-EM	3.37	closed[382]	38.4
CLC-K, *B. taurus*	5TQQ	cryo-EM	3.76	–[383]	42.6
TehA, *H. influenzae*	3M71	X-ray	1.20	closed[384]	52.3
TehA, *H. influenzae*	4YCR	X-ray	2.30	–[385]	29.0
TMEM16A, *M. musculus*	5OYB	cryo-EM	3.75	closed[386]	9.2
TMEM16A, *M. musculus*	5OYG	cryo-EM	4.06	closed[386]	32.0
TMEM16A, *M. musculus*	6BGI	cryo-EM	3.80	closed[387]	25.9
TMEM16A, *M. musculus*	6BGJ	cryo-EM	3.80	closed[387]	3.4

4.2.4 Analysis of all residues lining ion channel pores

Further to surveying amino acid side chains present at dehydration barriers, the relationship between local pore dimensions, hydrophobicity, and water behaviour in any given region through a channel pathway became clearer when all pore-lining residue positions in the 190 structures were considered. Examination of the distribution of water density values estimated at the time-averaged position of each pore-lining residue

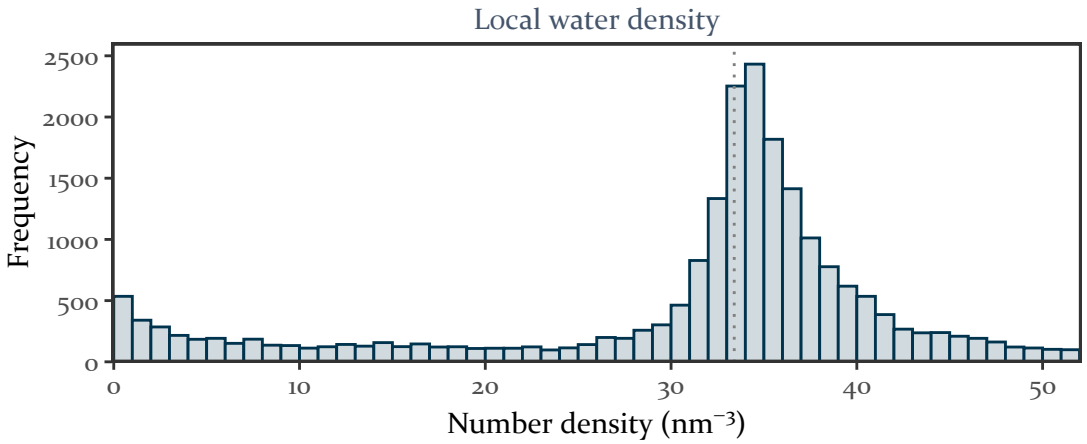


Figure 4.8 Distribution of local pore water density values sampled at time-averaged centre-of-geometry positions of all pore-lining residues in equilibrium simulations of the set of 190 ion channel structures. The approximate bulk water number density of 33.4 nm^{-3} is indicated by the dotted line.

revealed a (skewed) bimodal appearance (Figure 4.8). There was substantive sampling of regions where the number density of water was reduced relative to that of bulk water, with a small peak towards zero density, corresponding to de-wetted regions.

Construction of a local pore water free energy landscape in the hydrophobicity-radius plane based on approximately 22,000 measurements across simulation replicates revealed a notable divide between lower- and higher-energy areas corresponding, respectively, to hydrated and de-wetted pores (Figure 4.9). Towards the hydrophobic end of the landscape, an energetic barrier may be encountered in channel regions with radii of up to around 0.4 nm. Conversely, the hydrophilic side of the plot included regions which became hydrated at much smaller radii, below 0.2 nm. The relative hydrophobicity of channel pore regions was estimated based on six alternative experimental scales for amino acids (Figure 4.1), yielding a very similar pattern of water free energy in each case (Figure 4.9).

The mean free energy landscape was also determined using subsets of the data from which lower-resolution structures were excluded. A resolution cut-off of greater than or equal to 4.5 Å, 4.0 Å, or 3.5 Å was applied, reducing the set of structures to a size of 184, 165, or 113, respectively, with little effect on the resultant water free energy values in the plane of local hydrophobicity and radius (Figure 4.10).

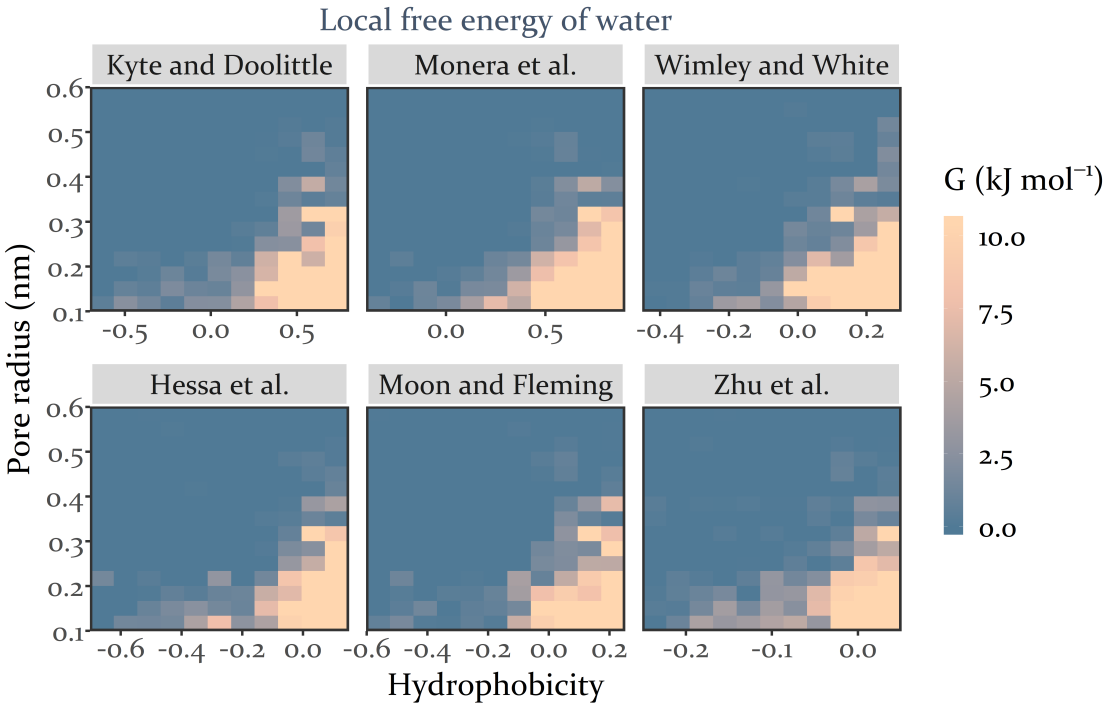


Figure 4.9 Local water free energy analysis for all pore-lining residue positions sampled in the 570 simulations of ion channel structures. Mean measurements were taken from each set of simulation-derived pore radius, hydrophobicity, and water free energy profiles (Figure 4.5A) at the time-averaged axial coordinates of individual side chains that were oriented towards the pore in over half of the analysed trajectory frames. Relative hydrophobicity of the channel pore lining was estimated based on alternative experimental scales for amino acids, namely those determined by Kyte and Doolittle [233], Monera *et al.* [238], Wimley and White [231], Hessa *et al.* [240], Moon and Fleming [241], and Zhu *et al.* [242], in chronological order of their publication. The original hydrophobicity scales were linearly normalised such that the zero position was unshifted and the largest absolute value among amino acids was equal to one unit, with more positive values indicating greater hydrophobicity. Two-dimensional histograms are plotted in the resulting hydrophobicity-radius planes, coloured by the mean energy value between data points falling within each bin. Regions with energy values outside the colour scale range are shown in the same colour as the lower or upper bound.

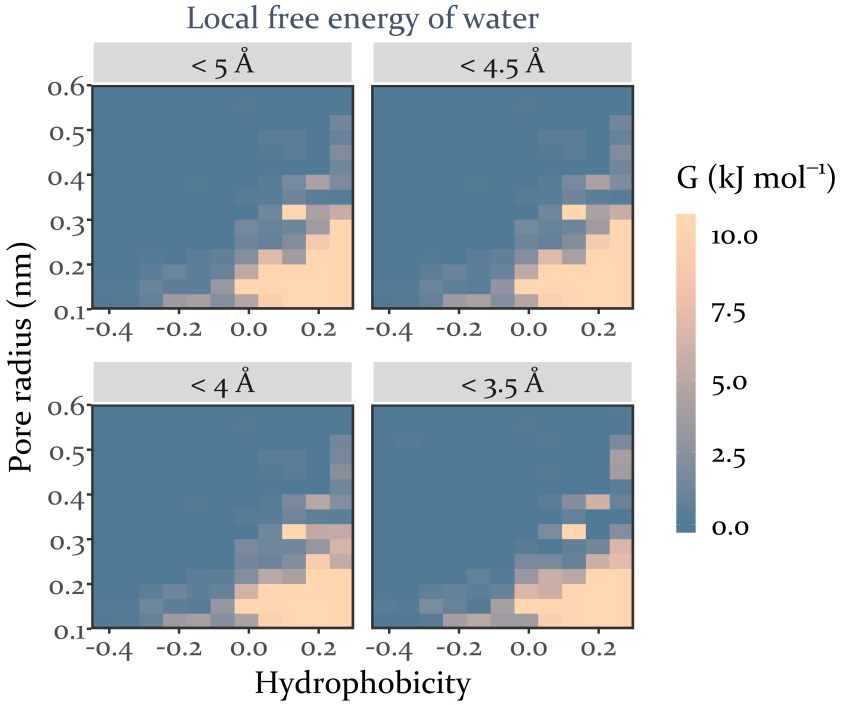


Figure 4.10 Mean water free energy in the local hydrophobicity-radius plane, as calculated using simulations of the 190 structures (< 5 Å) or of subsets where lower-resolution structures were excluded. Mean measurements were taken from simulation-derived pore radius, hydrophobicity, and water free energy profiles (Figure 4.5A) at the time-averaged axial coordinates of individual side chains that were oriented towards the pore in over half of the analysed trajectory frames. A two-dimensional histogram is plotted, coloured by the mean energy value between data points falling within each bin. Regions with energy values outside the colour scale range are shown in the same colour as the lower or upper bound. Relative hydrophobicity was estimated based on the Wimley and White [231] scale, linearly normalised such that the zero position was unshifted and the largest absolute value among amino acids was equal to one unit, with more positive values indicating greater hydrophobicity.

A support vector machine was trained on the dependence of pore water free energy on local radius and hydrophobicity, upon random partitioning of the 190 channel structures into training, validation, and testing sets at a ratio of 64 %:16 %:20 %. The transition threshold between hydrated and de-wetted states, with the critical radius increasing in the direction of positive hydrophobicity, could be approximated by a polynomial regression line from the support vector analysis (Figure 4.11). The mean thermal energy, 1 *RT*, or approximately 2.6 kJ mol^{-1} at 37 °C, was taken as a reference value for the division.

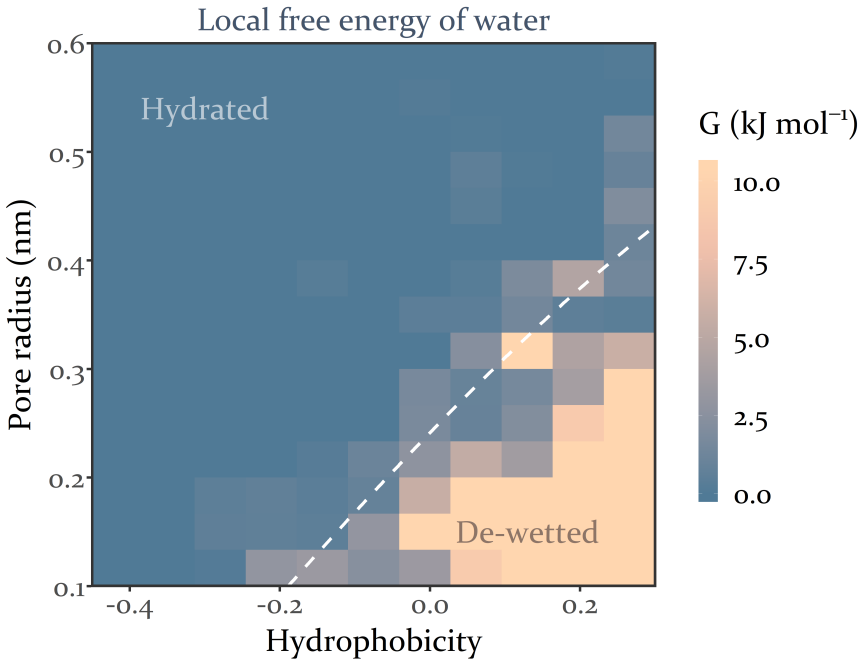


Figure 4.11 Division of the local pore hydrophobicity-radius plane based on mean water free energy values calculated from simulations of the training set of ion channel structures, via support vector regression with a polynomial kernel. The white dashed contour line indicates the 1 *RT* (2.6 kJ mol^{-1}) position. The water free energy landscape was obtained by taking mean measurements from pore radius, hydrophobicity, and water free energy profiles (Figure 4.5A) at the time-averaged axial coordinates of individual side chains that were oriented towards the pore in over half of the analysed trajectory frames. A two-dimensional histogram is plotted, coloured by the mean energy value between data points falling within each bin. Regions with energy values outside the colour scale range are shown in the same colour as the lower or upper bound. Relative hydrophobicity was estimated based on the Wimley and White [231] scale, linearly normalised such that the zero position was unshifted and the largest absolute value among amino acids was equal to one unit, with more positive values indicating greater hydrophobicity.

4.2.5 A heuristic for prediction of pore hydration state

The water free energy landscape derived above and the contour line obtained from support vector regression allow a simple simulation-free heuristic method to be devised for predicting hydration levels in ion channel pores, based upon the correlation with pore dimensions and hydrophobicity alone (Figure 4.12), as illustrated on the following page (Figure 4.13). Having used CHAP[80] to identify pore-lining amino acid side chains and to estimate pore radius and hydrophobicity profiles for an experimental structure of interest, the pair of hydrophobicity and radius values associated with each pore-lining residue position are mapped onto the hydrophobicity-radius plane. Any residue points falling below the $1\,RT$ contour line, representing relatively hydrophobic and narrow regions of the pore, are considered to be potential contributors towards a hydrophobic barrier to permeation. As a measure of the combined effect of hydrophobicity and radius, summation of the shortest distance d from each of these residue points to the dividing line provides a score, $\sum d$, that positively correlates with the likelihood of a channel pore undergoing hydrophobic de-wetting.

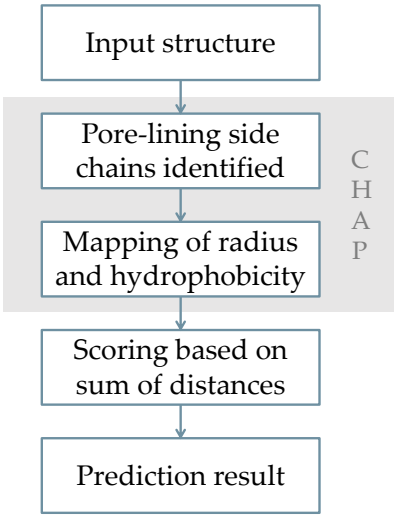


Figure 4.12 Schematic of a heuristic prediction approach for the permeation state of an ion channel structure based on analysis of pore radius and hydrophobicity profiles, both of which may be computed from a static structure using the CHAP analysis tool[80].

Such a structure-based predictive approach may be performed for a channel conformation within a few seconds on a standard desktop computer, via automated analysis of a single set of atomic coordinates. For the 190 selected structures, for example, the total CPU time of the heuristic analysis process was less than 15 minutes.

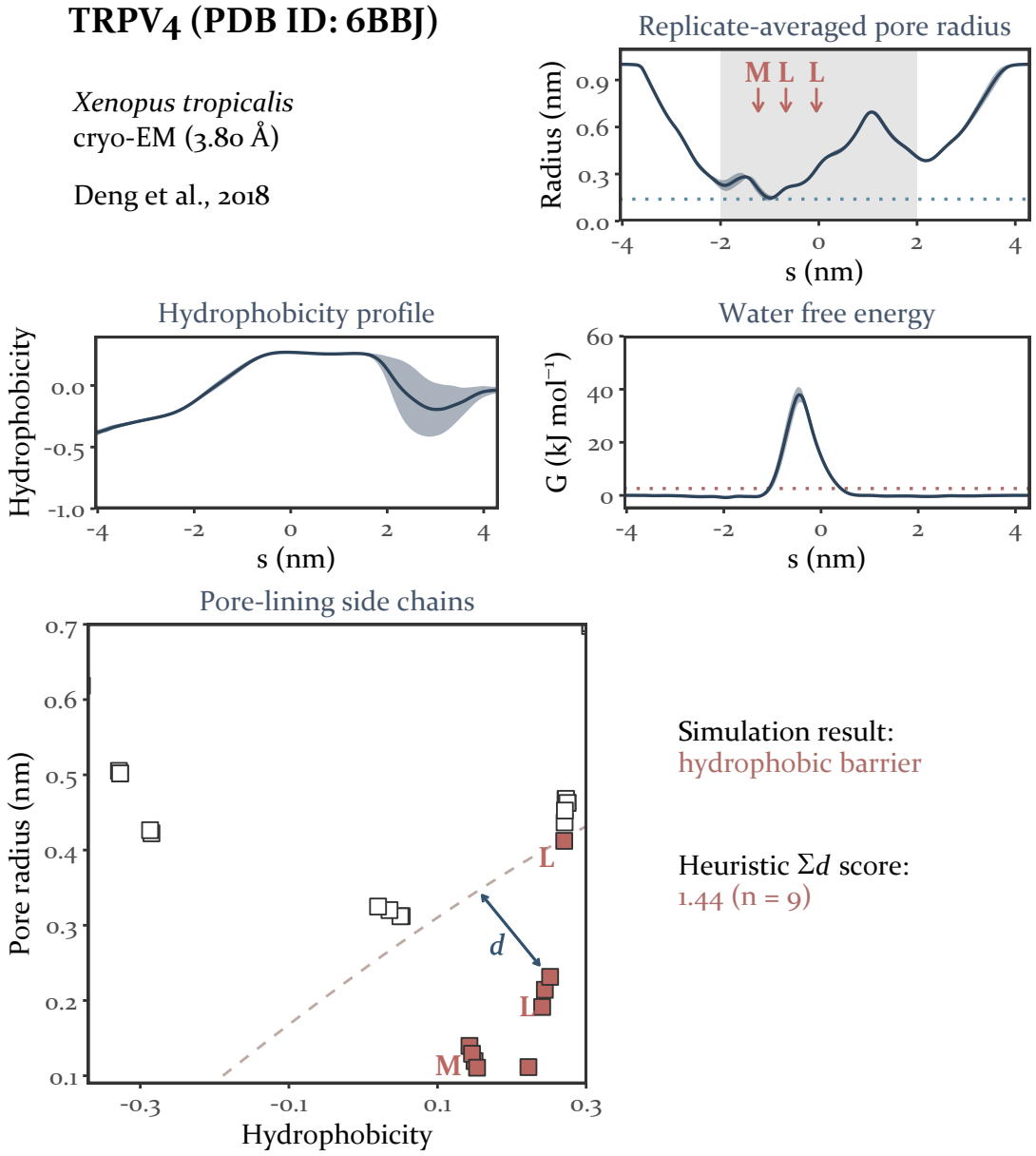


Figure 4.13 Illustrative example of a channel annotation summary page, showing replicate-averaged pore radius, hydrophobicity, and water free profiles from three independent 30 ns equilibrium simulations, followed by heuristic $\sum d$ scoring of pore-lining side chains performed on the original structure. The channel is oriented with the cytoplasmic side in the negative s direction. The approximate position of the membrane is indicated by the grey shading. The blue and red dotted lines indicate, respectively, the approximate radius of a water molecule and an energy value of 1 RT (2.6 kJ mol^{-1}). The dashed contour line represents the 1 RT position in the hydrophobicity-radius plane as given by the support vector regression model. The full set of results for all analysed structures may be found as a 190-page supplementary data file at: `https://www.pnas.org/content/suppl/2019/06/21/1902702116.DCSupplemental`.

Receiver operating characteristic analysis was applied to evaluate the capability of the $\sum d$ scores to predict the presence or absence of a closed hydrophobic gate among the testing set of 38 channel structures, as indicated by their water free energy profiles determined from equilibrium simulations. A reasonably high value of 0.91 was produced for the area under the receiver operating characteristic (Figure 4.14A). In comparison, predictions based on minimum pore radius alone, using either CHAP[80] or the HOLE programme[84] with or without manual curation to exclude potassium channel selectivity filter regions, yielded lower values of 0.59 and 0.81, respectively (Figure 4.14). This suggests that the heuristic scoring method, with its modelling of the effect of hydrophobicity, provides an advance on assessing pore dimensions, traditionally conducted as an initial step for functional annotation of channel structures.

A cut-off of $\sum d > 0.55$ was selected, on the basis of the receiver operating characteristic evaluation, for predicting the presence of a significant water free energy barrier of greater than 1 RT. Such a cut-off position corresponded to a sensitivity of 88 % and specificity of 93 % in the heuristic assessment of the testing set of structures (Figure 4.14A).

The effectiveness of the approach was additionally illustrated using two structures that had been recently resolved at the time of the investigation (Figure 4.15), the TRPV3 channel in a putative sensitised but non-conductive state (PDB ID: 6MHS)[388] and a gain-of-function mutant of the calcium release-activated Orai channel (PDB ID: 6BBF)[389]. None of the pore-lining side chain positions identified in the Orai channel structure were mapped below the 1 RT support vector regression line. The structure was therefore assigned a $\sum d$ score of 0.00 and was predicted to be fully hydrated, potentially representing a functionally open conformation of the channel. By marked contrast, 12 residue positions in the TRPV3 structure, namely the pore-lining isoleucine, asparagine, and leucine rings formed by the four protein subunits, fell below the chosen contour line. The sum of their shortest distances to the line was calculated to be 1.44, leading to prediction of a closed hydrophobic gate in this particular channel conformation. The two structures were subsequently subjected to the complete MD simulation and analysis protocol described above for the larger set of structures. Their resulting water free energy profiles were consistent with both predictions made by the heuristic model (Figure 4.15C).

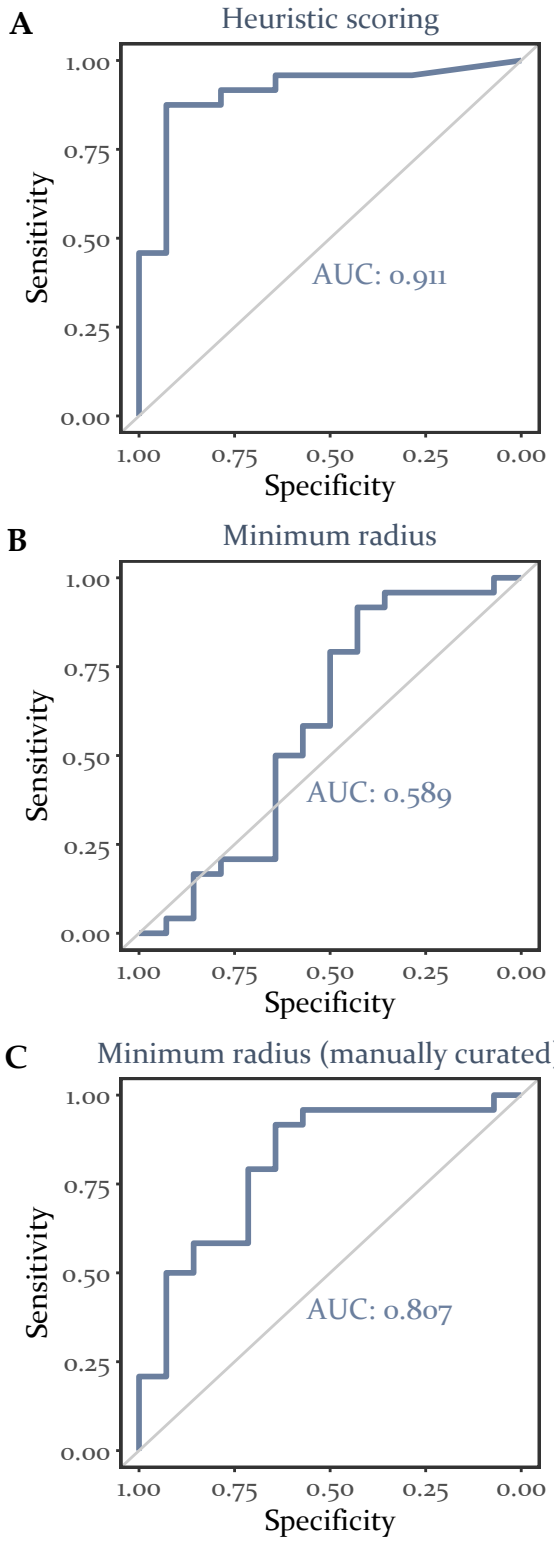


Figure 4.14 Receiver operating characteristic evaluation for predicting de-wetted channel pores using (**A**) the heuristic scoring model, (**B**) minimum pore radius values, and (**B**) minimum pore radius upon manual exclusion of potassium channel selectivity filter regions. Predictions were assessed against equilibrium simulation results, and the relationship between the true positive rate (or sensitivity) and the false positive rate (or one minus the specificity) is displayed in the standard manner and annotated with the area under the receiver operating characteristic curve (AUC) in each case.

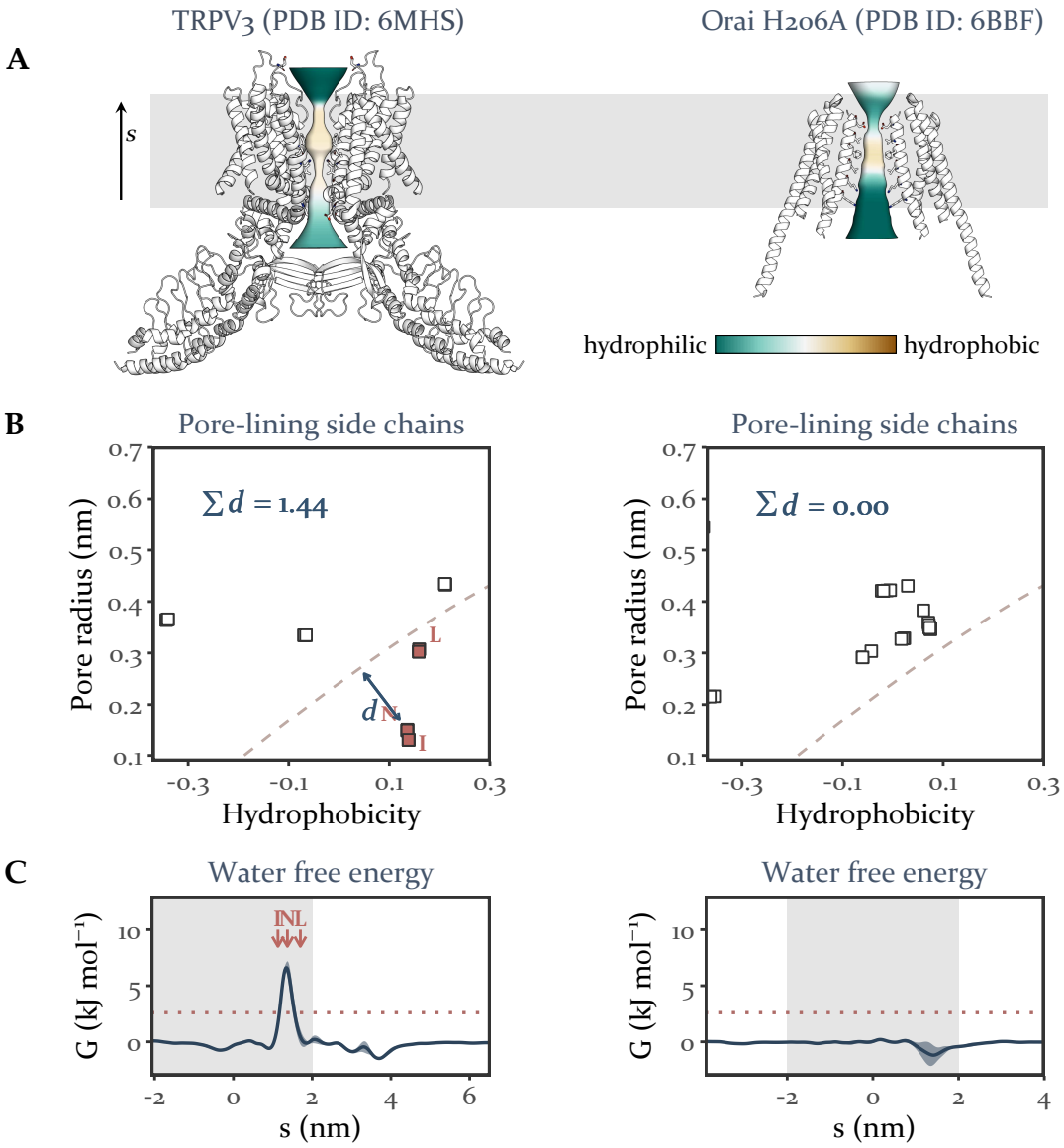


Figure 4.15 Illustration of the structure-based heuristic prediction approach using two recent structures, respectively of the tetrameric TRPV3 channel (PDB ID: 6MHS)[388] and a gain-of-function mutant of the hexameric Orai channel (PDB ID: 6BBF)[389]. (**A**) Pore surface profiles of the two structures as determined using CHAP[80] and coloured by relative hydrophobicity, employing the Wimley and White [231] scale for amino acids. For clarity, only two non-adjacent protein subunits are shown, in a ribbon representation. Channel structures are oriented with the cytoplasmic side in the negative s direction, with the approximate position of the membrane indicated by the grey shading. (**B**) Heuristic $\sum d$ scoring based on local hydrophobicity and radius at pore-lining residue positions. The dashed 1 RT contour line was given by the support vector regression model. (**C**) Water free energy profiles derived from three independent 30 ns simulations of each membrane-embedded structure, showing the mean and standard deviation between replicates. The red dotted line represents a reference energy value of 1 RT (2.6 kJ mol^{-1})

As a further test of the ability of the simulation protocol to provide an estimate of the free energy landscape for water within an ion channel, 500 ns equilibrium simulations of water behaviour were performed for three structures, two of which contained maximum water free energy positions that were mapped close to the dividing line from the support vector regression (Figure 4.16A). The structures are, namely, of the calcium- and voltage-

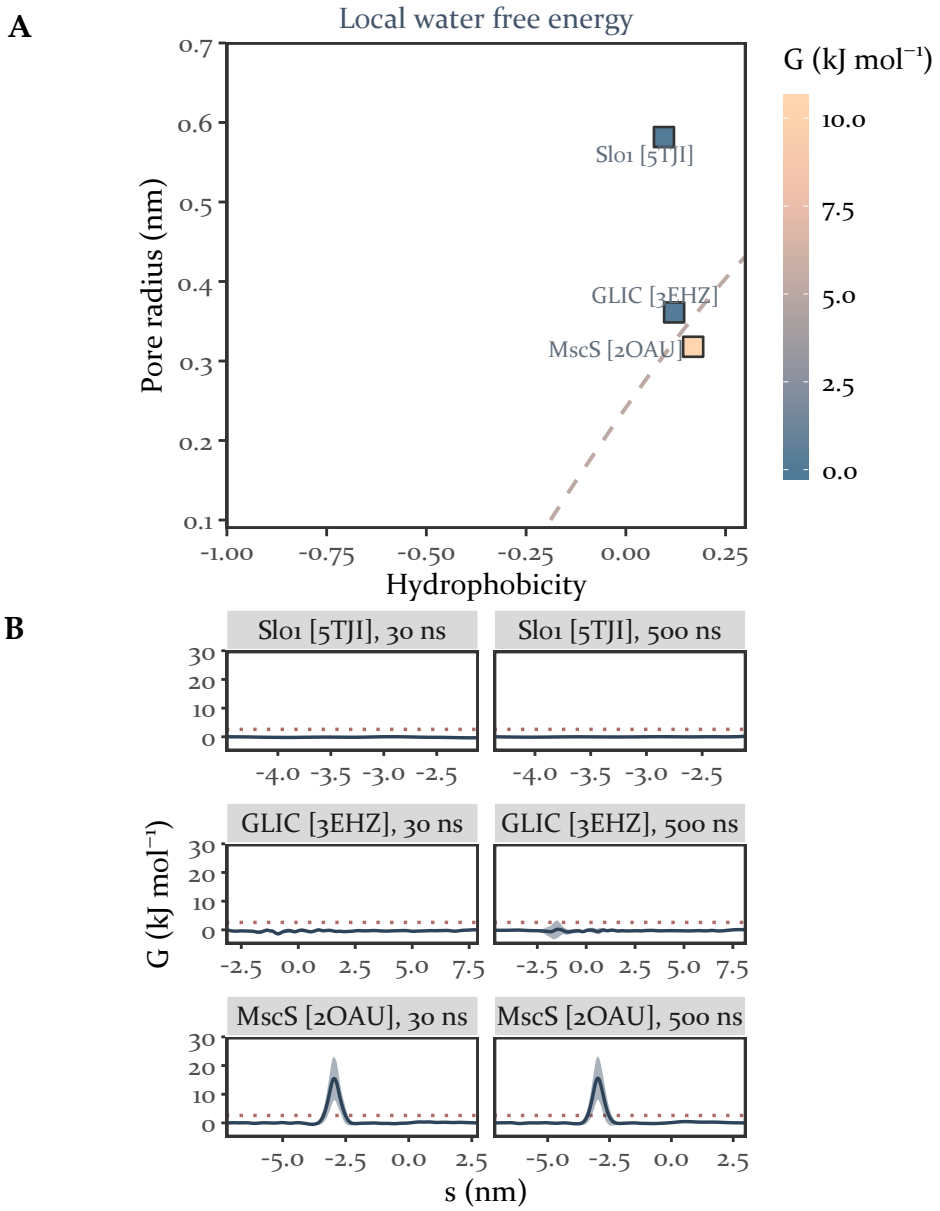


Figure 4.16 (**A**) Local radius, hydrophobicity, and maximum free energy of water at the main hydrophobic barrier or putative gate region of three ion channel structures (Table 4.1), and (**B**) their water free energy profiles derived from 30 ns or 500 ns of equilibrium simulations, during which positional restraints were applied to protein backbone atoms. In the case of the Slo1 channel, its profile below the selectivity filter region is shown.

activated Slo1 potassium channel (PDB ID: 5TJI)[337], the *Gloeobacter* ligand-gated ion channel, GLIC (PDB ID: 3EHZ)[262], and the small-conductance mechanosensitive MscS channel (PDB ID: 2OAU)[107]. In each case, the extended simulation did not change the mean free energy profile for water within the channel relative to that calculated from the 30 ns simulations of the same structure (Figure 4.16B).

4.3 Conclusion

In this chapter, equilibrium MD simulations of water behaviour in a large number of channel pores have been employed to sample the range of pore hydrophobicity-radius combinations represented by the available ion channel structural proteome. A systematic analysis of the density and corresponding free energy of water within these structures, as a function of local hydrophobicity and radius, has revealed a near-linear dependence of the critical radius for the transition between hydrated and de-wetted states upon the hydrophobicity of the pore lining.

As the amino acid composition of a channel pore lining may be determined, and the pore radius and hydrophobicity profiles readily estimated for any known structure, a simple simulation-free heuristic model has been proposed for identifying closed hydrophobic gates in newly resolved structures of ion channels or other protein- or peptide-based transmembrane pores. The support vector regression model and an executable R[250] script for obtaining prediction results have been made available on the CHAP website (`https://www.channotation.org/`)[80].

Derived from an underlying energy landscape calculated via MD simulations with a combined duration of approximately 17 µs, the model provides a rapid exploratory approach to the functional annotation of novel channel structures. Importantly, such an analysis may be performed in a matter of seconds, prior to more detailed computational or experimental characterisation of the relationship between ion channel structure and function. Furthermore, the method may also facilitate design and engineering of novel nanopores that contain switchable hydrophobic gates[244].

"From a drop of water," said the writer, "a logician could infer the possibility of an Atlantic or a Niagara without having seen or heard of one or the other."

From *A Study in Scarlet* by Sir A. C. Doyle, 1887

5

From water to ions: Assessment of channel conduction state

5.1 Methods 84
5.1.1 Structure-based analysis and equilibrium simulations 84
5.1.2 Computational electrophysiology 85
5.1.3 Continuum electrostatic calculations 86
5.2 Results and Discussion 86
5.2.1 Choice of simulation conditions and robustness of the approach 86
5.2.2 A pipeline for functional annotation of new channel structures 91
5.2.3 Pore hydration level as indicator of ion channel conduction state 102
5.3 Conclusion 113

As discussed in Chapter 1, ion permeation through channel pores are physiologically driven by a transmembrane electrochemical potential difference, which consists of contribution from both the concentration gradient of the ionic species and the electric potential across the membrane (Equation 1.1). In electrophysiology experiments, ionic flux through individual ion channels may be monitored by sealing a small patch of membrane within the glass pipette tip of a microelectrode and, with application of the voltage clamp technique, recording the transmembrane current flow whilst the potential difference is controlled[390,391]. The current-voltage relationship exhibited by the channel in the presence of one or more ionic species may thus enable characterisation of its conductive properties[392,393], including the ion selectivity, any voltage dependence of its

gating kinetics, and its levels of conductance as defined based on Ohm's law[28,394],

$$g_x = \frac{I_x}{V - V_x} \tag{5.1}$$

where the chord conductance g_x of the channel for a permeant species x relates its net ionic current I_x to the difference between the membrane potential, V, and the Nernst potential, V_x, at which the ion is in thermodynamic equilibrium across the membrane[27].

The same concepts have been explored in molecular dynamics (MD) studies of ion channel structures to extract information on their functional states by directly simulating ionic flux as driven by a modelled transmembrane potential difference. Two main such methods of computational electrophysiology have been developed (Figure 5.1), in which the potential difference may arise from an ionic imbalance between two aqueous compartments, separated by parallel membranes[395–397], or from a uniform external electric field orthogonal to the plane of an individual membrane[398–402].

To establish an unequal distribution of ions on either side of the membrane, the ionic imbalance approach necessitates creation of two physically distinct bulk phases unconnected by the periodic boundary conditions applied (Section 2.1.2.2), which can be achieved through the addition of vacuum slabs[404] or, in this case, a dual-membrane configuration, with one of the aqueous phases continuous across the periodic boundary[395]. The transmembrane potential difference ΔV generated by a charge difference Δq between the two compartments is given by

$$\Delta V = \frac{\Delta q}{C} \tag{5.2}$$

with the phospholipid bilayer behaving approximately as a parallel-plate capacitor of electrical capacitance C,

$$C = \frac{\epsilon_0 \epsilon A}{d} \tag{5.3}$$

where ϵ_0 is the vacuum permittivity, ϵ the relative permittivity or dielectric constant of the membrane, and A and d the membrane area and thickness, respectively. Consequent of the high capacitance per unit area of biological membranes, typically in the order of $1\,\mu F\,cm^{-2}$, a significant electric potential may be produced by small differences in ionic charge[405–408]. For a simulation unit cell of dimensions $13 \times 13\,nm^2$ in the membrane

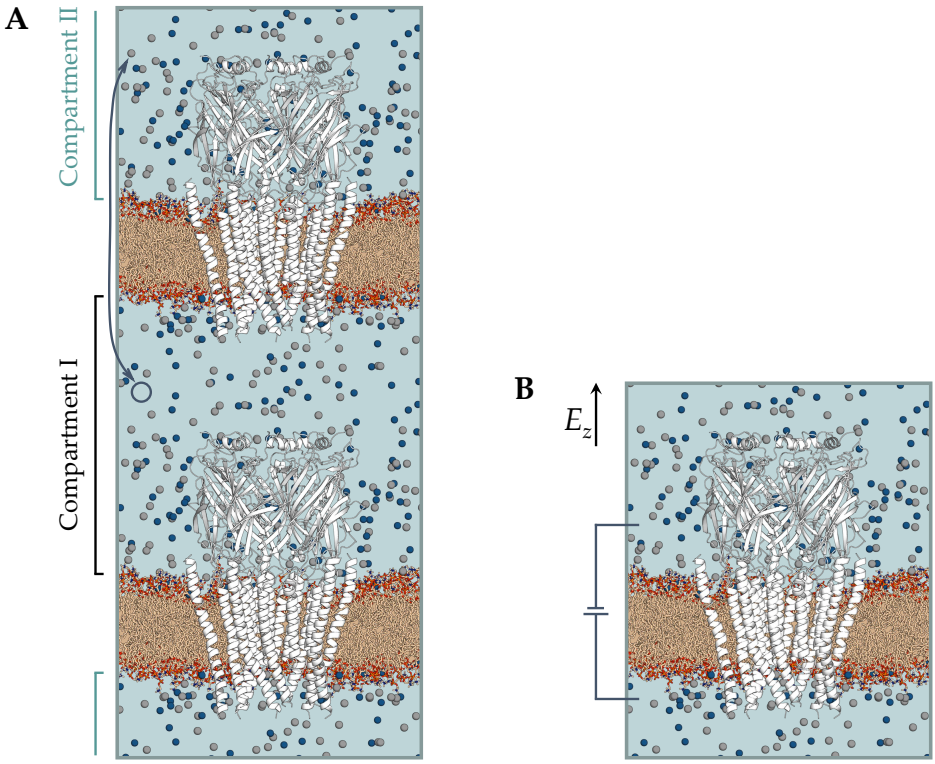


Figure 5.1 Two simulation systems illustrating alternative methods of computational electrophysiology, with the transmembrane potential difference arising from either (**A**) an ionic imbalance between two aqueous compartments (coloured pale blue) or (**B**) a constant, uniform external electric field E_z orthogonal to the plane of the membrane (orange). As ions (shown as spheres) are driven through the channel protein, in this case the glycine receptor in a ribbon representation[403], the ionic imbalance method uses an exchange of water-ion pairs to maintain the potential difference.

plane, with both aqueous compartments containing cations and anions at physiological concentration or above (corresponding to at least one or several hundreds of ions of each species), an imbalance of one elementary charge, $1\,e$, would be sufficient to yield a transmembrane potential of approximately 100 mV (Equation 5.2), whereas the concentration gradient term of any electrochemical driving force associated with such an ionic imbalance is comparatively minute (Equation 1.1).

In addition to employing a dual-membrane system[395,409,410], the ionic imbalance method relies on introduction of particle exchange protocols to maintain the potential difference against dissipation by transmembrane ion translocation[396]. An ion from one compartment is exchanged with a water molecule in another at sub-picosecond intervals, thereby restoring the charge imbalance and allowing measurement of steady-state ionic flux over

time. Both particles of the pair are selected at a distance from the compartment boundaries to minimise the impact of the positional exchange, and the level of perturbation caused to the simulation has been demonstrated to be low[396,397].

The uniform electric field method, which provides an alternative approach for representing the membrane potential during MD simulations, originates from a continuum electrostatic Poisson-Boltzmann theory, modified to describe the influence of an electromotive force between two infinite aqueous phases either side of a membrane[398,401]. A constant, uniform external field is applied in the membrane normal (z) direction and exerts a force on every charged particle in the system. In response to the linear potential generated across the unit cell, reorganisation of the bulk medium into a non-uniform distribution leads to a reaction field that acts to reduce the magnitude of the net electric field, where possible[402]. As a result, the change in potential across the system, ΔV, becomes concentrated across the immobile, insulating membrane (Figure 5.2). The transmembrane electric potential is thus directly proportional to the external electric field strength E_z and the z-dimension L_z of the unit cell,

$$\Delta V = E_z L_z \tag{5.4}$$

independent of the membrane thickness or geometry[402]. The relative ease of fine-tuning the effective potential *a priori* confers an advantage over simulating an ionic imbalance[402].

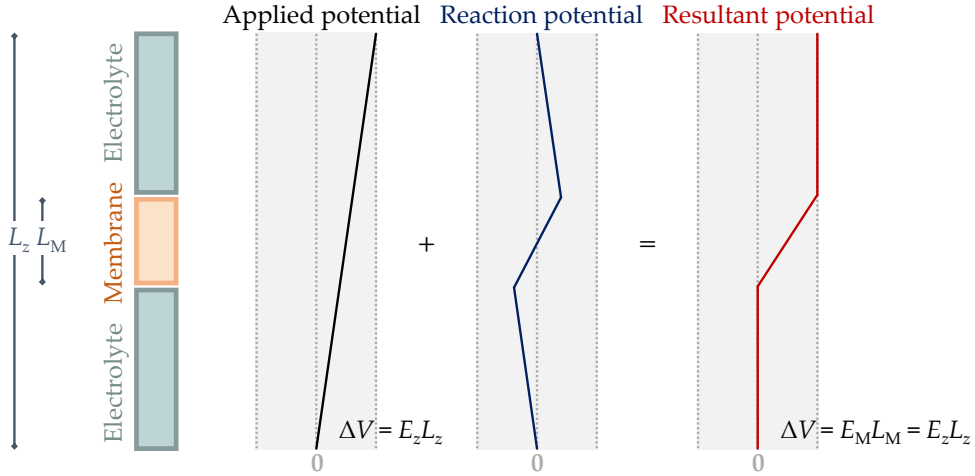


Figure 5.2 Schematic description of the uniform electric field method. Reorganisation of the bulk medium in response to the applied field generates a reaction potential that, when summed with the linear potential from the external field, yields a resultant net electric potential difference across the membrane. Adapted from Gumbart *et al.* [402]

When implemented in simulations of phospholipid bilayer systems solvated with a monovalent electrolyte, NaCl or KCl, the ionic imbalance and uniform field methods have been shown to produce membrane electrostatic properties that are indistinguishable within statistical error, with agreement between their transmembrane potential, electric field intensity, and charge density profiles[411]. It is, however, noted that measurements of non-equilibrium properties using the uniform field method may be prone to finite-size artefacts, for example with enhanced ionic fluxes in a simulation system of insufficient dimensions, due to a reduction in the dissipative effects from long-range fluctuations[401,402].

Both methods of computational electrophysiology have been increasingly applied to probe ion conduction in different channel proteins[82,83,131,412–421]. The uniform field method, which does not require a doubling of the size of the simulated system to accommodate more than one patch of membrane, has been favoured particularly for larger channels with substantial cytoplasmic or extracellular domains[82,83,412,421]. In the case of pentameric ligand-gated ion channels (pLGICs), simulations of truncated constructs comprising solely the transmembrane domain of the protein structure (Section 1.1.2.1) have been employed to further reduce the computational demand[82,83].

Having analysed the behaviour of water in ion channel structures in the preceding chapters, where closed hydrophobic gates were identified based on de-wetting of channel pores, this chapter turns its focus towards measurements of ion permeation as further assessment of functional state. The methods described above are used to examine recent structures[255,403,422] of two channels of the pLGIC superfamily, the anion-selective glycine receptor and the cation-selective serotonin 5-HT_3 receptor. Annotation results for these two pores as described in the chapter will include data forming the computational aspect of the structural studies by Kumar *et al.* [403] and Basak *et al.* [422], respectively. The simulation protocol is selected on the basis of (i) any observed impact of truncating portions of each experimental structure on the simulated ion conductance, as well as (ii) dependence of the conductance estimates on the concentration of ions in the system and the magnitude of the potential difference applied. Following the same protocol, the analysis is then extended to a larger set of structures, 22 in total, as a means of evaluating predictions from structure-based scoring and equilibrium simulations of water density (Chapter 4) for interpreting the functional significance of ion channel conformations.

5.1 Methods

5.1.1 Structure-based analysis and equilibrium simulations

For the more recently resolved ion channel structures that were not included among the data set sampled in the previous chapter, the same processing steps were applied to remove any bound ligands and repair incomplete side chains[248] prior to analysis of pore properties by the Channel Annotation Package (CHAP)[80]. The amino acid hydrophobicity scale determined by Wimley and White [231] were used with a bandwidth of 0.45 nm for estimating the hydrophobicity profile. The heuristic model derived in Section 4.2.5 was applied in R (`https://www.R-project.org/`)[250] to obtain prediction scores for pore hydration based on the local pore radius and hydrophobicity at pore-lining side chain positions along the channel axis of each structure.

MD simulations of the membrane-embedded structures were performed in GROMACS 2018[151]. All systems were prepared in independent triplicates, each simulated for 30 ns following the procedure and MD parameters detailed in Section 4.1.2. Protein backbone atoms were subjected to harmonic positional restraints, with force constant 1000 kJ mol^{-1} nm^{-2}, during these simulations. CHAP[80] was used to calculate pore water density and free energy profiles from the final 20 ns of trajectory frames, sampling at 0.5 ns intervals and with a kernel bandwidth of 0.14 nm, the approximate radius of a water molecule.

A separate set of triplicate equilibrium simulations were conducted for the glycine receptor structures[403] with Protein Data Bank (PDB) IDs 6UBS, 6UBT, and 6UD3, to monitor the stability of each protein conformation by sequential relaxation of positional restraints. During an initial 10 ns simulation, harmonic restraints (with force constant 1000 kJ mol^{-1} nm^{-2}) were placed on all non-hydrogen atoms of the protein. Restraints on side chain atoms were then released, and the protein subjected to a further 20 ns of simulation. In the next 20 ns, only the α-carbon atom of each residue remained under the positional restraining force. The resulting configuration of the system was subsequently simulated for 200 ns, unrestrained. The final 20 ns of each unrestrained simulation was again analysed using CHAP[80] for any change in pore profiles.

5.1.2 Computational electrophysiology

As with the equilibrium simulations, both types of computational electrophysiology systems contained an ion channel structure embedded within a lipid bilayer membrane[223] consisting entirely of POPC, 1-palmitoyl-2-oleoyl-*sn*-glycero-3-phosphocholine, and were simulated at 37 °C and 1 bar, with the temperature and pressure maintained by the velocity-rescaling thermostat[154] and a semi-isotropic Parrinello and Rahman barostat[155]. Their coupling constants τ_T and τ_P were 0.1 ps and 1 ps, respectively. The OPLS all-atom protein force field was employed with united-atom lipids[164], and the protein-membrane systems were solvated with the TIP4P/2005 water model[183]. Long-range electrostatic interactions were treated using the smooth particle mesh Ewald method[147,148] with a real-space cut-off of 1 nm, a Fourier spacing of 0.12 nm, and charge interpolation through fourth-order B-splines. Time integration was performed using a leap-frog integrator with a step size of 2 fs. Covalent bonds were constrained through the LINCS algorithm[226,227].

Each system was equilibrated for 10 ns, with the protein backbone under positional restraints of 1000 kJ mol^{-1} nm^{-2}, before the simulation unit cell was duplicated in the z dimension for the ionic imbalance approach. During triplicate 200 ns simulations, the deterministic protocol for particle exchange[396] was used to monitor, at 0.2 ps intervals, the number of cations and anions in the two compartments (averaged over a time window of 0.06 ps) against their reference counts, with water-ion pairs swapped where necessary. A charge difference of 2, 4, 6, 8, or 10 e was established between the compartments. The resulting electrostatic potential was assessed using the `gmx potential` utility of GROMACS[151], via integration of the charge density, and adjusted by altering the membrane area in subsequent simulations to yield the range of transmembrane potential difference of interest (100 to 500 mV).

Systems subjected to the uniform electric field approach contained NaCl either at 0.2 M, as present in the dual-membrane systems, or with the concentration increased to 0.5 M, and were simulated as at least three independent replicates for the same duration. The magnitude of the constant external field strength ranged from 10 to 50 mV nm^{-1}, depending on the z dimension of the system under investigation (11 to 19 nm), to generate an approximate potential difference of 200, 500, or 800 mV across the membrane, with negative or positive potential on the cytoplasmic side.

Conductance values were calculated from the number of ions traversing the channel structure or its transmembrane domain per unit time and averaged between replicates. Simulation trajectories were visualised and inspected in VMD[219], and permeant ions were identified using MDAnalysis[423,424].

5.1.3 Continuum electrostatic calculations

Electrostatic energy profiles of Na^+ and Cl^- ions through each channel pore were calculated by numerically solving the linearised Poisson-Boltzmann equation[194–196] using the Adaptive Poisson-Boltzmann Solver[425,426]. The multigrid finite-difference calculation[427] was performed on a $129 \times 129 \times 225$ grid with dimensions $13 \times 13 \times 21\,\mathrm{nm}^3$, applying Debye-Hückel boundary conditions, and the finer grid focused[428] into a $1 \times 1 \times 1\,\mathrm{nm}^3$ region centred on the ion coordinates. The grid dimensions and resolution were varied in preliminary calculations for the glycine and 5-HT_3 receptor structures[255,403,422] with PDB IDs 6UBS, 6UBT, 6UD3, 6BE1, 6DG7, and 6DG8, without notable changes in the resulting energies.

The ion was positioned along the central channel axis at 0.05 nm intervals, extending at least 2 nm into the bulk phase from either side of the channel. Born radii of 0.1680 nm and 0.1937 nm were used for Na^+ and Cl^- ions, respectively[429]. Protein atoms were assigned radii and partial charges from the CHARMM36 force field[140]. The radius of an implicit solvent molecule was set to 0.14 nm, the ionic strength to that of 0.15 M NaCl, and the dielectric constant to 78.5 for the solvent and 2 for the protein. The Born energy[430] for inserting an ion at each sampled position was calculated at a temperature of 37 °C by subtracting the individual electrostatic energies of the protein and the ion in solution from the electrostatic energy of the protein-ion system[99,431].

5.2 Results and Discussion

5.2.1 Choice of simulation conditions and robustness of the approach

Preliminary conductance measurements were taken on a recent putative open-state structure of the homomeric α_1 glycine receptor from zebrafish, captured in the presence of its agonist glycine and the open-channel blocker picrotoxin, a plant alkaloid that occurs as an equimolar mixture of picrotin and picrotoxinin[403]. The channel structure,

solved by cryo-electron microscopy to a resolution of 3.65 Å, was later superseded by a 3.51 Å model (PDB ID: 6UD3) that will be examined in Section 5.2.2 and included among the data set of Section 5.2.3. In simulation systems containing aqueous NaCl in the order of physiologically relevant concentrations, the original picrotoxin-bound glycine receptor conformation (upon removal of its bound ligands) exhibited only a low level of conductance (Figure 5.3A), with Cl^- ions rarely traversing the channel per 200 ns replicate. To increase the likelihood of observing permeation events and enable identification of lower-conductance structures among non-conductive states, a transmembrane potential difference of magnitude 500 mV was thus generated in subsequent simulations of channel structures.

When simulated in the absence of positional restraints, conductance values obtained for the glycine receptor structure showed large variations that likely corresponded to conformational fluctuations of the channel pore, with time-averaged pore radii differing by up to 0.15 nm between replicates (Figure 5.3). This could be a reflection of the structural ensemble adopted by the protein in its open, active state, for example with high mobility particularly at the -2' proline gate position, as previously reported[432]. Ideally, simulations of microsecond timescales, such as those employed in computational electrophysiology studies of the conduction mechanism of potassium channels[413,414], would be required to equilibrate these systems and to investigate the structural basis and functional significance of any differences between them. For the present purpose of examining any conductive properties of a structure in its experimentally determined state, positional restraints were applied onto the protein backbone atoms to preserve the overall conformation.

The impact of truncating portions of a channel structure on its levels of simulated ion conductance was assessed for two members of the pLGIC superfamily, using the glycine receptor structure introduced above[403] and the putative open conformation of a mouse 5-HT_3 receptor, composed of 5-HT_{3A} subunits (PDB ID: 6DG8)[422]. Under equivalent conditions, measurements on different protein constructs showed general agreement between the ionic imbalance and uniform electric field methods, accounting for the degree of variation between replicates due to the stochasticity of permeation processes (Figure 5.4). Whilst the difference in conductance between 5-HT_3 receptor constructs with or without the intracellular domain was relatively small, the presence or absence of the

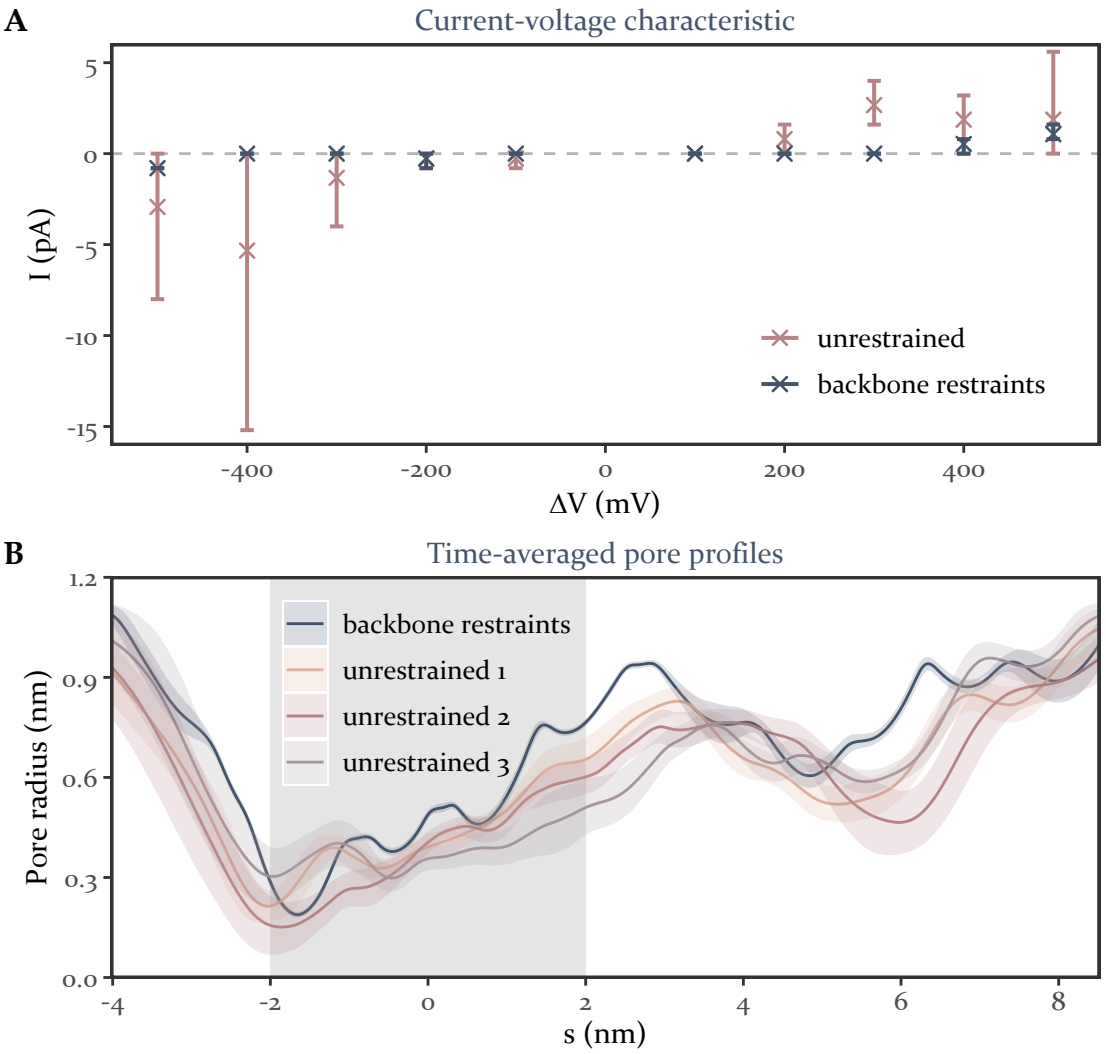


Figure 5.3 (**A**) Simulated Cl^- currents (I) through a glycine- and picrotoxin-bound conformation of the glycine receptor[403], with the transmembrane potential difference (ΔV, the sign of which indicates the potential on the cytoplasmic side) generated by an ionic imbalance between two aqueous compartments separated by parallel membranes, and (**B**) time-averaged pore radius profiles along the channel axis (s) during unrestrained simulations at -400 mV, in comparison to the typical fluctuations in radii when positional restraints were applied onto the protein backbone. Each protein-membrane system was solvated with NaCl at a concentration of 0.2 M. The mean and minimum-maximum range among independent 200 ns triplicates are shown for the currents. Pore profiles are oriented with the cytoplasmic side in the negative s direction and depict the mean and standard deviation for each individual replicate, sampling in 0.5 ns intervals. The grey shaded area represents the approximate position of the membrane, with the 9′ leucine residues of the glycine receptor located around 0 nm and the -2′ proline between -2 nm and -1.5 nm on the s-axis.

extracellular domain was observed to have a considerable effect on channel conductance estimates for both structures (Figure 5.4). Exclusion of the extracellular domain led to elevation of the number of ions traversing the channel during each 200 ns simulation, and thereby of the mean conductance calculated, by around a factor of five and about an order of magnitude (10- to 15-fold) for the glycine and 5-HT_3 receptor structures, respectively. These results suggest that the extracellular domain presents a rate-limiting step for Cl^- or Na^+ translocation through the two structural models under investigation.

There has been experimental evidence that sites within the transmembrane domain of the α_1 glycine receptor may form the main structural determinants of its single-channel conductance characteristics, which was preserved in constructs where the intracellular domain was removed[433,434] or where the extracellular domain was substituted by that from the *Gloeobacter* ligand-gated ion channel (GLIC), a cation-selective bacterial pLGIC[435]. However, contribution of residues in the extracellular domain towards modulating pLGIC conductance has been reported for both anion- and cation-selective channels of the family[436,437]. The role of intracellular domain residues in determining channel conductive properties has also been demonstrated[438–441], although such influences have not been reflected in the present set of computational data. Unlike for the $GABA_A$ receptor[260,442,443], there are currently no reports of glycans within the extracellular vestibule of the glycine or 5-HT_3 receptor that would constitute a known source of inaccuracy when simulating the protein with an unglycosylated extracellular domain. With the objective of extracting functional information from experimental structures in their most complete state, further simulations were therefore conducted without truncation of the channel. The uniform electric field method, being half as computationally demanding as the ionic imbalance approach, was employed.

From additional uniform field simulations of both structures, there was insufficient evidence of any significant shift in conductance estimates as the membrane potential was increased, even up to a value of ±800 mV, nor of a non-linear dependence on the concentration of ions present in the system within the range examined (Figure 5.5). On the basis of such data, channel structures subsequently simulated were solvated in the higher NaCl concentration of 0.5 M and remained under a transmembrane potential difference of ±500 mV, with negative potential on the cytoplasmic side as the default condition. The

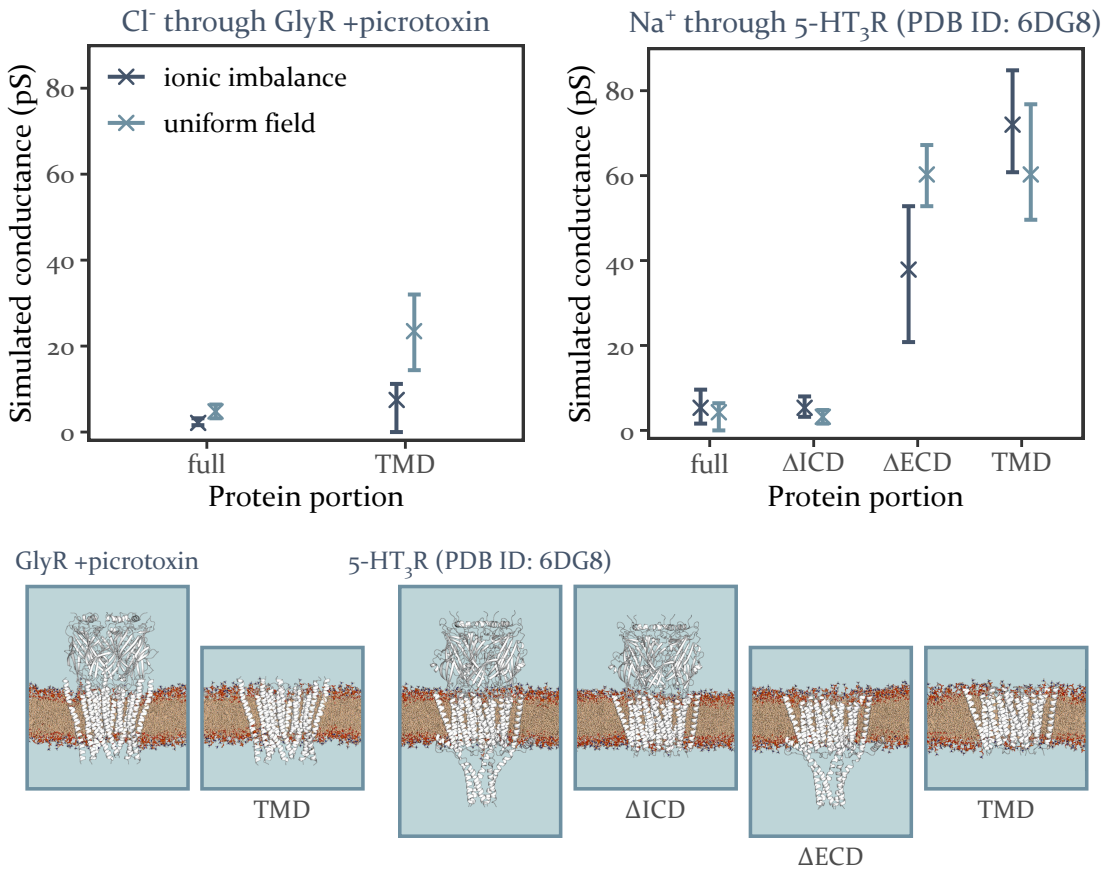


Figure 5.4 Simulated conductance levels for two pentameric ligand-gated ion channel structures[403,422], using two alternative methods of computational electrophysiology. Each simulation system, solvated with 0.2 M of NaCl, contained either the full-length experimental glycine receptor (GlyR) or 5-HT_3 receptor (5-HT_3R) structure or one of their truncated constructs, leaving only the transmembrane domain (TMD) or, in the case of 5-HT_3R, with deletion (Δ) of the intracellular (ICD) or extracellular protein domain (ECD). The bound picrotoxin was removed from the GlyR pore prior to simulations. Positional restraints were applied to protein backbone atoms. A membrane potential of +500 mV (with positive potential on the cytoplasmic side) was applied for the GlyR structure and -500 mV for 5-HT_3R, to measure the influx of Cl^- and Na^+ ions, respectively. The mean conductance and the minimum-maximum range across independent 200 ns triplicates are shown. Molecular graphics representations of the membrane-embedded protein constructs (white ribbons) correspond to simulation unit cells for the uniform electric field method and are each duplicated in the vertical direction for the ionic imbalance approach. Individual water molecules and ions in the systems are omitted for clarity.

direction of the external field was reversed where it would be in accordance with the main physiological direction of ionic flux through a given channel. A positive membrane potential was applied, for example, for structures of the glycine receptor which, in mature neurons, mediates Cl^- ion influx[444]. Simulations under the chosen conditions were intended to provide a consistent set of indicators for assessing the conductive state of ion channel structures, particularly for Section 5.2.3. Measurements made in the presence of a high concentration of NaCl could then be scaled down to a physiological level, with the assumption of approximate direct proportionality.

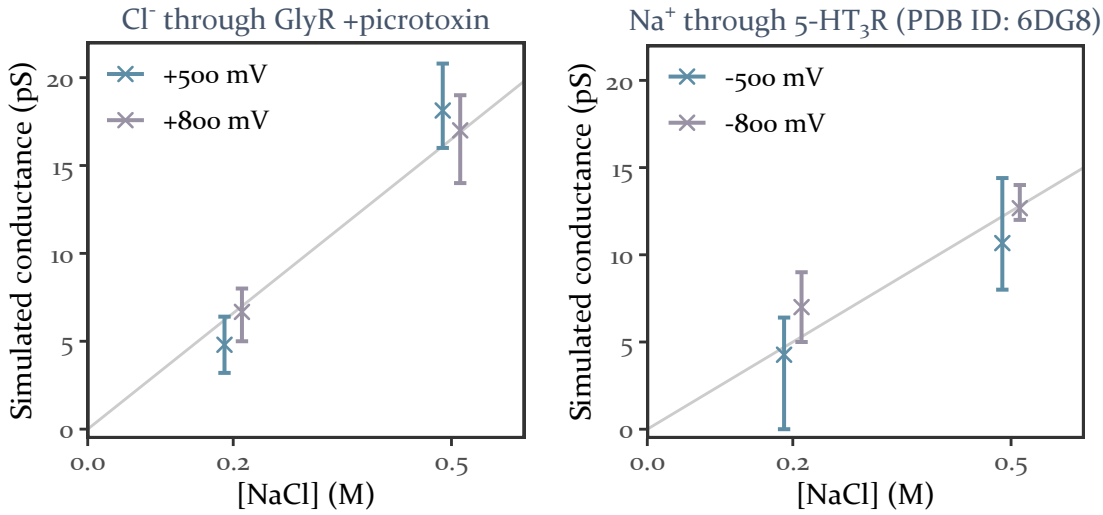


Figure 5.5 Simulated conductance levels for two pentameric ligand-gated ion channel structures[403,422], in the presence of 0.2 M or 0.5 M NaCl. A transmembrane potential difference of magnitude 500 mV or 800 mV was generated by applying an external uniform electric field orthogonal to the plane of the membrane, with positive potential on the cytoplasmic side in the case of the glycine receptor (GlyR) structure and negative potential for the 5-HT_3 receptor (5-HT_3R), to measure the influx of Cl^- and Na^+ ions, respectively. The bound picrotoxin was removed from the GlyR pore prior to simulations. Positional restraints were applied to protein backbone atoms. The mean conductance and the minimum-maximum range across independent 200 ns triplicates are shown.

5.2.2 A pipeline for functional annotation of new channel structures

Three recent structures of the zebrafish α_1 glycine receptor[403] were first examined for potential closure of the channel pore by hydrophobic de-wetting, prior to assessment of ion conduction. Each structure was correspondingly subjected to three types of analyses in increasing order of computational time and complexity: (i) simple scoring based on the heuristic model derived in Chapter 4, (ii) short equilibrium simulations as previously employed, and (iii) the computational electrophysiology protocol described above.

The glycine receptor structures had been captured in a membrane nanodisc environment by single-particle cryo-electron microscopy at resolutions between 3.33 Å and 3.51 Å[403] and represented, respectively, an unliganded (apo) state (PDB ID: 6UBS), a glycine-bound state (PDB ID: 6UBT), and a third conformation bound to both glycine and picrotoxin (PDB ID: 6UD3). The permeation pathway through each structure was identified using CHAP[80] (Figure 5.6A), and the three alternative pore conformations could be manifestly distinguished by an analysis of their geometry and hydrophobicity.

Several hydrophobic pore-lining side chains were found at relatively narrow regions within both the apo structure and the structure with glycine as its sole ligand, particularly around their 9′ leucine and -2′ proline positions, respectively. When mapped onto a landscape of local pore radius against Wimley-White[231] hydrophobicity, these residues fell below the 1 *RT* contour line from support vector regression based on previous data (Section 4.2.5) and corresponded to potential contributors towards an energetic barrier to permeation. Summation of their shortest distances ($\sum d$) to the dividing line, as a measure of the combined effect of radius and hydrophobicity, yielded prediction scores that would positively correlate with the likelihood of a structure undergoing hydrophobic de-wetting (Section 4.2.5). A value of 1.11 was obtained for the apo conformation, mainly due to its 9′ leucine and to a lesser extent 6′ threonine residues, respectively contributing 0.74 and 0.23 to the sum, with a minor contribution from the -2′ proline and 13′ threonine positions near the contour line (Figure 5.6B). In the glycine-bound conformation, where the 9′ gate had widened and the -2′ position narrowed relative to the apo state, the principal contributor was instead the -2′ proline ring, which constituted over 90 % of a total score of 0.80, with the remainder arising from the 1′ valine position. Assuming a cut-off of $\sum d > 0.55$ chosen in the previous chapter, the two structures were predicted to be non-conductive. By contrast, hydrophobic positions along the channel axis of the glycine- and picrotoxin-bound conformation were sufficiently large in pore radius to be excluded from the distance summation, giving a heuristic score of 0.00 (Figure 5.6B).

During equilibrium simulations of the membrane-embedded structures, with positional restraints applied to protein backbone atoms, the pore of the apo conformation remained devoid of water molecules at its 9′ leucine ring, as predicted. The thermodynamic barrier at this closed hydrophobic gate was estimated[80,131] from the water density distribution

to be approximately 6 kJ mol^{-1} (Figure 5.6C). The barrier disappeared in the case of the two glycine-stabilised conformations (simulated in the absence of any bound ligands), where the 9′ leucine side chains were rotated away from the pore and towards the adjacent M2 helices. In the picrotoxin-bound conformation, the centre of geometry of each 9′ leucine residue was, for over half of the analysed simulation trajectory frames, farther from the centre line of the channel pathway than its α-carbon was, and the 9′ leucine was no longer considered to be among the pore-lining side chains (labelled in their single-letter notation in Figure 5.6C) in this structure. Unlike the fully hydrated pore of the picrotoxin-stabilised state, the water free energy profile of the glycine-only conformation revealed a small peak at the -2′ proline position, as identified above by the structure-based scoring. The magnitude of the -2′ energetic barrier reached up to 3.1 kJ mol^{-1} in one replicate, although its mean value of 2.5 kJ mol^{-1} across triplicates was just below the 1 *RT* (approximately 2.6 kJ mol^{-1} at 37 °C) cut-off (Figure 5.6C).

Previous MD studies[83,432] had noted the instability of an earlier experimental structure of the same protein in its glycine-bound state (PDB ID: 3JAE)[79], where the open pore was observed to collapse inwards in the absence of protein restraints. This led to a considerable reduction in its minimum pore radius at the 9′ leucine position, from as high as approximately 0.4 nm to below 0.2 nm within 10 ns of equilibration time[83]. Whilst the reported behaviour was reproduced for the Du *et al.* [79] conformation alongside the present investigation, the three recent structures exhibited relatively minor deviations in their pore profiles in unrestrained equilibrium simulations of up to 200 ns in duration. The defining pore features were stably maintained (Figure 5.6C) and the picrotoxin-stabilised conformation, in particular, retained its minimum pore radius of above 0.3 nm. Prediction from water free energy analyses remained that the apo and glycine-only structures would be non-conductive, closed respectively at the 9′ leucine and -2′ proline rings, whereas the picrotoxin-stabilised state could potentially represent a functionally open conformation.

As expected, no Cl^- ion influx was observed through either the apo or the glycine-only conformation over 1 µs of total simulation time per structure, even at the elevated transmembrane potential of +500 mV (with positive potential on the cytoplasmic side) and NaCl concentration of 0.5 M. In the case of the glycine-only structure, Cl^- ions were able to travel into the transmembrane domain of the channel from the extracellular

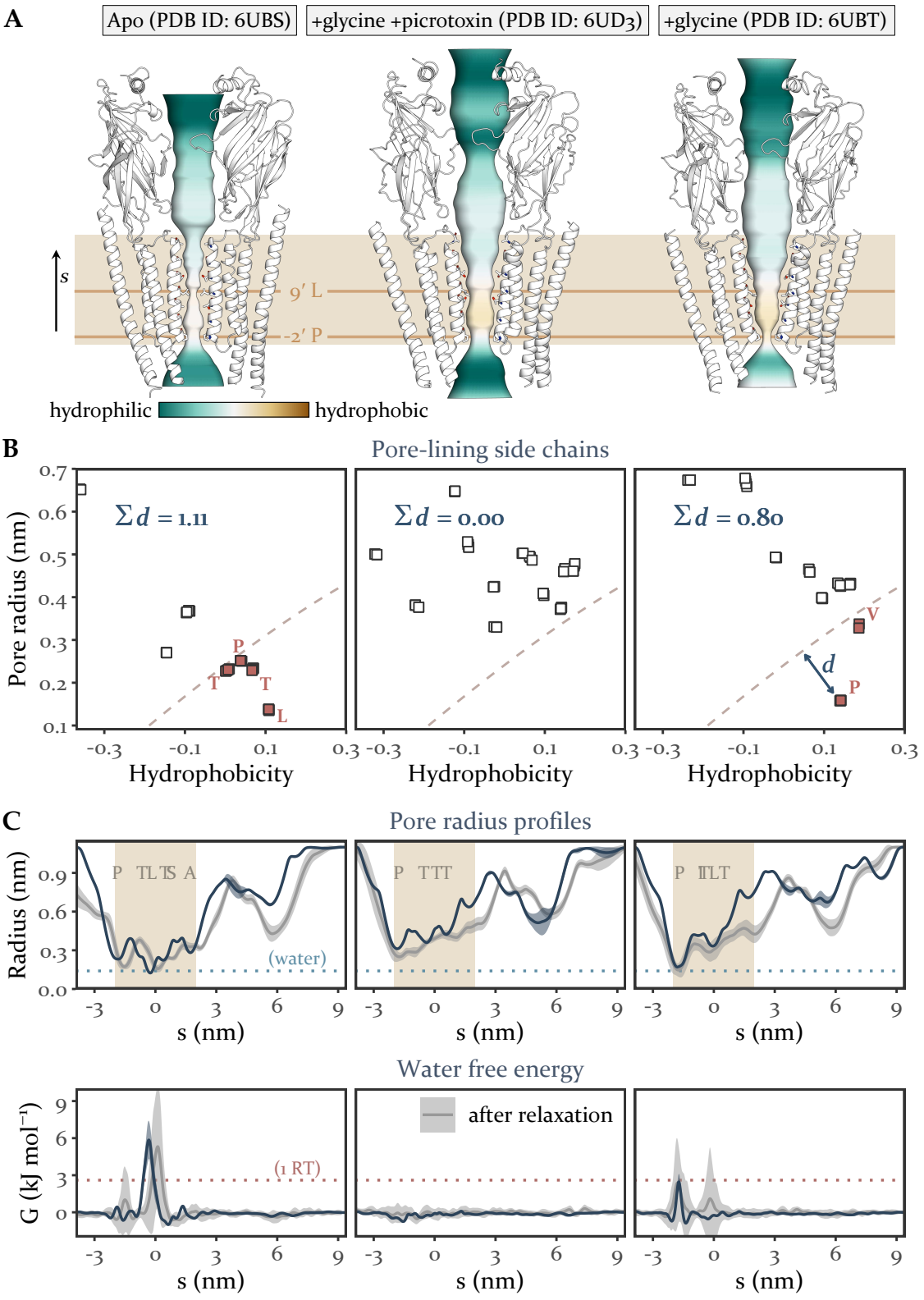


Figure 5.6 (**A**) Pore surface, (**B**) structure-based scoring, and (**C**) water equilibrium simulation analyses of three recent glycine receptor structures[403]. Pore profiles (dark blue) were derived from independent 30 ns simulations where positional restraints were applied to protein backbone atoms, showing the mean and standard deviation between triplicates. Time-averaged profiles (grey) from the final 20 ns of a 200 ns unrestrained replicate, sampling at 0.5 ns intervals, were also plotted for each structure.

side and cross the 9′ leucine ring, but none progressed beyond the -2′ proline position that presented a small energetic barrier to water (Figure 5.7; the reduced water density in the region cannot be discerned from the figure due to the size of the data points and the small sampling intervals).

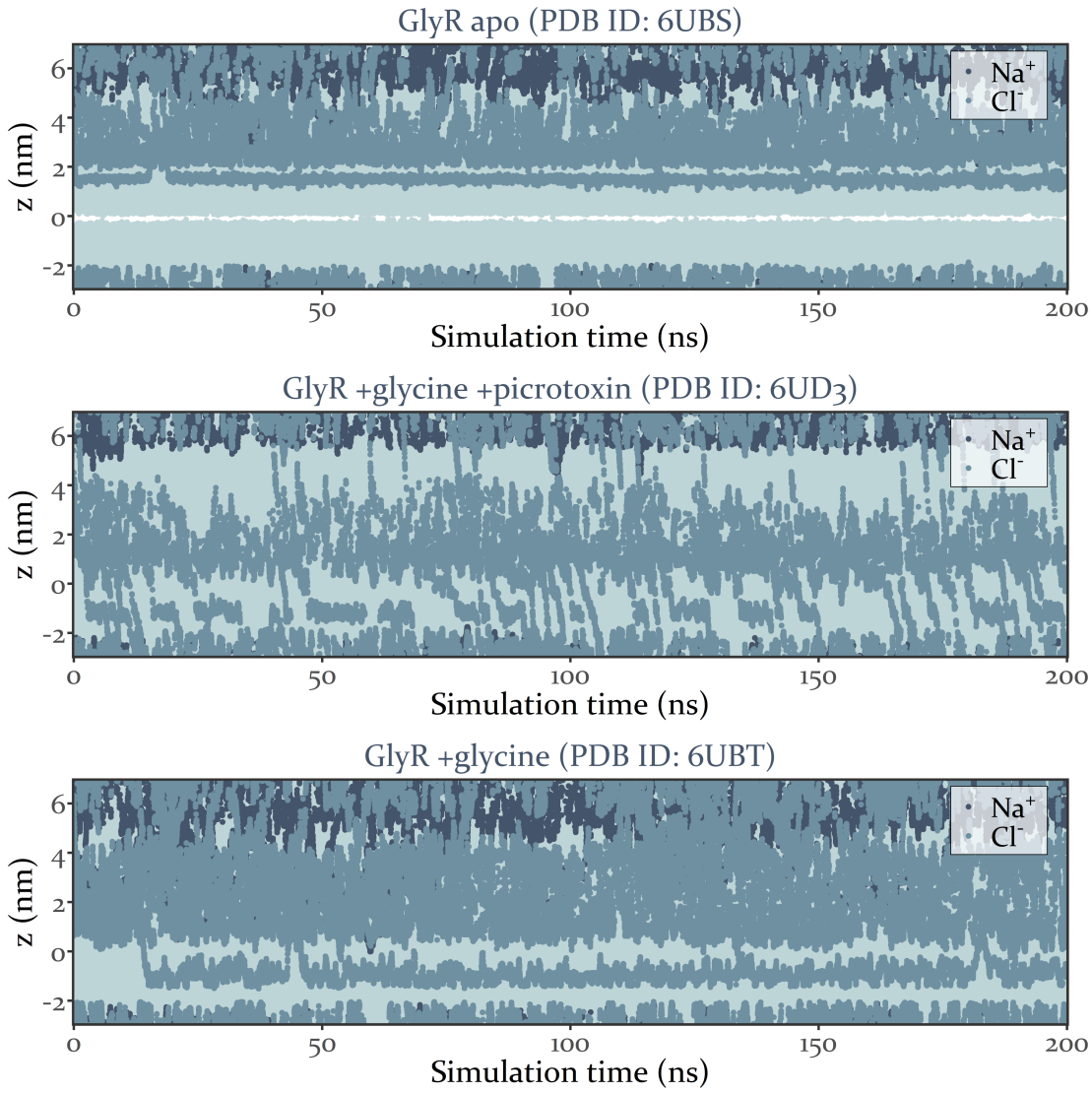


Figure 5.7 Water (pale blue) and ion coordinates in the pore of recent glycine receptor (GlyR) structures[403]. One of five independent 200 ns replicates are shown for each conformation. The z-axis represents the membrane normal direction, with negative z corresponding to the cytoplasmic side. The 9′ leucine residues are located around 0 nm and the -2′ proline between -2 nm and -1.5 nm. Positions of water molecules and Na^+ and Cl^- ions within a 0.5 nm radius of the channel centre line are plotted at 10 ps intervals. Simulation systems were solvated with 0.5 M of NaCl. A transmembrane potential of +500 mV was applied via a uniform external electric field, with positive potential on the cytoplasmic side. Any bound ligands, where present, were removed prior to simulation, and positional restraints were applied to protein backbone atoms.

By contrast, a total of 173 Cl^- ions traversed the pore of the picrotoxin-stabilised conformation. The simulated conductance was thus around 60 pS, with a standard deviation of 10 pS between five independent 200 ns replicates, corresponding to an estimated single-channel Cl^- ion conductance of approximately 20 pS when corrected to the value at 0.15 M NaCl. Ion entry into the channel was predominantly via the apex of the extracellular domain, with a smaller (20 %) fraction entering from the side, through inter-subunit gaps of the protein at the junction between its extracellular and transmembrane domains. Na^+ ions did not generally move beyond the positively charged 0′ arginine ring at the cytoplasmic end of the transmembrane M2 helices (Figure 5.7), with only one permeation event observed.

Computational electrophysiology results for these glycine receptor structures therefore agreed with predictions from the two simpler levels of analyses, further supporting the assignment of two non-conductive and one conductive conformation among the three structures. The apo, picrotoxin-stabilised, and glycine-bound structures[403] are annotated, respectively, as capturing the resting, open, and desensitised states, consistent with the dual gate mechanism[81], with the 9′ leucine position acting as the channel activation gate and -2′ proline conferring closure of the pore during desensitisation.

The simulated conductance of the open conformation is lower than the experimental values of 80 to 88 pS from single-channel electrophysiology[445], and exhibits greater apparent selectivity for anions than a permeability ratio of $P_{Cl^-}/P_{Na^+} \approx 25$ would suggest[446,447]. The discrepancy in measurements could be due to inaccurate representation of electrostatic effects exerted by the intracellular domain[441] in the absence of its unstructured region from the structural model. It may also reflect limitations of the computational protocol, including imposition of positional restraints on protein backbone atoms and the use of a classical, pairwise-additive force field for simulations (Section 2.1.1.1). Explicit inclusion of electronic polarisation effects[448] has been shown to improve conductance estimates through the ionophore gramicidin A[449]. Furthermore, the sensitivity of Cl^- ions, in particular, to induced polarisation as it permeates a channel pore has recently been demonstrated[450].

Notwithstanding its limitations, the computational electrophysiology protocol adopted appears to reproduce channel properties in qualitative agreement with experimental

evidence. Annotation and classification of structures according to their predicted conductive state are automatable at each of the three levels of analyses. Such data offer a starting point for full mechanistic investigations into the physiological significance of alternative conformations and transitions between them, for example employing longer-timescale simulations[76,451], enhanced sampling methods[76,452], or polarisable force fields[450].

The utility of the present pipeline for evaluating the functional state of channel pores may be similarly illustrated using three of the most recent cryo-electron microscopy structures of the mouse 5-HT_{3A} receptor: an apo state (PDB ID: 6BE1)[255] and two serotonin-bound conformations, referred to as state I (PDB ID: 6DG7) and state II (PDB ID: 6DG8)[422]. The overall resolutions of the structures are 4.31 Å, 3.32 Å, and 3.89 Å, respectively. The state II structure, which has the widest pore among the three, was also used to assess the impact of the choice of simulation conditions on computational electrophysiology results, as described in Section 5.2.1.

In each of the three structures, the channel pore is sterically unobstructed along the central symmetry axis formed by the five subunits, from the apex of the extracellular domain to the lower end of the intracellular portion (Figure 5.8A). The pore narrows within the transmembrane domain and below the intracellular vestibule. Despite the latter constriction having a moderate minimum pore radius of between 0.25 and 0.3 nm in the three original conformations, its hydrophobicity and the length extended along the channel axis led to the prediction of a hydrophobic barrier that would preclude permeation. Mapping the local pore radius and estimated hydrophobicity at residues lining the intracellular section of the linear pathway yielded $\sum d$ values of 1.00, 1.08, and 0.75 for the apo, state I, and state II structures, respectively, above the $\sum d > 0.55$ cut-off (Section 4.2.5).

The same analysis on pore-lining side chains in the transmembrane domain (Figure 5.8B), on the other hand, predicted de-wetting around the 9′ leucine position in the apo and state I structures and full hydration of the state II pore above the intracellular constriction. The $\sum d$ score of 1.37 obtained for the apo conformation consisted principally of a major contribution of 0.80 from the 9′ leucine residues and a minor one of 0.43 from the adjacent 13′ valine ring. These two positions in the state I pore were also almost entirely responsible for its lower score of 0.68, respectively contributing 0.33 and 0.31, even at much wider local pore radius than the third identified position surrounded by

the 2′ serine ring. The same leucine and valine residues in the state II conformation fell close to the 1 *RT* contour line (Section 4.2.5), corresponding to a small $\sum d$ value of 0.14.

The intracellular domain of the 5-HT_3 receptor is formed by the linker between the transmembrane M3 and M4 helices in each subunit, and the aforementioned constriction below the intracellular vestibule is through the membrane-associated MA helix bundle that immediately precedes the M4 in sequence (Figure 5.8A). It was noted that conformational rearrangements in state II relative to the state I and apo structures had resulted in displacement of post-M3 loops and outward movement of the MA helices, with broadening of gaps between the helices at the junction with the transmembrane domain. At their widest region, these lateral openings have an approximate radius of 0.3 nm as measured by CHAP[80]. A $\sum d$ score of 0.00 was calculated, as expected from their highly hydrophilic lining due to the presence of multiple polar and charged side chains. Rather than following the linear path along the central channel axis, the state II conformation was therefore suggested to potentially conduct ions via the lateral portals in the intracellular domain, bypassing the hydrophobic MA helix bundle at the bottom of the channel.

Structure-based predictions of pore de-wetting or hydration in all three regions were confirmed by analyses of simulated water density. Substantive energetic barriers were revealed in the intracellular constriction along the symmetry axis of each channel pore, as well as at the 9′ leucine and 13′ valine positions in the apo and state I structures (Figure 5.8C). In the case of the state II conformation, the sharp contrast between the maximum water free energy of 30 kJ mol^{-1} in the MA helix bundle and the value of 0 kJ mol^{-1} through the transmembrane domain was particularly notable. The minimum time-averaged pore radii in the two regions were similar, at approximately 0.41 nm and 0.38 nm, respectively, both above the radius of a hydrated Na^+ ion[228,453]. Their striking difference in water free energy arose from the greater hydrophobicity in the lining of the MA helix bundle.

Whilst the apo and state I structures each displayed no measurable level of conductance under the chosen computational electrophysiology conditions, the simulated rate of Na^+ ion influx through the state II pore corresponded to a single-channel conductance of 3 ± 1 pS across independent 200 ns triplicates, corrected to a NaCl concentration of 0.15 M. Na^+ ions invariably entered the channel from the apex of the extracellular domain and exited via the intracellular lateral portals (Figure 5.9), as was anticipated on the basis

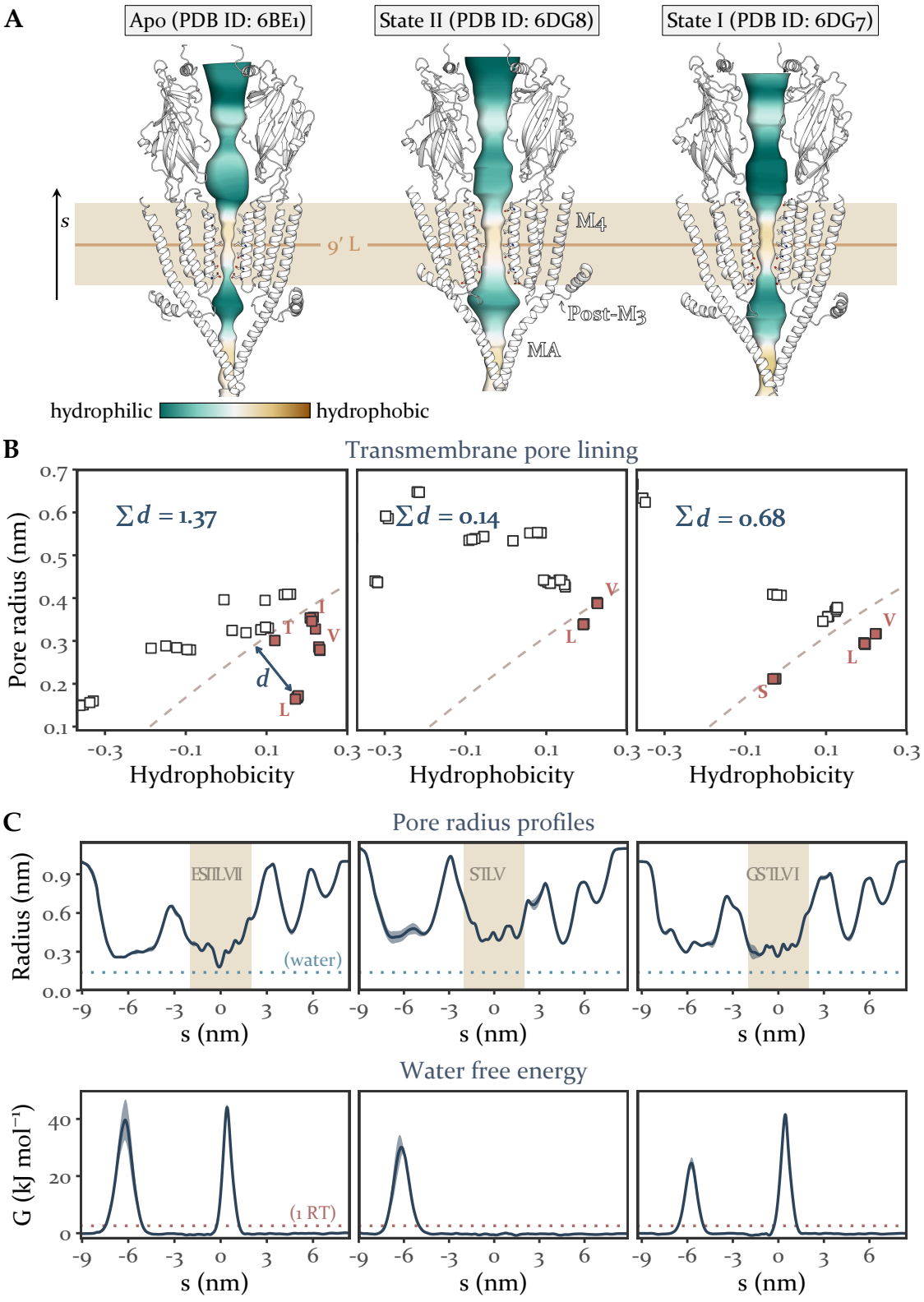


Figure 5.8 (**A**) Pore surface, (**B**) structure-based scoring (Section 4.2.5), and (**C**) water equilibrium simulation analyses of three serotonin 5-HT_{3A} receptor structures[255,422]. Pore profiles were derived from independent 30 ns simulations where positional restraints were applied to protein backbone atoms, showing the mean and standard deviation between triplicates. Amino acid side chains that were oriented towards the pore in over half of the analysed trajectory frames, sampling at 0.5 ns intervals, are labelled.

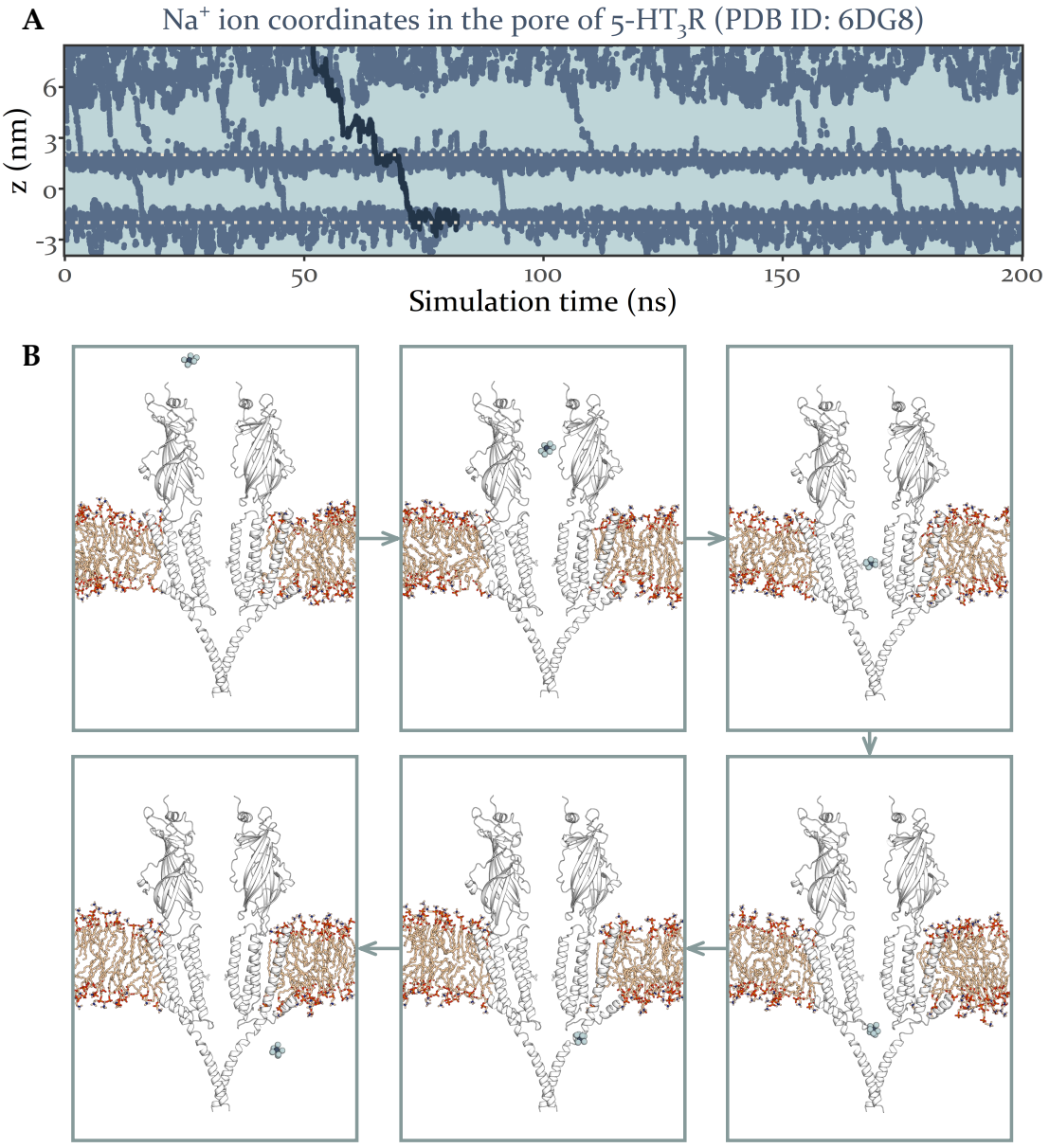


Figure 5.9 (**A**) Coordinates of water (pale blue) and Na^+ ions (dark blue) in the pore of a 5-HT_{3A} receptor structure[422] during one simulation replicate, highlighting the trajectory of one of the ions that traversed the channel, and (**B**) six snapshots illustrating Na^+ ion entry into the extracellular domain and exit from an intracellular lateral portal within 30 ns of simulation time. The z-axis represents the membrane normal direction, with negative z corresponding to the cytoplasmic side. The 9′ leucine residues are located around 0 nm, with the approximate location of the membrane indicated by the dotted lines. The de-wetted region in the intracellular constriction along the symmetry axis of the pore, which does not form part of the permeation pathway, is not included in the plot. For clarity, only two subunits of the pentameric protein (white ribbons) and a thin band of the membrane (orange) are shown in the molecular graphics images, with the Na^+ ion and water molecules within 0.4 nm of it, at each given instant, represented as spheres. Simulation systems were solvated with 0.5 M of NaCl. A transmembrane potential of -500 mV was applied via a uniform external electric field, with negative potential on the cytoplasmic side. Positional restraints were applied to protein backbone atoms.

of the hydrophobicity evaluation and equilibrium simulations. No Cl^- ion entry was observed, indicative of a permeability ratio P_{Na^+}/P_{Cl^-} of above 20.

Overall, the three levels of computational assessment of the 5-HT_3 receptor structures[255,422] each suggest that the apo and state I conformations are non-conductive. The serotonin-bound state I, with its transmembrane and intracellular pore features in between the apo and state II structures, may reflect a pre-open intermediate or a desensitised receptor, whereas state II likely represents a functionally open conformation, exhibiting the expected degree of cation-selectivity[53,454]. Its low level of simulated conductance is in accordance with the characteristically small single-channel conductance of the homomeric 5-HT_{3A} receptor[455], although the presently calculated value is higher than experimental estimates derived by variance analysis of macroscopic currents, ranging from 0.4 to 1 pS[455–457].

The observed trajectory of hydrated Na^+ ions through the state II structure is consistent with the lateral portals in the intracellular domain serving as ion exit pathways, as had been previously hypothesised for cation-selective members of the pLGIC family, based on the nicotinic acetylcholine receptor structure[458], electrophysiological data for the 5-HT_{3A} receptor[438], and the observation of Cl^- ion entry via the intracellular portals upon microsecond-timescale simulations of 5-HT_{3A} activation initiated from a closed structure[459]. Since the publication of present results as part of the study by Basak *et al.* [422], continuous hydration through the lateral pathway has also been reported in MD simulations of the nicotinic acetylcholine receptor[213].

In both the glycine and 5-HT_3 receptor examples above, channel pathways that were predicted to contain a closed hydrophobic gate based on the heuristic model were confirmed by equilibrium simulations to have reduced water density in the corresponding region, with water free energy of around or above 1 RT. Such dehydration barriers also impeded ion conduction through the structure, including a case where the minimum pore radius would sterically be sufficient to accommodate a hydrated ion. These results provide validation for the three-tiered pipeline (Figure 5.10) for efficient functional annotation of new channel structures as they continue to be resolved.

An assessment of pore radius and hydrophobicity is able to rapidly identify conformations that are likely non-conductive due to hydrophobic de-wetting, requiring mere seconds

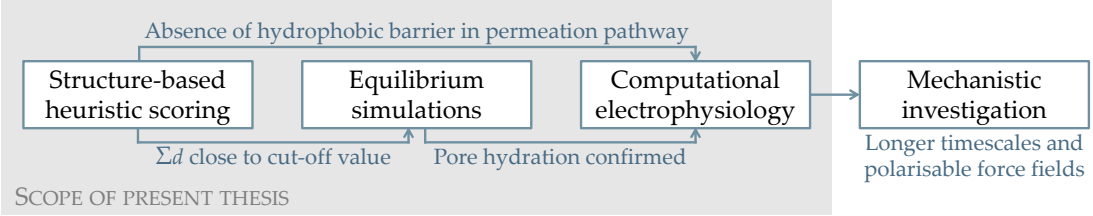


Figure 5.10 Proposed pipeline for functional annotation of new channel structures.

of computational time. Where the $\sum d$ score is close to the chosen borderline for structure-based predictions, water behaviour in the pore may be verified by short simulations. Structures that form a continuous pathway uninterrupted by hydrophobic gating, according to either or both types of pore hydration analyses, may then be subjected to the more computationally demanding measurements of conductive properties. The assignment of functional states via the proposed pipeline may be followed by mechanistic examinations in further detail, as discussed earlier, with use of polarisable force fields[450], longer-timescale simulations[76,451], or enhanced sampling methods[76,452].

5.2.3 Pore hydration level as indicator of ion channel conduction state

The extent of channel pore hydration has, thus far, been compared using a reference water free energy value of 1 RT or approximately 2.6 kJ mol^{-1}, the mean thermal energy at physiological temperature, with a corresponding cut-off of 0.55 for the $\sum d$ score. To evaluate the reliability of using the predicted or simulated minimum pore water density (or equivalently the maximum free energy) as an initial indicator of ion conduction state, and to explore the possibility of predicting channel conductance levels without simulations, a total of 22 ion channel structures (Table 5.1) were subjected to the same computational electrophysiology protocol decided in Section 5.2.1.

The structures were selected such that the water free energy maxima along their pores, as determined from equilibrium simulations, occurred in sterically unobstructed regions with a range of local radii and degrees of hydrophobicity (Figure 5.11), and corresponded to as much variation in minimum pore water densities as allowed by the finite number of structures available and the bimodal nature of the distribution (Figure 5.12A). 11 of the structures formed part of the larger set of channels surveyed in Chapter 4, including six that had been reported as potentially non-conductive states upon their publication

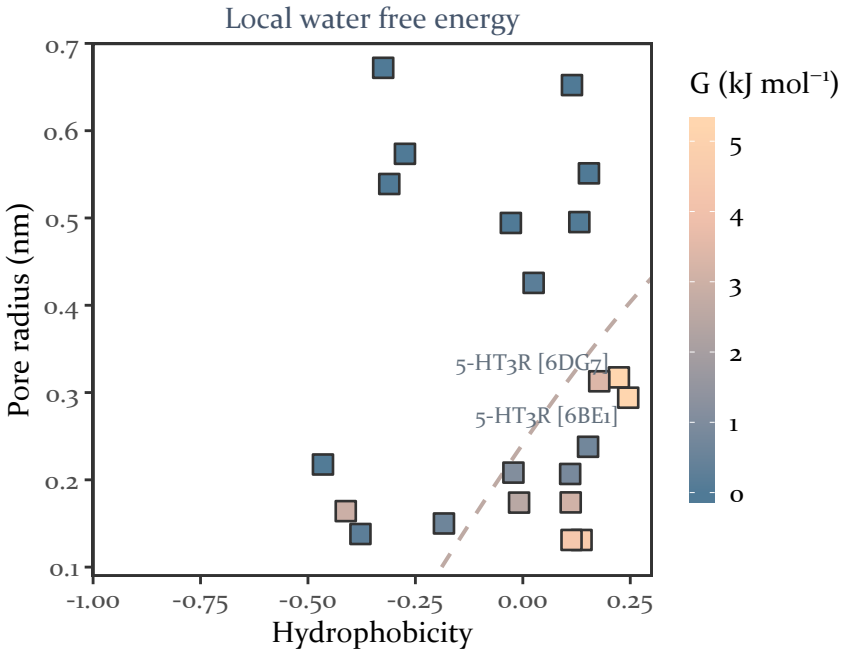


Figure 5.11 Distribution of local pore radii and degrees of hydrophobicity at residue positions with maximum water free energy along the permeation pathway in each of 22 channel structures, selected such that the pore radius at their free energy maxima is above 0.13 nm. Mean values from the final 20 ns of triplicate 30 ns equilibrium simulations are plotted. With the exception of the two labelled 5-HT_3 receptor (5-HT_3R) structures, all energetic barriers to water are below 2 *RT* (5.2 kJ mol^{-1}) and correspond to an estimated minimum water density of over 15 % of that of bulk water. Points with free energy values outside the colour scale range of 0 to 5.2 kJ mol^{-1} are shown in the same colour as the lower or upper bound. The dashed contour line indicates the 1 *RT* (2.6 kJ mol^{-1}) position on the hydrophobicity-radius grid as given by the support vector regression model trained on simulated free energies at all pore-lining side chain positions in 190 channel structures (Section 4.2.5). Hydrophobicity values are based on the Wimley-White scale[231], linearly normalised to between -1 and 0.34, in relative units.

(Table 5.1) but showed a negligible or small energetic barrier to water (between 0.0 and 1.1 kJ mol^{-1}), where the time-averaged density at the lowest-density region of the pore was above 65 % of the bulk water density. 11 more recently resolved structures that captured channels in alternative conformations were also added, among which were the glycine and 5-HT_3 receptor structures examined in Section 5.2.2. The subset thus produced consisted of 18 structures of five pLGIC proteins – namely of the glycine and 5-HT_3 receptors, the $GABA_A$ receptor, the nicotinic acetylcholine receptor, and GLIC – as well as four structures of two other ion channels, the large-conductance mechanosensitive MscL channel and the calcium release-activated Orai channel. Pore-loop cation channels, such as potassium channels in which ion desolvation through an extended, polar segment of the permeation pathway has an active role in the conduction mechanism[413,460–462], were not examined.

No ion permeation event was observed in any of the eight structures with a time-averaged minimum pore water density below 40 % of that of bulk water (Figure 5.12B), including seven pores in which the corresponding maximum water free energy was greater than 1 *RT* (calculated from a minimum density lower than 37 % of the bulk water density) and one structure, the glycine-bound glycine receptor conformation[403] annotated as desensitised in Section 5.2.2, for which the mean value was just below 1 *RT*. Any conductance through these structures was estimated to be smaller than 0.5 pS.

Towards the other end of the water number density distribution (Figure 5.12B), permeant ions were able to traverse all ten channel pores that were hydrated to above 80 % of the bulk density (corresponding to water free energies below 0.5 kJ mol^{-1}), including a nicotinic acetylcholine receptor structure and the two MscL structures (Table 5.1) that had been suggested to be non-conductive at the time of their publication. Expectably, beyond a certain level of pore hydration, hydrophobic de-wetting ceases to be the common limiting factor to ionic flux and, depending on the channel, additional properties need to be considered when assessing its likely ion conduction state. Among the four structures with a simulated minimum water density between 60 % and 80 % of that of bulk water, two structures, respectively of the $GABA_A$ receptor and GLIC, did not show a measurable level of conductance under the presently employed conditions, whereas ion passage was observed through two glycine receptor pores with lower minimum levels of hydration.

In both aforementioned glycine receptor structures, namely a glycine- and ivermectin-bound conformation (PDB ID: 3JAF)[79] and an unpublished tetrahydrocannabinol-bound state from the Chakrapani group (Table 5.1), the small peak in water free energy, respectively of magnitude 1.1 and 0.8 kJ mol^{-1}, occurred at their -2′ proline position with a pore radius of approximately 0.2 nm. During computational electrophysiology simulations, the small number of Cl^- ions permeating the channel transiently became partially dehydrated as they travelled through the -2′ constriction, such that their interactions with proline residues from the five subunits were not all water-mediated. Such an anisotropic organisation of the first hydration shell around Cl^- ions has also been captured in another MD study of the glycine receptor, leading to the suggestion that ion conduction through this member of the pLGIC family may not require full hydration of the anion[83].

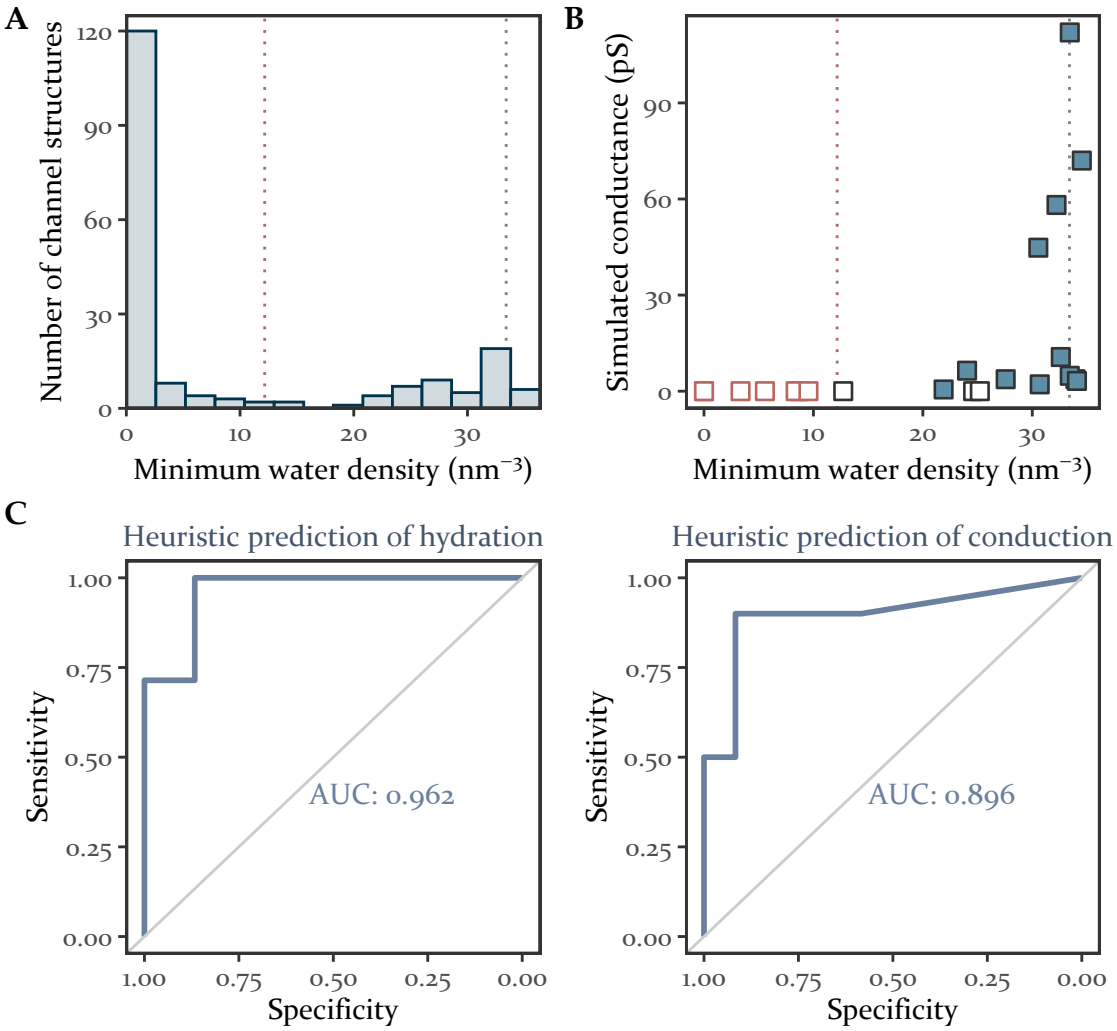


Figure 5.12 (**A**) Distribution of simulated minimum number densities of water in the 190 ion channel pores surveyed in Chapter 4, excluding potassium channel selectivity filter regions, (**B**) simulated levels of ion conductance and minimum water densities in 22 selected channel structures, and (**C**) receiver operating characteristic evaluation of the heuristic scoring model for prediction of de-wetted or non-conductive pores. Conductance and density values are, respectively, averaged between triplicates of 200 ns computational electrophysiology simulations (in the presence of 0.5 M NaCl) and 30 ns equilibrium simulations. Structures are identified as de-wetted (red-bordered squares) if their maximum water free energy is above 1 *RT* (2.6 kJ mol^{-1}, corresponding to a minimum water density below 12 nm^{-3}), indicated by the red dotted line, and as non-conductive (blue-centred squares) if no measurable conductance level (less than 0.5 pS) was observed. The grey dotted line represents the approximate bulk water density of 33.4 nm^{-3}. Heuristic $\sum d$ scores are respectively assessed against the two types of simulation results, and the relationship between the true positive rate (or sensitivity) and the false positive rate (or one minus the specificity) is displayed in the standard manner and annotated with the area under the receiver operating characteristic curve (AUC) in each case.

The subset of selected channel structures have been unable to sample the full range of minimum pore hydration levels, which exhibited a largely bimodal distribution (Figure 5.12A) reflective of two main globally stable conformational states of ion channels, interconverting between closed and conductive conformations. Even in the data set of 190 structures subjected to equilibrium simulations (Table 4.1), only two structures, both belonging to the pore-loop cation channel superfamily, showed water free energy maxima between 1.3 to 2.2 kJ mol^{-1} (corresponding to number densities between 14 to 20 nm^{-3} at the lowest-density region of the pore, approximately 40 % to 60 % of that of bulk water) along their permeation pathway, excluding potassium channel selectivity filter regions.

With a small sample size of 22 and discontinuity in the minimum pore water density values represented (Figure 5.12B), the present data could not reveal a common threshold level of hydration that would need to be exceeded for an apolar region to permit ion passage. In the absence of a well-defined reference threshold, setting a conservative cut-off value of 1 RT does appear to identify, with specificity, dehydration barriers that would render a channel structure non-conductive (Table 5.1). Structures with water free energy maxima below 1 RT, as calculated from equilibrium simulations, may be examined by computational electrophysiology for verification of their conductive state, following the suggested annotation pipeline (Figure 5.10).

Among the analysed subset, the seven structures that presented an energetic barrier to water of greater than 1 RT (and invariably showed no measurable level of conductance) also gave heuristic $\sum d$ scores higher than 0.55, ranging from 0.59 to 1.69 (Table 5.1), corroborating the ability of the structure-based method to sensitively identify hydrophobic gates. One structure, the tetrahydrocannabinol-stabilised conformation mentioned above, exhibited a moderate simulated conductance despite a $\sum d$ value of 0.85, suggesting that a margin of at least 0.3 above the cut-off may be required to improve the specificity of the initial classification and avoid falsely assigning a non-conductive state to channel pores without further investigation.

Overall, particularly considering that the subset of structures were selected with a focus on discrepancies between prior experimental evidence and predictions based on simulated water behaviour, the simple heuristic approach for modelling the likelihood of dehydration gating has performed reasonably reliably as a first indicator of ion

channel functional state. For the 22 channel structures, the use of $\sum d$ scores to identify non-conductive pores yielded an area under the corresponding receiver operating characteristic of 0.896 (Figure 5.12C). This was understandably lower than the value of 0.962 obtained for predicting de-wetted pores among the same set of structures (Figure 5.12C), consequent of the influence of additional factors as the pore becomes more fully hydrated, including characteristics that may be specific to particular channels, their pore-lining residues, and the permeant ionic species.

Earlier studies have demonstrated that continuum electrostatic approximations are often unable to provide an accurate description of energetic barriers to ions permeating a channel pore, particularly in narrow pores[463,464] and cases where desolvation effects constitute a crucial contribution[99], although qualitative agreement with potential of mean force profiles obtained from MD simulations was also reported[465], and functional insights were gained from comparative analyses across various channels and model nanopores[466,467]. To explore the possibility of using a second automatable and (relative to MD simulations) computationally inexpensive method to potentially complement pore radius- and hydrophobicity-based predictions of channel conduction state, Poisson-Boltzmann calculations were performed to assess the electrostatic environment encountered by a Na^+ or Cl^- ion as it traversed the pores of the 22 structures.

The calculations revealed distinct electrostatic (Born) energy[429,468] profiles between alternative channel conformations, such as those represented by the recent glycine and 5-HT_3 receptor structures[255,403,422] examined in Section 5.2.2 (Figure 5.13). Each profile approached zero in the electrolyte solution on either side of the channel. Consistent with results from computational electrophysiology simulations, the two pores annotated as conductive, namely the picrotoxin-stabilised glycine receptor structure (PDB ID: 6UD3) and the serotonin-bound state II structure of the 5-HT_3 receptor (PDB ID: 6DG8), showed much lower Born energy maxima (16 and 3 kJ mol^{-1}, excluding the intracellular constriction region along the channel symmetry axis in the latter case) for their permeant Cl^- and Na^+ ion, respectively, than the four structures through which no ionic flux was observed.

Whilst valid comparisons could be made between conformational states of the same protein, the maximum Born energy of the permeant ionic species along the centre line of a permeation pathway correlated poorly with the functional state suggested by

Protein	PDB	Proposed functional state	$\sum d$	G_{water} (kJ mol^{-1})	G_{Born} (kJ mol^{-1})	g (pS)
Pentameric ligand-gated ion channels						
5-HT$_3$R, *M. musculus*	6BE1	closed[255]	1.45	44.3	108	0
5-HT$_3$R, *M. musculus*	6DG7	desensitised/ intermediate[422]	0.67	41.7	71	0
5-HT$_3$R, *M. musculus*	6DG8	open[422]	0.14	0.1	3	11
GABA$_A$R, *H. sapiens*	4COF	desensitised[258]	0.00	0.8	31	0
GABA$_A$R, *H. sapiens*	6HUJ	closed[469]	1.69	3.5	114	0
GLIC, *G. violaceus*	4HFI	open[264]	0.04	0.5	20	4
GLIC, *G. violaceus*	4QH5	open[266]	0.07	0.2	35	2
GLIC, *G. violaceus*	5J0Z	desensitised[267]	0.54	0.7	29	0
GlyR, *D. rerio*	3JAD	closed[79]	1.59	4.6	81	0
GlyR, *D. rerio*	3JAE	open[79]	0.00	0.0	19	72
GlyR, *D. rerio*	3JAF	desensitised/ intermediate[79]	0.00	1.1	22	1
GlyR, *D. rerio*	6UBS	closed[403]	1.11	5.9	105	0
GlyR, *D. rerio*	6UBT	desensitised[403]	0.80	2.5	28	0
GlyR, *D. rerio*	6UD3	open[403]	0.00	0.1	16	58
GlyR, *D. rerio*	[+tetrahydrocannabinol]		0.85	0.8	20	6
nAChR, *T. marmorata*	2BG9	closed[273]	0.59	3.6	33	0
nAChR, *H. sapiens*	5KXI	desensitised[274]	0.00	0.0	139	5
nAChR, *H. sapiens*	6PV7	desensitised[213]	0.00	0.0	125	3
Other ion channels						
MscL, *S. aureus*	3HZQ	intermediate[372]	0.00	0.0	9	4
MscL, *M. acetivorans*	4Y7J	expanded/ intermediate[373]	0.11	0.0	6	112
Orai, *D. melanogaster*	6BBF	open[389]	0.00	0.2	53	45
Orai, *D. melanogaster*	6BBG	closed[389]	0.98	3.2	1,327	0

Table 5.1 Ion channel structures selected for computational electrophysiology analysis, including structures of the 5-HT$_3$ receptor (5-HT$_3$R), the GABA$_A$ receptor (GABA$_A$R), the *Gloeobacter* ligand-gated ion channel (GLIC), the glycine receptor (GlyR), the nicotinic acetylcholine receptor (nAChR), the large-conductance mechanosensitive MscL channel, and the calcium release-activated Orai channel. The likely functional states as suggested upon their publication are noted. The heuristic $\sum d$ score of each structure, maximum water free energy (G_{water}) through its permeation pathway, maximum Born energy (G_{Born}) of the permeant ion along the pathway centre line, and simulated conductance (g) in the presence of 0.5 M NaCl are recorded.

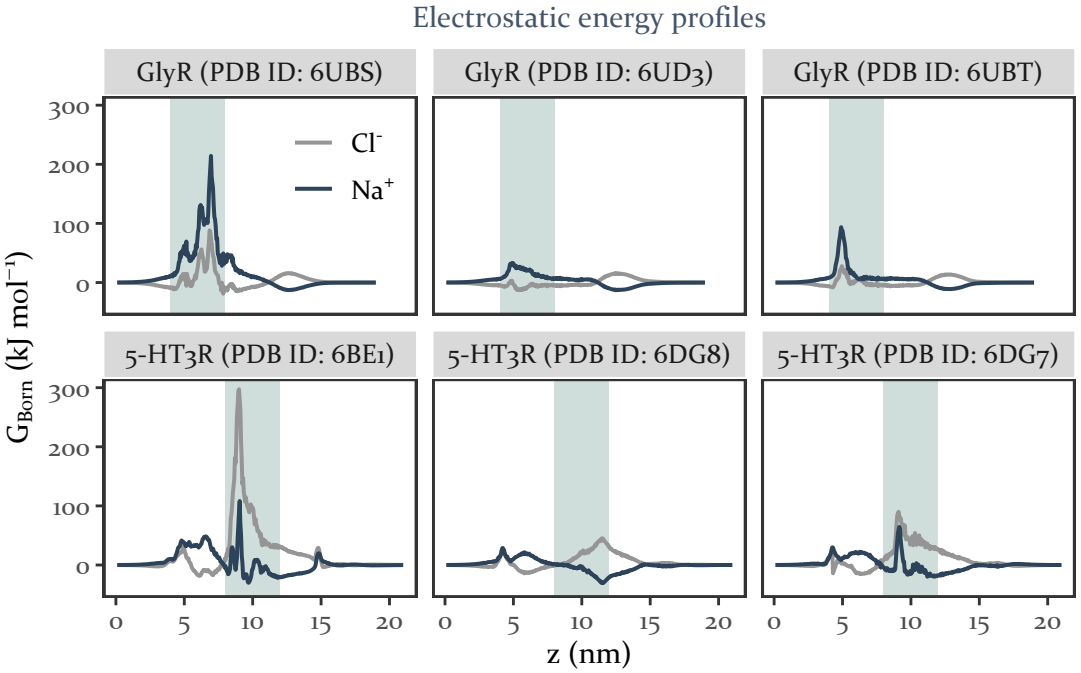


Figure 5.13 Born energy profiles through the central channel axis of six recent glycine receptor (GlyR) and 5-HT_3 receptor (5-HT_3R) structures, obtained by numerically solving the Poisson-Boltzmann equation using the Adaptive Poisson-Boltzmann Solver[425,426]. The GlyR structures[403] represent an apo state (PDB ID: 6UBS), a glycine- and picrotoxin-stablised state (PDB ID: 6UD3), and a third conformation bound to glycine (PDB ID: 6UBT), respectively annotated as resting, open, and desensitised (Section 5.2.2). The three 5-HT_3R structures include one apo (PDB ID: 6BE1)[255] and two serotonin-stablised conformations[422], state II (PDB ID: 6DG8) and state I (PDB ID: 6DG7), of which only state II exhibited a measurable level of conductance in computational electrophysiology simulations described in Section 5.2.2. The approximate z-positions of the transmembrane domain are indicated with light green background shading.

computational electrophysiology simulations across the different channel proteins (Table 5.1). Direct usage of these maximum energy values to predict whether the 22 ion channel pores were each likely to be non-conductive, for example, yielded an area under the receiver operating characteristic of 0.783 (Figure 5.14A), notably lower than the value of 0.896 given by the heuristic model (Figure 5.12C). For channel structures with high $\sum d$ scores, energetic barriers conferred by hydrophobic side chains lining relatively narrow pore regions were confirmed by corresponding peaks of at least 20 kJ mol^{-1} in their Born energy profiles. However, the magnitude of these Born energy maxima did not appear to aid in the identification of structures that would be energetically favourable for ion passage among pores where the heuristic scoring indicated absence of a hydrophobic gate (Figure 5.14B).

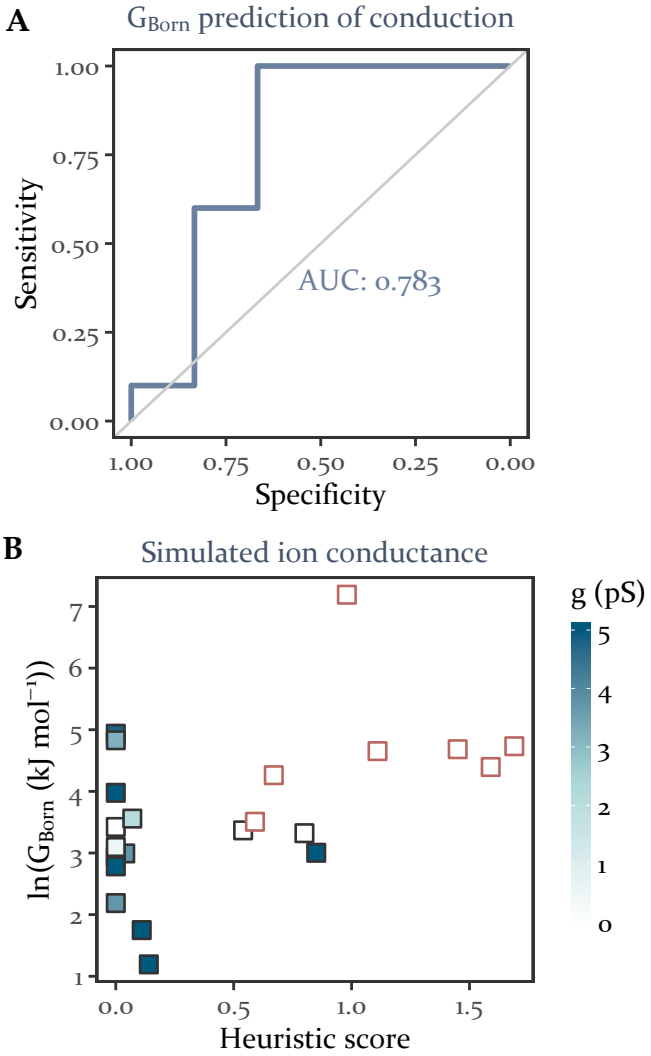


Figure 5.14 (**A**) Receiver operating characteristic evaluation of using the maximum Born energy, G_{Born}, calculated along the centre line of a channel permeation pathway for prediction of non-conductive pores and (**B**) heuristic $\sum d$ scores, natural logarithms of the maximum Born energies, and simulated conductance levels for the subset of 22 ion channel structures (Table 5.1). Born energy values are assessed against results from triplicates of 200 ns computational electrophysiology simulations in the presence of 0.5 M NaCl, and the relationship between the true positive rate (or sensitivity) and the false positive rate (or one minus the specificity) is displayed in the standard manner and annotated with the area under the receiver operating characteristic curve (AUC). Structures with maximum water free energy above 1 RT, as determined from triplicates of 30 ns equilibrium simulations, are indicated with red borders. Points with simulated conductance values beyond the colour scale range are filled with the same dark blue colour as the upper bound.

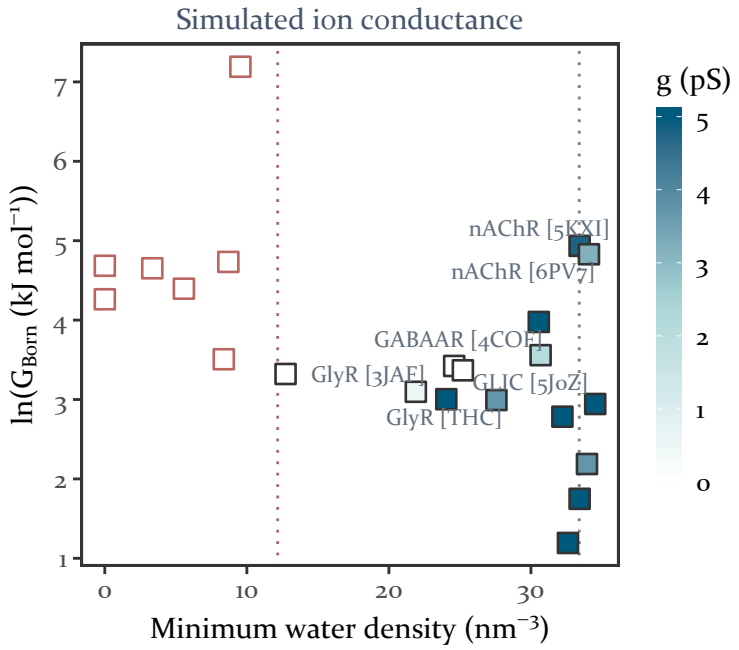


Figure 5.15 Minimum pore water densities, natural logarithms of maximum Born energies, and simulated conductance levels for the subset of 22 ion channel structures (Table 5.1). Density and conductance values are, respectively, averaged between triplicates of 30 ns equilibrium simulations and 200 ns computational electrophysiology simulations. Structures with maximum water free energy above 1 *RT* (corresponding to a minimum water density below 12 nm^{-3}, represented by the red dotted line), as determined from equilibrium simulations, are indicated with red borders. Points with simulated conductance values beyond the colour scale range are filled with the same dark blue colour as the upper bound. The six labelled structures include two nicotinic acetylcholine receptor (nAChR) pores that were calculated to have high Born energy peaks (greater than 100 kJ mol^{-1}) along the centre line of their permeation pathways but showed a low level of conductance (3 and 5 pS) at the elevated NaCl concentration of 0.5 M, as well as pores of the glycine receptor (GlyR), the $GABA_A$ receptor ($GABA_AR$), and the *Gloeobacter* ligand-gated ion channel (GLIC) in which the simulated minimum water density was between 60 % and 80 % of the number density of bulk water (grey dotted line).

Structures with more fully hydrated pores, as determined from equilibrium simulations, showed large variations in maximum Born energy through the centre of their permeation pathways, from below 10 kJ mol^{-1}, in the case of the state II 5-HT_3 receptor conformation (Section 5.2.2) and the two MscL structures, to above 100 kJ mol^{-1} (Figure 5.15). The particularly high energies in the two nicotinic acetylcholine receptor pores, which both showed a low level of conductance in computational electrophysiology simulations, occurred in a relatively narrow region between their two rings of -1′ glutamate and 2′ threonine residues, with an approximate pore radius of 0.25 nm. It was notable that repeating the calculations with the Na^+ ion positioned away from the pathway centre

line and in closer proximity to the pore-lining glutamate and threonine residues could reduce the Born energy value to around 10 kJ mol^{-1}. Apparent high energy barriers presently recorded in these regions thus likely exemplified a major limitation of deriving one-dimensional profiles from measurements taken at the axial centre of the pore. A more reliable indicator might be to determine minimum values in the radial direction for successive positions along channel pathways, with increased computational expense.

As mentioned earlier, among the four channel pores with simulated minimum water density between 60 % and 80 % of the bulk density, the two glycine receptor structures with lower water densities (at their -2′ proline rings) permitted passage of one or more ions during simulations under an external electric field, whereas the more hydrated GLIC and $GABA_A$ receptor structures did not. These four structures exhibited a moderate Born energy maxima for their respective cation or anion (Figure 5.15). The barrier height was approximately 30 kJ mol^{-1} in the GLIC and $GABA_A$ receptor pores, with smaller values of about 20 kJ mol^{-1} in the case of the two glycine receptor structures. Such a difference of 10 kJ mol^{-1} was greater than the degree of variation in estimates for individual structures as the grid dimensions and resolution were altered during calculations (Section 5.1.3), typically within 5 % of the values recorded in Table 5.1. Alongside the observation that the ten structures through which no ionic flux could be measured were each associated with a maximum Born energy of at least 28 kJ mol^{-1}, these data may potentially be indicative of a critical value between 20 and 30 kJ mol^{-1} that could form a reference point for distinguishing between conductive and non-conductive conformations among hydrated pores in future analyses. However, caution must be taken when interpreting results based on the small number of channels presently sampled, mostly belonging to the pLGIC family. The radial dependence of Born energy values mentioned above would first need to be accounted for, followed by rigorous statistical assessment across a larger set of ion channel structures.

It remains a subject of further investigation whether continuum electrostatic calculations, following an improved protocol, might constitute an informative addition to the heuristic evaluation of radius and hydrophobicity for annotation of static experimental structures. With advances in computing power, and as ion channel structures continue to be resolved in an expanding range of conformations, estimates from dielectric continuum models

for channels of different families could be systematically assessed against results from computational electrophysiology simulations and the more computationally demanding potential of mean force calculations[470]. Such surveys may further underline the importance of entropic contribution to ion permeation barriers[471], and of atomistic MD representations of protein flexibility[464,472] and explicit solvent interactions[465] even for a qualitative classification of structures. They may, alternatively, allow more accurate simulation-free predictive methods of functional state to be developed. Meanwhile, the presently suggested annotation pipeline (Figure 5.10) appears to provide an efficient approach.

5.3 Conclusion

The theme of this chapter has been to further assess the functional state of channel pore conformations beyond the identification of hydrophobic gates. Ionic flux through channel structures was directly simulated under a transmembrane potential difference, modelled using computational electrophysiology. The ionic imbalance and uniform electric field methods were able to yield comparable channel conductance estimates. The difference between simulations of intact experimental structures and of their truncated constructs, however, was not trivial. For the two pLGIC protein structures examined, namely of the glycine and 5-HT_3 receptors, removal of their extracellular domain led to an elevation in simulated conductance by up to an order of magnitude, suggesting that any decision to include or exclude portions of these structural models would need to be made with care.

Evaluated against computational electrophysiology simulations employing a common set of conditions, analyses of pore hydration has proved effective for identifying non-conductive conformations containing a sterically unobstructed dehydration barrier. A three-tiered pipeline has been suggested for efficient functional annotation of new structures, beginning from the simple heuristic $\sum d$ scoring of pore hydrophobicity and radius, introduced in Chapter 4. Short equilibrium simulations and water density estimation, as automated within CHAP[80], may be performed in cases where the $\sum d$ score is within a margin of a chosen cut-off. Structures that form a continuous channel pathway uninterrupted by hydrophobic de-wetting may then be subjected to the more computationally demanding measurements of conductive properties. The ion conduction state thus assigned to a channel pore is anticipated to offer a starting point for detailed examinations of its physiological significance and elucidation of functional mechanisms.

"Education never ends, Watson. It is a series of lessons, with the greatest for the last."

From *His Last Bow* by Sir A. C. Doyle, 1917

6

Summary and Future Directions

Building upon (i) earlier insights into the principles of hydrophobic gating, which were established in the 2000s[86,92–97] and have since received experimental validation across a number of ion channel families[85,473], and (ii) previous demonstration of channel structure annotation by molecular dynamics (MD) simulations of the equilibrium density of water in channel pores[131], the present project has sought to further investigate the application of MD-based analyses for efficient assessment of ion channel conductive state as molecular structures continue to be resolved for this class of biomedically important proteins.

In Chapter 3, structures of the bestrophin-1 chloride channel[217,220] were used both to examine the robustness of the equilibrium simulation protocol in detecting hydrophobic barriers and as a template for exploring the dependence of pore hydration on the polarity of pore-lining side chains. Estimated water free energies in the putative gate region of bestrophin-1 mutants, when visualised on axes of the local pore radius against relative hydrophobicity of each substituting amino acid, pointed towards a lowered radius threshold for the transition between de-wetted and hydrated states of more hydrophilic pores, in qualitative agreement with results from early studies on model nanopores[97].

A quantitative analysis of the influence of the degree of pore hydrophobicity in conjunction with local pore radius was presented in Chapter 4. Simulations of a representative set

of ion channel structures, about 20 % of those currently available in the Protein Data Bank (PDB)[63], allowed sampling of water behaviour over a range of pore hydrophobicity-radius combinations occurring within biological channels. By training a support vector machine[249] on the water free energy landscape thus derived, a simple, structure-based method has been devised for rapid detection of closed hydrophobic gates in ion channel pores via measurements of pore dimensions and hydrophobicity, as may be performed using the Channel Annotation Package (CHAP) recently developed by Klesse *et al.* [80] (`https://www.channotation.org/docs/heuristic_method/`).

Levels of pore hydration state as simulated by equilibrium MD or predicted by the heuristic $\sum d$ scoring method proposed in Chapter 4 were evaluated, in Chapter 5, against observations from computational electrophysiology simulations. An automatable protocol for simulating ionic flux through channel structures was decided on the basis of computational expense and preservation of structural features represented by the experimentally determined conformation. For putative open-state structures[403,422] of the glycine and serotonin 5-HT_3 receptors of the pentameric ligand-gated ion channel (pLGIC) superfamily, modelling of the transmembrane potential difference by application of a uniform external electric field[398,401,402] yielded channel conductance estimates comparable to those from the ionic imbalance approach[395–397], whereas truncation of the extracellular domain had a marked impact on simulated conductance.

A small set of 22 ion channel structures with sterically unobstructed pores were subjected to the same computational electrophysiology protocol for assessment of ion conduction state. It was demonstrated that structures exhibiting no measurable conductance level (less than 0.5 pS in the presence of 0.5 M NaCl) in these simulations could be identified, with specificity, based on their maximum pore water free energies computed by CHAP[80] from short equilibrium simulations, applying a cut-off value of 1 RT. These putative non-conductive conformations could also be predicted with reasonable accuracy by simple scoring of their pore radius and hydrophobicity. As may be expected, however, hydrophobic de-wetting ceases to be the common limiting factor to ionic flux above a certain level of pore hydration. The -2′ proline ring of the glycine receptor, for example, was observed to allow passage of partially dehydrated Cl^- ions, as has also been reported by another MD study[83]. A three-tiered pipeline is therefore suggested to efficiently

assign functional states for newly resolved channel pore conformations, beginning with identification of significant hydrophobic barriers to permeation. In the absence of such regions, simulations of ion behaviour under an electric field may be performed for verification of predictions from the two simpler, water-centric methods.

As noted in Chapter 5, the use of a pairwise-additive force field, with its simplified treatment of electrostatic interactions, constitutes an inherent limitation of the presently employed MD approach. Examined using the ionophore gramicidin A, explicit modelling of electronic polarisability via the Atomic Multipole Optimised Energetics for Biomolecular Applications (AMOEBA) polarisable force field[474] was previously shown to yield ion conductance estimates with improved accuracy[449]. In a recent study, Klesse *et al.* [450] compared the behaviour of water and ions within the M2 helix bundle of 5-HT_3 receptor structures as simulated with AMOEBA versus additive models. Whilst there was qualitative agreement between the levels of pore hydration as well as ion potential of mean force profiles calculated for the alternative simulation systems, effects of induced polarisation on hydration of the permeating ion and its interactions with pore-lining residues were also apparent[450].

With increasing availability of structural data and continuing advances in high-performance computing hardware and simulation software[475,476], a larger-scale analysis based on computational electrophysiology characterisation of ion channel structures may be conducted using a polarisable force field[477]. By surveying properties specific to particular channels, their pore-lining amino acids, and the permeant ionic species, more reliable predictive models of channel functional state may be developed in the light of additional insights into factors governing ion conduction through channel pores.

Meanwhile, it is hoped that the heuristic method and computational pipeline suggested on the basis of the present investigation will prove useful in further applications to channel structures across different families. Since the exemplifying analyses on pLGIC conformations illustrated in Chapter 5, the approach has more recently been employed to assess the likely functional states represented by new structures of two bacterial mechanosensitive channels, YnaI and YbiO, complementing structural studies by Flegler *et al.* [478]. Given the computational simplicity of the heuristic method, in particular, calculation of $\sum d$ scores upon weekly retrieval of ion channel structures from the

PDB[63] may potentially be fully automated, with annotation results made available as an online resource.

Finally, although derived from simulation data on α-helical pores of ion channels, the heuristic model has been demonstrated by preliminary examinations to be capable of predicting simulated pore hydration state within β-barrels containing hydrophobic constrictions, such as those being engineered for DNA sequencing[479], as well as for recent structures of *de novo* designed transmembrane channels[480]. A systematic evaluation of structure-based predictions on variants of these pores may serve to guide further engineering of nanopores for biotechnological applications.

References

1. Chen, I. A. and Walde, P. From self-assembled vesicles to protocells. *Cold Spring Harbor Perspectives in Biology* **2,** a002170 (2010).
2. Mojzsis, S. J., Arrhenius, G., McKeegan, K. D., Harrison, T. M., Nutman, A. P. and Friend, C. R. Evidence for life on Earth before 3,800 million years ago. *Nature* **384,** 55–59 (1996).
3. Kitadai, N. and Maruyama, S. Origins of building blocks of life: A review. *Geoscience Frontiers* **9,** 1117–1153 (2018).
4. Armstrong, C. M. Packaging life: The origin of ion-selective channels. *Biophysical Journal* **109,** 173–177 (2015).
5. Pohorille, A., Schweighofer, K. and Wilson, M. A. The origin and early evolution of membrane channels. *Astrobiology* **5,** 1–17 (2005).
6. Saier, M. H. Transport protein evolution deduced from analysis of sequence, topology and structure. *Current Opinion in Structural Biology* **38,** 17–25 (2016).
7. Saier, M. H. Tracing pathways of transport protein evolution. *Molecular Microbiology* **48,** 1145–1156 (2003).
8. Reddy, B. L. and Saier, M. H. Properties and phylogeny of 76 families of bacterial and eukaryotic organellar outer membrane pore-forming proteins. *PLoS ONE* **11,** e0152733 (2016).
9. Willson, B. J., Chapman, L. N. and Thomas, G. H. Evolutionary dynamics of membrane transporters and channels: enhancing function through fusion. *Current Opinion in Genetics and Development* **58-59,** 76–86 (2019).
10. Gennis, R. B. in *Biomembranes* 270–322 (Springer, New York, NY, 1989).
11. Morais-Cabral, J. H., Zhou, Y. and MacKinnon, R. Energetic optimization of ion conduction rate by the K^+ selectivity filter. *Nature* **414,** 37–40 (2001).
12. Kozono, D., Yasui, M., King, L. S. and Agre, P. Aquaporin water channels: Atomic structure molecular dynamics meet clinical medicine. *Journal of Clinical Investigation* **109,** 1395–1399 (2002).
13. Ashcroft, F., Gadsby, D. and Miller, C. Introduction. The blurred boundary between channels and transporters. *Philosophical Transactions of the Royal Society B: Biological Sciences* **364,** 145–147 (2009).
14. Jentsch, T. J. and Pusch, M. CLC chloride channels and transporters: Structure, function, physiology, and disease. *Physiological Reviews* **98,** 1493–1590 (2018).
15. Stockbridge, R. B., Kolmakova-Partensky, L., Shane, T., Koide, A., Koide, S., Miller, C. and Newstead, S. Crystal structures of a double-barrelled fluoride ion channel. *Nature* **525,** 548–551 (2015).

16. Gomes, D., Agasse, A., Thiébaud, P., Delrot, S., Gerós, H. and Chaumont, F. Aquaporins are multifunctional water and solute transporters highly divergent in living organisms. *Biochimica et Biophysica Acta - Biomembranes* **1788,** 1213–1228 (2009).

17. Yahalomi, D., Atkinson, S. D., Neuhof, M., Sally Chang, E., Philippe, H., Cartwright, P., Bartholomew, J. L. and Huchon, D. A cnidarian parasite of salmon (Myxozoa: *Henneguya*) lacks a mitochondrial genome. *Proceedings of the National Academy of Sciences of the United States of America* **117,** 5358–5363 (2020).

18. Vergalli, J., Bodrenko, I. V., Masi, M., Moynié, L., Acosta-Gutiérrez, S., Naismith, J. H., Davin-Regli, A., Ceccarelli, M., van den Berg, B., Winterhalter, M. and Pagès, J. M. Porins and small-molecule translocation across the outer membrane of Gram-negative bacteria. *Nature Reviews Microbiology* **18,** 164–176 (2020).

19. Güiza, J., Barría, I., Sáez, J. C. and Vega, J. L. Innexins: Expression, regulation, and functions. *Frontiers in Physiology* **9,** 1414 (2018).

20. Qu, Y. and Dahl, G. Function of the voltage gate of gap junction channels: Selective exclusion of molecules. *Proceedings of the National Academy of Sciences of the United States of America* **99,** 697–702 (2002).

21. Delano, W. L. PyMOL: An open-source molecular graphics tool. *CCP4 Newsletter On Protein Crystallography* **40,** 82–92 (2002).

22. Kern, D. M., Sorum, B., Hoel, C. M., Sridharan, S., Remis, J. P., Toso, D. B. and Brohawn, S. G. Cryo-EM structure of the SARS-CoV-2 3a ion channel in lipid nanodiscs. *bioRxiv* (2020).

23. Sui, H., Han, B. G., Lee, J. K., Walian, P. and Jap, B. K. Structural basis of water-specific transport through the AQP1 water channel. *Nature* **414,** 872–878 (2001).

24. Cowan, S. W., Schirmer, T., Rummel, G., Steiert, M., Ghosh, R., Pauptit, R. A., Jansonius, J. N. and Rosenbusch, J. P. Crystal structures explain functional properties of two *E. coli* porins. *Nature* **358,** 727–733 (1992).

25. Hille, B. *Ion Channels of Excitable Membranes* 3rd ed. (Sinauer Associates, Inc., 2001).

26. Fischer, W. B. and Sansom, M. S. P. Viral ion channels: Structure and function. *Biochimica et Biophysica Acta - Biomembranes* **1561,** 27–45 (2002).

27. Nernst, W. Zur Kinetik der in Lösung befindlichen Körper. *Zeitschrift für Physikalische Chemie* **2,** 613–637 (1888).

28. Hodgkin, A. L. and Huxley, A. F. Currents carried by sodium and potassium ions through the membrane of the giant axon of *Loligo*. *The Journal of Physiology* **116,** 449–472 (1952).

29. Cohen, S. N. DNA cloning: A personal view after 40 years. *Proceedings of the National Academy of Sciences of the United States of America* **110,** 15521–15529 (2013).

30. Noda, M., Takahashi, H., Tanabe, T., Toyosato, M., Furutani, Y., Hirose, T., Asai, M., Inayama, S., Miyata, T. and Numa, S. Primary structure of α-subunit precursor of *Torpedo californica* acetylcholine receptor deduced from cDNA sequence. *Nature* **299,** 793–797 (1982).

31. Goldschen-Ohm, M. P. and Chanda, B. SnapShot: Channel gating mechanisms. *Cell* **170,** 594–594.e1 (2017).

32. Plested, A. J. Structural mechanisms of activation and desensitization in neurotransmitter-gated ion channels. *Nature Structural and Molecular Biology* **23,** 494–502 (2016).
33. Mittal, R., Chan, B., Grati, M., Mittal, J., Patel, K., Debs, L. H., Patel, A. P., Yan, D., Chapagain, P. and Liu, X. Z. Molecular structure and regulation of P2X receptors with a special emphasis on the role of P2X2 in the auditory system. *Journal of Cellular Physiology* **231,** 1656–1670 (2016).
34. Hibino, H., Inanobe, A., Furutani, K., Murakami, S., Findlay, I. and Kurachi, Y. Inwardly rectifying potassium channels: Their structure, function, and physiological roles. *Physiological Reviews* **90,** 291–366 (2010).
35. Derler, I., Jardin, I. and Romanin, C. Molecular mechanisms of STIM/Orai communication. *American Journal of Physiology - Cell Physiology* **310,** C643–C662 (2016).
36. Boscardin, E., Alijevic, O., Hummler, E., Frateschi, S. and Kellenberger, S. The function and regulation of acid-sensing ion channels (ASICs) and the epithelial Na^+ channel (ENaC): IUPHAR Review 19. *British Journal of Pharmacology* **173,** 2671–2701 (2016).
37. Cuello, L. G., Romero, J. G., Marien Cortes, D. and Perozo, E. pH-dependent gating in the *Streptomyces lividans* K^+ channel. *Biochemistry* **37,** 3229–3236 (1998).
38. Yu, F. H., Yarov-Yarovoy, V., Gutman, G. A. and Catterall, W. A. Overview of molecular relationships in the voltage-gated ion channel superfamily. *Pharmacological Reviews* **57,** 387–395 (2005).
39. Lórenz-Fonfría, V. A. and Heberle, J. Channelrhodopsin unchained: Structure and mechanism of a light-gated cation channel. *Biochimica et Biophysica Acta - Bioenergetics* **1837,** 626–642 (2014).
40. Rasmussen, T. and Rasmussen, A. in *Subcellular Biochemistry* 83–116 (Springer New York, 2018).
41. Murthy, S. E., Dubin, A. E. and Patapoutian, A. Piezos thrive under pressure: Mechanically activated ion channels in health and disease. *Nature Reviews Molecular Cell Biology* **18,** 771–783 (2017).
42. Lamas, J. A., Rueda-Ruzafa, L. and Herrera-Pérez, S. Ion channels and thermosensitivity: TRP, TREK, or both? *International journal of molecular sciences* **20,** 2371 (2019).
43. Uysal, S., Cuello, L. G., Cortes, D. M., Koide, S., Kossiakoff, A. A. and Perozo, E. Mechanism of activation gating in the full-length KcsA K^+ channel. *Proceedings of the National Academy of Sciences of the United States of America* **108,** 11896–11899 (2011).
44. Hassaine, G., Deluz, C., Grasso, L., Wyss, R., Tol, M. B., Hovius, R., Graff, A., Stahlberg, H., Tomizaki, T., Desmyter, A., Moreau, C., Li, X. D., Poitevin, F., Vogel, H. and Nury, H. X-ray structure of the mouse serotonin 5-HT_3 receptor. *Nature* **512,** 276–281 (2014).
45. Doyle, D. A., Cabral, J. M., Pfuetzner, R. A., Kuo, A., Gulbis, J. M., Cohen, S. L., Chait, B. T. and MacKinnon, R. The structure of the potassium channel: Molecular basis of K^+ conduction and selectivity. *Science* **280,** 69–77 (1998).

46. Kopec, W., Rothberg, B. S. and de Groot, B. L. Molecular mechanism of a potassium channel gating through activation gate-selectivity filter coupling. *Nature Communications* **10,** 5366 (2019).
47. Oh, S., Paknejad, N. and Hite, R. K. Gating and selectivity mechanisms for the lysosomal K^+ channel TMEM175. *eLife* **9,** e53430 (2020).
48. Brunner, J. D., Jakob, R. P., Schulze, T., Neldner, Y., Moroni, A., Thiel, G., Maier, T. and Schenck, S. Structural basis for ion selectivity in TMEM175 K^+ channels. *eLife* **9,** e53683 (2020).
49. Jaiteh, M., Taly, A. and Hénin, J. Evolution of pentameric ligand-gated ion channels: Pro-loop receptors. *PLoS ONE* **11,** e0151934 (2016).
50. Tasneem, A., Iyer, L. M., Jakobsson, E. and Aravind, L. Identification of the prokaryotic ligand-gated ion channels and their implications for the mechanisms and origins of animal Cys-loop ion channels. *Genome Biology* **6,** R4 (2005).
51. Rendon, G., Kantorovitz, M. R., Tilson, J. L. and Jakobsson, E. Identifying bacterial and archaeal homologs of pentameric ligand-gated ion channel (pLGIC) family using domain-based and alignment-based approaches. *Channels (Austin, Tex.)* **5,** 325–344 (2011).
52. Miller, P. S. and Smart, T. G. Binding, activation and modulation of Cys-loop receptors. *Trends in Pharmacological Sciences* **31,** 161–174 (2010).
53. Thompson, A. J. and Lummis, S. C. A single ring of charged amino acids at one end of the pore can control ion selectivity in the 5-HT_3 receptor. *British Journal of Pharmacology* **140,** 359–365 (2003).
54. Kim, J.-B. Channelopathies. *Korean Journal of Pediatrics* **57,** 1–18 (2014).
55. Prevarskaya, N., Skryma, R. and Shuba, Y. Ion channels in cancer: Are cancer hallmarks oncochannelopathies? *Physiological Reviews* **98,** 559–621 (2018).
56. Cox, B. in *Ion Channel Drug Discovery* 1–15 (2014).
57. Santos, R., Ursu, O., Gaulton, A., Bento, A. P., Donadi, R. S., Bologa, C. G., Karlsson, A., Al-Lazikani, B., Hersey, A., Oprea, T. I. and Overington, J. P. A comprehensive map of molecular drug targets. *Nature Reviews Drug Discovery* **16,** 19–34 (2016).
58. Bagal, S. K., Brown, A. D., Cox, P. J., Omoto, K., Owen, R. M., Pryde, D. C., Sidders, B., Skerratt, S. E., Stevens, E. B., Storer, R. I. and Swain, N. A. Ion channels as therapeutic targets: A drug discovery perspective. *Journal of Medicinal Chemistry* **56,** 593–624 (2013).
59. Son, Y. Molecular mechanisms of general anesthesia. *Korean Journal of Anesthesiology* **59,** 3–8 (2010).
60. Hutchings, C. J., Colussi, P. and Clark, T. G. Ion channels as therapeutic antibody targets. *mAbs* **11,** 265–296 (2019).
61. Wickenden, A., Priest, B. and Erdemli, G. Ion channel drug discovery: Challenges and future directions. *Future Medicinal Chemistry* **4,** 661–679 (2012).
62. Arcangeli, A. and Becchetti, A. Novel perspectives in cancer therapy: Targeting ion channels. *Drug Resistance Updates* **21-22,** 11–19 (2015).
63. Berman, H. M., Westbrook, J., Feng, Z., Gilliland, G., Bhat, T. N., Weissig, H., Shindyalov, I. N. and Bourne, P. E. The Protein Data Bank. *Nucleic Acids Research* **28,** 235–242 (2000).

64. Thomaston, J. L., Woldeyes, R. A., Nakane, T., Yamashita, A., Tanaka, T., Koiwai, K., Brewster, A. S., Barad, B. A., Chen, Y., Lemmin, T., Uervirojnangkoorn, M., Arima, T., Kobayashi, J., Masuda, T., Suzuki, M., Sugahara, M., Sauter, N. K., Tanaka, R., Nureki, O., Tono, K., Joti, Y., Nango, E., Iwata, S., Yumoto, F., Fraser, J. S. and DeGrado, W. F. XFEL structures of the influenza M2 proton channel: Room temperature water networks and insights into proton conduction. *Proceedings of the National Academy of Sciences of the United States of America* **114,** 13357–13362 (2017).

65. Kühlbrandt, W. The resolution revolution. *Science* **343,** 1443–1444 (2014).

66. Earl, L. A., Falconieri, V., Milne, J. L. and Subramaniam, S. Cryo-EM: Beyond the microscope. *Current Opinion in Structural Biology* **46,** 71–78 (2017).

67. Cheng, Y. Membrane protein structural biology in the era of single particle cryo-EM. *Current Opinion in Structural Biology* **52,** 58–63 (2018).

68. McMullan, G., Faruqi, A. R. and Henderson, R. Direct electron detectors. *Methods in Enzymology* **579,** 1–17 (2016).

69. Scheres, S. H. RELION: Implementation of a Bayesian approach to cryo-EM structure determination. *Journal of Structural Biology* **180,** 519–530 (2012).

70. Punjani, A., Rubinstein, J. L., Fleet, D. J. and Brubaker, M. A. CryoSPARC: Algorithms for rapid unsupervised cryo-EM structure determination. *Nature Methods* **14,** 290–296 (2017).

71. Burley, S. K., Berman, H. M., Bhikadiya, C., Bi, C., Chen, L., Di Costanzo, L., Christie, C., Dalenberg, K., Duarte, J. M., Dutta, S., Feng, Z., Ghosh, S., Goodsell, D. S., Green, R. K., Guranović, V., Guzenko, D., Hudson, B. P., Kalro, T., Liang, Y., Lowe, R., Namkoong, H., Peisach, E., Periskova, I., Prlić, A., Randle, C., Rose, A., Rose, P., Sala, R., Sekharan, M., Shao, C., Tan, L., Tao, Y. P., Valasatava, Y., Voigt, M., Westbrook, J., Woo, J., Yang, H., Young, J., Zhuravleva, M. and Zardecki, C. RCSB Protein Data Bank: Biological macromolecular structures enabling research and education in fundamental biology, biomedicine, biotechnology and energy. *Nucleic Acids Research* **47,** D464–D474 (2019).

72. Yan, Z., Bai, X. C., Yan, C., Wu, J., Li, Z., Xie, T., Peng, W., Yin, C. C., Li, X., Scheres, S. H., Shi, Y. and Yan, N. Structure of the rabbit ryanodine receptor RyR1 at near-atomic resolution. *Nature* **517,** 50–55 (2015).

73. Saotome, K., Murthy, S. E., Kefauver, J. M., Whitwam, T., Patapoutian, A. and Ward, A. B. Structure of the mechanically activated ion channel Piezo1. *Nature* **554,** 481–486 (2018).

74. Infield, D. T., Matulef, K., Galpin, J. D., Lam, K., Tajkhorshid, E., Ahern, C. A. and Valiyaveetil, F. I. Main-chain mutagenesis reveals intrahelical coupling in an ion channel voltage-sensor. *Nature Communications* **9,** 5055 (2018).

75. Taberner, F. J., Prato, V., Schaefer, I., Schrenk-Siemens, K., Heppenstall, P. A. and Lechner, S. G. Structure-guided examination of the mechanogating mechanism of PIEZO2. *Proceedings of the National Academy of Sciences of the United States of America* **116,** 14260–14269 (2019).

76. Flood, E., Boiteux, C., Lev, B., Vorobyov, I. and Allen, T. W. Atomistic simulations of membrane ion channel conduction, gating, and modulation. *Chemical Reviews* **119,** 7737–7832 (2019).

77. Pan, A. C., Sezer, D. and Roux, B. Finding transition pathways using the string method with swarms of trajectories. *Journal of Physical Chemistry B* **112,** 3432–3440 (2008).

78. Lev, B., Murail, S., Poitevin, F., Cromer, B. A., Baaden, M., Delarue, M. and Allen, T. W. String method solution of the gating pathways for a pentameric ligand-gated ion channel. *Proceedings of the National Academy of Sciences of the United States of America* **114,** E4158–E4167 (2017).

79. Du, J., Lü, W., Wu, S., Cheng, Y. and Gouaux, E. Glycine receptor mechanism elucidated by electron cryo-microscopy. *Nature* **526,** 224–229 (2015).

80. Klesse, G., Rao, S., Sansom, M. S. P. and Tucker, S. J. CHAP: A versatile tool for the structural and functional annotation of ion channel pores. *Journal of Molecular Biology* **431,** 3353–3365 (2019).

81. Gielen, M. and Corringer, P. J. The dual-gate model for pentameric ligand-gated ion channels activation and desensitization. *Journal of Physiology* **596,** 1873–1902 (2018).

82. Gonzalez-Gutierrez, G., Wang, Y., Cymes, G. D., Tajkhorshid, E. and Grosman, C. Chasing the open-state structure of pentameric ligand-gated ion channels. *Journal of General Physiology* **149,** 1119–1138 (2017).

83. Cerdan, A. H., Martin, N. É. and Cecchini, M. An ion-permeable state of the glycine receptor captured by molecular dynamics. *Structure* **26,** 1555–1562 (2018).

84. Smart, O. S., Neduvelil, J. G., Wang, X., Wallace, B. A. and Sansom, M. S. P. HOLE: A program for the analysis of the pore dimensions of ion channel structural models. *Journal of Molecular Graphics* **14,** 354–360 (1996).

85. Aryal, P., Sansom, M. S. P. and Tucker, S. J. Hydrophobic gating in ion channels. *Journal of Molecular Biology* **427,** 121–130 (2015).

86. Beckstein, O., Biggin, P. C. and Sansom, M. S. P. A hydrophobic gating mechanism for nanopores. *Journal of Physical Chemistry B* **105,** 12902–12905 (2001).

87. Roth, R., Gillespie, D., Nonner, W. and Eisenberg, R. E. Bubbles, gating, and anesthetics in ion channels. *Biophysical Journal* **94,** 4282–4298 (2008).

88. Anishkin, A. and Sukharev, S. Water dynamics and dewetting transitions in the small mechanosensitive channel MscS. *Biophysical Journal* **86,** 2883–2895 (2004).

89. Stillinger, F. H. Structure in aqueous solutions of nonpolar solutes from the standpoint of scaled-particle theory. *Journal of Solution Chemistry* **2,** 141–158 (1973).

90. Lum, K., Chandler, D. and Weeks, J. D. Hydrophobicity at small and large length scales. *Journal of Physical Chemistry B* **103,** 4570–4577 (1999).

91. Rasaiah, J. C., Garde, S. and Hummer, G. Water in nonpolar confinement: From nanotubes to proteins and beyond. *Annual Review of Physical Chemistry* **59,** 713–740 (2008).

92. Hummer, G., Rasaiah, J. C. and Noworyta, J. P. Water conduction through the hydrophobic channel of a carbon nanotube. *Nature* **414,** 188–190 (2001).

93. Waghe, A., Rasajah, J. C. and Hummer, G. Filling and emptying kinetics of carbon nanotubes in water. *Journal of Chemical Physics* **117,** 10789–10795 (2002).

94. Beckstein, O. and Sansom, M. S. P. Liquid-vapor oscillations of water in hydrophobic nanopores. *Proceedings of the National Academy of Sciences of the United States of America* **100,** 7063–7068 (2003).

95. Allen, R., Melchionna, S. and Hansen, J. P. Intermittent permeation of cylindrical nanopores by water. *Physical Review Letters* **89,** 175502 (2002).

96. Allen, R., Hansen, J. P. and Melchionna, S. Molecular dynamics investigation of water permeation through nanopores. *Journal of Chemical Physics* **119,** 3905–3919 (2003).

97. Beckstein, O. and Sansom, M. S. P. The influence of geometry, surface character, and flexibility on the permeation of ions and water through biological pores. *Physical Biology* **1,** 42–52 (2004).

98. Schmid, R., Miah, A. M. and Sapunov, V. N. A new table of the thermodynamic quantities of ionic hydration: Values and some applications (enthalpy-entropy compensation and Born radii). *Physical Chemistry Chemical Physics* **2,** 97–102 (2000).

99. Beckstein, O., Tai, K. and Sansom, M. S. P. Not ions alone: Barriers to ion permeation in nanopores and channels. *Journal of the American Chemical Society* **126,** 14694–14695 (2004).

100. Dzubiella, J., Allen, R. J. and Hansen, J. P. Electric field-controlled water permeation coupled to ion transport through a nanopore. *Journal of Chemical Physics* **120,** 5001–5004 (2004).

101. Dzubiella, J. and Hansen, J. P. Electric-field-controlled water and ion permeation of a hydrophobic nanopore. *Journal of Chemical Physics* **122,** 234706 (2005).

102. Vaitheeswaran, S., Rasaiah, J. C. and Hummer, G. Electric field and temperature effects on water in the narrow nonpolar pores of carbon nanotubes. *Journal of Chemical Physics* **121,** 7955–7965 (2004).

103. Li, J., Gong, X., Lu, H., Li, D., Fang, H. and Zhou, R. Electrostatic gating of a nanometer water channel. *Proceedings of the National Academy of Sciences of the United States of America* **104,** 3687–3692 (2007).

104. Powell, M. R., Cleary, L., Davenport, M., Shea, K. J. and Siwy, Z. S. Electric-field-induced wetting and dewetting in single hydrophobic nanopores. *Nature Nanotechnology* **6,** 798–802 (2011).

105. Lynch, C. I., Rao, S. and Sansom, M. S. P. Water in nanopores and biological channels: A molecular simulation perspective. *Chemical Reviews* **120,** 10298–10335 (2020).

106. Naismith, J. H. and Booth, I. R. Bacterial mechanosensitive channels – MscS: Evolution's solution to creating sensitivity in function. *Annual Review of Biophysics* **41,** 157–177 (2012).

107. Bass, R. B., Strop, P., Barclay, M. and Rees, D. C. Crystal structure of *Escherichia coli* MscS, a voltage-modulated and mechanosensitive channel. *Science* **298,** 1582–1587 (2002).

108. Sotomayor, M. and Schulten, K. Molecular dynamics study of gating in the mechanosensitive channel of small conductance MscS. *Biophysical Journal* **87,** 3050–3065 (2004).

109. Wang, W., Black, S. S., Edwards, M. D., Miller, S., Morrison, E. L., Bartlett, W., Dong, C., Naismith, J. H. and Booth, I. R. The structure of an open form of an *E. coli* mechanosensitive channel at 3.45 Å resolution. *Science* **321,** 1179–1183 (2008).

110. Anishkin, A., Akitake, B., Kamaraju, K., Chiang, C. S. and Sukharev, S. Hydration properties of mechanosensitive channel pores define the energetics of gating. *Journal of Physics Condensed Matter* **22,** 454120 (2010).

111. Miyazawa, A., Fujiyoshi, Y. and Unwin, N. Structure and gating mechanism of the acetylcholine receptor pore. *Nature* **423,** 949–955 (2003).

112. Beckstein, O. and Sansom, M. S. P. A hydrophobic gate in an ion channel: The closed state of the nicotinic acetylcholine receptor. *Physical Biology* **3,** 147–159 (2006).

113. Revah, F., Bertrand, D., Galzi, J. L., Devillers-Thiéry, A., Mulle, C., Hussy, N., Bertrand, S., Ballivet, M. and Changeux, J. P. Mutations in the channel domain alter desensitization of a neuronal nicotinic receptor. *Nature* **353,** 846–849 (1991).

114. Labarca, C., Nowak, M. W., Zhang, H., Tang, L., Deshpande, P. and Lester, H. A. Channel gating governed symmetrically by conserved leucine residues in the M2 domain of nicotinic receptors. *Nature* **376,** 514–516 (1995).

115. Filatov, G. N. and White, M. M. The role of conserved leucines in the M2 domain of the acetylcholine receptor in channel gating. *Molecular Pharmacology* **48,** 379–384 (1995).

116. Plazas, P. V., De Rosa, M. J., Gomez-Casati, M. E., Verbitsky, M., Weisstaub, N., Katz, E., Bouzat, C. and Elgoyhen, A. B. Key roles of hydrophobic rings of TM2 in gating of the $\alpha 9\alpha 10$ nicotinic cholinergic receptor. *British Journal of Pharmacology* **145,** 963–974 (2005).

117. Cheng, X., Ivanov, I., Wang, H., Sine, S. M. and McCammon, J. A. Molecular-dynamics simulations of ELIC – A prokaryotic homologue of the nicotinic acetylcholine receptor. *Biophysical Journal* **96,** 4502–4513 (2009).

118. Nury, H., Poitevin, F., Van Renterghem, C., Changeux, J. P., Corringer, P. J., Delarue, M. and Baaden, M. One-microsecond molecular dynamics simulation of channel gating in a nicotinic receptor homologue. *Proceedings of the National Academy of Sciences of the United States of America* **107,** 6275–6280 (2010).

119. Zhu, F. and Hummer, G. Pore opening and closing of a pentameric ligand-gated ion channel. *Proceedings of the National Academy of Sciences of the United States of America* **107,** 19814–19819 (2010).

120. Zhu, F. and Hummer, G. Drying transition in the hydrophobic gate of the GLIC channel blocks ion conduction. *Biophysical Journal* **103,** 219–227 (2012).

121. Jensen, M., Borhani, D. W., Lindorff-Larsen, K., Maragakis, P., Jogini, V., Eastwood, M. P., Dror, R. O. and Shaw, D. E. Principles of conduction and hydrophobic gating in K^+ channels. *Proceedings of the National Academy of Sciences of the United States of America* **107,** 5833–5838 (2010).

122. Jensen, M., Jogini, V., Borhani, D. W., Leffler, A. E., Dror, R. O. and Shaw, D. E. Mechanism of voltage gating in potassium channels. *Science* **336,** 229–233 (2012).

123. Aryal, P., Abd-Wahab, F., Bucci, G., Sansom, M. S. P. and Tucker, S. J. A hydrophobic barrier deep within the inner pore of the TWIK-1 K_{2P} potassium channel. *Nature Communications* **5,** 4377 (2014).

124. Jia, Z., Yazdani, M., Zhang, G., Cui, J. and Chen, J. Hydrophobic gating in BK channels. *Nature Communications* **9,** 3408 (2018).

125. Zheng, W., Hu, R., Cai, R., Hofmann, L., Hu, Q., Fatehi, M., Long, W., Kong, T., Tang, J., Light, P., Flockerzi, V., Cao, Y. and Chen, X. Z. Identification and characterization of hydrophobic gate residues in TRP channels. *FASEB Journal* **32,** 639–653 (2018).

126. Zheng, W., Yang, X., Hu, R., Cai, R., Hofmann, L., Wang, Z., Hu, Q., Liu, X., Bulkey, D., Yu, Y., Tang, J., Flockerzi, V., Cao, Y., Cao, E. and Chen, X. Z. Hydrophobic pore gates regulate ion permeation in polycystic kidney disease 2 and 2L1 channels. *Nature Communications* **9,** 2302 (2018).

127. Kasimova, M. A., Yazici, A., Yudin, Y., Granata, D., Klein, M. L., Rohacs, T. and Carnevale, V. Ion channel sensing: Are fluctuations the crux of the matter? *Journal of Physical Chemistry Letters* **9,** 1260–1264 (2018).

128. Neale, C., Chakrabarti, N., Pomorski, P., Pai, E. F. and Pomès, R. Hydrophobic gating of ion permeation in magnesium channel CorA. *PLoS Computational Biology* **11,** e1004303 (2015).

129. Lórenz-Fonfría, V. A., Bamann, C., Resler, T., Schlesinger, R., Bamberg, E. and Heberle, J. Temporal evolution of helix hydration in a light-gated ion channel correlates with ion conductance. *Proceedings of the National Academy of Sciences of the United States of America* **112,** E5796–E5804 (2015).

130. Kato, H. E., Kim, Y. S., Paggi, J. M., Evans, K. E., Allen, W. E., Richardson, C., Inoue, K., Ito, S., Ramakrishnan, C., Fenno, L. E., Yamashita, K., Hilger, D., Lee, S. Y., Berndt, A., Shen, K., Kandori, H., Dror, R. O., Kobilka, B. K. and Deisseroth, K. Structural mechanisms of selectivity and gating in anion channelrhodopsins. *Nature* **561,** 349–371 (2018).

131. Trick, J. L., Chelvaniththilan, S., Klesse, G., Aryal, P., Wallace, E. J., Tucker, S. J. and Sansom, M. S. P. Functional annotation of ion channel structures by molecular simulation. *Structure* **24,** 2207–2216 (2016).

132. Stansfeld, P. J., Goose, J. E., Caffrey, M., Carpenter, E. P., Parker, J. L., Newstead, S. and Sansom, M. S. P. MemProtMD: Automated insertion of membrane protein structures into explicit lipid membranes. *Structure* **23,** 1350–1361 (2015).

133. Senn, H. M. and Thiel, W. QM/MM methods for biomolecular systems. *Angewandte Chemie - International Edition* **48,** 1198–1229 (2009).

134. Hug, S. Classical molecular dynamics in a nutshell. *Methods in molecular biology (Clifton, N.J.)* **924,** 127–152 (2013).

135. Vanommeslaeghe, K., Guvench, O. and MacKerell, A. D. Molecular mechanics. *Current Pharmaceutical Design* **20,** 3281–3292 (2014).

136. Monticelli, L. and Tieleman, D. P. Force fields for classical molecular dynamics. *Methods in Molecular Biology (Clifton, N.J.)* **924,** 197–213 (2013).

137. Born, M. and Oppenheimer, R. Zur Quantentheorie der Molekeln. *Annalen der Physik* **389,** 457–484 (1927).

138. Jorgensen, W. L. and Tirado-Rives, J. The OPLS [optimized potentials for liquid simulations] potential functions for proteins, energy minimizations for crystals of cyclic peptides and crambin. *Journal of the American Chemical Society* **110,** 1657–1666 (1988).

139. Lifson, S. and Waeshel, A. Consistent force field for calculations of conformations, vibrational spectra, and enthalpies of cycloalkane and *n*-alkane molecules. *The Journal of Chemical Physics* **49,** 5104–5107 (1968).

140. Best, R. B., Zhu, X., Shim, J., Lopes, P. E., Mittal, J., Feig, M. and MacKerell, A. D. Optimization of the additive CHARMM all-atom protein force field targeting improved sampling of the backbone ϕ, ψ and side-chain χ_1 and χ_2 dihedral angles. *Journal of Chemical Theory and Computation* **8,** 3257–3273 (2012).

141. Vanommeslaeghe, K., Hatcher, E., Acharya, C., Kundu, S., Zhong, S., Shim, J., Darian, E., Guvench, O., Lopes, P., Vorobyov, I. and Mackerell, A. D. CHARMM general force field: A force field for drug-like molecules compatible with the CHARMM all-atom additive biological force fields. *Journal of Computational Chemistry* **31,** 671–690 (2010).

142. Leach, A. R. *Molecular Modelling: Principles and Applications* 2nd ed. (Prentice Hall, 2001).

143. Wang, Y. and McCammon, J. A. in *Computational Modeling of Biological Systems* 3–30 (Springer, Boston, MA, 2012).

144. Zhu, X., Lopes, P. E. and Mackerell, A. D. Recent developments and applications of the CHARMM force fields. *Wiley Interdisciplinary Reviews: Computational Molecular Science* **2,** 167–185 (2012).

145. Jones, J. E. On the determination of molecular fields. —II. From the equation of state of a gas. *Proceedings of the Royal Society of London. Series A, Containing Papers of a Mathematical and Physical Character* **106,** 463–477 (1924).

146. Tieleman, D. P. in *Molecular Simulations and Biomembranes: From Biophysics to Function* 1–25 (2010).

147. Darden, T., York, D. and Pedersen, L. Particle mesh Ewald: An $N \cdot \log(N)$ method for Ewald sums in large systems. *The Journal of Chemical Physics* **98,** 10089–10092 (1993).

148. Essmann, U., Perera, L., Berkowitz, M. L., Darden, T., Lee, H. and Pedersen, L. G. A smooth particle mesh Ewald method. *The Journal of Chemical Physics* **103,** 8577–8593 (1995).

149. Ewald, P. P. Die Berechnung optischer und elektrostatischer Gitterpotentiale. *Annalen der Physik* **369,** 253–287 (1921).

150. Berendsen, H. J., van der Spoel, D. and van Drunen, R. GROMACS: A message-passing parallel molecular dynamics implementation. *Computer Physics Communications* **91,** 43–56 (1995).

151. Abraham, M. J., Murtola, T., Schulz, R., Páll, S., Smith, J. C., Hess, B. and Lindahl, E. GROMACS: High performance molecular simulations through multi-level parallelism from laptops to supercomputers. *SoftwareX* **1-2,** 19–25 (2015).

152. Hockney, R. W. The potential calculation and some applications. *Methods in Computational Physics* **9,** 135–211 (1970).

153. Verlet, L. Computer "experiments" on classical fluids. I. Thermodynamical properties of Lennard-Jones molecules. *Physical Review* **159,** 98–103 (1967).

154. Bussi, G., Donadio, D. and Parrinello, M. Canonical sampling through velocity rescaling. *Journal of Chemical Physics* **126,** 014101 (2007).

155. Parrinello, M. and Rahman, A. Polymorphic transitions in single crystals: A new molecular dynamics method. *Journal of Applied Physics* **52,** 7182–7190 (1981).

156. Berendsen, H. J., Postma, J. P., Van Gunsteren, W. F., Dinola, A. and Haak, J. R. Molecular dynamics with coupling to an external bath. *The Journal of Chemical Physics* **81,** 3684–3690 (1984).

157. Abraham, M. J., van der Spoel, D., Lindahl, E., Hess, B. and the GROMACS development team. *GROMACS Reference Manual Version 5.1* 2015.

158. Case, D. A., Cheatham, T. E., Darden, T., Gohlke, H., Luo, R., Merz, K. M., Onufriev, A., Simmerling, C., Wang, B. and Woods, R. J. The Amber biomolecular simulation programs. *Journal of Computational Chemistry* **26,** 1668–1688 (2005).

159. Maier, J. A., Martinez, C., Kasavajhala, K., Wickstrom, L., Hauser, K. E. and Simmerling, C. ff14SB: Improving the accuracy of protein side chain and backbone parameters from ff99SB. *Journal of Chemical Theory and Computation* **11,** 3696–3713 (2015).

160. Brooks, B. R., Bruccoleri, R. E., Olafson, B. D., States, D. J., Swaminathan, S. and Karplus, M. CHARMM: A program for macromolecular energy, minimization, and dynamics calculations. *Journal of Computational Chemistry* **4,** 187–217 (1983).

161. Huang, J., Rauscher, S., Nawrocki, G., Ran, T., Feig, M., De Groot, B. L., Grubmüller, H. and MacKerell, A. D. CHARMM36m: An improved force field for folded and intrinsically disordered proteins. *Nature Methods* **14,** 71–73 (2016).

162. Scott, W. R., Hünenberger, P. H., Tironi, I. G., Mark, A. E., Billeter, S. R., Fennen, J., Torda, A. E., Huber, T., Krüger, P. and Van Gunsteren, W. F. The GROMOS biomolecular simulation program package. *Journal of Physical Chemistry A* **103,** 3596–3607 (1999).

163. Reif, M. M., Hünenberger, P. H. and Oostenbrink, C. New interaction parameters for charged amino acid side chains in the GROMOS force field. *Journal of Chemical Theory and Computation* **8,** 3705–3723 (2012).

164. Jorgensen, W. L., Maxwell, D. S. and Tirado-Rives, J. Development and testing of the OPLS all-atom force field on conformational energetics and properties of organic liquids. *Journal of the American Chemical Society* **118,** 11225–11236 (1996).

165. Ponder, J. W. and Case, D. A. Force fields for protein simulations. *Advances in Protein Chemistry* **66,** 27–85 (2003).

166. Mackerell, A. D. Empirical force fields for biological macromolecules: Overview and issues. *Journal of Computational Chemistry* **25,** 1584–1604 (2004).

167. Pastor, R. W. and MacKerell, A. D. Development of the CHARMM force field for lipids. *Journal of Physical Chemistry Letters* **2,** 1526–1532 (2011).

168. Berger, O., Edholm, O. and Jähnig, F. Molecular dynamics simulations of a fluid bilayer of dipalmitoylphosphatidylcholine at full hydration, constant pressure, and constant temperature. *Biophysical Journal* **72,** 2002–2013 (1997).

169. Tieleman, D. P., MacCallum, J. L., Ash, W. L., Kandt, C., Xu, Z. and Monticelli, L. Membrane protein simulations with a united-atom lipid and all-atom protein model: Lipid-protein interactions, side chain transfer free energies and model proteins. *Journal of Physics Condensed Matter* **18,** S1221–S1234 (2006).

170. Ouyang, J. F. and Bettens, R. P. Modelling water: A lifetime enigma. *Chimia* **69,** 104–111 (2015).

171. Onufriev, A. V. and Izadi, S. Water models for biomolecular simulations. *Wiley Interdisciplinary Reviews: Computational Molecular Science* **8,** e1347 (2018).

172. Berendsen, H. J. C., Postma, J. P. M., van Gunsteren, W. F. and Hermans, J. in *Intermolecular Forces* 331–342 (Springer, Dordrecht, 1981).

173. Jorgensen, W. L. Transferable Intermolecular potential functions for water, alcohols, and ethers. Application to liquid water. *Journal of the American Chemical Society* **103,** 335–340 (1981).

174. Berendsen, H. J., Grigera, J. R. and Straatsma, T. P. The missing term in effective pair potentials. *Journal of Physical Chemistry* **91,** 6269–6271 (1987).

175. Jorgensen, W. L., Chandrasekhar, J., Madura, J. D., Impey, R. W. and Klein, M. L. Comparison of simple potential functions for simulating liquid water. *The Journal of Chemical Physics* **79,** 926–935 (1983).

176. Jorgensen, W. L. and Madura, J. D. Temperature and size dependence for Monte Carlo simulations of TIP4P water. *Molecular Physics* **56,** 1381–1392 (1985).

177. Bernal, J. D. and Fowler, R. H. A theory of water and ionic solution, with particular reference to hydrogen and hydroxyl ions. *The Journal of Chemical Physics* **1,** 515–548 (1933).

178. Izadi, S., Anandakrishnan, R. and Onufriev, A. V. Building water models: A different approach. *Journal of Physical Chemistry Letters* **5,** 3863–3871 (2014).

179. Mahoney, M. W. and Jorgensen, W. L. A five-site model for liquid water and the reproduction of the density anomaly by rigid, nonpolarizable potential functions. *Journal of Chemical Physics* **112,** 8910–8922 (2000).

180. Nada, H. and Van Der Eerden, J. P. An intermolecular potential model for the simulation of ice and water near the melting point: A six-site model of H_2O. *Journal of Chemical Physics* **118,** 7401–7413 (2003).

181. Nada, H. Anisotropy in geometrically rough structure of ice prismatic plane interface during growth: Development of a modified six-site model of H_2O and a molecular dynamics simulation. *Journal of Chemical Physics* **145,** 244706 (2016).

182. Zhao, C. L., Zhao, D. X., Bei, C. C., Meng, X. N., Li, S. and Yang, Z. Z. Seven-site effective pair potential for simulating liquid water. *Journal of Physical Chemistry B* **123,** 4594–4603 (2019).

183. Abascal, J. L. and Vega, C. A general purpose model for the condensed phases of water: TIP4P/2005. *Journal of Chemical Physics* **123,** 234505 (2005).

184. Vega, C. and De Miguel, E. Surface tension of the most popular models of water by using the test-area simulation method. *Journal of Chemical Physics* **126,** 154707 (2007).

185. Vega, C. and Abascal, J. L. Simulating water with rigid non-polarizable models: A general perspective. *Physical Chemistry Chemical Physics* **13,** 19663–19688 (2011).

186. Zhang, H., Yin, C., Jiang, Y. and Van Der Spoel, D. Force field benchmark of amino acids: I. Hydration and diffusion in different water models. *Journal of Chemical Information and Modeling* **58,** 1037–1052 (2018).

187. Kirkwood, J. G. Statistical mechanics of fluid mixtures. *The Journal of Chemical Physics* **3,** 300–313 (1935).

188. Roux, B. The calculation of the potential of mean force using computer simulations. *Computer Physics Communications* **91,** 275–282 (1995).

189. Yang, Y. I., Shao, Q., Zhang, J., Yang, L. and Gao, Y. Q. Enhanced sampling in molecular dynamics. *Journal of Chemical Physics* **151,** 070902 (2019).

190. Torrie, G. M. and Valleau, J. P. Monte Carlo free energy estimates using non-Boltzmann sampling: Application to the sub-critical Lennard-Jones fluid. *Chemical Physics Letters* **28,** 578–581 (1974).

191. Torrie, G. M. and Valleau, J. P. Nonphysical sampling distributions in Monte Carlo free-energy estimation: Umbrella sampling. *Journal of Computational Physics* **23,** 187–199 (1977).

192. Kumar, S., Rosenberg, J. M., Bouzida, D., Swendsen, R. H. and Kollman, P. A. The weighted histogram analysis method for free-energy calculations on biomolecules. I. The method. *Journal of Computational Chemistry* **13,** 1011–1021 (1992).

193. Hub, J. S., De Groot, B. L. and Van Der Spoel, D. g_wham – A free weighted histogram analysis implementation including robust error and autocorrelation estimates. *Journal of Chemical Theory and Computation* **6,** 3713–3720 (2010).

194. Davis, M. E. and Mccammon, J. A. Electrostatics in biomolecular structure and dynamics. *Chemical Reviews* **90,** 509–521 (1990).

195. Honig, B. and Nicholls, A. Classical electrostatics in biology and chemistry. *Science* **268,** 1144–1149 (1995).

196. Sharp, K. A. and Honig, B. Calculating total electrostatic energies with the nonlinear Poisson-Boltzmann equation. *Journal of Physical Chemistry* **94,** 7684–7692 (1990).

197. Debye, P. and Hückel, E. Zur Theorie der Elektrolyte. I. Gefrierpunktserniedrigung und verwandte Erscheinungen. *Physikalische Zeitschrift* **24,** 185–206 (1923).

198. Baker, N. A. Poisson-Boltzmann methods for biomolecular electrostatics. *Methods in Enzymology* **383,** 94–118 (2004).

199. Holst, M. and Saied, F. Multigrid solution of the Poisson-Boltzmann equation. *Journal of Computational Chemistry* **14,** 105–113 (1993).

200. Holst, M. J. and Saied, F. Numerical solution of the nonlinear Poisson–Boltzmann equation: Developing more robust and efficient methods. *Journal of Computational Chemistry* **16,** 337–364 (1995).

201. Fogolari, F., Zuccato, P., Esposito, G. and Viglino, P. Biomolecular electrostatics with the linearized Poisson-Boltzmann equation. *Biophysical Journal* **76,** 1–16 (1999).

202. Krone, M., Kozlíková, B., Lindow, N., Baaden, M., Baum, D., Parulek, J., Hege, H.-C. and Viola, I. Visual analysis of biomolecular cavities: State of the art. *Computer Graphics Forum* **35,** 527–551 (2016).

203. Simões, T., Lopes, D., Dias, S., Fernandes, F., Pereira, J., Jorge, J., Bajaj, C. and Gomes, A. Geometric detection algorithms for cavities on protein surfaces in molecular graphics: A survey. *Computer Graphics Forum* **36,** 643–683 (2017).

204. Petřek, M., Košinová, P., Koča, J. and Otyepka, M. MOLE: A Voronoi diagram-based explorer of molecular channels, pores, and tunnels. *Structure* **15,** 1357–1363 (2007).

205. Sehnal, D., Vařeková, R. S., Berka, K., Pravda, L., Navrátilová, V., Banáš, P., Ionescu, C. M., Otyepka, M. and Koča, J. MOLE 2.0: Advanced approach for analysis of biomacromolecular channels. *Journal of Cheminformatics* **5,** 39 (2013).

206. Petřek, M., Otyepka, M., Banáš, P., Košinová, P., Koča, J. and Damborský, J. CAVER: A new tool to explore routes from protein clefts, pockets and cavities. *BMC Bioinformatics* **7,** 316 (2006).

207. Chovancová, E., Pavelka, A., Beneš, P., Strnad, O., Brezovský, J., Kozlíková, B., Gora, A., Šustr, V., Klvaňa, M., Medek, P., Biedermannová, L., Sochor, J. and Damborský, J. CAVER 3.0: A tool for the analysis of transport pathways in dynamic protein structures. *PLoS Computational Biology* **8,** e1002708 (2012).

208. Pavelka, A., Šebestová, E., Kozlíková, B., Brezovský, J., Sochor, J. and Damborský, J. CAVER: Algorithms for analyzing dynamics of tunnels in macromolecules. *IEEE/ACM Transactions on Computational Biology and Bioinformatics* **13,** 505–517 (2016).

209. Smart, O. S., Goodfellow, J. M. and Wallace, B. A. The pore dimensions of gramicidin A. *Biophysical Journal* **65,** 2455–2460 (1993).

210. Metropolis, N., Rosenbluth, A. W., Rosenbluth, M. N., Teller, A. H. and Teller, E. Equation of state calculations by fast computing machines. *The Journal of Chemical Physics* **21,** 1087–1092 (1953).

211. Kirkpatrick, S., Gelatt, C. D. and Vecchi, M. P. Optimization by simulated annealing. *Science* **220,** 671–680 (1983).

212. Nelder, J. A. and Mead, R. A simplex method for function minimization. *The Computer Journal* **7,** 308–313 (1965).

213. Gharpure, A., Teng, J., Zhuang, Y., Noviello, C. M., Walsh, R. M., Cabuco, R., Howard, R. J., Zaveri, N. T., Lindahl, E. and Hibbs, R. E. Agonist selectivity and ion permeation in the $\alpha_3\beta_4$ ganglionic nicotinic receptor. *Neuron* **104,** 501–511.e6 (2019).

214. Hartzell, H. C., Qu, Z., Yu, K., Xiao, Q. and Chien, L. T. Molecular physiology of bestrophins: Multifunctional membrane proteins linked to best disease and other retinopathies. *Physiological Reviews* **88,** 639–672 (2008).

215. Petrukhin, K., Koisti, M. J., Bakall, B., Li, W., Xie, G., Marknell, T., Sandgren, O., Forsman, K., Holmgren, G., Andreasson, S., Vujic, M., Bergen, A. A., McGarty-Dugan, V., Figueroa, D., Austin, C. P., Metzker, M. L., Caskey, C. T. and Wadelius, C. Identification of the gene responsible for best macular dystrophy. *Nature Genetics* **19,** 241–247 (1998).

216. Johnson, A. A., Guziewicz, K. E., Lee, C. J., Kalathur, R. C., Pulido, J. S., Marmorstein, L. Y. and Marmorstein, A. D. Bestrophin 1 and retinal disease. *Progress in Retinal and Eye Research* **58,** 45–69 (2017).

217. Kane Dickson, V., Pedi, L. and Long, S. B. Structure and insights into the function of a Ca^{2+}-activated Cl^- channel. *Nature* **516,** 213–218 (2014).

218. Yang, T., Liu, Q., Kloss, B., Bruni, R., Kalathur, R. C., Guo, Y., Kloppmann, E., Rost, B., Colecraft, H. M. and Hendrickson, W. A. Structure and selectivity in bestrophin ion channels. *Science* **346,** 355–359 (2014).

219. Humphrey, W., Dalke, A. and Schulten, K. VMD: Visual molecular dynamics. *Journal of Molecular Graphics* **14,** 33–38 (1996).

220. Vaisey, G., Miller, A. N. and Long, S. B. Distinct regions that control ion selectivity and calcium-dependent activation in the bestrophin ion channel. *Proceedings of the National Academy of Sciences of the United States of America* **113,** E7399–E7408 (2016).

223. Stansfeld, P. J. and Sansom, M. S. P. From coarse grained to atomistic: A serial multiscale approach to membrane protein simulations. *Journal of Chemical Theory and Computation* **7,** 1157–1166 (2011).

224. Marrink, S. J., Risselada, H. J., Yefimov, S., Tieleman, D. P. and De Vries, A. H. The MARTINI force field: Coarse grained model for biomolecular simulations. *Journal of Physical Chemistry B* **111,** 7812–7824 (2007).

225. Monticelli, L., Kandasamy, S. K., Periole, X., Larson, R. G., Tieleman, D. P. and Marrink, S. J. The MARTINI coarse-grained force field: Extension to proteins. *Journal of Chemical Theory and Computation* **4,** 819–834 (2008).

226. Hess, B., Bekker, H., Berendsen, H. J. C. and Fraaije, J. G. E. M. LINCS: A linear constraint solver for molecular simulations. *Journal of Computational Chemistry* **18,** 1463–1472 (1997).

227. Hess, B. P-LINCS: A parallel linear constraint solver for molecular simulation. *Journal of Chemical Theory and Computation* **4,** 116–122 (2008).

228. Nightingale, E. R. Phenomenological theory of ion solvation. Effective radii of hydrated ions. *Journal of Physical Chemistry* **63,** 1381–1387 (1959).

229. Miller, A. N., Vaisey, G. and Long, S. B. Molecular mechanisms of gating in the calcium-activated chloride channel bestrophin. *eLife* **8,** e43231 (2019).

230. Souaille, M. and Roux, B. Extension to the weighted histogram analysis method: Combining umbrella sampling with free energy calculations. *Computer Physics Communications* **135,** 40–57 (2001).

231. Wimley, W. C. and White, S. H. Experimentally determined hydrophobicity scale for proteins at membrane interfaces. *Nature Structural Biology* **3,** 842–848 (1996).

232. Simm, S., Einloft, J., Mirus, O. and Schleiff, E. 50 years of amino acid hydrophobicity scales: Revisiting the capacity for peptide classification. *Biological Research* **49,** 31 (2016).

233. Kyte, J. and Doolittle, R. F. A simple method for displaying the hydropathic character of a protein. *Journal of Molecular Biology* **157,** 105–132 (1982).

234. Chothia, C. The nature of the accessible and buried surfaces in proteins. *Journal of Molecular Biology* **105,** 1–12 (1976).

235. Hine, J. and Mookerjee, P. K. The intrinsic hydrophilic character of organic compounds. Correlations in terms of structural contributions. *Journal of Organic Chemistry* **40,** 292–298 (1975).

236. Wolfenden, R. V., Cullis, P. M. and Southgate, C. C. Water, protein folding, and the genetic code. *Science* **206,** 575–577 (1979).

237. Wolfenden, R., Andersson, L., Cullis, P. M. and Southgate, C. C. Affinities of amino acid side chains for solvent water. *Biochemistry* **20,** 849–855 (1981).

238. Monera, O. D., Sereda, T. J., Zhou, N. E., Kay, C. M. and Hodges, R. S. Relationship of sidechain hydrophobicity and α-helical propensity on the stability of the single-stranded amphipathic α-helix. *Journal of Peptide Science* **1,** 319–329 (1995).

239. Wimley, W. C., Creamer, T. P. and White, S. H. Solvation energies of amino acid side chains and backbone in a family of host-guest pentapeptides. *Biochemistry* **35,** 5109–5124 (1996).

240. Hessa, T., Kim, H., Bihlmaier, K., Lundin, C., Boekel, J., Andersson, H., Nilsson, I. M., White, S. H. and Von Heijne, G. Recognition of transmembrane helices by the endoplasmic reticulum translocon. *Nature* **433,** 377–381 (2005).

241. Moon, C. P. and Fleming, K. G. Side-chain hydrophobicity scale derived from transmembrane protein folding into lipid bilayers. *Proceedings of the National Academy of Sciences of the United States of America* **108,** 10174–10177 (2011).

242. Zhu, C., Gao, Y., Li, H., Meng, S., Li, L., Francisco, J. S. and Zeng, X. C. Characterizing hydrophobicity of amino acid side chains in a protein environment via measuring contact angle of a water nanodroplet on planarpeptide network. *Proceedings of the National Academy of Sciences of the United States of America* **113,** 12946–12951 (2016).

243. Weeks, J. D., Chandler, D. and Andersen, H. C. Role of repulsive forces in determining the equilibrium structure of simple liquids. *The Journal of Chemical Physics* **54,** 5237–5247 (1971).

244. Chowdhury, R., Ren, T., Shankla, M., Decker, K., Grisewood, M., Prabhakar, J., Baker, C., Golbeck, J. H., Aksimentiev, A., Kumar, M. and Maranas, C. D. PoreDesigner for tuning solute selectivity in a robust and highly permeable outer membrane pore. *Nature Communications* **9,** 3661 (2018).

245. Trick, J. L., Song, C., Wallace, E. J. and Sansom, M. S. P. Voltage Gating of a Biomimetic Nanopore: Electrowetting of a Hydrophobic Barrier. *ACS Nano* **11,** 1840–1847 (2017).

246. Haynes, T., Smith, I. P., Wallace, E. J., Trick, J. L., Sansom, M. S. P. and Khalid, S. Electric-field-driven translocation of ssDNA through hydrophobic nanopores. *ACS Nano* **12,** 8208–8213 (2018).

248. Vriend, G. WHAT IF: A molecular modeling and drug design program. *Journal of Molecular Graphics* **8,** 52–56 (1990).

249. Kuhn, M. Building predictive models in R using the caret package. *Journal of Statistical Software* **28,** 1–26 (2008).

250. R Core Team. *R: A language and environment for statistical computing*. R Foundation for Statistical Computing, Vienna, Austria, 2018.

251. Nadaraya, E. A. On estimating regression. *Theory of Probability and Its Applications* **9,** 141–142 (1964).

252. Watson, G. S. Smooth regression analysis. *Sankhyā: The Indian Journal of Statistics, Series A* **26,** 359–372 (1964).

253. Trick, J. L., Wallace, E. J., Bayley, H. and Sansom, M. S. P. Designing a hydrophobic barrier within biomimetic nanopores. *ACS Nano* **8,** 11268–11279 (2014).

254. Deng, Z., Paknejad, N., Maksaev, G., Sala-Rabanal, M., Nichols, C. G., Hite, R. K. and Yuan, P. Cryo-EM and X-ray structures of TRPV4 reveal insight into ion permeation and gating mechanisms. *Nature Structural and Molecular Biology* **25,** 252–260 (2018).

255. Basak, S., Gicheru, Y., Samanta, A., Molugu, S. K., Huang, W., Fuente, M. L. D., Hughes, T., Taylor, D. J., Nieman, M. T., Moiseenkova-Bell, V. and Chakrapani, S. Cryo-EM structure of 5-HT_{3A} receptor in its resting conformation. *Nature Communications* **9,** 514 (2018).

256. Hilf, R. J. and Dutzler, R. X-ray structure of a prokaryotic pentameric ligand-gated ion channel. *Nature* **452,** 375–379 (2008).

257. Pan, J., Chen, Q., Willenbring, D., Yoshida, K., Tillman, T., Kashlan, O. B., Cohen, A., Kong, X. P., Xu, Y. and Tang, P. Structure of the pentameric ligand-gated ion channel ELIC cocrystallized with its competitive antagonist acetylcholine. *Nature Communications* **3,** 714 (2012).

258. Miller, P. S. and Aricescu, A. R. Crystal structure of a human $GABA_A$ receptor. *Nature* **512,** 270–275 (2014).

259. Liu, S., Xu, L., Guan, F., Liu, Y. T., Cui, Y., Zhang, Q., Zheng, X., Bi, G. Q., Zhou, Z. H., Zhang, X. and Ye, S. Cryo-EM structure of the human $\alpha_5\beta_3$ $GABA_A$ receptor. *Cell Research* **28,** 958–961 (2018).

260. Zhu, S., Noviello, C. M., Teng, J., Walsh, R. M., Kim, J. J. and Hibbs, R. E. Structure of a human synaptic $GABA_A$ receptor. *Nature* **559,** 67–88 (2018).

261. Hilf, R. J., Bertozzi, C., Zimmermann, I., Reiter, A., Trauner, D. and Dutzler, R. Structural basis of open channel block in a prokaryotic pentameric ligand-gated ion channel. *Nature Structural and Molecular Biology* **17,** 1330–1336 (2010).

262. Hilf, R. J. and Dutzler, R. Structure of a potentially open state of a proton-activated pentameric ligand-gated ion channel. *Nature* **457,** 115–118 (2009).

263. Pan, J., Chen, Q., Willenbring, D., Mowrey, D., Kong, X. P., Cohen, A., Divito, C. B., Xu, Y. and Tang, P. Structure of the pentameric ligand-gated ion channel GLIC bound with anesthetic ketamine. *Structure* **20,** 1463–1469 (2012).

264. Sauguet, L., Poitevin, F., Murail, S., Van Renterghem, C., Moraga-Cid, G., Malherbe, L., Thompson, A. W., Koehl, P., Corringer, P. J., Baaden, M. and Delarue, M. Structural basis for ion permeation mechanism in pentameric ligand-gated ion channels. *EMBO Journal* **32,** 728–741 (2013).

265. Sauguet, L., Shahsavar, A., Poitevin, F., Huon, C., Menny, A., Nemecz, À., Haouz, A., Changeux, J. P., Corringer, P. J. and Delarue, M. Crystal structures of a pentameric ligand-gated ion channel provide a mechanism for activation. *Proceedings of the National Academy of Sciences of the United States of America* **111,** 966–971 (2014).

266. Fourati, Z., Sauguet, L. and Delarue, M. Genuine open form of the pentameric ligand-gated ion channel GLIC. *Acta Crystallographica Section D: Biological Crystallography* **71,** 454–460 (2015).

267. Basak, S., Schmandt, N., Gicheru, Y. and Chakrapani, S. Crystal structure and dynamics of a lipid-induced potential desensitized-state of a pentameric ligand-gated channel. *eLife* **6,** e23886 (2017).

268. Fourati, Z., Ruza, R. R., Laverty, D., Drège, E., Delarue-Cochin, S., Joseph, D., Koehl, P., Smart, T. and Delarue, M. Barbiturates bind in the GLIC ion channel pore and cause inhibition by stabilizing a closed state. *Journal of Biological Chemistry* **292,** 1550–1558 (2017).

269. Hibbs, R. E. and Gouaux, E. Principles of activation and permeation in an anion-selective Cys-loop receptor. *Nature* **474,** 54–60 (2011).

270. Althoff, T., Hibbs, R. E., Banerjee, S. and Gouaux, E. X-ray structures of GluCl in apo states reveal a gating mechanism of Cys-loop receptors. *Nature* **512,** 333–337 (2014).

271. Huang, X., Chen, H., Michelsen, K., Schneider, S. and Shaffer, P. L. Crystal structure of human glycine receptor-α_3 bound to antagonist strychnine. *Nature* **526,** 277–280 (2015).

272. Huang, X., Chen, H. and Shaffer, P. L. Crystal structures of human GlyRα_3 bound to ivermectin. *Structure* **25,** 945–950.e2 (2017).

273. Unwin, N. Refined structure of the nicotinic acetylcholine receptor at 4 Å resolution. *Journal of Molecular Biology* **346,** 967–989 (2005).

274. Morales-Perez, C. L., Noviello, C. M. and Hibbs, R. E. X-ray structure of the human $\alpha_4\beta_2$ nicotinic receptor. *Nature* **538,** 411–415 (2016).

275. Twomey, E. C., Yelshanskaya, M. V., Grassucci, R. A., Frank, J. and Sobolevsky, A. I. Channel opening and gating mechanism in AMPA-subtype glutamate receptors. *Nature* **549,** 60–65 (2017).

276. Lü, W., Du, J., Goehring, A. and Gouaux, E. Cryo-EM structures of the triheteromeric NMDA receptor and its allosteric modulation. *Science* **355,** eaal3729 (2017).

277. Mansoor, S. E., Lü, W., Oosterheert, W., Shekhar, M., Tajkhorshid, E. and Gouaux, E. X-ray structures define human $P2X_3$ receptor gating cycle and antagonist action. *Nature* **538,** 66–71 (2016).

278. Kawate, T., Michel, J. C., Birdsong, W. T. and Gouaux, E. Crystal structure of the ATP-gated $P2X_4$ ion channel in the closed state. *Nature* **460,** 592–598 (2009).

279. Hattori, M. and Gouaux, E. Molecular mechanism of ATP binding and ion channel activation in P2X receptors. *Nature* **485,** 207–212 (2012).

280. Kasuya, G., Yamaura, T., Ma, X. B., Nakamura, R., Takemoto, M., Nagumo, H., Tanaka, E., Dohmae, N., Nakane, T., Yu, Y., Ishitani, R., Matsuzaki, O., Hattori, M. and Nureki, O. Structural insights into the competitive inhibition of the ATP-gated P2X receptor channel. *Nature Communications* **8,** 876 (2017).

281. Jin, P., Bulkley, D., Guo, Y., Zhang, W., Guo, Z., Huynh, W., Wu, S., Meltzer, S., Cheng, T., Jan, L. Y., Jan, Y. N. and Cheng, Y. Electron cryo-microscopy structure of the mechanotransduction channel NOMPC. *Nature* **547,** 118–122 (2017).

282. Grieben, M., Pike, A. C., Shintre, C. A., Venturi, E., El-Ajouz, S., Tessitore, A., Shrestha, L., Mukhopadhyay, S., Mahajan, P., Chalk, R., Burgess-Brown, N. A., Sitsapesan, R., Huiskonen, J. T. and Carpenter, E. P. Structure of the polycystic kidney disease TRP channel Polycystin-2 (PC2). *Nature Structural and Molecular Biology* **24,** 114–122 (2017).

283. Wilkes, M., Madej, M. G., Kreuter, L., Rhinow, D., Heinz, V., De Sanctis, S., Ruppel, S., Richter, R. M., Joos, F., Grieben, M., Pike, A. C., Huiskonen, J. T., Carpenter, E. P., Kühlbrandt, W., Witzgall, R. and Ziegler, C. Molecular insights into lipid-assisted Ca^{2+} regulation of the TRP channel Polycystin-2. *Nature Structural and Molecular Biology* **24,** 123–130 (2017).

284. Shen, P. S., Yang, X., DeCaen, P. G., Liu, X., Bulkley, D., Clapham, D. E. and Cao, E. The structure of the polycystic kidney disease channel PKD2 in lipid nanodiscs. *Cell* **167,** 763–773.e11 (2016).

285. Su, Q., Hu, F., Liu, Y., Ge, X., Mei, C., Yu, S., Shen, A., Zhou, Q., Yan, C., Lei, J., Zhang, Y., Liu, X. and Wang, T. Cryo-EM structure of the polycystic kidney disease-like channel PKD2L1. *Nature Communications* **9,** 1192 (2018).

286. Paulsen, C. E., Armache, J. P., Gao, Y., Cheng, Y. and Julius, D. Structure of the TRPA1 ion channel suggests regulatory mechanisms. *Nature* **520,** 511–517 (2015).

287. Zhang, Z., Tóth, B., Szollosi, A., Chen, J. and Csanády, L. Structure of a TRPM2 channel in complex with Ca^{2+} explains unique gating regulation. *eLife* **7,** e36409 (2018).

288. Guo, J., She, J., Zeng, W., Chen, Q., Bai, X. C. and Jiang, Y. Structures of the calcium-activated, non-selective cation channel TRPM4. *Nature* **552,** 205–209 (2017).

289. Autzen, H. E., Myasnikov, A. G., Campbell, M. G., Asarnow, D., Julius, D. and Cheng, Y. Structure of the human TRPM4 ion channel in a lipid nanodisc. *Science* **359,** 228–232 (2018).

290. Schmiege, P., Fine, M., Blobel, G. and Li, X. Human TRPML1 channel structures in open and closed conformations. *Nature* **550,** 366–370 (2017).

291. Chen, Q., She, J., Zeng, W., Guo, J., Xu, H., Bai, X. C. and Jiang, Y. Structure of mammalian endolysosomal TRPML1 channel in nanodiscs. *Nature* **550,** 415–418 (2017).

292. Hirschi, M., Herzik, M. A., Wie, J., Suo, Y., Borschel, W. F., Ren, D., Lander, G. C. and Lee, S. Y. Cryo-electron microscopy structure of the lysosomal calcium-permeable channel TRPML3. *Nature* **550,** 411–414 (2017).

293. Zhou, X., Li, M., Su, D., Jia, Q., Li, H., Li, X. and Yang, J. Cryo-EM structures of the human endolysosomal TRPML3 channel in three distinct states. *Nature Structural and Molecular Biology* **24,** 1146–1154 (2017).

294. Liao, M., Cao, E., Julius, D. and Cheng, Y. Structure of the TRPV1 ion channel determined by electron cryo-microscopy. *Nature* **504,** 107–112 (2013).

295. Cao, E., Liao, M., Cheng, Y. and Julius, D. TRPV1 structures in distinct conformations reveal activation mechanisms. *Nature* **504,** 113–118 (2013).

296. Gao, Y., Cao, E., Julius, D. and Cheng, Y. TRPV1 structures in nanodiscs reveal mechanisms of ligand and lipid action. *Nature* **534,** 347–351 (2016).

297. Zubcevic, L., Herzik, M. A., Chung, B. C., Liu, Z., Lander, G. C. and Lee, S. Y. Cryo-electron microscopy structure of the TRPV2 ion channel. *Nature Structural and Molecular Biology* **23,** 180–186 (2016).

298. Zubcevic, L., Le, S., Yang, H. and Lee, S. Y. Conformational plasticity in the selectivity filter of the TRPV2 ion channel. *Nature Structural and Molecular Biology* **25,** 405–415 (2018).

299. Huynh, K. W., Cohen, M. R., Jiang, J., Samanta, A., Lodowski, D. T., Zhou, Z. H. and Moiseenkova-Bell, V. Y. Structure of the full-length TRPV2 channel by cryo-EM. *Nature Communications* **7,** 11130 (2016).

300. Hughes, T. E., Lodowski, D. T., Huynh, K. W., Yazici, A., Del Rosario, J., Kapoor, A., Basak, S., Samanta, A., Han, X., Chakrapani, S., Zhou, Z. H., Filizola, M., Rohacs, T., Han, S. and Moiseenkova-Bell, V. Y. Structural basis of TRPV5 channel inhibition by econazole revealed by cryo-EM. *Nature Structural and Molecular Biology* **25,** 53–60 (2018).

301. Saotome, K., Singh, A. K., Yelshanskaya, M. V. and Sobolevsky, A. I. Crystal structure of the epithelial calcium channel TRPV6. *Nature* **534,** 506–511 (2016).

302. Singh, A. K., Saotome, K. and Sobolevsky, A. I. Swapping of transmembrane domains in the epithelial calcium channel TRPV6. *Scientific Reports* **7,** 10669 (2017).

303. McGoldrick, L. L., Singh, A. K., Saotome, K., Yelshanskaya, M. V., Twomey, E. C., Grassucci, R. A. and Sobolevsky, A. I. Opening of the human epithelial calcium channel TRPV6. *Nature* **553,** 233–237 (2018).

304. Kong, C., Zeng, W., Ye, S., Chen, L., Sauer, D. B., Lam, Y., Derebe, M. G. and Jiang, Y. Distinct gating mechanisms revealed by the structures of a multi-ligand gated K^+ channel. *eLife* **2012,** e00184 (2012).

305. Miller, A. N. and Long, S. B. Crystal structure of the human two-pore domain potassium channel $K_{2P}1$. *Science* **335,** 432–436 (2012).

306. Lolicato, M., Arrigoni, C., Mori, T., Sekioka, Y., Bryant, C., Clark, K. A. and Minor, D. L. $K_{2P}2.1$ (TREK-1)-activator complexes reveal a cryptic selectivity filter binding site. *Nature* **547,** 364–368 (2017).

307. Brohawn, S. G., Campbell, E. B. and MacKinnon, R. Physical mechanism for gating and mechanosensitivity of the human TRAAK K^+ channel. *Nature* **516,** 126–130 (2014).

308. Dong, Y. Y., Pike, A. C., Mackenzie, A., McClenaghan, C., Aryal, P., Dong, L., Quigley, A., Grieben, M., Goubin, S., Mukhopadhyay, S., Ruda, G. F., Clausen, M. V., Cao, L., Brennan, P. E., Burgess-Brown, N. A., Sansom, M. S. P., Tucker, S. J. and Carpenter, E. P. K_{2P} channel gating mechanisms revealed by structures of TREK-2 and a complex with Prozac. *Science* **347,** 1256–1259 (2015).

309. Zhou, Y., Morais-Cabral, J. H., Kaufman, A. and Mackinnon, R. Chemistry of ion coordination and hydration revealed by a K^+ channel-Fab complex at 2.0 Å resolution. *Nature* **414,** 43–48 (2001).

310. Lockless, S. W., Zhou, M. and MacKinnon, R. Structural and thermodynamic properties of selective ion binding in a K^+ channel. *PLoS Biology* **5,** 1079–1088 (2007).

311. Uysal, S., Vásquez, V., Tereshko, V., Esaki, K., Fellouse, F. A., Sidhu, S. S., Koide, S., Perozo, E. and Kossiakoff, A. Crystal structure of full-length KcsA in its closed conformation. *Proceedings of the National Academy of Sciences of the United States of America* **106,** 6644–6649 (2009).

312. Cuello, L. G., Jogini, V., Cortes, D. M. and Perozo, E. Structural mechanism of C-type inactivation in K^+ channels. *Nature* **466,** 203–208 (2010).

313. Lenaeus, M. J., Burdette, D., Wagner, T., Focia, P. J. and Gross, A. Structures of KcsA in complex with symmetrical quaternary ammonium compounds reveal a hydrophobic binding site. *Biochemistry* **53,** 5365–5373 (2014).

314. Tao, X., Avalos, J. L., Chen, J. and MacKinnon, R. Crystal structure of the eukaryotic strong inward-rectifier K^+ channel $K_{ir}2.2$ at 3.1 Å resolution. *Science* **326,** 1668–1674 (2009).

315. Hansen, S. B., Tao, X. and MacKinnon, R. Structural basis of PIP_2 activation of the classical inward rectifier K^+ channel $K_{ir}2.2$. *Nature* **477,** 495–498 (2011).

316. Whorton, M. R. and MacKinnon, R. Crystal structure of the mammalian GIRK2 K^+ channel and gating regulation by G proteins, PIP_2, and sodium. *Cell* **147,** 199–208 (2011).

317. Martin, G. M., Kandasamy, B., DiMaio, F., Yoshioka, C. and Shyng, S.-L. Anti-diabetic drug binding site in a mammalian K_{ATP} channel revealed by cryo-EM. *eLife* **6,** e31054 (2017).

318. Lee, K. P. K., Chen, J. and Mackinnon, R. Molecular structure of human K_{ATP} in complex with ATP and ADP. *eLife* **6,** e32481 (2017).

319. Kuo, A., Gulbis, J. M., Antcliff, J. F., Rahman, T., Lowe, E. D., Zimmer, J., Cuthbertson, J., Ashcroft, F. M., Ezaki, T. and Doyle, D. A. Crystal structure of the potassium channel K_{ir}Bac1.1 in the closed state. *Science* **300,** 1922–1926 (2003).

320. Nishida, M., Cadene, M., Chait, B. T. and MacKinnon, R. Crystal structure of a K_{ir}3.1-prokaryotic K_{ir} channel chimera. *EMBO Journal* **26,** 4005–4015 (2007).

321. Clarke, O. B., Caputo, A. T., Hill, A. P., Vandenberg, J. I., Smith, B. J. and Gulbis, J. M. Domain reorientation and rotation of an intracellular assembly regulate conduction in K_{ir} potassium channels. *Cell* **141,** 1018–1029 (2010).

322. Jiang, Y., Lee, A., Chen, J., Cadene, M., Chait, B. T. and MacKinnon, R. Crystal structure and mechanism of a calcium-gated potassium channel. *Nature* **417,** 515–522 (2002).

323. Shi, N., Ye, S., Alam, A., Chen, L. and Jiang, Y. Atomic structure of a Na^+- and K^+-conducting channel. *Nature* **440,** 570–574 (2006).

324. Alam, A. and Jiang, Y. High-resolution structure of the open NaK channel. *Nature Structural and Molecular Biology* **16,** 30–34 (2009).

325. Irie, K., Shimomura, T. and Fujiyoshi, Y. The C-terminal helical bundle of the tetrameric prokaryotic sodium channel accelerates the inactivation rate. *Nature Communications* **3,** 793 (2012).

326. Sun, J. and MacKinnon, R. Cryo-EM structure of a KCNQ1/CaM complex reveals insights into congenital long QT syndrome. *Cell* **169,** 1042–1050.e9 (2017).

327. Long, S. B., Campbell, E. B. and MacKinnon, R. Crystal structure of a mammalian voltage-dependent Shaker family K^+ channel. *Science* **309,** 897–903 (2005).

328. Long, S. B., Tao, X., Campbell, E. B. and MacKinnon, R. Atomic structure of a voltage-dependent K^+ channel in a lipid membrane-like environment. *Nature* **450,** 376–382 (2007).

329. Chen, X., Wang, Q., Ni, F. and Ma, J. Structure of the full-length Shaker potassium channel K_V1.2 by normal-mode-based X-ray crystallographic refinement. *Proceedings of the National Academy of Sciences of the United States of America* **107,** 11352–11357 (2010).

330. Whicher, J. R. and MacKinnon, R. Structure of the voltage-gated K^+ channel Eag1 reveals an alternative voltage sensing mechanism. *Science* **353,** 664–669 (2016).

331. Wang, W. and MacKinnon, R. Cryo-EM structure of the open human ether-à-go-go-related K^+ channel hERG. *Cell* **169,** 422–430.e10 (2017).

332. Jiang, Y., Lee, A., Chen, J., Ruta, V., Cadene, M., Chait, B. T. and MacKinnon, R. X-ray structure of a voltage-dependent K^+ channel. *Nature* **423,** 33–41 (2003).

333. Santos, J. S., Asmar-Rovira, G. A., Han, G. W., Liu, W., Syeda, R., Cherezov, V., Baker, K. A., Stevens, R. C. and Montal, M. Crystal structure of a voltage-gated K^+ channel pore module in a closed state in lipid membranes. *Journal of Biological Chemistry* **287,** 43063–43070 (2012).

334. Clayton, G. M., Altieri, S., Heginbotham, L., Unger, V. M. and Morais-Cabral, J. H. Structure of the transmembrane regions of a bacterial cyclic nucleotide-regulated channel. *Proceedings of the National Academy of Sciences of the United States of America* **105,** 1511–1515 (2008).

335. Kowal, J., Biyani, N., Chami, M., Scherer, S., Rzepiela, A. J., Baumgartner, P., Upadhyay, V., Nimigean, C. M. and Stahlberg, H. High-resolution cryoelectron microscopy structure of the cyclic nucleotide-modulated potassium channel MloK1 in a lipid bilayer. *Structure* **26,** 20–27.e3 (2018).

336. Tao, X., Hite, R. K. and MacKinnon, R. Cryo-EM structure of the open high-conductance Ca^{2+}-activated K^+ channel. *Nature* **541,** 46–51 (2017).

337. Hite, R. K., Tao, X. and MacKinnon, R. Structural basis for gating the high-conductance Ca^{2+}-activated K^+ channel. *Nature* **541,** 52–57 (2017).

338. Hite, R. K. and MacKinnon, R. Structural titration of Slo2.2, a Na^+-dependent K^+ channel. *Cell* **168,** 390–399.e11 (2017).

339. Wu, J., Yan, Z., Li, Z., Qian, X., Lu, S., Dong, M., Zhou, Q. and Yan, N. Structure of the voltage-gated calcium channel $Ca_V1.1$ at 3.6 Å resolution. *Nature* **537,** 191–196 (2016).

340. Tang, L., Gamal El-Din, T. M., Payandeh, J., Martinez, G. Q., Heard, T. M., Scheuer, T., Zheng, N. and Catterall, W. A. Structural basis for Ca^{2+} selectivity of a voltage-gated calcium channel. *Nature* **505,** 56–61 (2014).

341. Tang, L., El-Din, T. M., Swanson, T. M., Pryde, D. C., Scheuer, T., Zheng, N. and Catterall, W. A. Structural basis for inhibition of a voltage-gated Ca^{2+} channel by Ca^{2+} antagonist drugs. *Nature* **537,** 117–121 (2016).

342. Li, M., Zhou, X., Wang, S., Michailidis, I., Gong, Y., Su, D., Li, H., Li, X. and Yang, J. Structure of a eukaryotic cyclic-nucleotide-gated channel. *Nature* **542,** 60–65 (2017).

343. James, Z. M., Borst, A. J., Haitin, Y., Frenz, B., DiMaio, F., Zagotta, W. N. and Veesler, D. CryoEM structure of a prokaryotic cyclic nucleotide-gated ion channel. *Proceedings of the National Academy of Sciences of the United States of America* **114,** 4430–4435 (2017).

344. Lee, C. H. and MacKinnon, R. Structures of the human HCN1 hyperpolarization-activated channel. *Cell* **168,** 111–120.e11 (2017).

345. Takeshita, K., Sakata, S., Yamashita, E., Fujiwara, Y., Kawanabe, A., Kurokawa, T., Okochi, Y., Matsuda, M., Narita, H., Okamura, Y. and Nakagawa, A. X-ray crystal structure of voltage-gated proton channel. *Nature Structural and Molecular Biology* **21,** 352–357 (2014).

346. Fan, G., Baker, M. L., Wang, Z., Baker, M. R., Sinyagovskiy, P. A., Chiu, W., Ludtke, S. J. and Serysheva, I. I. Gating machinery of InsP3R channels revealed by electron cryomicroscopy. *Nature* **527,** 336–341 (2015).

347. Yan, Z., Zhou, Q., Wang, L., Wu, J., Zhao, Y., Huang, G., Peng, W., Shen, H., Lei, J. and Yan, N. Structure of the $Na_V1.4$-$\beta1$ complex from electric eel. *Cell* **170,** 470–482.e11 (2017).

348. Payandeh, J., Gamal El-Din, T. M., Scheuer, T., Zheng, N. and Catterall, W. A. Crystal structure of a voltage-gated sodium channel in two potentially inactivated states. *Nature* **486,** 135–139 (2012).

349. Ahuja, S., Mukund, S., Deng, L., Khakh, K., Chang, E., Ho, H., Shriver, S., Young, C., Lin, S., Johnson, J. P., Wu, P., Li, J., Coons, M., Tam, C., Brillantes, B., Sampang, H., Mortara, K., Bowman, K. K., Clark, K. R., Estevez, A., Xie, Z., Verschoof, H., Grimwood, M., Dehnhardt, C., Andrez, J. C., Focken, T., Sutherlin, D. P., Safina, B. S., Starovasnik, M. A., Ortwine, D. F., Franke, Y., Cohen, C. J., Hackos, D. H., Koth, C. M. and Payandeh, J. Structural basis of $Na_V1.7$ inhibition by an isoform-selective small-molecule antagonist. *Science* **350,** aac5464 (2015).

350. Lenaeus, M. J., Gamal El-Din, T. M., Ing, C., Ramanadane, K., Pomès, R., Zheng, N. and Catterall, W. A. Structures of closed and open states of a voltage-gated sodium channel. *Proceedings of the National Academy of Sciences of the United States of America* **114,** E3051–E3060 (2017).

351. Shaya, D., Findeisen, F., Abderemane-Ali, F., Arrigoni, C., Wong, S., Nurva, S. R., Loussouarn, G. and Minor, D. L. Structure of a prokaryotic sodium channel pore reveals essential gating elements and an outer ion binding site common to eukaryotic channels. *Journal of Molecular Biology* **426,** 467–483 (2014).

352. Bagnéris, C., DeCaen, P. G., Naylor, C. E., Pryde, D. C., Nobeli, I., Clapham, D. E. and Wallace, B. A. Prokaryotic Na_VMs channel as a structural and functional model for eukaryotic sodium channel antagonism. *Proceedings of the National Academy of Sciences of the United States of America* **111,** 8428–8433 (2014).

353. Shen, H., Zhou, Q., Pan, X., Li, Z., Wu, J. and Yan, N. Structure of a eukaryotic voltage-gated sodium channel at near-atomic resolution. *Science* **355,** eaal4326 (2017).

354. Zhang, X., Ren, W., Decaen, P., Yan, C., Tao, X., Tang, L., Wang, J., Hasegawa, K., Kumasaka, T., He, J., Wang, J., Clapham, D. E. and Yan, N. Crystal structure of an orthologue of the NaChBac voltage-gated sodium channel. *Nature* **486,** 130–134 (2012).

355. des Georges, A., Clarke, O. B., Zalk, R., Yuan, Q., Condon, K. J., Grassucci, R. A., Hendrickson, W. A., Marks, A. R. and Frank, J. Structural basis for gating and activation of RyR1. *Cell* **167,** 145–157.e17 (2016).

356. Peng, W., Shen, H., Wu, J., Guo, W., Pan, X., Wang, R., Chen, S. R. and Yan, N. Structural basis for the gating mechanism of the type 2 ryanodine receptor RyR2. *Science* **354,** aah5324 (2016).

357. Kintzer, A. F. and Stroud, R. M. Structure, inhibition and regulation of two-pore channel TPC1 from *Arabidopsis thaliana*. *Nature* **531,** 258–262 (2016).

358. She, J., Guo, J., Chen, Q., Zeng, W., Jiang, Y. and Bai, X. C. Structural insights into the voltage and phospholipid activation of the mammalian TPC1 channel. *Nature* **556,** 130–134 (2018).

359. Jasti, J., Furukawa, H., Gonzales, E. B. and Gouaux, E. Structure of acid-sensing ion channel 1 at 1.9 Å resolution and low pH. *Nature* **449,** 316–323 (2007).

360. Dawson, R. J., Benz, J., Stohler, P., Tetaz, T., Joseph, C., Huber, S., Schmid, G., Hügin, D., Pflimlin, P., Trube, G., Rudolph, M. G., Hennig, M. and Ruf, A. Structure of the acid-sensing ion channel 1 in complex with the gating modifier Psalmotoxin 1. *Nature Communications* **3,** 936 (2012).

361. Baconguis, I., Bohlen, C. J., Goehring, A., Julius, D. and Gouaux, E. X-ray structure of acid-sensing ion channel 1-snake toxin complex reveals open state of a Na^+-selective channel. *Cell* **156,** 717–729 (2014).

362. Gonzales, E. B., Kawate, T. and Gouaux, E. Pore architecture and ion sites in acid-sensing ion channels and P2X receptors. *Nature* **460,** 599–604 (2009).

363. Yoder, N., Yoshioka, C. and Gouaux, E. Gating mechanisms of acid-sensing ion channels. *Nature* **555,** 397–401 (2018).

364. Celia, H., Noinaj, N., Zakharov, S. D., Bordignon, E., Botos, I., Santamaria, M., Barnard, T. J., Cramer, W. A., Lloubes, R. and Buchanan, S. K. Structural insight into the role of the Ton complex in energy transduction. *Nature* **538,** 60–65 (2016).

365. Stouffer, A. L., Acharya, R., Salom, D., Levine, A. S., Di Costanzo, L., Soto, C. S., Tereshko, V., Nanda, V., Stayrook, S. and DeGrado, W. F. Structural basis for the function and inhibition of an influenza virus proton channel. *Nature* **451,** 596–599 (2008).

366. Thomaston, J. L., Alfonso-Prieto, M., Woldeyes, R. A., Fraser, J. S., Klein, M. L., Fiorin, G. and DeGrado, W. F. High-resolution structures of the M2 channel from influenza A virus reveal dynamic pathways for proton stabilization and transduction. *Proceedings of the National Academy of Sciences of the United States of America* **112,** 14260–14265 (2015).

367. Wang, J., Pielak, R. M., McClintock, M. A. and Chou, J. J. Solution structure and functional analysis of the influenza B proton channel. *Nature Structural and Molecular Biology* **16,** 1267–1271 (2009).

368. Oxenoid, K., Dong, Y., Cao, C., Cui, T., Sancak, Y., Markhard, A. L., Grabarek, Z., Kong, L., Liu, Z., Ouyang, B., Cong, Y., Mootha, V. K. and Chou, J. J. Architecture of the mitochondrial calcium uniporter. *Nature* **533,** 269–273 (2016).

369. Hattori, M., Iwase, N., Furuya, N., Tanaka, Y., Tsukazaki, T., Ishitani, R., Maguire, M. E., Ito, K., Maturana, A. and Nureki, O. Mg^{2+}-dependent gating of bacterial MgtE channel underlies Mg^{2+} homeostasis. *EMBO Journal* **28,** 3602–3612 (2009).

370. Takeda, H., Hattori, M., Nishizawa, T., Yamashita, K., Shah, S. T., Caffrey, M., Maturana, A. D., Ishitani, R. and Nureki, O. Structural basis for ion selectivity revealed by high-resolution crystal structure of Mg^{2+} channel MgtE. *Nature Communications* **5,** 5374 (2014).

371. Chang, G., Spencer, R. H., Lee, A. T., Barclay, M. T. and Rees, D. C. Structure of the MscL homolog from *Mycobacterium tuberculosis*: A gated mechanosensitive ion channel. *Science* **282,** 2220–2226 (1998).

372. Liu, Z., Gandhi, C. S. and Rees, D. C. Structure of a tetrameric MscL in an expanded intermediate state. *Nature* **461,** 120–124 (2009).

373. Li, J., Guo, J., Ou, X., Zhang, M., Li, Y. and Liu, Z. Mechanical coupling of the multiple structural elements of the large-conductance mechanosensitive channel during expansion. *Proceedings of the National Academy of Sciences of the United States of America* **112,** 10726–10731 (2015).

374. Padayatti, P. S., Leung, J. H., Mahinthichaichan, P., Tajkhorshid, E., Ishchenko, A., Cherezov, V., Soltis, S. M., Jackson, J. B., Stout, C. D., Gennis, R. B. and Zhang, Q. Critical role of water molecules in proton translocation by the membrane-bound transhydrogenase. *Structure* **25,** 1111–1119.e3 (2017).

375. Hou, X., Pedi, L., Diver, M. M. and Long, S. B. Crystal structure of the calcium release-activated calcium channel Orai. *Science* **338,** 1308–1313 (2012).

376. Lee, C., Guo, J., Zeng, W., Kim, S., She, J., Cang, C., Ren, D. and Jiang, Y. The lysosomal potassium channel TMEM175 adopts a novel tetrameric architecture. *Nature* **547,** 472–475 (2017).

377. Yang, H., Hu, M., Guo, J., Ou, X., Cai, T. and Liu, Z. Pore architecture of TRIC channels and insights into their gating mechanism. *Nature* **538,** 537–541 (2016).

378. Su, M., Gao, F., Yuan, Q., Mao, Y., Li, D. L., Guo, Y., Yang, C., Wang, X. H., Bruni, R., Kloss, B., Zhao, H., Zeng, Y., Zhang, F. B., Marks, A. R., Hendrickson, W. A. and Chen, Y. H. Structural basis for conductance through TRIC cation channels. *Nature Communications* **8,** 15103 (2017).

379. Chang, Y., Bruni, R., Kloss, B., Assur, Z., Kloppmann, E., Rost, B., Hendrickson, W. A. and Liu, Q. Structural basis for a pH-sensitive calcium leak across membranes. *Science* **344,** 1131–1135 (2014).

380. Liu, F., Zhang, Z., Csanády, L., Gadsby, D. C. and Chen, J. Molecular structure of the human CFTR ion channel. *Cell* **169,** 85–95.e8 (2017).

381. Zhang, Z. and Chen, J. Atomic structure of the cystic fibrosis transmembrane conductance regulator. *Cell* **167,** 1586–1597.e9 (2016).

382. Zhang, Z., Liu, F. and Chen, J. Conformational changes of CFTR upon phosphorylation and ATP binding. *Cell* **170,** 483–491.e8 (2017).

383. Park, E., Campbell, E. B. and MacKinnon, R. Structure of a CLC chloride ion channel by cryo-electron microscopy. *Nature* **541,** 500–505 (2017).

384. Chen, Y. H., Hu, L., Punta, M., Bruni, R., Hillerich, B., Kloss, B., Rost, B., Love, J., Siegelbaum, S. A. and Hendrickson, W. A. Homologue structure of the SLAC1 anion channel for closing stomata in leaves. *Nature* **467,** 1074–1080 (2010).

385. Axford, D., Foadi, J., Hu, N. J., Choudhury, H. G., Iwata, S., Beis, K., Evans, G. and Alguel, Y. Structure determination of an integral membrane protein at room temperature from crystals *in situ*. *Acta Crystallographica Section D: Biological Crystallography* **71,** 1228–1237 (2015).

386. Paulino, C., Kalienkova, V., Lam, A. K., Neldner, Y. and Dutzler, R. Activation mechanism of the calcium-activated chloride channel TMEM16A revealed by cryo-EM. *Nature* **552,** 421–425 (2017).

387. Dang, S., Feng, S., Tien, J., Peters, C. J., Bulkley, D., Lolicato, M., Zhao, J., Zuberbühler, K., Ye, W., Qi, L., Chen, T., Craik, C. S., Jan, Y. N., Minor, D. L., Cheng, Y. and Jan, L. Y. Cryo-EM structures of the TMEM16A calcium-activated chloride channel. *Nature* **552,** 426–429 (2017).

388. Zubcevic, L., Herzik, M. A., Wu, M., Borschel, W. F., Hirschi, M., Song, A. S., Lander, G. C. and Lee, S. Y. Conformational ensemble of the human TRPV3 ion channel. *Nature Communications* **9,** 4773 (2018).

389. Hou, X., Burstein, S. R. and Long, S. B. Structures reveal opening of the store-operated calcium channel Orai. *eLife* **7,** e36758 (2018).

390. Neher, E. and Sakmann, B. Single-channel currents recorded from membrane of denervated frog muscle fibres. *Nature* **260,** 799–802 (1976).

391. Sakmann, B and Neher, E. Patch clamp techniques for studying ionic channels in excitable membranes. *Annual Review of Physiology* **46,** 455–472 (1984).

392. Bormann, J., Hamill, O. P. and Sakmann, B. Mechanism of anion permeation through channels gated by glycine and gamma-aminobutyric acid in mouse cultured spinal neurones. *The Journal of Physiology* **385,** 243–286 (1987).

393. Lemasurier, M., Heginbotham, L. and Miller, C. KcsA: It's a potassium channel. *Journal of General Physiology* **118,** 303–313 (2001).

394. Thompson, S. M. Relations between chord and slope conductances and equivalent electromotive forces. *American Journal of Physiology - Cell Physiology* **250,** C333–C339 (1986).

395. Sachs, J. N., Crozier, P. S. and Woolf, T. B. Atomistic simulations of biologically realistic transmembrane potential gradients. *Journal of Chemical Physics* **121,** 10847–10851 (2004).

396. Kutzner, C., Grubmüller, H., De Groot, B. L. and Zachariae, U. Computational electrophysiology: The molecular dynamics of ion channel permeation and selectivity in atomistic detail. *Biophysical Journal* **101,** 809–817 (2011).

397. Kutzner, C., Köpfer, D. A., Machtens, J. P., De Groot, B. L., Song, C. and Zachariae, U. Insights into the function of ion channels by computational electrophysiology simulations. *Biochimica et Biophysica Acta - Biomembranes* **1858,** 1741–1752 (2016).

398. Roux, B. Influence of the membrane potential on the free energy of an intrinsic protein. *Biophysical Journal* **73,** 2980–2989 (1997).

399. Crozier, P. S., Henderson, D., Rowley, R. L. and Busath, D. D. Model channel ion currents in NaCl-extended simple point charge water solution with applied-field molecular dynamics. *Biophysical Journal* **81,** 3077–3089 (2001).

400. Aksimentiev, A. and Schulten, K. Imaging α-hemolysin with molecular dynamics: Ionic conductance, osmotic permeability, and the electrostatic potential map. *Biophysical Journal* **88,** 3745–3761 (2005).

401. Roux, B. The membrane potential and its representation by a constant electric field in computer simulations. *Biophysical Journal* **95,** 4205–4216 (2008).

402. Gumbart, J., Khalili-Araghi, F., Sotomayor, M. and Roux, B. Constant electric field simulations of the membrane potential illustrated with simple systems. *Biochimica et Biophysica Acta* **1818,** 294–302 (2012).

403. Kumar, A., Basak, S., Rao, S., Gicheru, Y., Mayer, M. L., Sansom, M. S. P. and Chakrapani, S. Mechanisms of activation and desensitization of full-length glycine receptor in lipid nanodiscs. *Nature Communications* **11,** 3752 (2020).

404. Delemotte, L., Dehez, F., Treptow, W. and Tarek, M. Modeling membranes under a transmembrane potential. *Journal of Physical Chemistry B* **112,** 5547–5550 (2008).

405. Curtis, H. J. and Cole, K. S. Transverse electric impedance of the squid giant axon. *Journal of General Physiology* **21,** 757–765 (1938).

406. Hodgkin, A. L. and Huxley, A. F. A quantitative description of membrane current and its application to conduction and excitation in nerve. *The Journal of Physiology* **117,** 500–544 (1952).

407. Sukhorukov, V. L., Arnold, W. M. and Zimmermann, U. Hypotonically induced changes in the plasma membrane of cultured mammalian cells. *The Journal of Membrane Biology* **132,** 27–40 (1993).

408. Solsona, C., Innocenti, B. and Fernández, J. M. Regulation of exocytotic fusion by cell inflation. *Biophysical Journal* **74,** 1061–1073 (1998).

409. Murad, S. and Powles, J. G. A computer simulation of the classic experiment on osmosis and osmotic pressure. *The Journal of Chemical Physics* **99,** 7271–7272 (1993).

410. Kalra, A., Garde, S. and Hummer, G. Osmotic water transport through carbon nanotube membranes. *Proceedings of the National Academy of Sciences of the United States of America* **100,** 10175–10180 (2003).

411. Melcr, J., Bonhenry, D., Timr, Š. and Jungwirth, P. Transmembrane potential modeling: Comparison between methods of constant electric field and ion imbalance. *Journal of Chemical Theory and Computation* **12,** 2418–2425 (2016).

412. Sotomayor, M., Vásquez, V., Perozo, E. and Schulten, K. Ion conduction through MscS as determined by electrophysiology and simulation. *Biophysical Journal* **92,** 886–902 (2007).

413. Köpfer, D. A., Song, C., Gruene, T., Sheldrick, G. M., Zachariae, U. and De Groot, B. L. Ion permeation in K^+ channels occurs by direct Coulomb knock-on. *Science* **346,** 352–355 (2014).

414. Kopec, W., Köpfer, D. A., Vickery, O. N., Bondarenko, A. S., Jansen, T. L., de Groot, B. L. and Zachariae, U. Direct knock-on of desolvated ions governs strict ion selectivity in K^+ channels. *Nature Chemistry* **10,** 813–820 (2018).

415. Schewe, M., Nematian-Ardestani, E., Sun, H., Musinszki, M., Cordeiro, S., Bucci, G., De Groot, B. L., Tucker, S. J., Rapedius, M. and Baukrowitz, T. A non-canonical voltage-sensing mechanism controls gating in K_{2P} K^+ channels. *Cell* **164,** 937–949 (2016).

416. Brennecke, J. T. and de Groot, B. L. Mechanism of mechanosensitive gating of the TREK-2 potassium channel. *Biophysical Journal* **114,** 1336–1343 (2018).

417. Bernsteiner, H., Zangerl-Plessl, E. M., Chen, X. and Stary-Weinzinger, A. Conduction through a narrow inward-rectifier K^+ channel pore. *Journal of General Physiology* **151,** 1231–1246 (2019).

418. Ulmschneider, M. B., Bagnéris, C., McCusker, E. C., DeCaen, P. G., Delling, M., Clapham, D. E., Ulmschneider, J. P. and Wallace, B. A. Molecular dynamics of ion transport through the open conformation of a bacterial voltage-gated sodium channel. *Proceedings of the National Academy of Sciences of the United States of America* **110,** 6364–6369 (2013).

419. Ke, S., Timin, E. N. and Stary-Weinzinger, A. Different inward and outward conduction mechanisms in Na_VMs suggested by molecular dynamics simulations. *PLoS Computational Biology* **10,** e1003746 (2014).

420. Callahan, K. M. and Roux, B. Molecular dynamics of ion conduction through the selectivity filter of the Na_VAb sodium channel. *Journal of Physical Chemistry B* **122,** 10126–10142 (2018).

421. Heinz, L. P., Kopec, W., De Groot, B. L. and Fink, R. H. In silico assessment of the conduction mechanism of the Ryanodine Receptor 1 reveals previously unknown exit pathways. *Scientific Reports* **8,** 6886 (2018).

422. Basak, S., Gicheru, Y., Rao, S., Sansom, M. S. P. and Chakrapani, S. Cryo-EM reveals two distinct serotonin-bound conformations of full-length 5-HT_{3A} receptor. *Nature* **563,** 270–274 (2018).

423. Michaud-Agrawal, N., Denning, E. J., Woolf, T. B. and Beckstein, O. MDAnalysis: A toolkit for the analysis of molecular dynamics simulations. *Journal of Computational Chemistry* **32,** 2319–2327 (2011).

424. Gowers, R., Linke, M., Barnoud, J., Reddy, T., Melo, M., Seyler, S., Domański, J., Dotson, D., Buchoux, S., Kenney, I. and Beckstein, O. *MDAnalysis: A Python package for the rapid analysis of molecular dynamics simulations* in *Proceedings of the 15th Python in Science Conference* (eds Benthall, S. and Rostrup, S.) (SciPy, Austin, TX, 2016), 98–105.

425. Baker, N. A., Sept, D., Joseph, S., Holst, M. J. and McCammon, J. A. Electrostatics of nanosystems: Application to microtubules and the ribosome. *Proceedings of the National Academy of Sciences of the United States of America* **98,** 10037–10041 (2001).

426. Jurrus, E., Engel, D., Star, K., Monson, K., Brandi, J., Felberg, L. E., Brookes, D. H., Wilson, L., Chen, J., Liles, K., Chun, M., Li, P., Gohara, D. W., Dolinsky, T., Konecny, R., Koes, D. R., Nielsen, J. E., Head-Gordon, T., Geng, W., Krasny, R., Wei, G. W., Holst, M. J., McCammon, J. A. and Baker, N. A. Improvements to the APBS biomolecular solvation software suite. *Protein Science* **27,** 112–128 (2018).

427. Gilson, M. K. and Honig, B. H. Calculation of electrostatic potentials in an enzyme active site. *Nature* **330,** 84–86 (1987).

428. Gilson, M. K., Sharp, K. A. and Honig, B. H. Calculating the electrostatic potential of molecules in solution: Method and error assessment. *Journal of Computational Chemistry* **9,** 327–335 (1988).

429. Rashin, A. A. and Honig, B. Reevaluation of the Born model of ion hydration. *Journal of Physical Chemistry* **89,** 5588–5593 (1985).

430. Born, M. Volumen und Hydratationswärme der Ionen. *Zeitschrift für Physik* **1,** 45–48 (1920).

431. Amiri, S., Tai, K., Beckstein, O., Biggin, P. C. and Sansom, M. S. P. The α_7 nicotinic acetylcholine receptor: Molecular modelling, electrostatics, and energetics. *Molecular Membrane Biology* **22,** 151–162 (2005).

432. Dämgen, M. A. and Biggin, P. C. A refined open state of the glycine receptor obtained via molecular dynamics simulations. *Structure* **28,** 130–139.e2 (2020).

433. Duret, G., Van Renterghem, C., Weng, Y., Prevost, M., Moraga-Cid, G., Huon, C., Sonner, J. M. and Corringer, P. J. Functional prokaryotic-eukaryotic chimera from the pentameric ligand-gated ion channel family. *Proceedings of the National Academy of Sciences of the United States of America* **108,** 12143–12148 (2011).

434. Moroni, M., Meyer, J. O., Lahmann, C. and Sivilotti, L. G. In glycine and $GABA_A$ channels, different subunits contribute asymmetrically to channel conductance via residues in the extracellular domain. *Journal of Biological Chemistry* **286,** 13414–13422 (2011).

435. Moraga-Cid, G., Sauguet, L., Huon, C., Malherbe, L., Girard-Blanc, C., Petres, S., Murail, S., Taly, A., Baaden, M., Delarue, M. and Corringer, P. J. Allosteric and hyperekplexic mutant phenotypes investigated on an α_1 glycine receptor transmembrane structure. *Proceedings of the National Academy of Sciences of the United States of America* **112,** 2865–2870 (2015).

436. Hansen, S. B., Wang, H. L., Taylor, P. and Sine, S. M. An ion selectivity filter in the extracellular domain of Cys-loop receptors reveals determinants for ion conductance. *Journal of Biological Chemistry* **283,** 36066–36070 (2008).

437. Moroni, M., Biro, I., Giugliano, M., Vijayan, R., Biggin, P. C., Beato, M. and Sivilotti, L. G. Chloride ions in the pore of glycine and GABA channels shape the time course and voltage dependence of agonist currents. *Journal of Neuroscience* **31,** 14095–14106 (2011).

438. Kelley, S. P., Dunlop, J. I., Kirkness, E. F., Lambert, J. J. and Peters, J. A. A cytoplasmic region determines single-channel conductance in 5-HT_3 receptors. *Nature* **424,** 321–324 (2003).

439. Hales, T. G., Dunlop, J. I., Deeb, T. Z., Carland, J. E., Kelley, S. P., Lambert, J. J. and Peters, J. A. Common determinants of single channel conductance within the large cytoplasmic loop of 5-hydroxytryptamine type 3 and $\alpha_4\beta_2$ nicotinic acetylcholine receptors. *Journal of Biological Chemistry* **281,** 8062–8071 (2006).

440. Kracun, S., Harkness, P. C., Gibb, A. J. and Millar, N. S. Influence of the M3-M4 intracellular domain upon nicotinic acetylcholine receptor assembly, targeting and function. *British Journal of Pharmacology* **153,** 1474–1484 (2008).

441. Carland, J. E., Cooper, M. A., Sugiharto, S., Jeong, H. J., Lewis, T. M., Barry, P. H., Peters, J. A., Lambert, J. J. and Moorhouse, A. J. Characterization of the effects of charged residues in the intracellular loop on ion permeation in α_1 glycine receptor channels. *Journal of Biological Chemistry* **284,** 2023–2030 (2009).

442. Phulera, S., Zhu, H., Yu, J., Claxton, D. P., Yoder, N., Yoshioka, C. and Gouaux, E. Cryo-EM structure of the benzodiazepine-sensitive $\alpha_1\beta_1\gamma_2$S tri-heteromeric $GABA_A$ receptor in complex with GABA. *eLife* **7,** e39383 (2018).

443. Laverty, D., Desai, R., Uchański, T., Masiulis, S., Stec, W. J., Malinauskas, T., Zivanov, J., Pardon, E., Steyaert, J., Miller, K. W. and Aricescu, A. R. Cryo-EM structure of the human $\alpha_1\beta_3\gamma_2$ $GABA_A$ receptor in a lipid bilayer. *Nature* **565,** 516–520 (2019).

444. Lynch, J. W. Molecular structure and function of the glycine receptor chloride channel. *Physiological Reviews* **84,** 1051–1095 (2004).

445. Legendre, P. Pharmacological evidence for two types of postsynaptic glycinergic receptors on the Mauthner cell of 52-h-old zebrafish larvae. *Journal of Neurophysiology* **77,** 2400–2415 (1997).

446. Keramidas, A., Moorhouse, A. J., French, C. R., Schofield, P. R. and Barry, P. H. M2 pore mutations convert the glycine receptor channel from being anion- to cation-selective. *Biophysical Journal* **79,** 247–259 (2000).

447. Keramidas, A., Moorhouse, A. J., Pierce, K. D., Schofield, P. R. and Barry, P. H. Cation-selective mutations in the M2 domain of the inhibitory glycine receptor channel reveal determinants of ion-charge selectivity. *Journal of General Physiology* **119,** 393–410 (2002).

448. Lopes, P. E., Roux, B. and MacKerell, A. D. Molecular modeling and dynamics studies with explicit inclusion of electronic polarizability: Theory and applications. *Theoretical Chemistry Accounts* **124,** 11–28 (2009).

449. Peng, X., Zhang, Y., Chu, H., Li, Y., Zhang, D., Cao, L. and Li, G. Accurate evaluation of ion conductivity of the gramicidin A channel using a polarizable force field without any corrections. *Journal of Chemical Theory and Computation* **12,** 2973–2982 (2016).

450. Klesse, G., Rao, S., Tucker, S. J. and Sansom, M. S. P. Induced polarization in molecular dynamics simulations of the 5-HT_3 receptor channel. *Journal of the American Chemical Society* **142,** 9415–9427 (2020).

451. Guros, N. B., Balijepalli, A. and Klauda, J. B. Microsecond-timescale simulations suggest 5-HT–mediated preactivation of the 5-HT_{3A} serotonin receptor. *Proceedings of the National Academy of Sciences of the United States of America* **117,** 405–414 (2020).

452. Lev, B. and Allen, T. W. Simulating ion channel activation mechanisms using swarms of trajectories. *Journal of Computational Chemistry* **41,** 387–401 (2020).

453. Marcus, Y. Ionic radii in aqueous solutions. *Chemical Reviews* **88,** 1475–1498 (1988).

454. Gunthorpe, M. J. and Lummis, S. C. Conversion of the ion selectivity of the 5-HT_{3A} receptor from cationic to anionic reveals a conserved feature of the ligand-gated ion channel superfamily. *Journal of Biological Chemistry* **276,** 10977–10983 (2001).

455. Barnes, N. M., Hales, T. G., Lummis, S. C. and Peters, J. A. The 5-HT_3 receptor – the relationship between structure and function. *Neuropharmacology* **56,** 273–284 (2009).

456. Hussy, N., Lukas, W. and Jones, K. A. Functional properties of a cloned 5-hydroxytryptamine ionotropic receptor subunit: Comparison with native mouse receptors. *The Journal of Physiology* **481,** 311–323 (1994).

457. Gunthorpe, M. J., Peters, J. A., Gill, C. H., Lambert, J. J. and Lummis, S. C. The 4′ lysine in the putative channel lining domain affects desensitization but not the single-channel conductance of recombinant homomeric 5-HT_{3A} receptors. *Journal of Physiology* **522,** 187–198 (2000).

458. Miyazawa, A., Fujiyoshi, Y., Stowell, M. and Unwin, N. Nicotinic acetylcholine receptor at 4.6 Å resolution: Transverse tunnels in the channel wall. *Journal of Molecular Biology* **288,** 765–786 (1999).

459. Yuan, S., Filipek, S. and Vogel, H. A gating mechanism of the serotonin 5-HT_3 receptor. *Structure* **24,** 816–825 (2016).

460. Kratochvil, H. T., Carr, J. K., Matulef, K., Annen, A. W., Li, H., Maj, M., Ostmeyer, J., Serrano, A. L., Raghuraman, H., Moran, S. D., Skinner, J. L., Perozo, E., Roux, B., Valiyaveetil, F. I. and Zanni, M. T. Instantaneous ion configurations in the K^+ ion channel selectivity filter revealed by 2D IR spectroscopy. *Science* **353,** 1040–1044 (2016).

461. Roux, B. Ion channels and ion selectivity. *Essays in Biochemistry* **61,** 201–209 (2017).

462. Öster, C., Hendriks, K., Kopec, W., Chevelkov, V., Shi, C., Michl, D., Lange, S., Sun, H., de Groot, B. L. and Lange, A. The conduction pathway of potassium channels is water free under physiological conditions. *Science Advances* **5,** 6756 (2019).

463. Edwards, S., Corry, B., Kuyucak, S. and Chung, S. H. Continuum electrostatics fails to describe ion permeation in the gramicidin channel. *Biophysical Journal* **83,** 1348–1360 (2002).

464. Allen, T. W., Andersen, O. S. and Roux, B. On the importance of atomic fluctuations, protein flexibility, and solvent in ion permeation. *Journal of General Physiology* **124,** 679–690 (2004).

465. Peter, C. and Hummer, G. Ion transport through membrane-spanning nanopores studied by molecular dynamics simulations and continuum electrostatics calculations. *Biophysical Journal* **89,** 2222–2234 (2005).

466. Jogini, V. and Roux, B. Electrostatics of the intracellular vestibule of K^+ channels. *Journal of Molecular Biology* **354,** 272–288 (2005).

467. Tai, K., Haider, S., Grottesi, A. and Sansom, M. S. P. Ion channel gates: Comparative analysis of energy barriers. *European Biophysics Journal* **38,** 347–354 (2009).

468. Parsegian, A. Energy of an ion crossing a low dielectric membrane: Solutions to four relevant electrostatic problems. *Nature* **221,** 844–846 (1969).

469. Masiulis, S., Desai, R., Uchański, T., Serna Martin, I., Laverty, D., Karia, D., Malinauskas, T., Zivanov, J., Pardon, E., Kotecha, A., Steyaert, J., Miller, K. W. and Aricescu, A. R. $GABA_A$ receptor signalling mechanisms revealed by structural pharmacology. *Nature* **565,** 454–459 (2019).

470. Allen, T. W., Andersen, O. S. and Roux, B. Molecular dynamics - potential of mean force calculations as a tool for understanding ion permeation and selectivity in narrow channels. *Biophysical Chemistry* **124,** 251–267 (2006).

471. Portella, G., Hub, J. S., Vesper, M. D. and De Groot, B. L. Not only enthalpy: Large entropy contribution to ion permeation barriers in single-file channels. *Biophysical Journal* **95,** 2275–2282 (2008).

472. Baştuğ, T., Gray-Weale, A., Patra, S. M. and Kuyucak, S. Role of protein flexibility in ion permeation: A case study in gramicidin A. *Biophysical Journal* **90,** 2285–2296 (2006).

473. Yazdani, M., Jia, Z. and Chen, J. Hydrophobic dewetting in gating and regulation of transmembrane protein ion channels. *Journal of Chemical Physics* **153,** 110901 (2020).

474. Shi, Y., Xia, Z., Zhang, J., Best, R., Wu, C., Ponder, J. W. and Ren, P. The polarizable atomic multipole-based AMOEBA force field for proteins. *Journal of Chemical Theory and Computation* **9,** 4046–4063 (2013).

475. Páll, S., Zhmurov, A., Bauer, P., Abraham, M., Lundborg, M., Gray, A., Hess, B. and Lindahl, E. Heterogeneous parallelization and acceleration of molecular dynamics simulations in GROMACS. *Journal of Chemical Physics* **153,** 134110 (2020).

476. Kohnke, B., Kutzner, C. and Grubmüller, H. A GPU-accelerated fast multipole method for GROMACS: Performance and accuracy. *Journal of Chemical Theory and Computation* **16,** 6938–6949 (2020).

477. Jing, Z., Liu, C., Cheng, S. Y., Qi, R., Walker, B. D., Piquemal, J. P. and Ren, P. Polarizable force fields for biomolecular simulations: Recent advances and applications. *Annual Review of Biophysics* **48,** 371–394 (2019).

478. Flegler, V. J., Rasmussen, A., Rao, S., Wu, N., Zenobi, R., Sansom, M. S. P., Hedrich, R., Rasmussen, T. and Böttcher, B. The MscS-like channel YnaI has a gating mechanism based on flexible pore helices. *Proceedings of the National Academy of Sciences* **117,** 28754–28762 (2020).

479. Rattu, P., Haynes, T., Wallace, E. J. and Khalid, S. Translocation of flexible and tensioned ssDNA through in silico designed hydrophobic nanopores with two constrictions. *Nanoscale.* doi:10.1039/d0nr04890a (2020).

480. Xu, C., Lu, P., Gamal El-Din, T. M., Pei, X. Y., Johnson, M. C., Uyeda, A., Bick, M. J., Xu, Q., Jiang, D., Bai, H., Reggiano, G., Hsia, Y., Brunette, T. J., Dou, J., Ma, D., Lynch, E. M., Boyken, S. E., Huang, P. S., Stewart, L., DiMaio, F., Kollman, J. M., Luisi, B. F., Matsuura, T., Catterall, W. A. and Baker, D. Computational design of transmembrane pores. *Nature* **585,** 129–134 (2020).